ISSUE 2007

PROGRESS IN PHYSICS

VOLUME 2

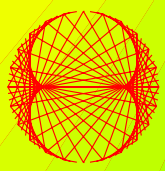

ISSN 1555-5534

The Journal on Advanced Studies in Theoretical and Experimental Physics, including Related Themes from Mathematics

PROGRESS IN PHYSICS

A quarterly issue scientific journal, registered with the Library of Congress (DC, USA). This journal is peer reviewed and included in the abstracting and indexing coverage of: Mathematical Reviews and MathSciNet (AMS, USA), DOAJ of Lund University (Sweden), Zentralblatt MATH (Germany), Referativnyi Zhurnal VINITI (Russia), etc.

Electronic version of this journal:
http://www.ptep-online.com
http://www.geocities.com/ptep_online

To order printed issues of this journal, contact the Editor-in-Chief.

Department of Mathematics and Science, University of New Mexico, 200 College Road, Gallup, NM 87301, USA

ISSN: 1555-5534 (print)
ISSN: 1555-5615 (online)

Standard Address Number: 297-5092
Printed in the United States of America

APRIL 2007 **VOLUME 2**

CONTENTS

Information for Authors and Subscribers

Progress in Physics has been created for publications on advanced studies in theoretical and experimental physics, including related themes from mathematics. All submitted papers should be professional, in good English, containing a brief review of a problem and obtained results.

All submissions should be designed in LaTeX format using *Progress in Physics* template. This template can be downloaded from *Progress in Physics* home page http://www.ptep-online.com. Abstract and the necessary information about author(s) should be included into the papers. To submit a paper, mail the file(s) to Chief Editor.

All submitted papers should be as brief as possible. Commencing 1st January 2006 we accept brief papers, no larger than 8 typeset journal pages. Short articles are preferable. Papers larger than 8 pages can be considered in exceptional cases to the section *Special Reports* intended for such publications in the journal.

All that has been accepted for the online issue of *Progress in Physics* is printed in the paper version of the journal. To order printed issues, contact Chief Editor.

This journal is non-commercial, academic edition. It is printed from private donations.

The Theory of Vortical Gravitational Fields

Dmitri Rabounski
E-mail: rabounski@yahoo.com

This paper treats of vortical gravitational fields, a tensor of which is the rotor of the general covariant gravitational inertial force. The field equations for a vortical gravitational field (the Lorentz condition, the Maxwell-like equations, and the continuity equation) are deduced in an analogous fashion to electrodynamics. From the equations it is concluded that the main kind of vortical gravitational fields is "electric", determined by the non-stationarity of the acting gravitational inertial force. Such a field is a medium for traveling waves of the force (they are different to the weak deformation waves of the space metric considered in the theory of gravitational waves). Standing waves of the gravitational inertial force and their medium, a vortical gravitational field of the "magnetic" kind, are exotic, since a non-stationary rotation of a space body (the source of such a field) is a very rare phenomenon in the Universe.

1 The mathematical method

There are currently two methods for deducing a formula for the Newtonian gravitational force in General Relativity. The first method, introduced by Albert Einstein himself, has its basis in an arbitrary interpretation of Christoffel's symbols in the general covariant geodesic equations (the equation of motion of a free particle) in order to obtain a formula like that by Newton (see [1], for instance). The second method is due to Abraham Zelmanov, who developed it in the 1940's [2, 3]. This method determines the gravitational force in an exact mathematical way, without any suppositions, as a part of the gravitational inertial force derived from the non-commutativity of the differential operators invariant in an observer's spatial section. This formula results from Zelmanov's mathematical apparatus of chronometric invariants (physical observable quantities in General Relativity).

The essence of Zelmanov's mathematical apparatus [4] is that if an observer accompanies his reference body, his observable quantities are the projections of four-dimensional quantities upon his time line and the spatial section — *chronometrically invariant quantities*, via the projecting operators $b^\alpha = \frac{dx^\alpha}{ds}$ and $h_{\alpha\beta} = -g_{\alpha\beta} + b_\alpha b_\beta$, which fully define his real reference space (here b^α is his velocity relative to his real references). So the chr.inv.-projections of a world-vector Q^α are $b_\alpha Q^\alpha = \frac{Q_0}{\sqrt{g_{00}}}$ and $h^i_\alpha Q^\alpha = Q^i$, while the chr.inv.-projections of a 2nd rank world-tensor $Q^{\alpha\beta}$ are $b^\alpha b^\beta Q_{\alpha\beta} = \frac{Q_{00}}{g_{00}}$, $h^{i\alpha} b^\beta Q_{\alpha\beta} = \frac{Q^i_0}{\sqrt{g_{00}}}$, $h^i_\alpha h^k_\beta Q^{\alpha\beta} = Q^{ik}$. The principal physical observable properties of a space are derived from the fact that the chr.inv.-differential operators $\frac{{}^*\partial}{\partial t} = \frac{1}{\sqrt{g_{00}}}\frac{\partial}{\partial t}$ and $\frac{{}^*\partial}{\partial x^i} = \frac{\partial}{\partial x^i} + \frac{1}{c^2} v_i \frac{{}^*\partial}{\partial t}$ are non-commutative as $\frac{{}^*\partial^2}{\partial x^i \partial t} - \frac{{}^*\partial^2}{\partial t \partial x^i} = \frac{1}{c^2} F_i \frac{{}^*\partial}{\partial t}$ and $\frac{{}^*\partial^2}{\partial x^i \partial x^k} - \frac{{}^*\partial^2}{\partial x^k \partial x^i} = \frac{2}{c^2} A_{ik} \frac{{}^*\partial}{\partial t}$, and also that the chr.inv.-metric tensor $h_{ik} = -g_{ik} + b_i b_k$ may not be stationary. The principal physical observable characteristics are the chr.inv.-vector of the gravitational inertial force F_i, the chr.inv.-tensor of the angular velocities of the space rotation A_{ik}, and the chr.inv.-tensor of the rates of the space deformations D_{ik}:

$$F_i = \frac{1}{\sqrt{g_{00}}}\left(\frac{\partial \mathrm{w}}{\partial x^i} - \frac{\partial v_i}{\partial t}\right), \quad \mathrm{w} = c^2\left(1 - \sqrt{g_{00}}\right), \tag{1}$$

$$A_{ik} = \frac{1}{2}\left(\frac{\partial v_k}{\partial x^i} - \frac{\partial v_i}{\partial x^k}\right) + \frac{1}{2c^2}\left(F_i v_k - F_k v_i\right), \tag{2}$$

$$D_{ik} = \frac{1}{2}\frac{{}^*\partial h_{ik}}{\partial t}, \; D^{ik} = -\frac{1}{2}\frac{{}^*\partial h^{ik}}{\partial t}, \; D = D^k_k = \frac{{}^*\partial \ln\sqrt{h}}{\partial t}, \tag{3}$$

where w is the gravitational potential, $v_i = -\frac{c\, g_{0i}}{\sqrt{g_{00}}}$ is the linear velocity of the space rotation, $h_{ik} = -g_{ik} + \frac{1}{c^2} v_i v_k$ is the chr.inv.-metric tensor, $h = \det\|h_{ik}\|$, $h\, g_{00} = -g$, and $g = \det\|g_{\alpha\beta}\|$. The observable non-uniformity of the space is set up by the chr.inv.-Christoffel symbols

$$\Delta^i_{jk} = h^{im}\Delta_{jk,m} = \frac{1}{2}\, h^{im}\left(\frac{{}^*\partial h_{jm}}{\partial x^k} + \frac{{}^*\partial h_{km}}{\partial x^j} - \frac{{}^*\partial h_{jk}}{\partial x^m}\right), \tag{4}$$

which are constructed just like Christoffel's usual symbols $\Gamma^\alpha_{\mu\nu} = g^{\alpha\sigma}\Gamma_{\mu\nu,\sigma}$ using h_{ik} instead of $g_{\alpha\beta}$.

A four-dimensional generalization of the chr.inv.-quantities F_i, A_{ik}, and D_{ik} is [5]

$$F_\alpha = -2c^2 b^\beta a_{\beta\alpha}\,, \tag{5}$$

$$A_{\alpha\beta} = c h^\mu_\alpha h^\nu_\beta a_{\mu\nu}\,, \tag{6}$$

$$D_{\alpha\beta} = c h^\mu_\alpha h^\nu_\beta d_{\mu\nu}\,, \tag{7}$$

where

$$a_{\alpha\beta} = \frac{1}{2}\left(\nabla_\alpha b_\beta - \nabla_\beta b_\alpha\right), \;\; d_{\alpha\beta} = \frac{1}{2}\left(\nabla_\alpha b_\beta + \nabla_\beta b_\alpha\right). \tag{8}$$

For instance, the chr.inv.-projections of F^α are

$$\varphi = b_\alpha F^\alpha = \frac{F_0}{\sqrt{g_{00}}} = 0\,, \qquad q^i = h^i_\alpha F^\alpha = F^i. \tag{9}$$

Proceeding from the exact formula for the gravitational inertial force above, we can, for the first time, determine vortical gravitational fields.

2 D'Alembert's equations of the force

It is a matter of fact that two bodies attract each other due to the transfer of the force of gravity. The force of gravity is absent in a homogeneous gravitational field, because the gradient of the gravitational potential $\mathfrak{w}$ is zero everywhere therein. Therefore it is reasonable to consider the field of the vector potential F^α as a medium transferring gravitational attraction via waves of the force.

D'Alembert's equations of the vector field F^α without its inducing sources

$$\Box F^\alpha = 0 \tag{10}$$

are the equations of propagation of waves traveling in the field*. The equations have two chr.inv.-projections

$$b_\sigma \Box F^\sigma = 0\,, \qquad h^i_\sigma \Box F^\sigma = 0\,, \tag{11}$$

which are the same as

$$b_\sigma\, g^{\alpha\beta}\nabla_\alpha\nabla_\beta F^\sigma = 0\,, \qquad h^i_\sigma\, g^{\alpha\beta}\nabla_\alpha\nabla_\beta F^\sigma = 0\,. \tag{12}$$

These are the chr.inv.-d'Alembert equations for the field $F^\alpha = -2c^2 a^{\cdot\alpha}_{\sigma\cdot} b^\sigma$ without its-inducing sources. To obtain the equations in detailed form isn't an easy process. Helpful here is the fact that the chr.inv.-projection of F^α upon a time line is zero. Following this path, after some algebra, we obtain the chr.inv.-d'Alembert equations (11) in the final form

$$\left.\begin{aligned}
&\frac{1}{c^2}\frac{{}^*\partial}{\partial t}\left(F_k F^k\right) + \frac{1}{c^2}F_i\frac{{}^*\partial F^i}{\partial t} + D^k_m\frac{{}^*\partial F^m}{\partial x^k} + \\
&+ h^{ik}\frac{{}^*\partial}{\partial x^i}\left[(D_{kn}+A_{kn})F^n\right] - \frac{2}{c^2}A_{ik}F^iF^k + \\
&+ \frac{1}{c^2}F_mF^mD + \Delta^m_{kn}D^k_mF^n - \\
&- h^{ik}\Delta^m_{ik}\left(D_{mn}+A_{mn}\right)F^n = 0\,, \\
&\frac{1}{c^2}\frac{{}^*\partial^2F^i}{\partial t^2} - h^{km}\frac{{}^*\partial^2F^i}{\partial x^k\partial x^m} + \frac{1}{c^2}\left(D^i_k + A^{\cdot i}_{k\cdot}\right)\frac{{}^*\partial F^k}{\partial t} + \\
&+ \frac{1}{c^2}\frac{{}^*\partial}{\partial t}\left[\left(D^i_k + A^{\cdot i}_{k\cdot}\right)F^k\right] + \frac{1}{c^2}D\frac{{}^*\partial F^i}{\partial t} + \frac{1}{c^2}F^k\frac{{}^*\partial F^i}{\partial x^k} + \\
&+ \frac{1}{c^2}\left(D^i_n + A^{\cdot i}_{n\cdot}\right)F^nD - \frac{1}{c^2}\Delta^i_{km}F^kF^m + \frac{1}{c^4}F_kF^kF^i - \\
&- h^{km}\left\{\frac{{}^*\partial}{\partial x^k}\left(\Delta^i_{mn}F^n\right) + \left(\Delta^i_{kn}\Delta^n_{mp} - \Delta^n_{km}\Delta^i_{np}\right)F^p + \right. \\
&\left. + \Delta^i_{kn}\frac{{}^*\partial F^n}{\partial x^m} - \Delta^n_{km}\frac{{}^*\partial F^i}{\partial x^n}\right\} = 0\,.
\end{aligned}\right\} \tag{13}$$

*The waves travelling in the field of the gravitational inertial force aren't the same as the waves of the weak perturbations of the space metric, routinely considered in the theory of gravitational waves.

3 A vortical gravitational field. The field tensor and pseudo-tensor. The field invariants

We introduce the tensor of the field as a rotor of its four-dimensional vector potential F^α as well as Maxwell's tensor of electromagnetic fields, namely

$$F_{\alpha\beta} = \nabla_\alpha F_\beta - \nabla_\beta F_\alpha = \frac{\partial F_\beta}{\partial x^\alpha} - \frac{\partial F_\alpha}{\partial x^\beta}\,. \tag{14}$$

We will refer to $F_{\alpha\beta}$ (14) as the *tensor of a vortical gravitational field*, because this is actual a four-dimensional vortex of an acting gravitational inertial force F^α.

Taking into account that the chr.inv.-projections of the field potential $F^\alpha = -2c^2 a^{\cdot\alpha}_{\sigma\cdot} b^\sigma$ are $\frac{F_0}{\sqrt{g_{00}}} = 0$, $F^i = h^{ik}F_k$, we obtain the components of the field tensor $F_{\alpha\beta}$:

$$F_{00} = F^{00} = 0\,, \qquad F_{0i} = -\frac{1}{c}\sqrt{g_{00}}\,\frac{{}^*\partial F_i}{\partial t}\,, \tag{15}$$

$$F_{ik} = \frac{{}^*\partial F_i}{\partial x^k} - \frac{{}^*\partial F_k}{\partial x^i} + \frac{1}{c^2}\left(v_i\frac{{}^*\partial F_k}{\partial t} - v_k\frac{{}^*\partial F_i}{\partial t}\right), \tag{16}$$

$$F^{\cdot 0}_{0\cdot} = \frac{1}{c^2}\,v^k\frac{{}^*\partial F_k}{\partial t}, \qquad F^{\cdot i}_{0\cdot} = \frac{1}{c}\sqrt{g_{00}}\,h^{ik}\frac{{}^*\partial F_k}{\partial t}, \tag{17}$$

$$\begin{aligned}
F^{\cdot 0}_{k\cdot} = \frac{1}{\sqrt{g_{00}}}\left[\frac{1}{c}\frac{{}^*\partial F_k}{\partial t} - \frac{1}{c^3}\,v_kv^m\frac{{}^*\partial F_m}{\partial t} + \right. \\
\left. + \frac{1}{c}\,v^m\left(\frac{{}^*\partial F_m}{\partial x^k} - \frac{{}^*\partial F_k}{\partial x^m}\right)\right],
\end{aligned} \tag{18}$$

$$F^{\cdot i}_{k\cdot} = h^{im}\left(\frac{{}^*\partial F_m}{\partial x^k} - \frac{{}^*\partial F_k}{\partial x^m}\right) - \frac{1}{c^2}\,h^{im}v_k\frac{{}^*\partial F_m}{\partial t}\,, \tag{19}$$

$$\begin{aligned}
F^{0k} = \frac{1}{\sqrt{g_{00}}}\left[\frac{1}{c}\,h^{km}\frac{{}^*\partial F_m}{\partial t} + \right. \\
\left. + \frac{1}{c}\,v^nh^{mk}\left(\frac{{}^*\partial F_n}{\partial x^m} - \frac{{}^*\partial F_m}{\partial x^n}\right)\right],
\end{aligned} \tag{20}$$

$$F^{ik} = h^{im}h^{kn}\left(\frac{{}^*\partial F_m}{\partial x^n} - \frac{{}^*\partial F_n}{\partial x^m}\right). \tag{21}$$

We see here two chr.inv.-projections of the field tensor $F_{\alpha\beta}$. We will refer to the time projection

$$E^i = \frac{F^{\cdot i}_{0\cdot}}{\sqrt{g_{00}}} = \frac{1}{c}\,h^{ik}\frac{{}^*\partial F_k}{\partial t}\,, \quad E_i = h_{ik}E^k = \frac{1}{c}\frac{{}^*\partial F_i}{\partial t} \tag{22}$$

as the "electric" observable component of the vortical gravitational field, while the spatial projection will be referred to as the "magnetic" observable component of the field

$$H^{ik} = F^{ik} = h^{im}h^{kn}\left(\frac{{}^*\partial F_m}{\partial x^n} - \frac{{}^*\partial F_n}{\partial x^m}\right), \tag{23}$$

$$H_{ik} = h_{im}h_{kn}H^{mn} = \frac{{}^*\partial F_i}{\partial x^k} - \frac{{}^*\partial F_k}{\partial x^i}\,, \tag{24}$$

which, after use of the 1st Zelmanov identity [2, 3] that links the spatial vortex of the gravitational inertial force to the non-stationary rotation of the observer's space

$$\frac{{}^*\partial A_{ik}}{\partial t}+\frac{1}{2}\left(\frac{{}^*\partial F_k}{\partial x^i}-\frac{{}^*\partial F_i}{\partial x^k}\right)=0\,, \qquad (25)$$

takes the form

$$H^{ik}=2h^{im}h^{kn}\frac{{}^*\partial A_{mn}}{\partial t}\,, \qquad H_{ik}=2\frac{{}^*\partial A_{ik}}{\partial t}\,. \qquad (26)$$

The "electric" observable component E^i of a vortical gravitational field manifests as the non-stationarity of the acting gravitational inertial force F^i. The "magnetic" observable component H_{ik} manifests as the presence of the spatial vortices of the force F^i or equivalently, as the non-stationarity of the space rotation A_{ik} (see formula 26). Thus, two kinds of vortical gravitational fields are possible:

1. Vortical gravitational fields of the "electric" kind ($H_{ik}=0,\ E^i\neq 0$). In this field we have no spatial vortices of the acting gravitational inertial force F^i, which is the same as a stationary space rotation. So a vortical field of this kind consists of only the "electric" component E^i (22) that is the non-stationarity of the force F^i. Note that a vortical gravitational field of the "electric" kind is permitted in both a non-holonomic (rotating) space, if its rotation is stationary, and also in a holonomic space since the zero rotation is the ultimate case of stationary rotations;
2. The "magnetic" kind of vortical gravitational fields is characterized by $E^i=0$ and $H_{ik}\neq 0$. Such a vortical field consists of only the "magnetic" components H_{ik}, which are the spatial vortices of the acting force F^i and the non-stationary rotation of the space. Therefore a vortical gravitational field of the "magnetic" kind is permitted only in a non-holonomic space. Because the d'Alembert equations (13), with the condition $E^i=0$, don't depend on time, a "magnetic" vortical gravitational field is a medium for *standing waves* of the gravitational inertial force.

In addition, we introduce the pseudotensor $F^{*\alpha\beta}$ of the field dual to the field tensor

$$F^{*\alpha\beta}=\frac{1}{2}\,E^{\alpha\beta\mu\nu}F_{\mu\nu}\,, \qquad F_{*\alpha\beta}=\frac{1}{2}\,E_{\alpha\beta\mu\nu}F^{\mu\nu}, \qquad (27)$$

where the four-dimensional completely antisymmetric discriminant tensors $E^{\alpha\beta\mu\nu}=\frac{e^{\alpha\beta\mu\nu}}{\sqrt{-g}}$ and $E_{\alpha\beta\mu\nu}=e_{\alpha\beta\mu\nu}\sqrt{-g}$ transform tensors into pseudotensors in the inhomogeneous anisotropic four-dimensional pseudo-Riemannian space*.

Using the components of the field tensor $F_{\alpha\beta}$, we obtain the chr.inv.-projections of the field pseudotensor $F^{*\alpha\beta}$:

$$H^{*i}=\frac{F^{*\cdot i}_{0\cdot}}{\sqrt{g_{00}}}=\frac{1}{2}\,\varepsilon^{ikm}\left(\frac{{}^*\partial F_k}{\partial x^m}-\frac{{}^*\partial F_m}{\partial x^k}\right), \qquad (28)$$

$$E^{*ik}=F^{*ik}=-\frac{1}{c}\,\varepsilon^{ikm}\frac{{}^*\partial F_m}{\partial t}\,, \qquad (29)$$

where $\varepsilon^{ikm}=b_0\,E^{0ikm}=\sqrt{g_{00}}\,E^{0ikm}=\frac{e^{ikm}}{\sqrt{h}}$ and $\varepsilon_{ikm}=b^0E_{0ikm}=\frac{E_{0ikm}}{\sqrt{g_{00}}}=e_{ikm}\sqrt{h}$ are the chr.inv.-discriminant tensors [2]. Taking into account the 1st Zelmanov identity (25) and the formulae for differentiating ε^{ikm} and ε_{ikm} [2]

$$\frac{{}^*\partial\varepsilon_{imn}}{\partial t}=\varepsilon_{imn}\,D\,, \qquad \frac{{}^*\partial\varepsilon^{imn}}{\partial t}=-\varepsilon^{imn}D\,, \qquad (30)$$

we write the "magnetic" component H^{*i} as follows

$$H^{*i}=\varepsilon^{ikm}\frac{{}^*\partial A_{km}}{\partial t}=2\left(\frac{{}^*\partial\Omega^{*i}}{\partial t}+\Omega^{*i}D\right), \qquad (31)$$

where $\Omega^{*i}=\frac{1}{2}\,\varepsilon^{ikm}A_{km}$ is the chr.inv.-pseudovector of the angular velocity of the space rotation, while the trace $D=h^{ik}D_{ik}=D^n_n$ of the tensor D_{ik} is the rate of the relative expansion of an elementary volume permeated by the field.

Calculating the invariants of a vortical gravitational field ($J_1=F_{\alpha\beta}F^{\alpha\beta}$ and $J_2=F_{\alpha\beta}F^{*\alpha\beta}$), we obtain

$$J_1=h^{im}h^{kn}\left(\frac{{}^*\partial F_i}{\partial x^k}-\frac{{}^*\partial F_k}{\partial x^i}\right)\left(\frac{{}^*\partial F_m}{\partial x^n}-\frac{{}^*\partial F_n}{\partial x^m}\right)-\\ -\frac{2}{c^2}\,h^{ik}\frac{{}^*\partial F_i}{\partial t}\frac{{}^*\partial F_k}{\partial t}\,, \qquad (32)$$

$$J_2=-\frac{2}{c}\,\varepsilon^{imn}\left(\frac{{}^*\partial F_m}{\partial x^n}-\frac{{}^*\partial F_n}{\partial x^m}\right)\frac{{}^*\partial F_i}{\partial t}\,, \qquad (33)$$

which, with the 1st Zelmanov identity (25), are

$$J_1=4h^{im}h^{kn}\frac{{}^*\partial A_{ik}}{\partial t}\frac{{}^*\partial A_{mn}}{\partial t}-\frac{2}{c^2}\,h^{ik}\frac{{}^*\partial F_i}{\partial t}\frac{{}^*\partial F_k}{\partial t}\,, \qquad (34)$$

$$J_2=-\frac{4}{c}\,\varepsilon^{imn}\frac{{}^*\partial A_{mn}}{\partial t}\frac{{}^*\partial F_i}{\partial t}=\\ =-\frac{8}{c}\left(\frac{{}^*\partial\Omega^{*i}}{\partial t}+\Omega^{*i}D\right)\frac{{}^*\partial F_i}{\partial t}\,. \qquad (35)$$

By the strong physical condition of isotropy, a field is isotropic if both invariants of the field are zeroes: $J_1=0$ means that the lengths of the "electric" and the "magnetic" components of the field are the same, while $J_2=0$ means that the components are orthogonal to each other. Owning the case of a vortical gravitational field, we see that such a field is isotropic if the common conditions are true

$$\left.\begin{aligned} &h^{im}h^{kn}\frac{{}^*\partial A_{ik}}{\partial t}\frac{{}^*\partial A_{mn}}{\partial t}=\frac{1}{2c^2}\,h^{ik}\frac{{}^*\partial F_i}{\partial t}\frac{{}^*\partial F_k}{\partial t}\\ &\frac{{}^*\partial A_{mn}}{\partial t}\frac{{}^*\partial F_i}{\partial t}=0 \end{aligned}\right\} \qquad (36)$$

*Here $e^{\alpha\beta\mu\nu}$ and $e_{\alpha\beta\mu\nu}$ are Levi-Civita's unit tensors: the four-dimensional completely antisymmetric unit tensors which transform tensors into pseudotensors in a Galilean reference frame in the four-dimensional pseudo-Euclidean space [1].

however their geometrical sense is not clear.

Thus the anisotropic field can only be a mixed vortical gravitational field bearing both the "electric" and the "magnetic" components. A strictly "electric" or "magnetic" vortical gravitational field is always spatially isotropic.

Taking the above into account, we arrive at the necessary and sufficient conditions for the existence of *standing waves of the gravitational inertial force*:

1. A vortical gravitational field of the strictly "magnetic" kind is the medium for standing waves of the gravitational inertial force;
2. Standing waves of the gravitational inertial force are permitted only in a non-stationary rotating space.

As soon as one of the conditions ceases, the acting gravitational inertial force changes: the standing waves of the force transform into traveling waves.

4 The field equations of a vortical gravitational field

It is known from the theory of fields that the field equations of a field of a four-dimensional vector-potential A^α is a system consisting of 10 equations in 10 unknowns:

- Lorentz's condition $\nabla_\sigma A^\sigma = 0$ states that the four-dimensional potential A^α remains unchanged;
- the continuity equation $\nabla_\sigma j^\sigma = 0$ states that the field-inducing sources ("charges" and "currents") can not be destroyed but merely re-distributed in the space;
- two groups ($\nabla_\sigma F^{\alpha\sigma} = \frac{4\pi}{c} j^\alpha$ and $\nabla_\sigma F^{*\alpha\sigma} = 0$) of the Maxwell-like equations, where the 1st group determines the "charge" and the "current" as the components of the four-dimensional current vector j^α of the field.

This system completely determines a vector field A^α and its sources in a pseudo-Riemannian space. We shall deduce the field equations for a vortical gravitational field as a field of the four-dimensional potential $F^\alpha = -2c^2 a^{\cdot\alpha}_{\sigma\cdot} b^\sigma$.

Writing the divergence $\nabla_\sigma F^\sigma = \frac{\partial F^\sigma}{\partial x^\sigma} + \Gamma^\sigma_{\sigma\mu} F^\mu$ in the chr.inv.-form [2, 3]

$$\nabla_\sigma F^\sigma = \frac{1}{c}\left(\frac{{}^*\partial\varphi}{\partial t} + \varphi D\right) + \frac{{}^*\partial q^i}{\partial x^i} + q^i \frac{{}^*\partial \ln\sqrt{h}}{\partial x^i} - \frac{1}{c^2} F_i q^i \quad (37)$$

where $\frac{{}^*\partial \ln\sqrt{h}}{\partial x^i} = \Delta^j_{ji}$ and $\frac{{}^*\partial q^i}{\partial x^i} + q^i \Delta^j_{ji} = {}^*\nabla_i q^i$, we obtain the *chr.inv.-Lorentz condition* in a vortical gravitational field

$$\frac{{}^*\partial F^i}{\partial x^i} + F^i \Delta^j_{ji} - \frac{1}{c^2} F_i F^i = 0\,. \quad (38)$$

To deduce the Maxwell-like equations for a vortical gravitational field, we collect together the chr.inv.-projections of the field tensor $F_{\alpha\beta}$ and the field pseudotensor $F^{*\alpha\beta}$. Expressing the necessary projections with the tensor of the rate of the space deformation D^{ik} to eliminate the free h^{ik} terms, we obtain

$$E^i = \frac{1}{c} h^{ik} \frac{{}^*\partial F_k}{\partial t} = \frac{1}{c}\frac{{}^*\partial F^i}{\partial t} + \frac{2}{c} F_k D^{ik}, \quad (39)$$

$$H^{ik} = 2h^{im}h^{kn}\frac{{}^*\partial A_{mn}}{\partial t} = \\ = 2\frac{{}^*\partial A^{ik}}{\partial t} + 4\left(A^{i\cdot}_{\cdot n} D^{kn} - A^{k\cdot}_{\cdot m} D^{im}\right), \quad (40)$$

$$H^{*i} = \varepsilon^{imn}\frac{{}^*\partial A_{mn}}{\partial t} = 2\frac{{}^*\partial \Omega^{*i}}{\partial t} + 2\Omega^{*i} D\,, \quad (41)$$

$$E^{*ik} = -\frac{1}{c}\varepsilon^{ikm}\frac{{}^*\partial F_m}{\partial t}\,. \quad (42)$$

After some algebra, we obtain the *chr.inv.-Maxwell-like equations* for a vortical gravitational field

$$\left.\begin{aligned} &\frac{1}{c}\frac{{}^*\partial^2 F^i}{\partial x^i \partial t} + \frac{2}{c}\frac{{}^*\partial}{\partial x^i}\left(F_k D^{ik}\right) + \frac{1}{c}\left(\frac{{}^*\partial F^i}{\partial t} + 2F_k D^{ik}\right)\Delta^j_{ji} - \\ &\qquad - \frac{2}{c} A_{ik}\left(\frac{{}^*\partial A^{ik}}{\partial t} + A^{i\cdot}_{\cdot n} D^{kn}\right) = 4\pi\rho \\ &2\frac{{}^*\partial^2 A^{ik}}{\partial x^k \partial t} - \frac{1}{c^2}\frac{{}^*\partial^2 F^i}{\partial t^2} + 4\frac{{}^*\partial}{\partial x^k}\left(A^{i\cdot}_{\cdot n} D^{kn} - A^{k\cdot}_{\cdot m} D^{im}\right) + \\ &+ 2\left(\Delta^j_{jk} - \frac{1}{c^2} F_k\right)\left\{\frac{{}^*\partial A^{ik}}{\partial t} + 2\left(A^{i\cdot}_{\cdot n} D^{kn} - A^{k\cdot}_{\cdot m} D^{im}\right)\right\} - \\ &- \frac{2}{c^2}\frac{{}^*\partial}{\partial t}\left(F_k D^{ik}\right) - \frac{1}{c^2}\left(\frac{{}^*\partial F^i}{\partial t} + 2F_k D^{ik}\right) D = \frac{4\pi}{c} j^i \end{aligned}\right\} \text{Group I,} \quad (43)$$

$$\left.\begin{aligned} &\frac{{}^*\partial^2 \Omega^{*i}}{\partial x^i \partial t} + \frac{{}^*\partial}{\partial x^i}\left(\Omega^{*i} D\right) + \frac{1}{c^2}\Omega^{*m}\frac{{}^*\partial F_m}{\partial t} + \\ &\qquad + \left(\frac{{}^*\partial \Omega^{*i}}{\partial t} + \Omega^{*i} D\right)\Delta^j_{ji} = 0 \\ &\varepsilon^{ikm}\frac{{}^*\partial^2 F_m}{\partial x^k \partial t} + \varepsilon^{ikm}\left(\Delta^j_{jk} - \frac{1}{c^2} F_k\right)\frac{{}^*\partial F_m}{\partial t} + 2\frac{{}^*\partial^2 \Omega^{*i}}{\partial t^2} + \\ &\qquad + 4D\frac{{}^*\partial \Omega^{*i}}{\partial t} + 2\left(\frac{{}^*\partial D}{\partial t} + D^2\right)\Omega^{*i} = 0 \end{aligned}\right\} \text{Group II.} \quad (44)$$

The *chr.inv.-continuity equation* $\nabla_\sigma j^\sigma = 0$ for a vortical gravitational field follows from the 1st group of the Maxwell-like equations, and is

$$\begin{aligned} &\frac{{}^*\partial^2}{\partial x^i \partial x^k}\left(\frac{{}^*\partial A^{ik}}{\partial t}\right) - \frac{1}{c^2}\left(\frac{{}^*\partial A^{ik}}{\partial t} + A^{i\cdot}_{\cdot n} D^{kn}\right)\left(A_{ik} D + \frac{{}^*\partial A_{ik}}{\partial t}\right) - \\ &- \frac{1}{c^2}\left[\frac{{}^*\partial^2 A^{ik}}{\partial t^2} + \frac{{}^*\partial}{\partial t}\left(A^{i\cdot}_{\cdot n} D^{nk}\right)\right] A_{ik} + \frac{1}{2c^2}\left(\frac{{}^*\partial F^i}{\partial t} + 2F_k D^{ik}\right)\times \\ &\times\left(\frac{{}^*\partial \Delta^j_{ji}}{\partial t} + \frac{D}{c^2} F_i - \frac{{}^*\partial D}{\partial x^i}\right) + 2\frac{{}^*\partial^2}{\partial x^i \partial x^k}\left(A^{i\cdot}_{\cdot n} D^{kn} - A^{k\cdot}_{\cdot m} D^{im}\right) + \\ &+ \left[\frac{{}^*\partial A^{ik}}{\partial t} + 2\left(A^{i\cdot}_{\cdot n} D^{kn} - A^{k\cdot}_{\cdot m} D^{im}\right)\right]\left[\frac{{}^*\partial}{\partial x^i}\left(\Delta^j_{jk} - \frac{1}{c^2} F_k\right) + \right. \\ &\left. + \left(\Delta^j_{ji} - \frac{1}{c^2} F_i\right)\left(\Delta^l_{lk} - \frac{1}{c^2} F_k\right)\right] = 0\,. \end{aligned} \quad (45)$$

To see a simpler sense of the obtained field equations, we take the field equations in a homogeneous space ($\Delta^i_{km} = 0$)

free of deformation ($D_{ik}=0$)*. In such a space the chr.inv.-Maxwell-like equations obtained take the simplified form

$$\left.\begin{aligned} &\frac{1}{c}\frac{{}^*\partial^2 F^i}{\partial x^i \partial t}-\frac{2}{c}A_{ik}\frac{{}^*\partial A^{ik}}{\partial t}=4\pi\rho \\ &2\frac{{}^*\partial^2 A^{ik}}{\partial x^k \partial t}-\frac{2}{c^2}F_k\frac{{}^*\partial A^{ik}}{\partial t}-\frac{1}{c^2}\frac{{}^*\partial^2 F^i}{\partial t^2}=\frac{4\pi}{c}\,j^i \end{aligned}\right\}\ \text{Group I,} \tag{46}$$

$$\left.\begin{aligned} &\frac{{}^*\partial^2\Omega^{*i}}{\partial x^i \partial t}+\frac{1}{c^2}\,\Omega^{*m}\frac{{}^*\partial F_m}{\partial t}=0 \\ &\varepsilon^{ikm}\frac{{}^*\partial^2 F_m}{\partial x^k \partial t}-\frac{1}{c^2}\,\varepsilon^{ikm}F_k\frac{{}^*\partial F_m}{\partial t}+2\frac{{}^*\partial^2\Omega^{*i}}{\partial t^2}=0 \end{aligned}\right\}\ \text{Group II,} \tag{47}$$

where the field-inducing sources are

$$\rho=\frac{1}{4\pi c}\left(\frac{{}^*\partial^2 F^i}{\partial x^i \partial t}-2A_{ik}\frac{{}^*\partial A^{ik}}{\partial t}\right), \tag{48}$$

$$j^i=\frac{c}{2\pi}\left(\frac{{}^*\partial^2 A^{ik}}{\partial x^k \partial t}-\frac{1}{c^2}F_k\frac{{}^*\partial A^{ik}}{\partial t}-\frac{1}{2c^2}\frac{{}^*\partial^2 F^i}{\partial t^2}\right), \tag{49}$$

and the chr.inv.-continuity equation (45) takes the form

$$\frac{{}^*\partial^2}{\partial x^i \partial x^k}\left(\frac{{}^*\partial A^{ik}}{\partial t}\right)-\frac{1}{c^2}A_{ik}\frac{{}^*\partial^2 A^{ik}}{\partial t^2}-\frac{1}{c^2}\frac{{}^*\partial A_{ik}}{\partial t}\frac{{}^*\partial A^{ik}}{\partial t}-\\ -\frac{1}{c^2}\left(\frac{{}^*\partial F_k}{\partial x^i}-\frac{1}{c^2}F_i F_k\right)\frac{{}^*\partial A^{ik}}{\partial t}=0\,. \tag{50}$$

The obtained field equations describe the main properties of vortical gravitational fields:

1. The chr.inv.-Lorentz condition (38) shows the inhomogeneity of a vortical gravitational field depends on the value of the acting gravitational inertial force F^i and also the space inhomogeneity Δ^j_{ji} in the direction the force acts;
2. The 1st group of the chr.inv.-Maxwell-like equations (43) manifests the origin of the field-inducing sources called "charges" ρ and "currents" j^i. The "charge" ρ is derived from the inhomogeneous oscillations of the acting force F^i and also the non-stationary rotation of the space (to within the space inhomogeneity and deformation withheld). The "currents" j^i are derived from the non-stationary rotation of the space, the spatial inhomogeneity of the non-stationarity, and the non-stationary oscillations of the force F^i (to within the same approximation);
3. The 2nd group of the chr.inv.-Maxwell-like equations (44) manifests the properties of the "magnetic" component H^{*i} of the field. The oscillations of the acting force F^i is the main factor making the "magnetic" component distributed inhomogeneously in the space. If there is no acting force ($F^i=0$) and the space is free of deformation ($D_{ik}=0$), the "magnetic" component is stationary.
4. The chr.inv.-continuity equation (50) manifests in the fact that the "charges" and the "currents" inducing a vortical gravitational field, being located in a non-deforming homogeneous space, remain unchanged while the space rotation remains stationary.

Properties of waves travelling in a field of a gravitational inertial force reveal themselves when we equate the field sources ρ and j^i to zero in the field equations (because a free field is a wave):

$$\frac{{}^*\partial^2 F^i}{\partial x^i \partial t}=2A_{ik}\frac{{}^*\partial A^{ik}}{\partial t}\,, \tag{51}$$

$$\frac{{}^*\partial^2 A^{ik}}{\partial x^k \partial t}=\frac{1}{c^2}F_k\frac{{}^*\partial A^{ik}}{\partial t}+\frac{1}{2c^2}\frac{{}^*\partial^2 F^i}{\partial t^2}\,, \tag{52}$$

which lead us to the following conclusions:

1. The inhomogeneous oscillations of the gravitational inertial force F^i, acting in a free vortical gravitational field, is derived mainly from the non-stationary rotation of the space;
2. The inhomogeneity of the non-stationary rotations of a space, filled with a free vortical gravitational field, is derived mainly from the non-stationarity of the oscillations of the force and also the absolute values of the force and the angular acceleration of the space.

The foregoing results show that numerous properties of vortical gravitational fields manifest only if such a field is due strictly to the "electric" or the "magnetic" kind. This fact forces us to study these two kinds of vortical gravitational fields separately.

5 A vortical gravitational field of the "electric" kind

We shall consider a vortical gravitational field strictly of the "electric" kind, which is characterized as follows

$$H_{ik}=\frac{{}^*\partial F_i}{\partial x^k}-\frac{{}^*\partial F_k}{\partial x^i}=2\frac{{}^*\partial A_{ik}}{\partial t}=0\,, \tag{53}$$

$$H^{ik}=2h^{im}h^{kn}\frac{{}^*\partial A_{mn}}{\partial t}=0\,, \tag{54}$$

$$E_i=\frac{1}{c}\frac{{}^*\partial F_i}{\partial t}\neq 0\,, \tag{55}$$

$$E^i=\frac{1}{c}\,h^{ik}\frac{{}^*\partial F_k}{\partial t}=\frac{1}{c}\frac{{}^*\partial F^i}{\partial t}+\frac{2}{c}\,F_k D^{ik}\neq 0\,, \tag{56}$$

$$H^{*i}=\varepsilon^{imn}\frac{{}^*\partial A_{mn}}{\partial t}=2\frac{{}^*\partial\Omega^{*i}}{\partial t}+2\Omega^{*i}D=0\,, \tag{57}$$

$$E^{*ik}=-\frac{1}{c}\,\varepsilon^{ikm}\frac{{}^*\partial F_m}{\partial t}\neq 0\,. \tag{58}$$

*Such a space has no waves of the space metric (waves the space deformation), however waves of the gravitational inertial force are permitted therein.

We are actually considering a stationary rotating space (if it rotates) filled with the field of a non-stationary gravitational inertial force without spatial vortices of the force. This is the main kind of vortical gravitational fields, because a non-stationary rotation of a space body is very rare (see the "magnetic" kind of fields in the next Section).

In this case the chr.inv.-Lorentz condition doesn't change to the general formula (38), because the condition does not have the components of the field tensor $F_{\alpha\beta}$.

The field invariants $J_1 = F_{\alpha\beta}F^{\alpha\beta}$ and $J_2 = F_{\alpha\beta}F^{*\alpha\beta}$ (34, 35) in this case are

$$J_1 = -\frac{2}{c^2}\, h^{ik}\frac{{}^*\partial F_i}{\partial t}\frac{{}^*\partial F_k}{\partial t}\,, \qquad J_2 = 0\,. \tag{59}$$

The chr.inv.-Maxwell-like equations for a vortical gravitational field strictly of the "electric" kind are

$$\left.\begin{aligned} &{}^*\nabla_i E^i = 4\pi\rho \\ &\frac{1}{c}\left(\frac{{}^*\partial E^i}{\partial t} + E^i D\right) = -\frac{4\pi}{c}\, j^i \end{aligned}\right\} \text{ Group I,} \tag{60}$$

$$\left.\begin{aligned} &E^{*ik}A_{ik} = 0 \\ &{}^*\nabla_k E^{*ik} - \frac{1}{c^2}F_k E^{*ik} = 0 \end{aligned}\right\} \text{ Group II,} \tag{61}$$

and, after E^i and E^{*ik} are substituted, take the form

$$\left.\begin{aligned} &\frac{1}{c}\frac{{}^*\partial^2 F^i}{\partial x^i \partial t} + \frac{1}{c}\left(\frac{{}^*\partial F^i}{\partial t} + 2F_k D^{ik}\right)\Delta^j_{ji} + \\ &\qquad + \frac{2}{c}\frac{{}^*\partial}{\partial x^i}\left(F_k D^{ik}\right) = 4\pi\rho \\ &\frac{1}{c^2}\frac{{}^*\partial^2 F^i}{\partial t^2} + \frac{2}{c^2}\frac{{}^*\partial}{\partial t}\left(F_k D^{ik}\right) + \\ &\qquad + \frac{1}{c^2}\left(\frac{{}^*\partial F^i}{\partial t} + 2F_k D^{ik}\right)D = -\frac{4\pi}{c}\, j^i \end{aligned}\right\} \text{ Group I,} \tag{62}$$

$$\left.\begin{aligned} &\frac{1}{c^2}\,\Omega^{*m}\frac{{}^*\partial F_m}{\partial t} = 0 \\ &\varepsilon^{ikm}\frac{{}^*\partial^2 F_m}{\partial x^k \partial t} + \varepsilon^{ikm}\left(\Delta^j_{jk} - \frac{1}{c^2}F_k\right)\frac{{}^*\partial F_m}{\partial t} = 0 \end{aligned}\right\} \text{ Group II.} \tag{63}$$

The chr.inv.-continuity equation for such a field, in the general case of a deforming inhomogeneous space, takes the following form

$$\left(\frac{{}^*\partial F^i}{\partial t} + 2F_k D^{ik}\right)\left(\frac{{}^*\partial \Delta^j_{ji}}{\partial t} - \frac{{}^*\partial D}{\partial x^i} + \frac{D}{c^2}F_i\right) = 0\,, \tag{64}$$

and becomes the identity "zero equal to zero" in the absence of space inhomogeneity and deformation. In fact, the chr. inv.-continuity equation implies that one of the conditions

$$\frac{{}^*\partial F^i}{\partial t} = -2F_k D^{ik}, \qquad \frac{{}^*\partial \Delta^j_{ji}}{\partial t} = \frac{{}^*\partial D}{\partial x^i} - \frac{D}{c^2}F_i \tag{65}$$

or both, are true in such a vortical gravitational field.

The chr.inv.-Maxwell-like equations (62, 63) in a non-deforming homogeneous space become much simpler

$$\left.\begin{aligned} &\frac{1}{c}\frac{{}^*\partial^2 F^i}{\partial x^i \partial t} = 4\pi\rho \\ &\frac{1}{c^2}\frac{{}^*\partial^2 F^i}{\partial t^2} = -\frac{4\pi}{c}\, j^i \end{aligned}\right\} \text{ Group I,} \tag{66}$$

$$\left.\begin{aligned} &\frac{1}{c^2}\,\Omega^{*m}\frac{{}^*\partial F_m}{\partial t} = 0 \\ &\varepsilon^{ikm}\frac{{}^*\partial^2 F_m}{\partial x^k \partial t} - \frac{1}{c^2}\,\varepsilon^{ikm}F_k\frac{{}^*\partial F_m}{\partial t} = 0 \end{aligned}\right\} \text{ Group II.} \tag{67}$$

The field equations obtained specify the properties for vortical gravitational fields of the "electric" kind:

1. The field-inducing sources ρ and j^i are derived mainly from the inhomogeneous oscillations of the acting gravitational inertial force F^i (the "charges" ρ) and the non-stationarity of the oscillations (the "currents" j^i);
2. Such a field is permitted in a rotating space $\Omega^{*i} \neq 0$, if the space is inhomogeneous ($\Delta^i_{kn} \neq 0$) and deforming ($D_{ik} \neq 0$). The field is permitted in a non-deforming homogeneous space, if the space is holonomic ($\Omega^{*i} = 0$);
3. Waves of the acting force F^i travelling in such a field are permitted in the case where the oscillations of the force are homogeneous and stable;
4. The sources ρ and q^i inducing such a field remain constant in a non-deforming homogeneous space.

6 A vortical gravitational field of the "magnetic" kind

A vortical gravitational field strictly of the "magnetic" kind is characterized by its own observable components

$$H_{ik} = \frac{{}^*\partial F_i}{\partial x^k} - \frac{{}^*\partial F_k}{\partial x^i} = 2\frac{{}^*\partial A_{ik}}{\partial t} \neq 0\,, \tag{68}$$

$$H^{ik} = 2h^{im}h^{kn}\frac{{}^*\partial A_{mn}}{\partial t} \neq 0\,, \tag{69}$$

$$E_i = \frac{1}{c}\frac{{}^*\partial F_i}{\partial t} = 0\,, \tag{70}$$

$$E^i = \frac{1}{c}\,h^{ik}\frac{{}^*\partial F_k}{\partial t} = \frac{1}{c}\frac{{}^*\partial F^i}{\partial t} + \frac{2}{c}\,F_k D^{ik} = 0\,, \tag{71}$$

$$H^{*i} = \varepsilon^{imn}\frac{{}^*\partial A_{mn}}{\partial t} = 2\frac{{}^*\partial \Omega^{*i}}{\partial t} + 2\Omega^{*i}D \neq 0\,, \tag{72}$$

$$E^{*ik} = -\frac{1}{c}\,\varepsilon^{ikm}\frac{{}^*\partial F_m}{\partial t} = 0\,. \tag{73}$$

Actually, in such a case, we have a non-stationary rotating space filled with the spatial vortices of a stationary gravitational inertial force F_i. Such kinds of vortical gravitational fields are exotic compared to those of the "electric"

kind, because a non-stationary rotation of a bulky space body (planet, star, galaxy) — the generator of such a field — is a very rare phenomenon in the Universe.

In this case the chr.inv.-Lorentz condition doesn't change to the general formula (38) or for a vortical gravitational field of the "electric" kind, because the condition has no components of the field tensor $F_{\alpha\beta}$.

The field invariants (34, 35) in the case are

$$J_1 = 4h^{im}h^{kn}\frac{{}^*\partial A_{ik}}{\partial t}\frac{{}^*\partial A_{mn}}{\partial t}\,, \qquad J_2 = 0\,. \tag{74}$$

The chr.inv.-Maxwell-like equations for a vortical gravitational field strictly of the "magnetic" kind are

$$\left.\begin{aligned} &\frac{1}{c}\,H^{ik}A_{ik} = -4\pi\rho \\ &{}^*\nabla_k\,H^{ik} - \frac{1}{c^2}F_k H^{ik} = \frac{4\pi}{c}\,j^i \end{aligned}\right\} \text{ Group I,} \tag{75}$$

$$\left.\begin{aligned} &{}^*\nabla_i\,H^{*i} = 0 \\ &\frac{{}^*\partial H^{*i}}{\partial t} + H^{*i}D = 0 \end{aligned}\right\} \text{ Group II,} \tag{76}$$

which, after substituting for H^{ik} and H^{*i}, are

$$\left.\begin{aligned} &\frac{1}{c}\,A^{ik}\frac{{}^*\partial A_{ik}}{\partial t} = -2\pi\rho \\ &\frac{{}^*\partial^2 A^{ik}}{\partial x^k\partial t} + 2\frac{{}^*\partial}{\partial x^k}\left(A^{i\cdot}_{\cdot n}D^{kn} - A^{k\cdot}_{\cdot m}D^{im}\right) + \left(\Delta^j_{jk} - \frac{1}{c^2}F_k\right)\times \\ &\qquad\times\left\{\frac{{}^*\partial A^{ik}}{\partial t} + 2\left(A^{i\cdot}_{\cdot n}D^{kn} - A^{k\cdot}_{\cdot m}D^{im}\right)\right\} = \frac{2\pi}{c}\,j^i \end{aligned}\right\} \text{ Group I,} \tag{77}$$

$$\left.\begin{aligned} &\frac{{}^*\partial^2\Omega^{*i}}{\partial x^i\partial t} + \frac{{}^*\partial}{\partial x^i}\left(\Omega^{*i}D\right) + \left(\frac{{}^*\partial\Omega^{*i}}{\partial t} + \Omega^{*i}D\right)\Delta^j_{ji} = 0 \\ &\frac{{}^*\partial^2\Omega^{*i}}{\partial t^2} + \frac{{}^*\partial}{\partial t}\left(\Omega^{*i}D\right) + \left(\frac{{}^*\partial\Omega^{*i}}{\partial t} + \Omega^{*i}D\right)D = 0 \end{aligned}\right\} \text{ Group II.} \tag{78}$$

The chr.inv.-continuity equation for such a field, in a deforming inhomogeneous space, is

$$\begin{aligned} &\frac{{}^*\partial^2}{\partial x^i\partial x^k}\left(\frac{{}^*\partial A^{ik}}{\partial t}\right) - \frac{1}{c^2}A^{ik}\frac{{}^*\partial^2 A_{ik}}{\partial t^2} - \frac{1}{c^2}\left(\frac{{}^*\partial A^{ik}}{\partial t} + A^{ik}D\right)\times \\ &\times\frac{{}^*\partial A_{ik}}{\partial t} + 2\frac{{}^*\partial^2}{\partial x^i\partial x^k}\left(A^{i\cdot}_{\cdot n}D^{kn} - A^{k\cdot}_{\cdot m}D^{im}\right) + \left\{\frac{{}^*\partial A^{ik}}{\partial t} + \right. \\ &\left. + 2\left(A^{i\cdot}_{\cdot n}D^{kn} - A^{k\cdot}_{\cdot m}D^{im}\right)\right\}\left\{\left(\frac{{}^*\partial\Delta^j_{jk}}{\partial x^i} - \frac{1}{c^2}\frac{{}^*\partial F_k}{\partial x^i} + \right.\right. \\ &\left.\left. + \left(\Delta^j_{jk} - \frac{1}{c^2}F_k\right)\left(\Delta^l_{li} - \frac{1}{c^2}F_i\right)\right\} = 0\,. \end{aligned} \tag{79}$$

If the space is homogeneous and free of deformation, the continuity equation becomes

$$\begin{aligned} &\frac{{}^*\partial^2}{\partial x^i\partial x^k}\left(\frac{{}^*\partial A^{ik}}{\partial t}\right) - \frac{1}{c^2}A^{ik}\frac{{}^*\partial^2 A_{ik}}{\partial t^2} - \\ &- \frac{1}{c^2}\left(\frac{{}^*\partial A_{ik}}{\partial t} + \frac{{}^*\partial F_k}{\partial x^i} - \frac{1}{c^2}F_iF_k\right)\frac{{}^*\partial A^{ik}}{\partial t} = 0\,. \end{aligned} \tag{80}$$

In such a case (a homogeneous space free of deformation) the chr.inv.-Maxwell-like equations (77, 78) become

$$\left.\begin{aligned} &\frac{1}{c}\,A^{ik}\frac{{}^*\partial A_{ik}}{\partial t} = -2\pi\rho \\ &\frac{{}^*\partial^2 A^{ik}}{\partial x^k\partial t} - \frac{1}{c^2}F_k\frac{{}^*\partial A^{ik}}{\partial t} = \frac{2\pi}{c}\,j^i \end{aligned}\right\} \text{ Group I,} \tag{81}$$

$$\left.\begin{aligned} &\frac{{}^*\partial^2\Omega^{*i}}{\partial x^i\partial t} = 0 \\ &\frac{{}^*\partial^2\Omega^{*i}}{\partial t^2} = 0 \end{aligned}\right\} \text{ Group II.} \tag{82}$$

The obtained field equations characterizing a vortical gravitational field of the "magnetic" kind specify the properties of such kinds of fields:

1. The field-inducing "charges" ρ are derived mainly from the non-stationary rotation of the space, while the field "currents" j^i are derived mainly from the non-stationarity and its spatial inhomogeneity;
2. Such a field is permitted in a non-deforming homogeneous space, if the space rotates homogeneously at a constant acceleration;
3. Waves in such a field are standing waves of the acting gravitational inertial force. The waves are permitted only in a space which is inhomogeneous ($\Delta^i_{kn} \neq 0$) and deforming ($D_{ik} \neq 0$);
4. The sources ρ and j^i inducing such a field remain unchanged in a non-deforming homogeneous space where $F^i \neq 0$.

7 Conclusions

According the foregoing results, we conclude that the main kind of vortical gravitational fields is "electric", derived from a non-stationary gravitational inertial force and, in part, the space deformation. Such a field is a medium for traveling waves of the gravitational inertial force. Standing waves of a gravitational inertial force are permitted in a vortical gravitational field of the "magnetic" kind (spatial vortices of a gravitational inertial force or, that is the same, a non-stationary rotation of the space). Standing waves of the gravitational inertial force and their medium, a vortical gravitational field of the "magnetic" kind, are exotic, due to a non-stationary rotation of a bulky space body (the source of such a field) is a very rare phenomenon in the Universe.

It is a matter of fact that gravitational attraction is an everyday reality, so the traveling waves of the gravitational inertial force transferring the attraction should be incontrovertible. I think that the satellite experiment, propounded in [6], would detect the travelling waves since the amplitudes of the lunar or the solar flow waves should be perceptible.

Submitted on September 11, 2006
Accepted on November 15, 2006

References

1. Landau L. D. and Lifshitz E. M. The classical theory of fields. Butterworth–Heinemann, 2003, 428 pages (4th edition).
2. Zelmanov A. L. Chronometric invariants. Dissertation thesis, 1944. American Research Press, Rehoboth (NM), 2006.
3. Zelmanov A. L. Chronometric invariants and co-moving coordinates in the general relativity theory. *Doklady Acad. Nauk USSR*, 1956, v. 107(6), 815 – 818.
4. Rabounski D. Zelmanov's anthropic principle and the infinite relativity principle. *Progress in Physics*, 2005, v. 1, 35 –37.
5. Zelmanov A. L. Orthometric form of monad formalism and its relations to chronometric and kinemetric invariants. *Doklady Acad. Nauk USSR*, 1976, v. 227 (1), 78–81.
6. Rabounski D. A new method to measure the speed of gravitation. *Progress in Physics*, 2005, v. 1, 3–6; The speed of gravitation. *Proc. of the Intern. Meeting PIRT-2005*, Moscow, 2005, 106–111.

Forces of Space Non-Holonomity as the Necessary Condition for Motion of Space Bodies

Larissa Borissova
E-mail: lborissova@yahoo.com

The motion of a satellite in the gravitational field of the Earth is studied. The condition of weightlessness in terms of physical observable quantities is formulated. It is shown that the motion of all planets in the Solar system satisfy this condition. The exact solution of non-null geodesic lines describing the motion of a satellite in a state of weightlessness is obtained. It is shown that two kinds of rotational forces (forces of non-holonomity) exist: the inner force is linked to a gravitational potential, the outer force changes geometric properties of a space. The latter force causes both anisotropy of the velocity of light and additional displacement of mass-bearing bodies.

1 Introduction

We continue studies commenced in [1], where, using General Relativity, the space metric along the Earth's trajectory in the Galaxy was constructed. This metric was constructed in two steps: (i) the metric along the Earth's transit in the gravitational field of the Sun; (ii) using the Lorenz transformation to change to the reference frame moving along the z-axis coinciding with the direction in which the Earth moves in the Galaxy. The behaviour of a light ray in a reference body's space described by the obtained metric was studied in [1]. It follows from exact solutions of the isotropic geodesic lines equations for the obtained metric, that an anisotropy of the velocity of light exists in the z-direction. This anisotropy is due to the motion of the Earth in the Galaxy. The Earth's motion in the Galaxy causes additional spreading of the light ray in this direction: harmonic oscillations with a 24-hour period and amplitude $\frac{\mathrm{v}}{2}$, where v is the velocity of concomitant motion of the Earth with the Solar system in the Galaxy.

The metric describing a satellite's motion around the Earth as it moves concomitantly with the Earth in the gravitational field of the Sun is applied in this paper. The motion of a satellite by means of non-isotropic (non-null) geodesic lines equations is described. The motion of a satellite in a state of weightlessness is realised. The strong mathematical definition of this state in terms of physically observed (chronometrically invariant) quantities of A. L. Zelmanov [2, 3] is formulated. It is shown that the condition of weightlessness means that gravitational-inertial forces are absent in the region in which a satellite moves. The condition of weightlessness is a *condition of a equilibrium* between the gravitational (Newtonian) force F_N attracting a satellite towards the Earth's centre and the force F_ω directing it from the Earth. We called it the *inner force of non-holonomity*. We describe this force as a vector product of two quantities: (1) a pseudo-vector of the angular velocity of the Earth's daily rotation ω; (2) a vector of the linear velocity V of orbital motion of a satellite. The result of vectorial multiplication of these quantities is a pseudo-vector, directed always in the direction opposite to the force of gravitational attraction. If the forces of attraction and rejection are not equal one to other, a satellite: (1) falls to Earth if $F_\omega < F_N$; (2) escapes Earth if $F_\omega > F_N$. It is shown that the condition of weightlessness applies to all planets of the Solar system. Moreover, it is in accordance with Kepler's third law: *the cube of the mean distance of a planet from the Sun is proportional to the square of the period of rotation of the planet around the Sun*.

We obtain the exact solution of the non-isotropic (non-null) geodesic lines equations. It follows from them that the relativistic mass of a satellite in a state of weightlessness is constant; space velocities and space displacements in the r- and z-directions include additions caused by the Earth's daily rotation; the motion in the z-direction coinciding with the Earth's motion in the Solar system includes the effect which is described by harmonic oscillations having a period of 24 hours and an amplitude of 13 cm.

The question as to why the z-direction is preferred, is studied. It is shown that motion along the z-axis is also a rotational motion, with the angular velocity Ω, around the gravitational centre of a greater body. This body attracts the studied body and the gravitational centre around which the studied body rotates with the angular velocity ω. In order that this situation can be realized it is necessary that both these motions satisfy the condition of weightlessness.

It is shown that two kinds of forces exist, linked to a rotational motion. Because rotation of a space means that this space is non-holonomic [2, 3], we called these forces the inner and the outer force of non-holonomity, respectively. They have a different physical nature. From the physical viewpoint the inner force F_ω counteracts the Newtonian force F_N, the outer force F_Ω causes the motion in the z-direction. This action is an interaction of two rotations with the angular velocities ω and Ω, respectively. From the mathematical viewpoint these forces are different, because they are included in different terms of the space-time metric.

2 The weightlessness condition in terms of physical observable quantities

We consider, using the methods of General Relativity, the space of a body which: (1) rotates on its own axis, passing through its centre of gravity; (2) moves as a whole around the centre of gravity of a greater body. For example, the Earth rotates on its axis and simultaneously rotates around the Sun. The period of one rotation of the Earth on its axis is *one astronomical day*, or 86,400 sec. The linear velocity v_{rot} of this rotation depends on geographic latitude ϕ: $\mathrm{v}_{rot} = 500\cos\phi$ m/sec ($\mathrm{v}_{rot} = 0$ at the Earth's poles). The Earth rotates around the Sun with the velocity $\mathrm{v} = 30$ km/sec. The period of this rotation is *one astronomical year*, or 365.25 of astronomical days. The Earth's radius is 6,370 km, the distance between the Earth and the Sun is 150×10^6 km, and therefore we can consider the orbital motion of the Earth approximately as a forward motion.

We will consider every parallel of the Earth as a cylinder oriented in interplanetary space along the Earth's axis, passing through its poles. Every point of the Earth: (1) rotates around the axis with a velocity depending on its geographic latitude; (2) moves together with the Earth in the Sun's space with the velocity 30 km/sec. It is necessary to note that the points of the Earth space, which are on the Earth axis, move forward only. It is evident that, not only for the Earth's poles but also for all points along this direction, the linear velocity of rotation is zero. The combined motion of every point of the Earth's space (except axial points) is a very elongated spiral [1].

This metric is applicable to the general case of one body rotating around another body, moving concomitantly with the latter in the gravitational field of a greater body. For example, the Earth rotates around the Sun with the velocity 30 km/sec and simultaneously moves together with the Sun in the galactic space with the velocity 222 km/sec. The combined motion of the Earth motion in the Galaxy is described by a very elongated spiral. This case is studied in detail in [1]. The combined motion of every point of the Earth's surface in the Galaxy is more complicated trajectory.

The metric describing the space of a body which rotates around another body (or around its own centre of gravity) and moves together with the latter in the gravitational field of a greater body is [1]:

$$ds^2 = \left(1-\frac{2GM}{c^2r}\right)c^2dt^2 + \frac{2\omega r^2}{c}cdtd\varphi - \\ -\left(1+\frac{2GM}{c^2r}\right)dr^2 - r^2d\varphi^2 + \frac{2\omega\mathrm{v}r^2}{c^2}d\varphi dz - dz^2, \quad (1)$$

where $G = 6.67\times10^{-8}$ cm^3/g$\times$sec^2 is Newton's gravitational constant, ω is the angular velocity of the rotation around the axis, v is the orbital velocity of the body, r, φ and z are cylindrical coordinates. We direct the z-axis along a direction of a forward motion. This metric describes the motion of all points of the rotating body, besides axial points.

We apply Zelmanov's theory of physically observed quantities (chronometrically invariants) [2, 3] in order to describe this gravitational field. The three-dimensional observed space of the space-time (1) has a metric h_{ik} ($i = 1, 2, 3$). Its components are

$$\begin{aligned} h_{11} &= 1+\frac{2GM}{c^2r}, \quad h_{22} = r^2\left(1+\frac{\omega^2r^2}{c^2}\right), \\ h_{23} &= -\frac{\omega r^2\mathrm{v}}{c^2}, \qquad h_{33} = 1; \\ h^{11} &= 1-\frac{2GM}{c^2r}, \quad h^{22} = \frac{1}{r^2}\left(1-\frac{\omega^2r^2}{c^2}\right), \\ h^{23} &= \frac{\omega\mathrm{v}}{c^2}, \qquad h^{33} = 1. \end{aligned} \quad (2)$$

Physically observed (chronometrically invariant) characteristics of this space are

$$F^1 = \left(\omega^2r - \frac{GM}{r^2}\right)\left(1+\frac{\omega^2r^2}{c^2}\right), \quad (3)$$

$$A^{12} = -\frac{\omega}{r}\left(1-\frac{2GM}{c^2r}+\frac{\omega^2r^2}{2c^2}\right), \quad A^{31} = \frac{\omega^2\mathrm{v}r}{c^2}, \quad (4)$$

where F^i is a vector of a gravitational-inertial force, A^{ik} is a tensor of an angular velocity of a rotation (a tensor of a non-holonomity). The third characteristic is a tensor of velocities of a deformation $D_{ik} = 0$.

Geometric space characteristics of (2) are chronometrically invariant Christoffel symbols Δ^k_{ij} of the second kind:

$$\Delta^k_{ij} = h^{km}\Delta_{ij,m} = \frac{1}{2}h^{km}\left(\frac{{}^*\partial h_{im}}{\partial x^j} + \frac{{}^*\partial h_{jm}}{\partial x^i} - \frac{{}^*\partial h_{ij}}{\partial x^m}\right), \quad (5)$$

where $\Delta_{ij,m}$ are Christoffel symbols of the first kind, while $\frac{{}^*\partial}{\partial x^i} = \frac{\partial}{\partial x^i} - \frac{1}{c^2}v_i\frac{{}^*\partial}{\partial t}$ is chronometric differentiation with respect to spatial coordinates, and $\frac{{}^*\partial}{\partial t}$ is chronometric differentiation with respect to time. Because the gravitational field described by the metric (1) is stationary, we have $\frac{{}^*\partial}{\partial x^i} = \frac{\partial}{\partial x^i}$

The non-zero components of Δ^k_{ij} for (1) are

$$\begin{aligned} \Delta^1_{11} &= \frac{GM}{c^2r}, \quad \Delta^1_{22} = -r\left(1-\frac{2GM}{c^2r}+\frac{2\omega^2r^2}{c^2}\right), \\ \Delta^1_{23} &= \frac{\omega\mathrm{v}r}{c^2}, \quad \Delta^2_{12} = \frac{1}{r}\left(1+\frac{\omega^2r^2}{c^2}\right), \quad \Delta^2_{13} = -\frac{\omega\mathrm{v}}{c^2r}. \end{aligned} \quad (6)$$

Let's consider the particular case of this motion when the gravitational-inertial force is absent:

$$F^i = 0. \quad (7)$$

We rewrite it for the metric (1) in the form

$$\frac{GM}{r} = \omega^2r^2 = V^2, \quad (8)$$

where V is the linear velocity of a rotational motion.

Substituting into (8) the Earth's mass $M_\oplus = 6\times10^{27}$g and the Earth's radius $R_\oplus = 6.37\times10^8$ cm we obtain the value of a velocity of a rotation $\mathrm{V} = 7.9$ km/sec. This value is the *first space velocity*, which we denote by V_I. If we accelerate a body located on the Earth in this way, so that its velocity acquires the value 7.9 km/sec, it will move freely in the gravitational field of the Earth as an Earth satellite. This means that condition (7) is the *weightlessness condition* in General Relativity, formulated in terms of physically observed quantities.

Substituting into (8) the mass of the Sun $M_\odot = 2\times10^{33}$ g and the distance between the Earth and the Sun $r = 15\times10^{12}$ cm we obtain $\mathrm{v} = 30$ km/sec — the orbital velocity of the Earth in the gravitational field of the Sun. This means that *the Earth rotates around the Sun in the state of weightlessness*.

Analogous calculations show [4] that *the orbital motion of the Moon around the Earth and orbital motions of all planets of the Solar system satisfy the weightlessness condition*. We conclude that the weightlessness condition is the condition by which the force of Newton's attraction F_N equals the force F_ω connected with a rotational motion. It is evident that this force must be directed opposite to that of the Newtonian force. It is possible to consider this force as a vector product of two quantities: (1) a pseudo-scalar of an angular velocity of rotation ω directed along the Earth's axis; (2) a vector $V = \omega \times r$ in a direction tangential to the satellite's orbit. Thus we have

$$F_\omega = \omega \times V = \omega \times \big[\omega \times r\big]. \tag{9}$$

This force is directed opposite to the Newtonian force in a right coordinate frame. Its value is $\omega \mathrm{V} \sin\alpha$, α the angle between these vectors; it equals $\omega^2 r$ if these quantities are orthogonal to one another.

We call this force the *inner force of non-holonomity*, because it acts on a body moving in the inner gravitational field of another body. This force is included in the g_{00}-component of the fundamental metric tensor $g_{\alpha\beta}$.

It is necessary to explain why we consider ω a pseudo-vector. In general, Zelmanov defines a pseudo-vector of an angular velocity $\Omega^i = \frac{1}{2}\,\varepsilon^{imn} A_{mn}$, where ε^{imn} is a completely antisymmetric chronometrically invariant unit tensor. For it we have $\varepsilon^{123} = \frac{1}{\sqrt{h}}$, where h is the determinant of a three-dimensional fundamental metric tensor h_{ik}.

Taking (8) into account, we calculate for the metric (1):

$$h = r^2\left(1 + \frac{3\omega^2 r^2}{c^2}\right), \tag{10}$$

$$A_{12} = -\omega r\left(1 + \frac{3\omega^2 r^2}{2c^2}\right), \tag{11}$$

with the other components of A_{ik} all zero. Consequently only the component $\Omega^3 = -\omega$ is not zero for this metric.

It is easy to calculate for all planets that orbital motion satisfies Kepler's third law.

3 The motion of a satellite in the gravitational field of the Earth

We consider the motion of a satellite in the gravitational field of the Earth rotating around the its own axis and moving in the gravitational field of the Sun (rotating around its centre). This is a motion of a free body, so it is consequently described by the geodesic equations

$$\frac{d^2x^\alpha}{ds^2} + \Gamma^\alpha_{\mu\nu}\frac{dx^\mu}{ds}\frac{dx^\nu}{ds} = 0, \tag{12}$$

where $\frac{dx^\alpha}{ds}$ is a vector of a four-dimensional velocity, $\Gamma^\alpha_{\mu\nu}$ are four-dimensional Christoffel symbols. In terms of observed quantities, these equations have the form

$$\begin{aligned}&\frac{dm}{d\tau} - \frac{m}{c^2}F_i V^i + \frac{m}{c^2}D_{ik}V^iV^k = 0,\\ &\frac{d(mV^i)}{d\tau} + 2m\big(D^i_k + A^{\cdot i}_{k\cdot}\big)V^k - mF^i + m\Delta^i_{nk}V^nV^k = 0,\end{aligned} \tag{13}$$

where τ is proper (observed) time, $V^i = \frac{dx^i}{d\tau}$ is a three-dimensional observed velocity, m is the relativistic mass of a satellite. It is evident that its gravitational field is negligible.

Substituting into these equations the calculated values of A^{ik} and Δ^k_{ij} for the metric (1) and taking into account the condition of weightlessness (8), we obtain a system of equations

$$\frac{dm}{d\tau} = 0\,, \tag{14}$$

$$\begin{aligned}\frac{d}{d\tau}\left(m\frac{dr}{d\tau}\right) + 2m\omega r\left(1 - \frac{\omega^2 r^2}{2c^2}\right)\frac{d\varphi}{d\tau} + \frac{m\omega^2 r}{c^2}\left(\frac{dr}{d\tau}\right)^2 -\\ - mr\left(\frac{d\varphi}{d\tau}\right)^2 + \frac{2m\omega\,\mathrm{v}r}{c^2}\frac{d\varphi}{d\tau}\frac{dz}{d\tau} = 0\,,\end{aligned} \tag{15}$$

$$\begin{aligned}&\frac{d}{d\tau}\left(m\frac{d\varphi}{d\tau}\right) - \frac{2m\omega}{r}\left(1 + \frac{\omega^2 r^2}{2c^2}\right)\frac{dr}{d\tau} +\\ &+ \frac{2m}{r}\left(1 + \frac{\omega^2 r^2}{c^2}\right)\frac{dr}{d\tau}\frac{d\varphi}{d\tau} - \frac{2m\omega\,\mathrm{v}}{c^2 r}\frac{dr}{d\tau}\frac{dz}{d\tau} = 0\,,\end{aligned} \tag{16}$$

$$\frac{d}{d\tau}\left(m\frac{dz}{d\tau}\right) - \frac{2m\omega^2\,\mathrm{v}r}{c^2}\frac{dr}{d\tau} = 0. \tag{17}$$

We obtain from equation (14) that the relativistic mass of a space body is, by a condition of weightlessness, constant: $m = \mathrm{const}$. Using this condition we calculate the first integral of equation (17)

$$\dot z = \dot z_0 + \frac{\omega^2\,\mathrm{v}\left(r^2 - r_0^2\right)}{c^2}, \tag{18}$$

where $\dot z$ denotes differentiation with respect to τ, $\dot z_0$ and r_0 are initial values.

Taking into account that $m=\text{const}$ and also $\frac{GM}{c^2r}=\frac{\omega^2r^2}{c^2}$ (the condition of weightlessness) we rewrite (15) and (16) as

$$\ddot{r}+2\omega r\left(1-\frac{\omega^2r^2}{2c^2}\right)\dot{\varphi}+\frac{\omega^2r}{c^2}\dot{r}^2-r\dot{\varphi}^2+\frac{2\omega\mathrm{v}r}{c^2}\dot{\varphi}\dot{z}=0, \quad (19)$$

$$\ddot{\varphi}-\frac{2\omega}{r}\left(1+\frac{\omega^2r^2}{c^2}\right)\dot{r}+\frac{2}{r}\left(1+\frac{\omega^2r^2}{c^2}\right)\dot{r}\dot{\varphi}-\frac{2\omega\mathrm{v}}{c^2r}\dot{r}\dot{z}=0. \quad (20)$$

The linear velocity of the Earth's rotation around its axis, $\omega r\cos\phi$, has the maximum value, at the equator, $\omega r=$ 500 m/sec, and consequently the maximum value of $\frac{\omega^2r^2}{c^2}=$ $=6\times10^{-11}$. Substituting (18) into (19–20) and neglecting the terms $\frac{\omega^2r^2}{c^2}$ and $\frac{\omega^2r\dot{r}^2}{c^2}$, we obtain

$$\ddot{r}+2\omega r\dot{\varphi}-r\dot{\varphi}^2+\frac{2\omega\mathrm{v}r}{c^2}\dot{\varphi}\dot{z}_0=0\,, \quad (21)$$

$$\ddot{\varphi}-2\omega\frac{\dot{r}}{r}+2\dot{\varphi}\frac{\dot{r}}{r}-\frac{2\omega\mathrm{v}\dot{z}_0}{c^2}\frac{\dot{r}}{r}=0\,. \quad (22)$$

We rewrite (24) in the form

$$\ddot{\varphi}+2\left(\dot{\varphi}-\widetilde{\omega}\right)\frac{\dot{r}}{r}=0\,, \quad (23)$$

where $\widetilde{\omega}=\omega\left(1+\frac{\mathrm{v}\dot{z}_0}{c^2}\right)$. The quantity $\widetilde{\omega}$ is the angular velocity of an Earth point daily rotation containing a correction $\frac{\mathrm{v}\dot{z}_0}{c^2}$ which is due to the orbital motion of the Earth around the Sun. It is necessary that we do not neglect the term $\frac{\mathrm{v}\dot{z}_0}{c^2}$, because its order is 2.7×10^{-9}: we propose $\mathrm{v}=30$ km/sec (the orbital velocity of the Earth) and $\dot{z}_0=8$ km/sec (the initial value of the satellite velocity).

The variable in equation (23) can be separated, and therefore it is easily integrated. The first integral is

$$\dot{\varphi}=\widetilde{\omega}+\frac{\left(\dot{\varphi}_0-\widetilde{\omega}\right)r_0^2}{r^2}\,, \quad (24)$$

where $\dot{\varphi}$ and r_0 are initial values.

Substituting (24) into (21) we obtain, after transformations, the second order differential equation relative to r

$$\ddot{r}+\widetilde{\omega}^2r-\frac{\left(\dot{\varphi}_0-\widetilde{\omega}\right)r_0^4}{r^3}=0\,. \quad (25)$$

We introduce the new variable $p=\dot{r}$. Then $\ddot{r}=p\frac{dp}{dr}$ and (25) becomes

$$p\,dp=\frac{\left(\dot{\varphi}_0-\widetilde{\omega}\right)^2r_0^4}{r^3}\,dr-\widetilde{\omega}^2r\,dr=0\,, \quad (26)$$

the variables of which are also separable. It is easily integrated to

$$\dot{r}^2=\left(\frac{dr}{d\tau}\right)^2=-\omega^2r^2-\frac{\left(\dot{\varphi}_0-\widetilde{\omega}\right)^2r_0^4}{r^2}+K, \quad (27)$$

where the constant of integration K is

$$K=\dot{r}_0^2+r_0^2\left[2\widetilde{\omega}^2+\dot{\varphi}_0\left(\dot{\varphi}_0-2\widetilde{\omega}\right)\right]. \quad (28)$$

We obtain

$$\dot{r}=\frac{dr}{d\tau}=\pm\sqrt{K-\widetilde{\omega}^2r^2-\frac{\left(\dot{\varphi}_0-\widetilde{\omega}\right)^2r_0^4}{r^2}}\,. \quad (29)$$

This too is an equation with separable variables. Considering the positive sign we obtain, after elementary transformations,

$$d\tau=\frac{r\,dr}{\sqrt{-\widetilde{\omega}^2r^4+Kr^2-\left(\dot{\varphi}_0-\widetilde{\omega}\right)^2r_0^4}}\,. \quad (30)$$

Introducing the new variable $y=r^2$ we have

$$d\tau=\frac{1}{2}\frac{dy}{\sqrt{-\widetilde{\omega}^2y^2+Ky-\left(\dot{\varphi}_0-\widetilde{\omega}\right)^2r_0^4}}. \quad (31)$$

Integrating (31) and returning to the old variable r we obtain the expression for τ

$$\tau=-\frac{1}{2\widetilde{\omega}}\arcsin\frac{K-2\widetilde{\omega}^2r^2}{\sqrt{K^2-4\widetilde{\omega}^2\left(\dot{\varphi}_0-\widetilde{\omega}\right)r_0^4}}+B, \quad (32)$$

where B is a constant of integration. Calculating $B=0$ for the initial value of $\tau_0=0$ we rewrite (32) as

$$\sin2\widetilde{\omega}\tau=\frac{2\widetilde{\omega}^2\left(r^2-r_0^2\right)}{\sqrt{K^2-4\widetilde{\omega}^2\left(\dot{\varphi}_0-\omega\right)^2r_0^4}}\,, \quad (33)$$

where r_0 is the initial value of r. It is easy to express r^2 as

$$r^2=r_0^2+\frac{\sqrt{K^2-4\widetilde{\omega}^2\left(\dot{\varphi}_0-\widetilde{\omega}\right)}}{2\widetilde{\omega}^2}\sin2\widetilde{\omega}\tau. \quad (34)$$

Expressing $K^2-4\widetilde{\omega}^2B^2$ through initial values we obtain

$$r=\sqrt{r_0^2+\frac{Q}{2\widetilde{\omega}^2}\sin2\widetilde{\omega}\tau}\,, \qquad Q=\text{const}, \quad (35)$$

where $Q=\sqrt{\left(\dot{r}_0^2+r_0^2\dot{\varphi}_0^2\right)\left[\dot{r}_0^2+r_0^2(\dot{\varphi}_0+2\widetilde{\omega})^2\right]}$.

Substituting (35) into (18) and integrating the resulting expression we have

$$z=\dot{z}_0\tau+\frac{\mathrm{v}Q}{2\widetilde{\omega}c^2}\left(1-\cos2\widetilde{\omega}\tau\right)+z_0\,, \quad (36)$$

where z_0 and $\dot{z}_0$ are initial values.

Substituting (34) into (24) and integrating we obtain for φ the expression

$$\varphi=\widetilde{\omega}\tau+\frac{2\widetilde{\omega}^2r_0^2\left(\dot{\varphi}_0-\widetilde{\omega}\right)}{\sqrt{Q^2-4\widetilde{\omega}^4r_0^4}}\times \times\ln\left|\frac{2\widetilde{\omega}^2r_0^2\tan\widetilde{\omega}\tau+Q-\sqrt{Q^2-4\widetilde{\omega}^4r_0^4}}{2\widetilde{\omega}^2r_0^2\tan\widetilde{\omega}\tau+Q+\sqrt{Q^2-4\widetilde{\omega}^4r_0^4}}\right|+P\,, \quad (37)$$

where the integration constant equals $P=\varphi_0-\frac{2\widetilde{\omega}^2r_0^2(\dot{\varphi}_0-\widetilde{\omega})}{Q^2-4\widetilde{\omega}^4r_0^4}\times$ $\times\ln\left|\frac{Q-\sqrt{Q^2-4\widetilde{\omega}^4r_0^4}}{Q+\sqrt{Q^2-4\widetilde{\omega}^4r_0^4}}\right|$.

We see from (35–37) that trajectories of a freely falling satellite in the Earth's gravitational field conclude corrections for the daily rotation of the Earth. Besides that, the motion in the z-direction coinciding with a forward motion of the Earth includes the velocity of the orbital motion of the Earth around the Sun. Let's estimate the correction in the z-direction caused the orbital motion of the Earth with velocity 30 km/sec. In order to estimate the value Q, we propose that the satellite moved vertically at the initial moment. This means that only the radial component of the initial velocity is not zero: $\dot{r}_0 \neq 0$. Let it be equal to the first space velocity: $\dot{r}_0 \simeq V_I = 8$ km/sec. In this case $Q = V_I^2 \simeq 64$ km^2/sec^2. Taking into account the angular velocity of the daily rotation $\omega = 8 \times 10^{-5}$ sec^{-1} we obtain the correction $\frac{\mathrm{v}Q}{2\widetilde{\omega}c^2} = 13$ cm. This means that a satellite not only moves forward with a velocity $\dot{z}_0$ in the z-direction, it also undergoes harmonic oscillations with the amplitude 13 cm during the 24-hour period.

It is necessary to take into account these corrections in relation to some experiments with satellites. For example, experiments, the aim of which is to discover gravitational waves: two geostationary satellites are considered as two free particles. Measuring changes of the distance between them by means of laser interferometer, scientists propose to discover gravitational waves emitted by different space sources. It is evident, it is necessary to take into account changes of this distance caused by motion of satellites in the gravitational field of the Sun.

Let's study in detail why the z-direction is preferred. The displacement in the z-direction includes the velocity $\mathrm{v} = 30$ km/sec of the Earth's motion in the gravitational field of the Sun. We consider this motion as a "forward" motion. On the other hand, this motion is as well rotation, because the Earth rotates around the Sun. Therefore we can consider v as a vector product of two quantities

$$\mathrm{v} = \Omega \times R\,, \tag{38}$$

where $\Omega = 2 \times 10^{-7}$ sec^{-1} is the angular velocity of the Earth's orbital rotation, $R = 150 \times 10^6$ km is the distance between the Earth and the Sun.

Now we define the *outer force of non-holonomity* F_Ω as a force of a kind different to F_ω. This definition corresponds to the case where one body rotates around another as the latter rotates around a greater body. We define this force also as a force of non-holonomity, because Zelmanov proved that a rotation of a three-dimensional space means that this space is non-holonomic. The metric of the corresponding space-time in this case necessarily includes the mixed (space-time) terms g_{0i}, because it is impossible to transform coordinates in such a way that all $g_{0i} = 0$.

We define the outer force of non-holonomity as

$$F_\Omega = \omega \times \left[\Omega \times R\right], \tag{39}$$

where ω and Ω are angular velocities of two different rotations: ω is the angular velocity of rotation of a space body around a centre of attraction; Ω is the angular velocity of rotation of the concomitant rotation of a space body and its centre of attraction around a greater space body. The interaction of both rotations produces a real force, acting on masses the fields of which are in the region of this force.

We see that this force is included in metric (1) as an off-diagonal term $\frac{\omega \mathrm{v} r^2}{c^2}$. It is also contained in the chronometrically invariant Christoffel symbols (6). Solving the null geodesic lines equations for this metric, we obtained in [1] that an anisotropy of the velocity of light exists in the z-direction. The z-axis in (1) coincides with the direction of the concomitant motion of the Earth with the Solar system. This motion realises the velocity 222 km/sec. The anisotropy correction appearing in this direction as

$$\Delta\dot{z} = \frac{\mathrm{v}}{2} \sin 2\widetilde{\omega}\tau\,, \tag{40}$$

where $\dot{z} = \frac{dz}{d\tau}$, $\widetilde{\omega}$ is the angular velocity of the Earth's orbital motion. thus the value of $\dot{z}$ is realised during one astronomic year harmonic oscillation, with the amplitude 111 km/sec.

4 Conclusion. Further perspectives

We studied in this paper the motion of a satellite in the Earth's gravitational field. This motion is realised by the condition of weightlessness, defined as a state of equilibrium between two forces: the Newtonian force of attraction F_N and the force of repulsion F_ω, caused by a rotational motion. The existence of a rotation means the existence of a field of non-holonomity, and, consequently, the existence of forces of non-holonomity. The inner force of non-holonomity F_ω is a pseudo-tensor, always directed opposite to the direction to the centre of attraction. This is a real force countering the Newtonian force F_N. The equality of these two forces means that a satellite moves around the Earth in a state of weightlessness.

A satellite moves freely, and consequently moves along non-isotropic geodesic lines. We obtain from these equations that the relativistic mass of a satellite is constant. Displacements of a satellite in the r- and φ-directions include components caused by the daily rotation of the Earth. Solving the non-null geodesic lines equations describing its motion, we obtained from formula (36)

$$\Delta\dot{z} = \frac{\mathrm{v}Q}{2c^2} \simeq \frac{\mathrm{v}V_I^2}{2c^2} = 10^{-8} \text{ km}, \tag{41}$$

where $\mathrm{v} = 30$ km/sec, $V_I = 8$ km/sec is the first space velocity. This correction is very small, but it has the same origin as the anisotropy of the velocity of light. Calculating the displacement of a satellite in the z-direction, we obtain the correction as a harmonic oscillation with the amplitude 13 cm and of 24-hour period.

The expression (36) is the exact solution of the equation (17). It is easy to see that the second term of (17) includes the quantity $m\omega \mathrm{v} = m\omega\Omega R$, where R is the distance between the Earth and the Sun. We can rewrite it as the angular momentum L of the outer force of non-holonomity

$$L = mF_{\Omega}R = m\omega\Omega R\,. \tag{42}$$

We conclude that:

1. If a body rotating around a centre of attraction also rotates with the latter around a greater origin of attraction, these fields of rotation interact.

This interaction exists only by the condition that both bodies rotate. The interaction of two fields of non-holonomity (the inner and the outer) causes an anisotropy in the velocity of light in the direction of the motion in the gravitational field of a greater body [1]. This interaction causes the displacement in this equation of a mass-bearing body (a satellite) obtained in the present paper. Both effects have the same nature: the angular moment of the outer force of non-holonomity deviates null and non-null trajectories of light-like particles and mass-bearing bodies.

We conclude that the inner and the outer forces of non-holonomity have a different nature, and therefore produce different effects on the motion of space bodies (and light).

2. The inner force of non-holonomity counters the Newtonian force of attraction. It is included in a three-dimensional potential of a gravitational field

$$\mathrm{w} = c^2\left(1 - \sqrt{g_{00}}\right) \simeq \frac{GM}{r} + \frac{\omega^2 r^2}{2}\,. \tag{43}$$

This field of non-holonomity is linked to the weightlessness condition: the motion of a space body satisfies the weightlessness condition if $\frac{\partial \mathrm{w}}{\partial r} = 0$. This result follows from the definition of a gravitational-inertial force vector

$$F_i = \frac{1}{1 - \frac{\mathrm{w}}{c^2}}\left(\frac{\partial \mathrm{w}}{\partial x^i} - \frac{\partial v_i}{\partial t}\right). \tag{44}$$

We see that if a rotation is stationary (i. e. $\frac{\partial v_i}{\partial t} = 0$) the condition of weightlessness has the form $\frac{\partial \mathrm{w}}{\partial x^i} = 0$. It is evident that if a rotation is non-stationary, the condition of the weightlessness takes the form

$$\frac{\partial \mathrm{w}}{\partial x^i} = \frac{\partial v_i}{\partial t}\,. \tag{45}$$

It is interesting to note that a stationary rotation of a three-dimensional space is linked with motions of the space-time. It is shown in [4] that a stationary rotation of a three-dimensional space is a motion of the space-time itself due to the fact that a Lie derivative for this metric is zero.

3. The outer force of non-holonomity acts on the geometry of the space of transit of a body which rotates around another body and moves with the latter in the gravitational field of a greater body. It imparts energy to a moving (rotating) system of bodies, the gravitational fields of which are part of the gravitational field. We obtain the following chain: the gravitational field of the Earth (and all other planets) is a part of the Sun's gravitational field; the gravitational field of the Sun is a part of the galactic gravitational field, etc. All these space bodies are linked by gravitational forces and forces of non-holonomity. Its equilibrium is a necessary condition of existence for the Universe.

A study of spaces with non-stationary rotation is the theme of further papers. A necessary consideration of this problem involves the microwave radiation in the observed Universe. We have shown in the second part of [1] that the space-time satisfying to metric (1) can be permeated only by matter with stationary characteristics: a density, a stream of energy, a stress tensor, etc. Proposing that the Universe is filled by an ideal fluid (gas) and electromagnetic radiation, we showed that the electromagnetic field can only be stationary. If we consider this electromagnetic field as an electromagnetic wave, we conclude that these waves can only be standing waves. But observations show that in our Universe a microwave electromagnetic radiation exists. We therefore must initially choice a non-stationary metric. Such a metric can allow non-stationary electromagnetic radiation. It is possible that microwave radiation is linked with non-stationary fields of non-holonomity. But this is a theme for further studies.

Submitted on October 18, 2006
Accepted on December 14, 2006

References

1. Borissova L. Preferred spatial directions in the Universe: a General Relativity approach. *Progress in Physics*, 2006, v. 4, 51–64.
2. Zelmanov A. L. Chronometric invariants and co-moving coordinates in the general relativity theory. *Doklady Acad. Nauk USSR*, 1956, v. 107(6), 815–818.
3. Zelmanov A. L. Chronometric invariants. Dissertation thesis, 1944. American Research Press, Rehoboth (NM), 2006.
4. Rabounski D. and Borissova L. Particles here and beyond the Mirror. Editorial URSS, Moscow, 2001; arXiv: gr-qc/0304018.

Evidence of Non-local Chemical, Thermal and Gravitational Effects

Huping Hu and Maoxin Wu

Biophysics Consulting Group, 25 Lubber Street, Stony Brook, NY 11790, USA

E-mail: hupinghu@quantumbrain.org

Quantum entanglement is ubiquitous in the microscopic world and manifests itself macroscopically under some circumstances. But common belief is that it alone cannot be used to transmit information nor could it be used to produce macroscopic non-local effects. Yet we have recently found evidence of non-local effects of chemical substances on the brain produced through it. While our reported results are under independent verifications by other groups, we report here our experimental findings of non-local chemical, thermal and gravitational effects in simple physical systems such as reservoirs of water quantum-entangled with water being manipulated in a remote reservoir. With the aids of high-precision instruments, we have found that the pH value, temperature and gravity of water in the detecting reservoirs can be non-locally affected through manipulating water in the remote reservoir. In particular, the pH value changes in the same direction as that being manipulated; the temperature can change against that of local environment; and the gravity apparently can also change against local gravity. These non-local effects are all reproducible and can be used for non-local signalling and many other purposes. We suggest that they are mediated by quantum entanglement between nuclear and/or electron spins in treated water and discuss the implications of these results.

1 Introduction

Scientific methods require that one conform one's knowledge of nature to repeatable observations. Thus, it is unscientific to reject what's observed repeatedly and consistently. With this in mind, we comment that quantum entanglement has been recently shown to be physically real in many laboratories [1, 2]. Indeed, spins of electrons, photons and nuclei have now been successfully entangled in various ways for the purposes of quantum computation and communication [3, 4]. On the other hand, we have recently observed non-local effects of chemical substances on the brain produced through quantum entanglement [5, 6] which are commonly thought to be impossible [7]. Here we report our work carried out on simple physical systems, in particular, water, using simple physical/chemical observables such as pH, temperature and gravity measured with high-precision instruments. Our motivation for measuring pH change of water in one reservoir, while manipulating water in a remote reservoir quantum-entangled with the former, is to investigate whether and how pH value in the water being measured shifts under non-local influences. Our motivation for measuring temperature variation of water in one reservoir, while manipulating water in a remote reservoir quantum-entangled with the former, is to investigate whether and how the thermodynamics of water being measured changes under non-local influences. Our motivation for measuring gravity change of one reservoir of water, while manipulating water in a remote reservoir quantum-entangled with the former, is to investigate whether gravity also change under non-local influences.

The successes of the experiments described herein were achieved with the aids of high-precision analytical instruments. They include an Ohaus Voyager Analytical Balance with capacity 210 g, resolution 0.1 mg, repeatability 0. 1mg and sensitivity drift 3PPM/°C, a Control Company traceable-calibration digital thermometer with resolution 0.001°C and repeatability 0.002°C near 25°C in liquid such as water (estimated from calibration data provided), and a Hanna microprocessor pH meter Model 213 with resolution 0.001 and repeatability 0.002. The other key apparatus is a 25-litre Dewar filled with liquid nitrogen and positioned remotely at a desired distance which not only provided the drastic changes in the water being manipulated but also served as a natural Faraday cage blocking any possible electromagnetic influence between the water being measured and the water being manipulated. Also vital to the success of the experiments described herein was the stable environment found in an underground room which shields many external noises such as mechanical vibration, air turbulence and large temperature change.

2 Materials and methods

Quantum-entangled stock water in individual volumes of 500 ml or similar quantities was prepared as described previously [5] which might then be split into smaller volumes or combined into larger ones based on needs.Briefly, in one procedure 500 ml fresh tap water in a closed plastic reservoir was exposed to microwave radiation in a 1500 W microwave oven for 2 min and then left in room temperature for 24 hours

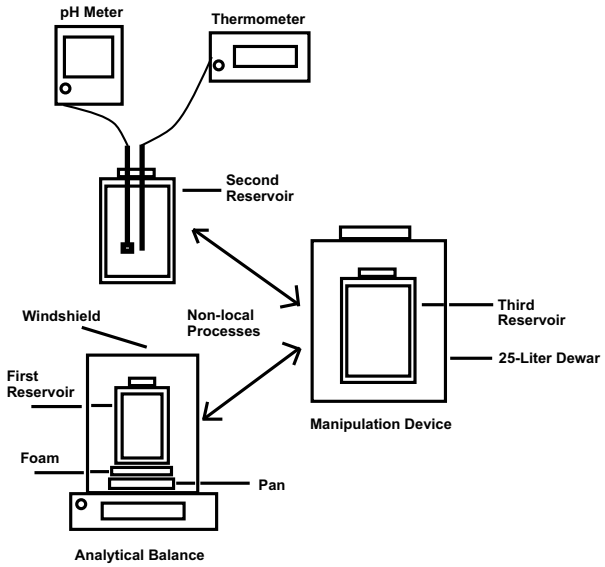

Fig. 1: Illustration of the key experimental setup. Several variations of this setup were also used in the actual experiments as described in the text. For example, in one variation, the manipulation was heating the water in the 3rd reservoir to boiling point and then cooling it down. In a second variation, the gravity measurement was eliminated and the manipulations were first adding 5 ml concentrated HCl (38%) to the third reservoir, then adding 20 g NaOH to the same and third heating the same to boiling point. In a third variation, the Dewar was located more than 500 feet away from the site of measurement. In fourth variation, the gravity and pH measurements were eliminated and the temperature measurements were carried out more than 50 miles away from the location of the Dewar.

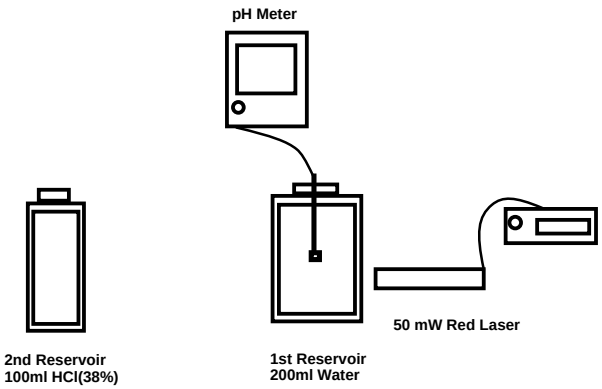

Fig. 2: Illustration of the second experimental setup which allows the measurement of pH value in the presence or absence of concentrated HCl about 500 cm away from and behind the water being measured. If no quantum entanglement is involved, the presence or absence of the HCl should not affect the pH value.

before use. In a second procedure 500 ml fresh tap water in the closed plastic reservoir was exposed to audio-frequency radiations of a 20 W magnetic coil for 30 min and then left in room temperature for 24 hours before use. In a third procedure, 500 ml bottled natural water was simply left in room temperature for at least 30 days before use. In a fourth procedure, 500 ml bottled distilled water was simply left in room temperature for at least 30 days before use. It was found previously that the stock water prepared according to these procedures is quantum-entangled [5].

Figure 1 shows a diagram of the key experimental setup. It includes (1) the analytical balance calibrated internally and stabilized in the underground room for more than one week before use and a tightly closed plastic first reservoir containing 175 ml water split from the 500 ml stock water which is placed on the wind-shielded pan of the balance with 1-inch white foam in between as insulation; (2) the digital thermometer and calibrated pH meter placed into the middle of a glass second reservoir containing 75 ml water split from the 500 ml stock water which is closed to prevent air exchange; and (3) the 25-litre Dewar containing 15–25 litres of liquid nitrogen which is located at a distant of 50 feet from the underground room and a tightly closed plastic third-reservoir containing 250 ml water split from the 500 ml stock water to be submerged into the liquid nitrogen in the Dewar at a specified time.

Experiments with the above first-setup were carried out as follows: (1) prepare the 500 ml quantum entangled stock water, divide the same into 175 ml, 75 ml and 250 ml portions and put them into their respective reservoirs described above; (2) set up the experiment according to Figure 1 and let the instruments to stabilize for 30 min before any measurements is taken; (3) record for 20 min minute-by-minute changes of pH value and temperature of the water in the first-reservoir and weight of the second reservoir with water before submerging the third reservoir into liquid nitrogen; (4) submerge the third-reservoir with water into liquid nitrogen for 15 min or another desired length of time and record the instrument readings as before; and (5) take the third-reservoir out of liquid nitrogen, thaw the same in warm water for 30 min or longer and, at the same time, record the instrument readings as before. Control experiments were carried out in same steps with nothing done to the water in the third-reservoir.

In one variation of the above setup, the closed plastic third-reservoir was replaced with a metal container and instead of freeze-thaw treatment the water in the metal container was quickly heated to boiling within 4–5 minutes and then cooled in cold water. In a second variation of the above setup, the gravity portion of the experiment was eliminated and the water in the first and second reservoirs was combined into a closed thermal flask which prevents heat exchange between the water being measured and its local environment. In a third variation of the above setup, the gravity portion of the experiment was eliminated and the water in the first and second reservoirs was combined into a fourth plastic container in which 5 ml concentrated HCl (38% by weight) was first added, then 20 g NaOH powder was added and next the same water was transferred to a metal container and heated to boiling on a stove. In a fourth

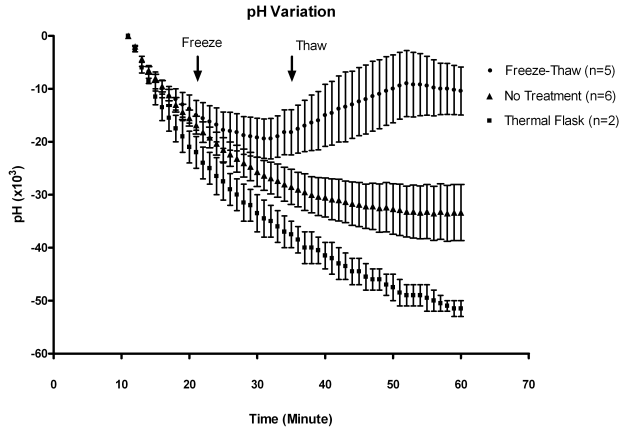

Fig. 3: pH variations under remote manipulations of water quantum-entangled with water being measured. The pH value at the starting point is set to zero and the results shown were obtained from one batch of quantum-entangled water. The difference in pH values from control in which no freeze-thaw was done at the point of thawing is about 0.010. However, if the water being measured was kept in a thermal flask to prevent energy exchange with the local environment, no effect on pH value was observed during freeze-thaw treatment of remote water. Statistical analysis on data collected after freezing for 10 min show that the results are significantly different under the different treatments/settings shown.

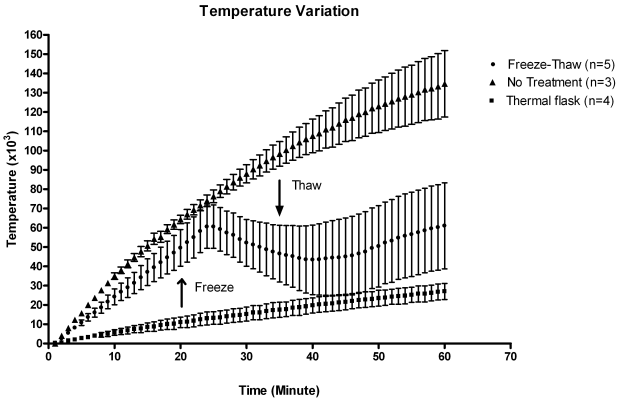

Fig. 4: Temperature variations under remote manipulations of water quantum-entangled with water being measured. The temperature at the starting point is set to zero and the results shown were obtained from one batch of quantum-entangled water. The temperature difference from control in which no freeze-thaw was done at the point of thawing is about 0.05°C. However, if the water being measured is kept in a thermal flask to prevent heat exchange with the local environment, no dropping of temperature were observed under freeze-thaw treatment. Statistical analysis performed on data collected after freezing for 10 min show that the results are significantly different under the different treatments/settings shown.

variation of the above first-setup, the 25-litre Dewar containing liquid nitrogen was replaced by a large water tank located 20-feet above the underground room which contained 200-gallon tap water sitting in room temperature for months and, instead of submersion, the water in the third-reservoir was poured into the large water tank the purpose of which was to quantum-entangle the poured water with the water in the large tank. In a fifth variation of the above setup, the gravity portion of the experiment was eliminated and the water in the first and second reservoirs was combined into a closed glass fourth-reservoir which was moved to a location more than 50 miles away from the Dewar for temperature measurement.

Figure 2 shows a diagram of the second experimental setup. It includes: (1) a red laser with a 50 mW output and wavelengths 635–675 nm placed next and pointed to a flat glass first-reservoir containing 200 ml tap water sitting in room temperature for more than a week without air exchange; (2) the calibrated pH meter and optionally the digital thermometer placed into the middle of the said flat glass reservoir which was closed to prevent air exchange; and (3) a round glass second-reservoir containing 100 ml concentrated HCl (38% by weight) to be placed 500 cm away from the first-reservoir at a specified time.

Experiments with the above second setup were carried out as follows: (1) prepare the 200 ml tap water and set up the experiment according Figure 2; turn on the laser so that the laser light first passes through the first-reservoir and then gets scattered on a nearby concrete wall, and let the instruments to stabilize for 30 min before any measurement is taken; (2) record for 10 min minute-by-minute changes of pH value and optionally temperature of the water in the first-reservoir; and (3) place the second reservoir containing 100 ml HCl on the path of the laser light and at a distance of 500 cm from the first reservoir and record for 60 min or longer instrument readings as before. Control experiments were carried out in same steps in the absence of HCl.

3 Results

Figures 3, 4 and 5 summarize the results obtained from experiments conducted with the key setup and one batch of quantum-entangled water which were simply bottled natural water with a shelf time of more than 90 days. Similar results were also obtained with water prepared according to other quantum entanglement methods mentioned above and other quantum-entangled liquid such as olive oil, alcohol and even Coca Cola as discussed later. The different distances of the Dewar from the underground room where most measurements were done made no noticeable differences with respect to the results obtained.

Figure 3 shows changes of pH value of the water in the second-reservoir during the three stages of manipulations of the water in the remote third-reservoir. As shown, within minutes after the remote third-reservoir was submerged into liquid nitrogen, during which the temperature of water being manipulated would drop from about 25°C to −193°C, the pH value of the water in the second reservoir steadily stopped dropping and then started rising, but about 20 min after the

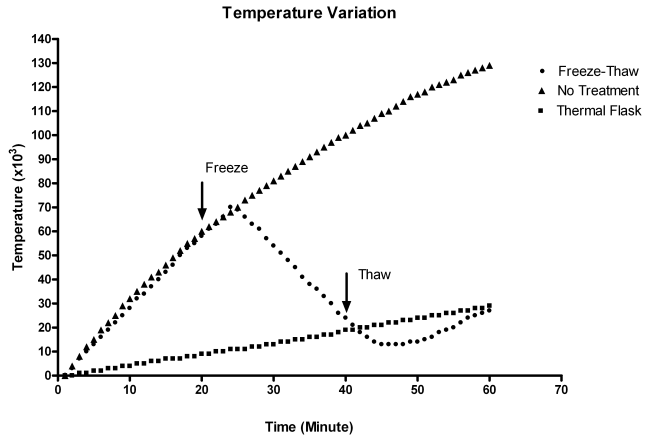

Fig 4A: One particular example detailing temperature variations under remote manipulation. The temperature difference from control at the point of thawing is about 0.08°C. However, if the water being measured is kept in a thermal flask, no dropping of temperature were observed under freeze-thaw treatment.

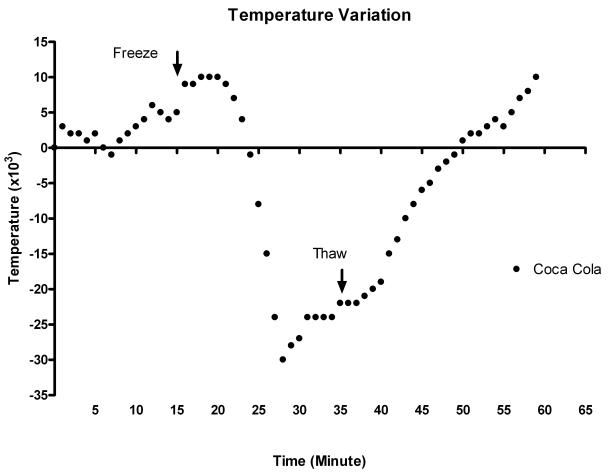

Fig 4B: One example showing temperature variation of a different liquid, Coca Cola, under remote manipulation of a portion of the said liquid quantum-entangled with another portion of the liquid being measured. Other liquids such as distilled water, olive oil and alcohol also showed similar qualitative results under the same treatment.

frozen water was taken out of liquid nitrogen and thawed in warm water the pH value of the same steadily levelled off and started dropping again. In contrast, the control experiments did not show such dynamics. It is known that the pH value of water increases as its temperature goes down to 0°C. Therefore, the pH value of water being measured goes in the same direction as the remote water when the latter is manipulated. The difference in pH values from control in which no freeze-thaw was done at the point of thawing is about 0.010. However, if the water being measured is kept in a thermal flask to prevent heat exchange with the local environment, no effect on pH value was observed under freeze-thaw treatment of the remote water. Statistical analysis performed on data collected after freezing for 10 minutes show that the results are significantly different under these different treatments/settings.

Figure 4 shows temperature variations of the water in the second-reservoir during the three stages of manipulations of the water in the remote third-reservoir. As shown, before the submersion of the remote third-reservoir into liquid nitrogen the temperature of the water in the second-reservoir rose in small increments due to, by design, the slight temperature difference between the local environment and the water inside the second reservoir; but within about 4–5 minutes after the remote third-reservoir was submerged into liquid nitrogen, during which the temperature of water being manipulated would drop from about 25°C to −193°C, the temperature of the water in the second reservoir first stopped rising and then steadily dropped in small increments; and then within about 4–5 minutes after the frozen water was taken out of liquid nitrogen and thawed in warm water the temperature of the same first stopped dropping and then steadily rose again in small increments. In contrast, the control experiments did not show such dynamics. The temperature difference from control in which no freeze-thaw was done at the point of thawing is about 0.05°C. However, if the water being measured is kept in a thermal flask to prevent heat exchange with the local environment, no dropping of temperature were observed under freeze-thaw treatment of the remote water. Statistical analysis performed on data collected after freezing for 10 minutes show that the results are significantly different under these different treatments/settings.

In addition, Figure 4A shows one particular example of temperature variations under remote manipulation of water quantum-entangled with water being measured. In this case, the temperature difference from control at the point of thawing is about 0.08°C. Further, Figure 4B shows one example of temperature variation of a different liquid, Coca Cola, under remote manipulation of a portion of the said liquid quantum-entangled with another portion being measured. Other liquids such as distilled water, olive oil and alcohol also showed similar qualitative results under the same freeze-thaw treatment. Furthermore, preliminary experiments conducted with the temperature measurement done at a location more than 50 miles way from the Dewar also show results similar to those obtained at distances of 50 and 500 feet respectively.

Figure 5 shows weight variations of the first reservation during the three stages of manipulation of the water in the remote third-reservoir. Before the submersion of the remote third-reservoir into liquid nitrogen the weight being measured drifted lower very slowly. But almost immediately after the remote third-reservoir was submerged into liquid nitrogen, during which the temperature and physical properties of water being manipulated drastically changed, the weight of the first-reservoir dropped at an increased rate, and after the

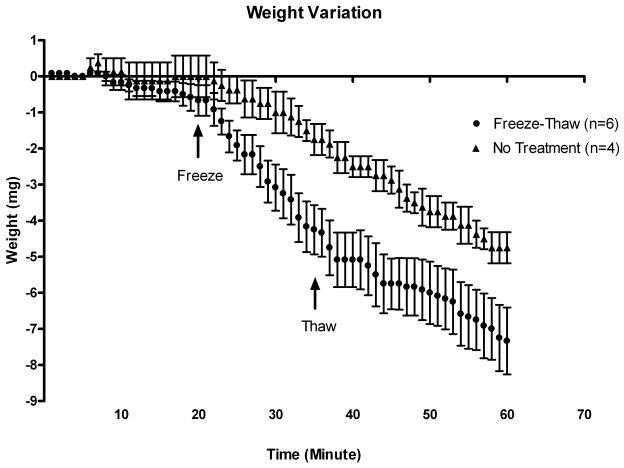

Fig 5: Weight variations under remote manipulations of water quantum-entangled with water being weighed. The weight at the starting point is set to zero and the results shown were obtained from one batch of quantum-entangled water. The weight differences from control in which no freeze-thaw was done at the point of thawing is about 2.5 mg. In some cases, the weight of the water being weighed not only briefly stop dropping for several minutes but also rose briefly for several seconds to minutes as shown in Figure5A. Also when the remote water was quickly heated to boiling on a stove instead of being frozen in liquid nitrogen, a brief rise of weight in the range of about 0.5 mg were repeated observed in one variation of the key setup. Further, when the remote water was poured into a 200-gallon water tank, small but noticeably increased weight losses were also observed in several experiments conducted to date. Statistical analysis performed on data collected after freezing for 10 min show that the results are significantly different under the different treatments/settings shown.

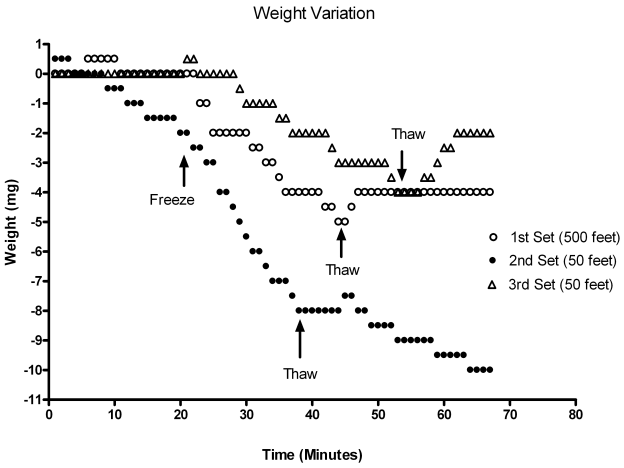

Fig 5A: Examples of weight variations under remote manipulations of water quantum-entangled with water being weighed. The onset of increased weight loss started either at the time of freezing treatment or slightly later. The signatures of thawing induced weight increases were clear for the three different thawing times. The distances shown are the respectively distances of the Dewar to the location of measurement in each experiment.

frozen water was taken out the liquid nitrogen and thawed in warm water the weight of the same first stopped dropping and, in some cases, even rose before resuming drifting lower as further discussed below. In contrast, the control experiments did not show such dynamics. The weight difference from control in which no freeze-thaw was done at the point of thawing is about 2.5 mg. Statistical analysis performed on data collected after freezing for 10 minutes show that the results are significantly different under these different treatments/settings.

As shown in Figure 5A, in some cases, the weight of the water being measured not only stopped dropping for several minutes but also rose. The signatures of freezing induced weight decreases and thawing induced weight increases for three different thawing times are very clear. In addition, Figure 5B shows one example of weight and temperature variations under the same remote manipulation of water quantum-entangled with water being weighed and measured respectively. Again, the signatures of freezing and thawing induced weight and temperature decreases and increases are respectively very clear. Further, Figure 5C shows another example of weight and temperature variations under another same remote manipulation in which the Dewar was located about 500 feet away from where the measurements were taken. The general background trend of decreasing temperature was due to environmental temperature change. Yet again, the signatures of freezing and thawing induced weight and temperature variations were respectively are very clear. Also, when the remote water was quickly heated to boiling on a stove instead of being frozen in liquid nitrogen, a brief rise of weight in the range of about 0.5 mg were repeated observed in several experiments conducted so far.

Furthermore, when the remote water was poured into the 200-gallon water tank instead of being frozen in liquid nitrogen, small but noticeably increased weight losses were repeatedly observed in the several experiments conducted to date. More specifically, before mixing of the water in the remote third-reservoir with water in the water tank the measured weight drifted lower very slowly, but within short time measured in minutes after the water in the remote third-reservoir was poured into the water tank, during which the water in the said tank got quantum-entangled with the water in the third-reservoir, the weight of the first-reservoir dropped at small but increased rate for a period of time. In contrast, the control experiments did not show such dynamics.

Figure 6 shows an example of temperature variations under the respective treatments of adding 5 ml concentrated HCl (38%) to the third reservoir, then adding 20 g NaOH to the same and third heating the same to boiling point. The signatures of these remote treatments induced temperature changes were clear and repeatedly observable in quite a few experiments conducted to date.

Figure 7 shows the variations of pH value of the water in

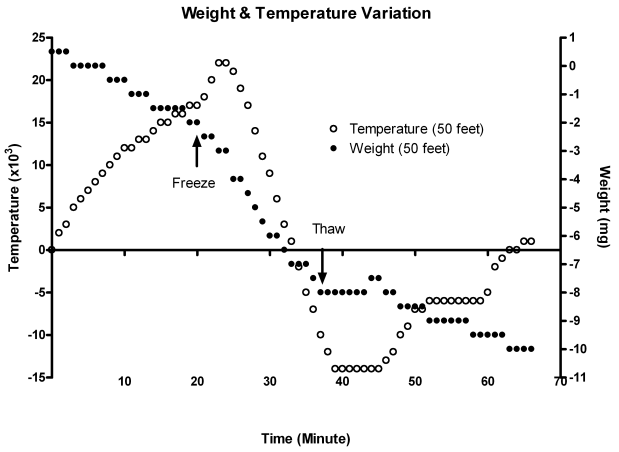

Fig 5B: One example of weight and temperature variations under the same remote manipulation of water quantum-entangled with water being weighed and measured respectively. The onset of increased weight loss started at the time of freezing treatment but the onset of temperature decrease against environmental temperature started a few minutes later after freezing treatment started. The signatures of thawing induced weight and temperature increases were clear. The distance shown is the distance of the Dewar to the location of measurement.

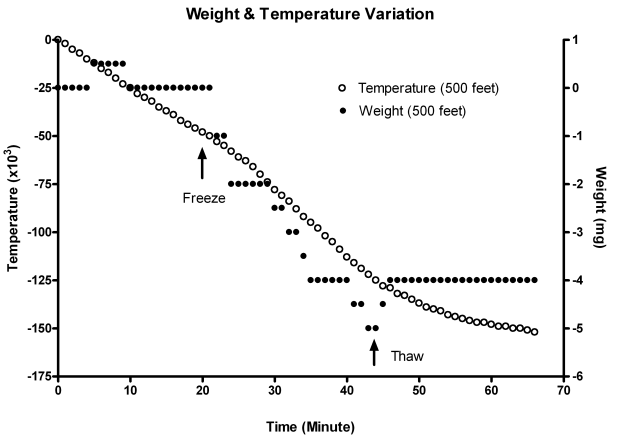

Fig 5C: Second example of weight and temperature variations under another same remote manipulation of water quantum-entangled with water being weighed and measured respectively. The general background trend of decreasing temperature was due to environmental temperature change. The onset of increased weight loss started at the time of freezing treatment but the onset of increased temperature loss started a few minutes later after freezing treatment started. The signatures of thawing induced weight increase and slow down of temperature loss were again clear. The distance shown is the distance of the Dewar to the location of measurement.

the first reservoir in experiments done with the setup in Figure 2. As shown, in about 30 min after the second-reservoir containing 100 ml concentrated HCl (38% by weight) was placed behind the first-reservoir at a distance of 500 cm and on the path of the laser beam, during which the water in the first-reservoir got quantum-entangled with the content in the second reservoir, the pH value of the water in the first-reservoir steadily decreased. In contrast, the control experiments did not show such dynamics. Also, the 50 mW red laser did not affect the temperature of the water in the first reservoir significantly during the whole treatment. The difference in pH value from control in which HCl was absence is about 0.070 after 50 min of exposure to HCl. Statistical analysis performed on data collected after exposure to HCl for 30 min show that the results are significantly different from control. Various experiments done with direct additions of HCl to the remote water also repeated showed decreases in pH value in the water being measured.

4 Discussions

With all experimental setups and their variations described herein, we have observed clear and reproducible non-local effects with the aids of high-precision analytical instruments and under well-controlled conditions. The physical observables used for measuring the non-local effects are simple ones which can be measured with high precisions. These effects are, even under the most stringent statistical analysis, significantly above and beyond what were noticeable in the control experiments.

Through careful analysis, we have likely excluded the possibility that the observed weight variation was a secondary local effect due to heat loss and/or sensitivity drift of balance associated with temperature change induced by the remote manipulation. First, during the period of remote manipulation the total temperature change was less than 0.08°C so the total heat loss for the 175 ml water in the first-reservoir is about 60 J. In contrast, the weight loss during remote manipulation was on average about 2.5 mg which is 22.5×10^9 J in energy unit. Second, the first-reservoir and the pan of the balance were separated by 1-inch white foam to prevent heat transfer to the analytic balance. Even in the highly unlikely scenario that this temperature change somehow affected the overall temperature of the balance, the associated sensitivity drift of the balance was about 0.03 mg which is 10 times smaller than what's actually observed. In addition, Figures 5A, 5B and 5C also show several other signatures of remote freeze-thaw treatment as the sole cause of the observed weight variations. Therefore, we cautiously suggest that the observed gravity variation is a genuine and direct non-local effect associated with quantum entanglement. However, as with many other important new results, replications by others are the key to independently confirm our results reported here.

We chose to use liquid nitrogen in a large Dewar placed at a distant location for manipulating water in our experiments because it can provide drastic changes in temperature and properties of water in a very short period of time. Our expectation was that, if the quantum entities inside the water being measured are able to sense the changes experienced by

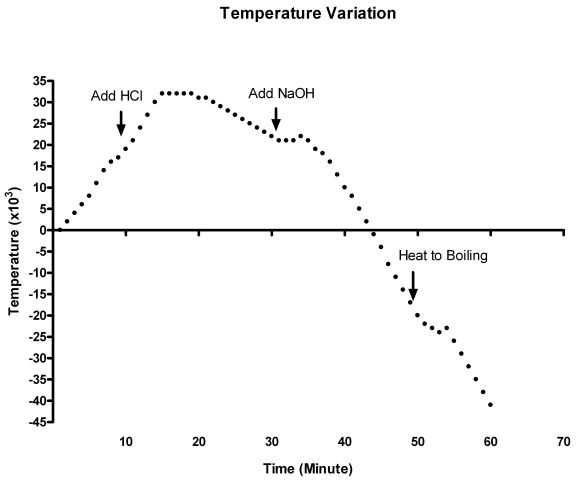

Fig 6: An example of temperature variations under the respective treatments of adding 5 ml concentrated HCl (38%) to the third reservoir, then adding 20 g NaOH to the same and third heating the same to boiling point. The signatures of these remote treatments induced temperature changes were clear and repeatedly observable in quite a few experiments conducted to date. The general background trend of the temperature first increasing, flattening and decreasing was due to environmental temperature change.

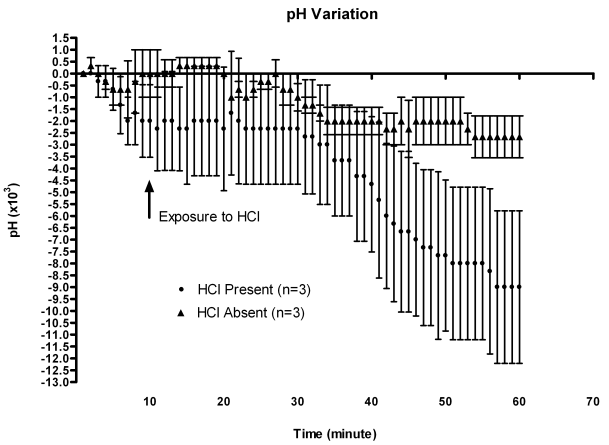

Fig 7: pH variations under laser treatment in the presence and absence of concentrated HCl with the setup in Figure 2. The pH value at the starting point is set to zero. The difference in pH value from control in which HCl was absence is about 0.07 after 50 min of exposure to HCl. Various experiments done with direct additions of HCl to the remote water also repeated showed decreases in pH value in the water being measured. Statistical analysis performed on data collected after exposure to HCl for 30 min show that the results are significant different from control.

the quantum entities in the water being manipulated through quantum entanglement and further utilize the information associated with the said changes, the chemical, thermal and even possibly gravitational properties of the water might be affected through quantum entanglement mediated non-local processes [5, 6]. The most logical explanation for these observed non-local effects is that they are the consequences of non-local processes mediated by quantum entanglement between quantum entities in the water being measured and the remote water being manipulated as more specifically illustrated below.

First, when pH value of the water in the manipulation reservoir is high or low or is changing under direct manipulation such as extreme cooling or heating or addition of acidic or alkaline chemical, the measured pH in the detecting reservoir shifts in the same direction under the non-local influence of the water in the manipulation reservoir mediated through quantum entanglement and, under the condition that the detecting reserve is able to exchange energy with its local environment, as if H+ in the latter is directly available to water in the detecting reservoir.

Second, when the temperature in the manipulation reservoir is extremely low or high or is changing under direct manipulation such as extreme cooling or heating or addition of heat-generating and/or property-changing chemical such as concentrated HCl or NaOH powder, the temperature in the detecting reservoir changes in the same direction under non-local influence of the water in the manipulation reservoir mediated through quantum entanglement and, under the condition that the detecting reserve is able to exchange heat with its local environment so that the local thermodynamic energy is conserved, as if the heat or lack of it in manipulation reservoir is directly available to the water in the detecting reservoir.

Third, when water in manipulation reservoir is manipulated though extreme cooling, heating or mixing with large quantum-entangled mass, e.g., water, such that, it is hereby cautiously suggested, the quantum entanglement of the water under manipulation with its local environment changes, the weight of the water in the detecting reservoir also changes under the presumed non-local influence of the manipulation reservoir mediated through quantum entanglement. However, independent and vigorous replications should be carried out before a definite conclusion is drawn.

We suggest here that the said quantum entities inside water are likely nuclear spins for the reasons discussed below. Water contains vast numbers of nuclear spins carried by 1H. These spins form complex intra- and inter-molecular networks through various intra-molecular J- and dipolar couplings and both short- and long-range intermolecular dipolar couplings. Further, nuclear spins have relatively long relaxation times after excitations [8]. Thus, when a nematic liquid crystal is irradiated with multi-frequency pulse magnetic fields, its 1H spins can form long-lived intra-molecular quantum coherence with entanglement for information storage [9]. Long-lived entanglement of two macroscopic electron spin ensembles in room temperature (0.05 ms) has also been achieved [1]. Furthermore, spin is a fundamental quantum process and was shown to be responsible for the quantum effects in both Hestenes and Bohmian quantum mechanics

[10, 11]. Thus, we suggest that quantum-entangled nuclear spins and/or electron spins are likely the mediators of all observed non-local effects reported here [5, 6].

5 Conclusions

Several important conclusions can be drawn from our findings. First, we have realized non-local signalling using three different physical observables, pH value, temperature and apparently gravity. Second, we have shown that the temperature of water in a detecting reservoir quantum entangled with water in a remote reservoir can change against the temperature of its local environment when the latter is manipulated under the condition that the water the detecting reservoir is able to exchange heat with its local environment. Third, we have also shown that the gravity of water in a detecting reservoir quantum entangled with water in a remote reservoir apparently also change when the latter was remotely manipulated. Our findings imply that the properties of all matters can be affected non-locally through quantum entanglement mediated processes.

Finally, with respect applications, our findings enable various quantum entanglement assisted technologies be developed. Some of these technologies can be used to manipulate and/or affect remotely various physical, chemical and/or biological systems including human bodies. Other such technologies can be used for non-local signalling and communications between remote locations of arbitrary distances in various ways. Potentially, other novel and practical applications can also be developed based on our experimental findings.

Acknowledgements

We wish to thank Yongchang Hu for assisting the authors with some of the experiments and Danielle Graham for showing her research at a 2006 conference.

Submitted on November 16, 2006
Re-submitted after revision on November 23, 2006
Accepted on November 30, 2006

References

1. Julsgaard B., Kozhekin A., Polzik E. S. Experimentally long-lived entanglement of two macroscopic objects. *Nature*, 2001, v. 413, 400–403.
2. Ghosh S., Rosenbaum T. F., Aeppli G., Coppersmith S. N. Entangled quantum state of magnetic dipoles. *Nature*, 2003, v. 425, 48–51.
3. Matsukevich D. N. and Kuzmich A. Quantum state transfer between matter and light. *Science*, 2004, v. 306, 663–666.
4. Chanelière T. et al. Storage and retrieval of single photons transmitted between remote quantum memorie. *Nature*, 2005, v. 438, 833–836.
5. Hu H. P. and Wu M. X. Nonlocal effects of chemical substances on the brain produced through quantum entanglement. *Progress in Physics*, 2006, v. 3 , 20–26; *NeuroQuantology*, 2006, v. 4, 17–31.
6. Hu H. P. and Wu M. X. Thinking outside the box: the essence and imications of quantum entanglement. *NeuroQuantology*, 2006, v. 4, 5–16; Cogprints: ID4581.
7. Eberhard P. Bell's theorem and the different concepts of locality. *Nuovo Cimento*, 2004, v. 46B, 392–419.
8. Gershenfeld N. and Chuang I. L. Bulk spin resonance quantum computation. *Science*, 1997, v. 275, 350–356.
9. Khitrin A. K., Ermakov V. L., Fung B. M. Information storage using a cluster of dipolar-coupled spins. *Chem. Phys. Lett.*, 2002, v. 360, 160–166.
10. Hestenes D. Quantum mechanics from self-interaction. *Found. Phys.*, 1983, v. 15, 63–78.
11. Salesi G. and Recami E. Hydrodynamics of spinning particles. *Phys. Rev.*, 2004, v. A57, 98–105.

On Line-Elements and Radii: A Correction

Stephen J. Crothers

Queensland, Australia
E-mail: thenarmis@yahoo.com

Using a manifold with boundary various line-elements have been proposed as solutions to Einstein's gravitational field. It is from such line-elements that black holes, expansion of the Universe, and big bang cosmology have been alleged. However, it has been proved that black holes, expansion of the Universe, and big bang cosmology are not consistent with General Relativity. In a previous paper disproving the black hole theory, the writer made an error which, although minor and having no effect on the conclusion that black holes are inconsistent with General Relativity, is corrected herein for the record.

1 Introduction

In a previous paper [1] (see page 8 therein) the writer made the following claim:

"*the ratio* $\frac{\chi}{R_p} > 2\pi$ *for all finite* R_p"

where R_p is the proper radius and χ is the circumference of a great circle. This is not correct. In fact, the ratio $\frac{\chi}{R_p}$ is greater than 2π for some values of R_p and is less than 2π for other values of R_p. Furthermore, there is a value of χ for which $\frac{\chi}{R_p} = 2\pi$, thereby making $R_p = R_c$, where R_c is the radius of curvature. Thus, if the transitional value of the circumference of a great circle is χ_e, then

$$\chi < \chi_e \Rightarrow \frac{\chi}{R_p} > 2\pi,$$

$$\chi = \chi_e \Rightarrow \frac{\chi}{R_p} = 2\pi,$$

$$\chi > \chi_e \Rightarrow \frac{\chi}{R_p} < 2\pi.$$

2 Correction — details

Consider the general static vacuum line-element

$$ds^2 = A(r)dt^2 - B(r)dr^2 - C(r)\left(d\theta^2 + \sin^2\theta\, d\varphi^2\right), \quad (1)$$

$$A(r), B(r), C(r) > 0.$$

It has been shown in [1] that the solution to (1) is

$$ds^2 = \left(1 - \frac{\alpha}{\sqrt{C(r)}}\right)dt^2 - \frac{1}{1 - \frac{\alpha}{\sqrt{C(r)}}}\, d\sqrt{C(r)}^2 - C(r)\left(d\theta^2 + \sin^2\theta\, d\varphi^2\right), \quad (2)$$

$$\alpha < \sqrt{C(r)} < \infty,$$

where, using $c = G = 1$,

$$R_c = R_c(r) = \sqrt{C(r)} = \left(\left|r - r_0\right|^n + \alpha^n\right)^{\frac{1}{n}},$$

$$R_p = R_p(r) = \sqrt{R_c(r)\left(R_c(r) - \alpha\right)} + \alpha \left|\frac{R_c(r) + \sqrt{R_c(r) - \alpha}}{\sqrt{\alpha}}\right|, \quad (3)$$

$$r \in \Re, \quad n \in \Re^+, \quad r \neq r_0,$$

and where r_0 and n are entirely arbitrary constants, and α is a function of the mass M of the source of the gravitational field: $\alpha = \alpha(M)$. Clearly, $\lim_{r \to r_0^\pm} R_p(r) = 0^+$ and also $\lim_{r \to r_0^\pm} R_c(r) = \alpha^+$ irrespective of the values of r_0 and n. Usually $\alpha = 2m \equiv 2GM/c^2$ by means of a comparision with the Newtonian potential, but this identification is rather dubious.

Setting $R_p = R_c$, one finds that this occurs only when

$$R_c \approx 1.467\alpha.$$

Then

$$\chi_e \approx 2.934\pi\alpha.$$

Thus, at χ_e the Euclidean relation $R_p = R_c$ holds. This means that when $\chi = \chi_e$ the line-element takes on a Euclidean character.

An analogous consideration applies for the case of a point-mass endowed with charge or with angular momentum or with both. In those cases α is replaced with the corresponding constant, as developed in [2].

3 Summary

The circumference of a great circle in Einstein's gravitational field is given by

$$\chi = 2\pi R_c,$$

$$2\pi\alpha < \chi < \infty.$$

In the case of the static vacuum field, the great circle with circumference $\chi = \chi_e \approx 2.934\,\pi\alpha$ takes on a Euclidean character in that $R_p = R_c \approx 1.467\,\alpha$ there, and so χ_e marks a transition from spacetime where $\frac{\chi}{R_p} < 2\pi$ to spacetime where $\frac{\chi}{R_p} > 2\pi$. Thus,

$$\lim_{r\to\infty^{\pm}} \frac{\chi}{R_p(r)} = 2\pi,$$

$$\lim_{r\to r_0^{\pm}} \frac{\chi}{R_p(r)} = \infty\,,$$

$$\lim_{\chi\to\chi_e^{\pm}} \frac{\chi}{R_p(r)} = 2\pi.$$

Similar considerations must be applied for a point-mass endowed with charge, angular momentum, or both, but with α replaced by the corresponding constant β in the expression for R_p [2],

$$\beta = \frac{\alpha}{2} + \sqrt{\frac{\alpha^2}{4} - (q^2 + a^2\cos^2\theta)}\,,$$

$$q^2 + a^2 < \frac{\alpha^2}{4}\,, \qquad a = \frac{2L}{\alpha}\,,$$

where q is the charge and L is the angular momentum, and so

$$R_c = R_c(r) = \left(\left|r - r_0\right|^n + \beta^n\right)^{\frac{1}{n}},$$

$$r \in \Re, \quad n \in \Re^+, \quad r \neq r_0,$$

where both r_0 and n are entirely arbitrary constants.

Submitted on December 26, 2006
Accepted on January 06, 2007

References

1. Crothers S. J. On the geometry of the general solution for the vacuum field of the point-mass. *Progress in Physics*, 2005, v. 2, 3–14.
2. Crothers S. J. On the ramifications of the Schwarzschild space-time metric. *Progress in Physics*, 2005, v. 1, 74–80.

Relativistic Cosmology Revisited

Stephen J. Crothers
Queensland, Australia
E-mail: thenarmis@yahoo.com

In a previous paper the writer treated of particular classes of cosmological solutions for certain Einstein spaces and claimed that no such solutions exist in relation thereto. In that paper the assumption that the proper radius is zero when the line-element is singular was generally applied. This general assumption is unjustified and must be dropped. Consequently, solutions do exist in relation to the aforementioned types, and are explored herein. The concept of the Big Bang cosmology is found to be inconsistent with General Relativity.

1 Introduction

In a previous paper [1] the writer considered what he thought was a general problem statement in relation to certain Einstein spaces, and concluded that no such solutions exist for those types. However, the problem statement treated in the aforementioned paper adopted an unjustified assumption — that the proper radius is zero when the line-element is singular. Although this occurs in the case of the gravitational field for $R_{\mu\nu}=0$, it is not a general principle and so it cannot be generally applied, even though it can be used to amplify various errors in the usual analysis of the well known cosmological models, as done in [1]. By dropping the assumption it is found that cosmological solutions do exist, but none are consistent with the alleged Big Bang cosmology.

2 The so-called "Schwarzschild — de Sitter model"

Consider the line-element

$$ds^2 = \left(1-\frac{\alpha}{R_c}-\frac{\lambda}{3}R_c^2\right)dt^2 - \\ -\left(1-\frac{\alpha}{R_c}-\frac{\lambda}{3}R_c^2\right)^{-1}dR_c^2 - R_c^2\left(d\theta^2+\sin^2\theta\, d\varphi^2\right), \tag{1}$$

where $R_c = R_c(r)$ is the radius of curvature, r a parameter, and α a function of mass. This has no solution for some function $R_c(r)$ on $R_c(r)\to\infty$ [1].

If $\alpha = 0$, (1) reduces to

$$ds^2 = \left(1-\frac{\lambda}{3}R_c^2\right)dt^2 - \\ -\left(1-\frac{\lambda}{3}R_c^2\right)^{-1}dR_c^2 - R_c^2\left(d\theta^2+\sin^2\theta\, d\varphi^2\right). \tag{2}$$

This has no solution for some function $R_c(r)$ on values $\sqrt{\frac{3}{\lambda}} < R_c(r) < \infty$ [1].

For $1-\frac{\lambda}{3}R_c^2 > 0$ and $R_c \geqslant 0$, it is required that

$$0 \leqslant R_c < \sqrt{\frac{3}{\lambda}}. \tag{3}$$

The proper radius on (2) is

$$R_p = \int \frac{dR_c}{\sqrt{1-\frac{\lambda}{3}R_c^2}} = \sqrt{\frac{3}{\lambda}}\,\arcsin\sqrt{\frac{\lambda}{3}}\,R_c^2 + K,$$

where K is a constant. $R_p = 0$ is satisfied if $R_c = 0 = K$, in accord with (3). Then

$$R_p = \sqrt{\frac{3}{\lambda}}\,\arcsin\sqrt{\frac{\lambda}{3}}\,R_c^2.$$

Now

$$\sqrt{\frac{3}{\lambda}}\,\arcsin 1 = \sqrt{\frac{3}{\lambda}}\,\frac{(1+4n)\,\pi}{2} = \\ = \lim_{R_c\to\sqrt{\frac{3}{\lambda}}^-}\sqrt{\frac{3}{\lambda}}\,\arcsin\sqrt{\frac{\lambda}{3}}\,R_c = \lim_{R_c\to\sqrt{\frac{3}{\lambda}}^-}R_p, \tag{4}$$
$$n = 0, 1, 2, \ldots$$

in accord with (3). Thus, R_p can be arbitrarily large. Moreover, R_p can be arbitrarily large for any R_c satisfying (3) since

$$R_p = \sqrt{\frac{3}{\lambda}}\,\arcsin\sqrt{\frac{\lambda}{3}}\,R_c = \sqrt{\frac{3}{\lambda}}\,(\psi+2n\pi), \\ n = 0, 1, 2, \ldots$$

where ψ is in radians, $0 \leqslant \psi < \frac{\pi}{2}$.

In the case of (1), the mutual constraints on the radius of curvature are

$$\frac{\lambda}{3}R_c^3 - R_c + \alpha < 0 \\ 0 < R_c(r). \tag{5}$$

The proper radius on (1) is

$$R_p(r) = \int \frac{dR_c}{\sqrt{1-\frac{\alpha}{R_c}-\frac{\lambda}{3}R_c^2}} + K, \tag{6}$$

where K is a constant, subject to $R_p \geqslant 0$. The difficulty here is the cubic in (5) and (6). The approximate positive roots to the cubic are α and $\sqrt{\frac{3}{\lambda}}$. These must correspond

to limiting values in the integral (6). Both $R_c(r)$ and $R_p(r)$ also contain α and λ.

In addition, it was argued in [1] that the admissible form for $R_c(r)$ in (1) must reduce, when $\lambda = 0$, to the Schwarzschild form

$$R_c(r) = \left(|r - r_0|^n + \alpha^n\right)^{\frac{1}{n}} \qquad n \in \Re^+, \quad r \in \Re, \quad r \neq r_0\,, \tag{7}$$

where r_0 and n are entirely arbitrary constants. Note that when $\alpha = 0$ and $\lambda = 0$, (1) reduces to Minkowski space and (7) reduces to the radius of curvature in Minkowski space, as necessary.

Determination of the required general parametric expression for $R_c(r)$ in relation to (1), having all the required properties, is not a simple problem. Numerical methods suggest however [1], that there may in fact be no solution for $R_c(r)$ in relation to (1), subject to the stated constraints. At this time the question remains open.

3 Einstein's cylindrical model

Consider the line-element

$$ds^2 = dt^2 - \left[1 - (\lambda - 8\pi P_0)\, R_c^2\right]^{-1} dR_c^2 - \\ - R_c^2\left(d\theta^2 + \sin^2\theta\, d\varphi^2\right). \tag{8}$$

This of course has no Lorentz signature solution in $R_c(r)$ for $\frac{1}{\sqrt{\lambda - 8\pi P_0}} < R_c(r) < \infty$ [1].

For $1 - (\lambda - 8\pi P_0)\, R_c^2 > 0$ and $R_c = R_c(r) \geqslant 0$,

$$0 \leqslant R_c < \frac{1}{\sqrt{\lambda - 8\pi P_0}}. \tag{9}$$

The proper radius is

$$R_p = \int \frac{dR_c}{\sqrt{1 - (\lambda - 8\pi P_0)\, R_c^2}} = \\ = \frac{1}{\sqrt{\lambda - 8\pi P_0}} \arcsin\sqrt{(\lambda - 8\pi P_0)\, R_c^2} + K,$$

where K is a constant. $R_p = 0$ is satisfied for $R_c = 0 = K$, so that

$$R_p = \frac{1}{\sqrt{\lambda - 8\pi P_0}} \arcsin\sqrt{(\lambda - 8\pi P_0)\, R_c^2}\,,$$

in accord with (9).

Now

$$\frac{1}{\sqrt{\lambda - 8\pi P_0}} \arcsin 1 = \frac{(1 + 4n)\,\pi}{2\sqrt{\lambda - 8\pi P_0}} = \\ = \lim_{R_c \to \frac{1}{\sqrt{\lambda - 8\pi P_0}}^-} \frac{1}{\sqrt{\lambda - 8\pi P_0}} \arcsin\sqrt{(\lambda - 8\pi P_0)\, R_c^2} \\ n = 0, 1, 2, \ldots$$

in accord with (9). Thus R_p can be arbitrarily large. Moreover, R_p can be arbitrarily large for any R_c satisfying (9), since

$$R_p = \frac{1}{\sqrt{\lambda - 8\pi P_0}} \arcsin\sqrt{(\lambda - 8\pi P_0) R_c^2} = \frac{(\psi + 2n\pi)}{\sqrt{\lambda - 8\pi P_0}}\,, \\ n = 0, 1, 2, \ldots$$

where ψ is in radians, $0 \leqslant \psi < \frac{\pi}{2}$.

4 De Sitter's spherical model

Consider the line-element

$$ds^2 = \left(1 - \frac{\lambda + 8\pi\rho_{00}}{3} R_c^2\right) dt^2 - \\ - \left(1 - \frac{\lambda + 8\pi\rho_{00}}{3} R_c^2\right)^{-1} dR_c^2 - R_c^2\left(d\theta^2 + \sin^2\theta\, d\varphi^2\right). \tag{10}$$

This has no Lorentz signature solution in some $R_c(r)$ on $\sqrt{\frac{3}{\lambda + 8\pi\rho_{00}}} < R_c(r) < \infty$ [1].

For $1 - \frac{\lambda + 8\pi\rho_{00}}{3} R_c^2 > 0$ and $R_c = R_c(r) \geqslant 0$,

$$0 \leqslant R_c < \sqrt{\frac{3}{\lambda + 8\pi\rho_{00}}}\,. \tag{11}$$

The proper radius is

$$R_p = \int \frac{dR_c}{\sqrt{\left(1 - \frac{\lambda + 8\pi\rho_{00}}{3}\right) R_c^2}} = \\ = \sqrt{\frac{3}{\lambda + 8\pi\rho_{00}}} \arcsin\sqrt{\left(\frac{\lambda + 8\pi\rho_{00}}{3}\right) R_c^2} + K,$$

where K is a constant. $R_p = 0$ is satisfied for $R_c = 0 = K$, so

$$R_p = \sqrt{\frac{3}{\lambda + 8\pi\rho_{00}}} \arcsin\sqrt{\left(\frac{\lambda + 8\pi\rho_{00}}{3}\right) R_c^2}\,,$$

in accord with (11).

Now

$$\sqrt{\frac{3}{\lambda + 8\pi\rho_{00}}} \arcsin 1 = \sqrt{\frac{3}{\lambda + 8\pi\rho_{00}}} \frac{(1 + 4n)\,\pi}{2} = \\ = \lim_{R_c \to \sqrt{\frac{3}{\lambda + 8\pi\rho_{00}}}^-} \sqrt{\frac{3}{\lambda + 8\pi\rho_{00}}} \arcsin\sqrt{\left(\frac{\lambda + 8\pi\rho_{00}}{3}\right) R_c^2}\,, \\ n = 0, 1, 2, \ldots$$

in accord with (11). Thus R_p can be arbitrarily large. Moreover, R_p can be arbitrarily large for any R_c satisfying (11), since

$$R_p = \sqrt{\frac{3}{\lambda + 8\pi\rho_{00}}} \arcsin\sqrt{\left(\frac{\lambda + 8\pi\rho_{00}}{3}\right) R_c^2} = \\ = \sqrt{\frac{3}{\lambda + 8\pi\rho_{00}}}\,(\psi + 2n\pi)\,, \qquad n = 0, 1, 2, \ldots$$

where ψ is in radians, $0 \leqslant \psi < \frac{\pi}{2}$.

5 Cosmological models of expansion

Transform (10) by

$$\bar{R}_c = \frac{R_c}{\sqrt{1-\frac{R_c^2}{W^2}}}\, e^{-\frac{t}{W}}, \quad \bar{t} = t + \frac{1}{2} W \ln\left(1-\frac{R_c^2}{W^2}\right),$$

$$W^2 = \frac{3}{\lambda + 8\pi\rho_{00}},$$

to get

$$ds^2 = d\bar{t}^2 - e^{\frac{2\bar{t}}{W}}\left(d\bar{R}_c^2 + \bar{R}_c^2 d\theta^2 + \bar{R}_c^2 \sin^2\theta\, d\varphi^2\right), \quad (12)$$

where according to (11), $0 \leqslant \bar{R}_c < \infty$. Clearly the proper radius on (12) is

$$\bar{R}_p = \lim_{\bar{R}_c\to\infty} e^{\frac{\bar{t}}{W}} \int_0^{\bar{R}_c} d\bar{R}_c = \infty\,,$$

therefore (12) describes an infinite Universe for all $\bar{t}$.

Consider the line-element

$$ds^2 = dt^2 - \frac{e^{g(t)}}{\left(1+\frac{k}{4}G^2\right)^2}\left[dG^2 + G^2(d\theta^2 + \sin^2\theta d\varphi^2)\right], \quad (13)$$

where $G = G(r)$, r a parameter. If $k = 0$ a form of (12) is obtained. If $k > 0$,

$$R_p = e^{\frac{1}{2}g(t)} \int \frac{dG}{1+\frac{k}{4}G^2} = e^{\frac{1}{2}g(t)}\left[\frac{2}{\sqrt{k}} \arctan\frac{\sqrt{k}}{2} G + K\right],$$

where K is a constant. $R_p = 0$ is satisfied by $G = 0 = K$, so

$$R_p = e^{\frac{1}{2}g(t)} \int \frac{dG}{1+\frac{k}{4}G^2} = e^{\frac{1}{2}g(t)} \frac{2}{\sqrt{k}} \arctan\frac{\sqrt{k}}{2} G.$$

Now for (13), the radius of curvature is

$$R_c = \frac{G}{1+\frac{k}{4}G^2}\,, \quad (14)$$

which is maximum when $G = \frac{2}{\sqrt{k}}$, i. e.

$$R_{c_{max}} = R_c\left(\frac{2}{\sqrt{k}}\right) = \frac{1}{\sqrt{k}}\,.$$

Also, $\lim_{G\to\infty} R_c = 0$. Therefore, on (13),

$$0 \leqslant R_c \leqslant \frac{1}{\sqrt{k}}\,, \quad (15)$$

or equivalently

$$0 \leqslant G \leqslant \frac{2}{\sqrt{k}}\,. \quad (16)$$

Now

$$R_p\left(G = \frac{2}{\sqrt{k}}\right) = e^{\frac{1}{2}g(t)} \arctan 1 = e^{\frac{1}{2}g(t)} \arctan 1 =$$

$$= e^{\frac{1}{2}g(t)} \frac{(1+4n)\,\pi}{4}, \qquad n = 0, 1, 2, \ldots$$

which is arbitrarily large. Moreover, R_p is arbitrarily large for any R_c satisfying (15), or equivalently for any G satisfying (16), since

$$R_p = e^{\frac{1}{2}g(t)} \frac{2}{\sqrt{k}}\,(\psi + n\pi)\,, \quad n = 0, 1, 2, \ldots$$

where ψ is in radians, $0 \leqslant \psi \leqslant \frac{\pi}{4}$.

If $k < 0$, set $k = -s$, $s > 0$. Then

$$R_p = e^{\frac{1}{2}g(t)} \int \frac{dG}{1+\frac{s}{4}G^2} = e^{\frac{1}{2}g(t)}\left[\frac{1}{\sqrt{s}} \ln\left|\frac{G+\frac{2}{\sqrt{s}}}{G-\frac{2}{\sqrt{s}}}\right| + K\right],$$

where K is a constant. $R_p = 0$ is satisfied for $G = 0 = K$. Then

$$R_p = e^{\frac{1}{2}g(t)} \frac{1}{\sqrt{s}} \ln\left|\frac{G+\frac{2}{\sqrt{s}}}{G-\frac{2}{\sqrt{s}}}\right|.$$

To maintain signature in (13),

$$-\frac{2}{\sqrt{s}} < G < \frac{2}{\sqrt{s}}\,.$$

However, since a negative radius of curvature is meaningless, and since on (13) the radius of curvature in this case is

$$R_c(G) = \frac{G}{1-\frac{s}{4}G^2}\,, \quad (17)$$

it is required that

$$0 \leqslant G < \frac{2}{\sqrt{s}}\,. \quad (18)$$

Now

$$\lim_{G\to\frac{2}{\sqrt{s}}^-} e^{\frac{1}{2}g(t)} \frac{1}{\sqrt{s}} \ln\left|\frac{G+\frac{2}{\sqrt{s}}}{G-\frac{2}{\sqrt{s}}}\right| = \infty,$$

in accord with (18). The proper radius of the space and the radius of curvature of the space are therefore infinite for all time t.

The usual transformation of (13) to obtain the Robertson-Walker line-element involves expressing (13) in terms of the radius of curvature of (13) instead of the quantity G, thus

$$\bar{G} = \frac{G}{1+\frac{k}{4}G^2}\,,$$

carrying (13) into

$$ds^2 = dt^2 - e^{g(t)}\left[\frac{d\bar{G}^2}{1-\frac{k}{4}\bar{G}^2} + \bar{G}^2\left(d\theta^2 + \sin^2\theta d\varphi^2\right)\right]. \quad (19)$$

If $k = 0$ a form of (12) is obtained.

Comparing $\bar{G}$ with (14) it is plain that $\bar{G} = R_c(G)$, where $0 \leqslant R_c \leqslant \frac{1}{\sqrt{k}}$ by (15), $k > 0$, and therefore $0 \leqslant \bar{G} \leqslant \frac{1}{\sqrt{k}}$. Now

$$R_p = e^{\frac{1}{2}g(t)} \int \frac{dR_c}{\sqrt{1-\frac{k}{4}R_c^2}} = e^{\frac{1}{2}g(t)}\left(\frac{2}{\sqrt{k}} \arcsin\frac{\sqrt{k}}{2} R_c + K\right),$$

where K is a constant. $R_p=0$ is satisfied for $R_c=0=K$, so

$$R_p = e^{\frac{1}{2}g(t)}\frac{2}{\sqrt{k}}\arcsin\frac{\sqrt{k}}{2}R_c\,,$$

in accord with (15).

Then

$$R_p\left(R_c=\frac{1}{\sqrt{k}}\right)=e^{\frac{1}{2}g(t)}\,\frac{2}{\sqrt{k}}\left(\frac{\pi}{6}+2n\pi\right), \qquad (20)$$
$$n=0,1,2,\ldots$$

in accord with (15), and so R_p is arbitrarily large for all time t. When making the transformation to the Robertson-Walker form the limits on the transformed coordinate cannot be ignored. Moreover, R_P is arbitrarily large for all time for any R_c satisfying (15), since

$$R_p = e^{\frac{1}{2}g(t)}\frac{2}{\sqrt{k}}\left(\psi+2n\pi\right), \qquad n=0,1,2,\ldots$$

where ψ is in radians, $0\leqslant\psi\leqslant\frac{\pi}{6}$.

If $k<0$ set $k=-s$ where $s>0$, then (19) becomes

$$ds^2=dt^2-e^{g(t)}\left[\frac{dR_c^2}{1+\frac{s}{4}R_c^2}+R_c^2\left(d\theta^2+\sin^2\theta\,d\varphi^2\right)\right]. \quad (21)$$

The proper radius is

$$R_p=e^{\frac{1}{2}g(t)}\int\frac{dR_c}{\sqrt{1+\frac{s}{4}R_c^2}}=e^{\frac{1}{2}g(t)}\left[\frac{2}{\sqrt{s}}\ln\left(R_c+\sqrt{R_c^2+\frac{4}{s}}\right)+K\right]$$

where K is a constant. $R_p=0$ is satisfied for $R_c=0$ and $K=-\frac{2}{\sqrt{s}}\ln\frac{2}{\sqrt{s}}$, in accord with (17) and (18). So

$$R_p=e^{\frac{1}{2}g(t)}\,\frac{2}{\sqrt{s}}\ln\left(\frac{R_c+\sqrt{R_c^2+\frac{4}{s}}}{\frac{2}{\sqrt{s}}}\right).$$

Now $R_p\to\infty$ as $R_c\to\infty$, in accord with (17) and (18). Thus, (21) describes an infinite Universe for any time t.

6 Conclusions

By the foregoing types of spacetimes, General Relativity permits cosmological solutions, contrary to the claims made in [1]. However, the Big Bang theory is not consistent with General Relativity, since the spacetimes permitted are all spatially infinite (arbitrarily large) for any time t.

Submitted on January 13, 2007
Re-submitted after revision on January 18, 2007
Accepted on January 19, 2007

References

1. Crothers S. J. On the general solution to Einstein's vacuum field for the point-mass when $\lambda\neq0$ and its consequences for relativistic cosmology. *Progress in Physics*, 2005, v. 3, 7–14.

Cosmological Redshift Interpreted as Gravitational Redshift

Franklin Potter* and Howard G. Preston†

*Sciencegems.com, 8642 Marvale Dr., Huntington Beach, CA 92646, USA
†15 Vista del Sol, Laguna Beach, CA 92651, USA

E-mail: *drpotter@lycos.com and †hpres@cox.net

Distant redshifted SNe1a light sources from the Universe that are usually interpreted as cosmological redshifts are shown to be universal *gravitational* redshifts seen by all observers in the quantum celestial mechanics (QCM) approach to cosmology. The increasingly negative QCM gravitational potential dictates a non-linear redshift with distance and an apparent gravitational repulsion. No space expansion is necessary. QCM is shown to pass the test of the five kinematical criteria for a viable approach to cosmology as devised by Shapiro and Turner, so the role of QCM in understanding the behavior of the Universe may be significant.

1 Introduction

The observed redshift from distant sources can be interpreted as (1) a velocity redshift called the Doppler Effect, (2) a cosmological redshift in which space itself is expanding during the transit time of the photons, and/or (3) a gravitational redshift as introduced by the General Theory of Relativity (GTR). High-z redshifts from distant SNe1a light sources in galaxies are presently being interpreted as cosmological redshifts, apparently providing observational evidence for the expansion of the Universe.

A new theory, Quantum Celestial Mechanics(QCM), developed from GTR by H. G. Preston and F. Potter [1, 2], accurately predicts the observed SNe1a redshifts from near and distant galaxies. For the Universe, there exists in QCM a previously unknown gravitational potential that is used to derive all of the observed SNe1a redshifts. In addition, QCM predicts no mass currents in any coordinate direction, i.e., no galaxies moving away anywhere. These results eliminate the need for a space expansion. The presently known average baryonic density of the Universe is sufficient for QCM to explain the critical matter/energy density of the Universe.

Observations of galaxies and distributions of galaxies are beginning to suggest conflicts with the standard concept of an expanding Universe and its interpretation of a high-z redshift as a cosmological redshift. For example, galaxies at $z = 2.5$ are reported [3] to be extremely dense when using the expanding Universe assumptions and standard galaxy modeling. However, if the Universe is not expanding, the linear scales of these galaxies would be much larger, eliminating the high density conflict and revealing galaxies much similar to galaxies seen locally.

Theoretical approaches are also beginning to inquire about what we really know about cosmic expansion and its acceleration. In an interesting paper, C. A. Shapiro and M. S. Turner [4] relax the assumption of GTR but retain the weaker assumption of an isotropic and homogeneous space-time described by a metric theory of gravity. Using the Robertson-Walker metric to describe the Universe and accepting the dimming and redshifting of a gold set of SNe1a data [5], they determine the cosmic acceleration kinematically and provide a list of five kinematical criteria that must be met by any approach to cosmology.

In this paper, we compare the QCM predictions for the state of the Universe to the five criteria provided by Shapiro and Turner. Our new result is that QCM agrees with the five criteria. Therefore, SNe1a redshifts can be interpreted as universal *gravitational* redshifts instead of cosmological redshifts. There is no need for space expansion.

2 Reviewing the QCM potential

In a series of papers [1, 2, 6] we derived and applied QCM to the Solar System, to other solar system-like systems such as the satellites of the Jovian planets and exoplanet systems, to the Galaxy, to other galaxies in general, and to clusters of galaxies [7]. In all these cases there is reasonable agreement with the observational data, i.e., the predicted QCM states of the gravitationally-bound systems were shown to be actual states of the systems without the need for dark matter. Recall that the QCM general wave equation derived from the general relativistic Hamilton-Jacobi equation is approximated by a Schrödinger-like wave equation and that a QCM quantization state is completely determined by the system's total baryonic mass M and its total angular momentum H_Σ.

These agreements with the data strongly suggest that QCM applies universally and that all gravitationally-bound systems should obey the quantization conditions dictated by QCM. Therefore, not only should the large-scale gravitationally bound systems like a solar system exhibit QCM behavior, but even a torsion balance near an attractor mass should have quantization states. And the largest gravitationally-bound system of all, the Universe, should also be describable by QCM. The QCM states of a torsion bar system will be

discussed in a future paper. In this paper we concentrate on the QCM Universe.

For gravitationally-bound smaller systems, we found that the Schwarzschild metric approximation produced an efffective gravitational potential for a particle of mass μ in orbit

$$V_{\text{eff}} = -\frac{GM}{r} + \frac{l\,(l+1)\,H^2c^2}{2r^2}\,, \qquad (1)$$

where G is the gravitational constant, c is the speed of light in vacuum, the characteristic length scale $H = H_\Sigma/Mc$, the angular momentum quantization number l originates from the θ-coordinate symmetry, and r is the r-coordinate distance from the origin in spherical coordinates. Therefore, in QCM the total angular momentum squared is $l\,(l+1)\mu^2H^2c^2$ instead of the classical Newtonian expression. Consequently, the quantization of angular momentum dictates which particular circular orbit expectation values $<r>$ in QCM correspond to equilibrium orbital radii, in contrast to Newtonian gravitation for which all radii are equilibrium radii.

In the case of the Universe we used the GTR interior metric approximation, which is directly related to the general Robertson-Walker type of metric. Omitting small terms in the r-coordinate equation, we derived a new Hubble relation that agrees with the SNe1a data. At the same time we showed that our QCM approach produced the required average matter/energy density of about 2×10^{-11} J/m^3, corresponding to the critical density $\rho_c = 8\times10^{-27}$ kg$\times$m^{-3}, with only a 5% contribution from known baryonic matter, i.e., without needing dark energy.

The QCM effective gravitational potential for all observers inside a static dust-filled, constant density universe with no pressure is

$$V_{\text{eff}} \approx -\frac{kr^2c^2}{2\,(1-kr^2)^2} + \frac{l\,(l+1)H^2c^2}{2r^2(1-kr^2)}\,, \qquad (2)$$

where $k = 8\pi G\rho_c/3c^2$. Figure 1 shows this QCM gravitational potential for an r-coordinate distance up to about 10 billion light-years.

If the total angular momentum of the Universe is zero or nearly zero, H can be ignored and then the negative gradient of the first term in V_{eff} produces an average *positive* radial acceleration

$$<\ddot{r}> = kc^2\,\frac{r\,(1+kr^2)}{(1-kr^2)^3} \qquad (3)$$

from which we derive a new Hubble relation

$$<\dot{r}> = r\,\frac{c\sqrt{k}}{1-kr^2}\,. \qquad (4)$$

For r-coordinate distances up to about one billion light-years, when $kr^2 \ll 1$, we recover the standard Hubble relation and have a Hubble constant $h \sim 2\times10^{-18}$ s^{-1}, about 62 km per second per megaparsec, an acceptable value [8]. Without the kr^2 in the denominator, $v/c \to 1$ at about 14.1 billion light-years; otherwise, the maximum visible coordinate distance $r = 8.74$ billion light-years, with more of the Universe beyond this distance.

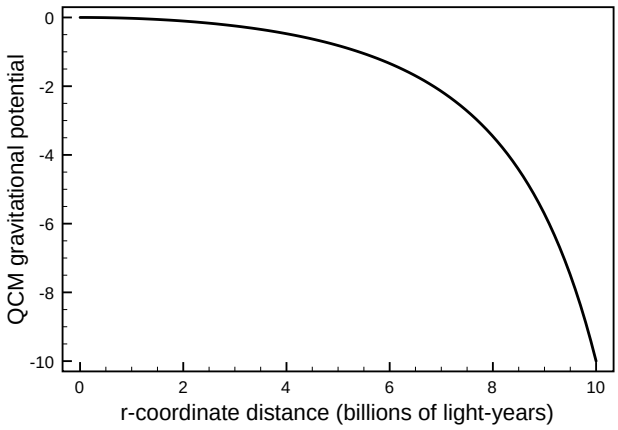

Fig. 1: QCM gravitational potential to 10 billion light-years.

Notice that the QCM effective gravitational potential is negative (when H can be ignored) but produces an apparent *repulsive* gravitational radial acceleration! Each observer anywhere in this Universe will determine that the incoming photons are redshifted. Why? Because the photons originate in a source that is in a more negative gravitational potential where the clock rates are slower than the clock rates at the observer. And this redshift increases non-linearly because the potential becomes more negative more rapidly with increasing distance away. There is no need for expansion of space and its cosmological redshift to explain the SNe1a data. There is no need for dark energy to explain the accelerated expansion.

3 The kinematical criteria

Our QCM approach to cosmology and an understanding of the behavior of the Universe must meet specific kinematical criteria. By analyzing the gold set of SNe1a data, Shapiro and Turner list these five kinematical criteria to be met by any viable approach to a cosmology:

1. Very strong evidence that the Universe once accelerated and that this acceleration is likely to have been relatively recent in cosmic history.
2. Strong evidence that the acceleration q was higher in the past and that the average dq/dz is positive, where z is the redshift.
3. Weak evidence that the Universe once decelerated, but this result may be a model-dependent feature.
4. Little or no evidence that the Universe is presently accelerating, i.e., it is difficult to constrain q for $z < 0.1$ with SNe1a data.
5. No particular models of the acceleration history provide more acceptable fits to the SNe1a data than any

others, i.e., several different kinematic models fit the data as well as the cold dark matter hypotheses called ΛCDM and wCDM.

The QCM effective gravitational potential V_{eff} and the new Hubble relation provide QCM explanations for these five criteria:

1. The light now just reaching us from farther and farther away exhibits an increasing redshift because the V_{eff} is increasingly more and more negative with increasing distance. Without QCM, the interpretation would be that the acceleration is recent.
2. The V_{eff} is increasingly more and more negative with increasing distance. Without QCM, a higher acceleration in the past is required for the space expansion approach to cosmology.
3. QCM shows no deceleration at the level of mathematical approximation we used.
4. The new Hubble relation of QCM reduces to the linear dependence of the standard Hubble relation for z small, agreeing with there being no acceleration presently.
5. Our QCM approach fits the SNe1a data as well as the other approaches, producing about a 12% increase from the linear Hubble when $kr^2 \sim 0.11$, consistent with the data.

QCM explains the five criteria in its unique way because the SNe1a redshift now originates in the properties of the static interior metric and its QCM gravitational potential. The important consequence is that QCM cannot be eliminated by any of the five criteria and must be considered as a viable approach to cosmology.

4 Final comments

The existence of a *repulsive* gravitational potential in the QCM wave equation for the Universe removes the necessity for invoking dark matter and dark energy. According to QCM, the Universe is not expanding and does not require dark energy in order for us to understand its behavior. Previously labelled cosmological redshifts are actually gravitational redshifts of the photons reaching us from distant sources in the Universe that are in greater negative gravitational potentials than the observer. Each and every observer experiences this same behavior. This static Universe is always in equilibrium.

Submitted on January 22, 2007
Accepted on January 24, 2007

References

1. Preston H. G. and Potter F. Exploring large-scale gravitational quantization without $\hbar$ in planetary systems, galaxies, and the Universe. arXiv: gr-qc/0303112.
2. Potter F. and Preston H. G. Quantum Celestial Mechanics: large-scale gravitational quantization states in galaxies and the Universe. *1st Crisis in Cosmology Conference: CCC-I*, Lerner E.J. and Almeida J.B., eds., AIP CP822, 2006, 239–252.
3. Zirm A. W. *et al.* NICMOS imaging of DRGs in the HDF-S: A relation between star-formation and size at $z \sim 2.5$. arXiv: astro-ph/0611245.
4. Shapiro C. A. and Turner M. S. What do we really know about cosmic acceleration? arXiv: astro-ph/0512586.
5. Riess A. G. *et al.* (Supernova Search Team). Observational evidence from supernovae for an accelerating universe and a cosmological constant. arXiv: astro-ph/9805201.
6. Potter F. and Preston H. G. Gravitational lensing by galaxy quantization states. arXiv: gr-qc/0405025.
7. Potter F. and Preston H. G. Quantization states of baryonic mass in clusters of galaxies. *Progress in Physics*, 2007, v. 1, 61–63.
8. Bonanos A. Z.*et al*. (DIRECT Project). The first DIRECT distance determination to a detached eclipsing binary in M33. arXiv: astro-ph/0606279.

Exact Solution of the Three-Body Santilli-Shillady Model of the Hydrogen Molecule

Raúl Pérez-Enríquez*, José Luis Marín† and Raúl Riera†

*Departamento de Física, Universidad de Sonora, Apdo. Postal 1626, Hermosillo 83000, Sonora, Mexico
E-mail: rpereze@fisica.uson.mx

†Departamento de Investigación en Física, Universidad de Sonora

The conventional representation of the H_2 molecule characterizes a 4-body system due to the independence of the orbitals of the two valence electrons as requested by quantum chemistry, under which conditions no exact solution is possible. To overcome this problem, Santilli and Shillady introduced in 1999 a new model of the H_2-molecule in which the two valence electrons are deeply bounded-correlated into a single quasi-particle they called isoelectronium that is permitted by the covering hadronic chemistry. They pointed out that their new H_2-model is a restricted 3-body system that, as such, is expected to admit an exact solution and suggested independent studies for its identification due to its relevance, e.g., for other molecules. In 2000, Aringazin and Kucherenko did study the Santilli-Shillady restricted 3-body model of the H_2 molecules, but they presented a variational solution that, as such, is not exact. In any case, the latter approach produced significant deviations from experimental data, such as a 19.6% inter-nuclear distance greater than the experimental value. In this paper we present, apparently for the first time, an exact solution of the Santilli-Shillady restricted 3-body model of the Hydrogen molecule along the lines of its originators and show that it does indeed represent correctly all basic data. Intriguingly, our solution confirms that the orbital of the isoelectronium (referred to as its charge distribution around the nuclei) must be concentrated in a limited region of space given by the Santilli-Shillady oo-shaped orbits. Our exact solution is constructed by following the Ley-Koo solution to the Schrödinger equation for a confined hydrogen molecular ion, H_2^+. We show that a confined model to the 3-body molecule reproduces the ground state curve as calculated by Kolos, Szalewics and Monkhorst with a precision up to the 4-th digit and a precision in the representation of the binding energy up to the 5-th digit.

1 Introduction

As it is well known, the conventional representation of the Hydrogen molecule characterizes a four-body system due to the independence of the orbitals of the two valence electrons as requested by quantum chemistry, under which conditions no exact solution is possible. To overcome this problem, R. M. Santilli and D. Shillady introduced in 1999 a new model of the H_2-molecule [1, 2], in which the two valence electrons are deeply bounded-correlated into a single quasi-particle they called isoelectronium that is permitted by the covering hadronic chemistry [3a].

They pointed out that their new model of Hydrogen molecule is a restricted three-body system that, as such, is expected to admit an exact solution; they suggested to carry out independent studies for its identification due to its relevance, e.g., for other molecules. In 2000, Aringazin and Kucherenko [4] did study the Santilli-Shillady restricted three-body model of the Hydrogen molecule, but they presented a variational solution that, as such, is not exact. In any case, the latter approach produced significant deviations from experimental data, such as a 19.6% inter-nuclear distance greater than the experimental value.

In this paper we present, apparently for the first time, an exact solution of the Santilli-Shillady restricted three-body model of the Hydrogen molecule along the lines of its originators and show that it does indeed represent correctly all basic data. Intriguingly, our solution confirms that the orbital of the isoelectronium (referred to as its charge distribution around the nuclei) must be concentrated in a limited region of space given by the Santilli-Shillady oo-shaped orbits. Our exact solution is constructed by following the E. Ley-Koo and A. Cruz solution to the Schrödinger equation for a confined hydrogen molecular ion, H_2^+ [5]. We show that a confined model to the three-body molecule reproduces the ground state curve as calculated by Kolos, Szalewics and Monkhorst [6] with a precision up to the 4-th digit and a precision in the representation of the binding energy up to the 5-th digit.

The suggestion that a kind of correlated state of electrons is present while they surround in closed paths the nuclei stimulates the search of a complementary quantum mechanical approach. In addition, Pérez-Enríquez [7], while working on high-Tc superconductivity, found that by using a Möbius-type orbital for Cooper pairs, there is a structural parameter in perovskite type superconductors that correlates linearly

with the critical temperature. Other contributions to the discussion about correlation between electrons were presented by Taut [8] in 1999. He reported that a one-particle representation could apply to systems with high densities of charge, based upon a pair-correlation function and density of charge for a system of two electrons in an external potential.

In our approach as it has been mentioned, we use the idea of a system under confinement as worked by E. Ley-Koo and A. Cruz for the hydrogen molecular ion and by other authors for molecules under pressure [9, 10]. Besides, previous studies related to the present discussion concerning hydrogenic impurities and excitons in quantum dots have been carried out by our team and others [11, 12, 13].

The main features of the restricted three-body Santilli-Shillady model, we discuss here, are summarized in section 2; special attention is drawn to the isoelectronium proposal. In this section, we also compare the results from this model with a standard ground state energy curve calculated by Kolos, Szalewics and Monkhorst (KSM curve) [6]. In section 3, we describe how to calculate the exact solution to the three-body model including a spheroidal confinement and a defect of mass parameters in order to reproduce the standard KSM curve, using a variational calculation. Finally, in section 4, some conclusions are made with regard to the accuracy of our results.

2 Iso-chemical model of the hydrogen molecule

The point of departure of the iso-chemical model of the hydrogen molecule, presented for the first time in 1999 by Santilli and Shillady [1], resides in the fact that the distance between nuclei is large; hence, the force binding them together comes form the orbiting electrons. The main hypothesis of the model describes how the valence electrons become involved in a binding process when they are at very short distance giving rise to a new state or quasi-particle, called isoelectronium. This particle would be responsible for the stability of the molecule and would describe a oo-shaped orbit around the nuclei "in a similar way as a planet orbits around binary stars" [1].

This hydrogen molecule model is forbidden by quantum mechanics and quantum chemistry since the proximity of electrons creates a repulsive Coulomb force between them; however, the authors assume that this difficulty can be overruled by a non-Hamiltonian interaction based on the overlapping of wave packets associated with each electron. This force surmounts the electrostatic one and allows the quasi-particle formation. They affirm that "the attractive force coming from the deep wave-overlapping does not have an equivalent in quantum mechanics and requires the new theory" [1]. This is the reason to introduce the so called iso-mechanics and iso-chemistry theories as part of hadronic mechanics [3b].

Our approach, however, uses the isoelectronium hypothesis and at the same time looks for a compatible state in the frame of quantum chemistry. We will show that there exists a state reproducing the ground state energy of the hydrogen molecule in the frame of the restricted three-body Santilli-Shillady model.

The two basic notions of hadronic chemistry that we need for understanding the iso-chemical model of the hydrogen molecule are:

(a) Hadronic horizon. The hadronic horizon is a distance between electrons, r_c, which measures one femtometer ($1\,\text{fm} = 10^{-15}\,\text{m}$). Outside this range quantum chemistry applies and within it hadronic chemistry is valid;

(b) The trigger, which is given by external (conventional) interactions, causes the identical electrons to move one toward the other and penetrate the hadronic horizon against Coulomb interaction (once inside the said horizon, the attractive hadronic force overcomes the repulsive Coulomb one), resulting in a bound state.

Santilli presented for the first time the hypothesis of a bound state between electrons in 1978 [3], while explaining the structure of a π^0 meson as a hadronic bound state of one electron and one positron. Later, Animalou [14] and Animalou and Santilli [15] extended the model to consider the Cooper pair in superconductivity as a hadronic bound state of two identical electrons.

According to Santilli, in the case of π^0 there is no need for a trigger because the involved particles have opposite charges. However, the existence of the Cooper pair requires a trigger, which Santilli and Animalou identified as the field of the copper ions. In the case of the hydrogen molecule, they conjecture that the trigger, constituted by the field between nuclei, is sufficiently intense (attractive for the electrons) enough to draw them together. They assume, essentially, that atom attraction is sufficient to cause the overlapping between wave packets, thus pushing electrons beyond the hadronic horizon.

2.1 Four-body Santilli-Shillady model

The iso-chemical model of the hydrogen molecule uses the conventional quantum model of the H_2 subject to a non-unitary transformation for the condition $r_c = r_{12}$. This inter electronic distance is small given that the electrons are inside the hadronic horizon. After using this transformation, one can reduce the problem to an equation that uses a Hulthén potential, recalling that at short distances, this behaves like a Coulomb potential,

$$\left\{-\frac{\hbar^2}{2\mu_1}\nabla_1^2-\frac{\hbar^2}{2\mu_2}\nabla_2^2-V_0\frac{e^{-r_{12}/r_c}}{1-e^{-r_{12}/r_c}}+\frac{e^2}{r_{12}}-\right.$$
$$\left.-\frac{e^2}{r_{1a}}-\frac{e^2}{r_{2a}}-\frac{e^2}{r_{1b}}-\frac{e^2}{r_{2b}}+\frac{e^2}{R}\right\}|\widehat{\psi}\rangle = E\,|\widehat{\psi}\rangle\,. \quad (1)$$

As Santilli and Shillady affirm, this equation exhibits a new explicitly attractive force among neutral atoms of the

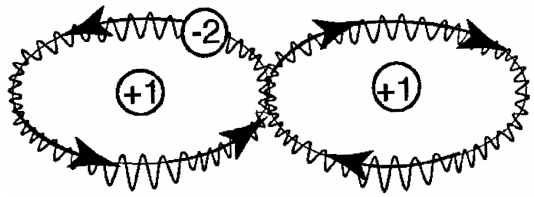

Fig. 1: Hydrogen molecule in the restricted three-body Santilli-Shillady model; a stable isoelectronium moves around nuclei in a oo-shaped orbit (figure taken from Santilli 1999, ref. [1]).

molecule in a way that is not possible within the quantum chemistry framework. They claim that Eq. (1) explains why only two hydrogen atoms make up the molecule and allows the exact representation of the binding energy in the full 4-body configuration.

A further simplification of the iso-chemical model can be introduced by making the two iso-electrons (electrons inside the hadronic horizon) be bound together into a state called isoelectronium as mentioned above. With this approximation, Equation (1) is reduced to a restricted three-body problem because one can consider $r_{1a} \approx r_{2a} = r_a$ and $r_{1b} \approx r_{2b} = r_a$ as $r_{12} \ll r_a, r_b$. In this manner, an exactly solvable problem similar to the conventional ion is obtained. One remarkable idea proposed by the authors consists in representing the isotopic model of the molecule as two H-protons at rest and the isoelectronium moving around them in a oo-shaped orbit, as it is shown in Figure 1 and described by the following structural equation:

$$\left\{ -\frac{\hbar^2}{2\mu_1}\nabla_1^2 - \frac{\hbar^2}{2\mu_2}\nabla_2^2 - V_0 \frac{e^{-r_{12}/r_c}}{1-e^{-r_{12}/r_c}} + \frac{e^2}{r_{12}} - \right. \\ \left. - \frac{2e^2}{r_a} - \frac{2e^2}{r_b} + \frac{e^2}{R} \right\} |\widehat{\psi}\rangle = E\,|\widehat{\psi}\rangle\,. \tag{2}$$

This simplification, impossible in a quantum chemistry environment, could be used to reach an exact solution of the H-molecule. At this point, it is worth mentioning that with the aid of this model, Santilli and Shillady extended their analysis to other molecules; in particular, they studied the hydrogen and oxygen atoms in order to form HO. This gave them elements to present, for the first time, an exact solution to the water molecule, treated as an HOH molecule, using an isotopic intersection of an HO and an OH [2]. They have further their research to extend their model to another type of molecular chains and molecules.

Results for the Santilli-Shillady model of molecular hydrogen were obtained by the standard Boys-Reeves model [1], using an attractive Gaussian-screened-Coulomb potential. These authors used their SASLOBE programme (Santilli-Animalou-Shillady LOBE) to calculate the energies reported in columns three and four of Table 1, which in turn are compared with the quantum chemical results (first column).

Results from Table 1 show that the energy calculated by the SASLOBE program (-1.174444 au) differs from the exact result in the 6th digit (a 3×10^{-5} error) with a 20 hours process time in a 320 MFLOPS Silicon Graphics computer. Notice that some changes in the most expensive routines in the iso-chemical model improve by a factor of 1000 the time used to compute a Boys-Reeves C.I. calculation. An important result is that with their method, they found a bound length ($R = 1.4011$ bohr) which coincides with that of the C.I. value.

Concept/species	H_2 [a)]	$\widehat{H}_2$ [b)]	$\widetilde{H}_2$ [c)]
Energy (variational)	-1.12822497	-7.61509174	*
Energy SCF (au)	1.14231305	*	-1.13291228
Energy SAS (au)	*	*	-1.174444
Energy exact[d)] (au)	-1.174474	*	-1.174474
Bond length (bohr)	1.4011	0.2592	1.4011
Isoelectronium radius (bohr)	*	*	0.01124995

Notes: [a)] Normal molecule in the quantum-chemical model
[b)] Molecule in the restricted three-body model (see)
[c)] Molecule in the iso-chemical model (stable isoelectronium)
[d)] Ground state energy by Kolos, Szalewicz and Monhorst

Table 1: Comparison of results from Iso-chemical model. Taken from Santilli 1999, ref. [1].

This new way to represent chemical bonding has allowed the opening of a whole field named Hadronic Mechanics. With this new tool, several problems of physics and chemistry have been worked, leading to new proposals that range from energetic problems to superconductivity issues [16]. Our work has not taken that road; it considers the solution of the restricted three-body in the frame of Quantum Mechanics, two protons bound by an orbiting stable isoelectronium. This approach uses the solution of an H_2^+ ion but with a charge $q = -2e$ for the quasi-particle.

2.2 Restricted three-body Santilli-Shillady model

The four-body Santilli-Shillady model, as described by Eq. (2), was modified by Aringazin and Kucherenko [4] in order to restrict it to an explicit three-body approach. Within this restricted three-body Santilli-Shillady model (M3CS-S), these authors found a set of two equations that can be solved exactly. In this section we follow the main features of their method and show some of their results to contrast them with the results from our approach. The restricted Santilli-Shillady model assumes three basic conditions:

(a) A stable isoelectronium;

(b) The size of the isoelectronium can be neglected as compared with the inter nuclear distance; and,

(c) The Born-Oppenheimer approximation is valid.

When we combine these conditions with Eq. (2), representing a four-body equation, we arrive at a couple of differential equations which can be exactly solved. Aringazin and Kucherenko assumed that:

$$\mu_1 = \mu_2 = m_e\,. \tag{3}$$

And that the isoelectronium mass and reduced mass were

$$M = \mu_1 + \mu_2\,; \qquad m = \frac{\mu_1\mu_2}{M}\,. \tag{4}$$

In order to simplify expressions, they transformed the momentum operators

$$\overline{p}_i = -i\hbar\,\frac{\partial}{\partial r_i}\,, \qquad i = 1, 2; \tag{5}$$

into generalized ones:

$$\overline{P}_M = -i\hbar\,\frac{\partial}{\partial \overline{r}_{ab}}, \qquad \overline{p}_{12} = -i\hbar\,\frac{\partial}{\partial \overline{r}_{12}}\,. \tag{6}$$

Through them, Aringazin and his colleague arrived to a new equation from which the three-body equation can be derived by a variable separation method; i.e., from equation

$$\left\{-\frac{\hbar^2}{2M}\nabla^2_{ab} - \frac{\hbar^2}{2m}\nabla^2_{12} - V_0\frac{e^{-r_{12}/r_c}}{1-e^{-r_{12}/r_c}} + \frac{e^2}{r_{12}} - \right. \\ \left. - \frac{2e^2}{r_a} - \frac{2e^2}{r_b} + \frac{e^2}{R}\right\}|\widehat{\psi}\rangle = E\,|\widehat{\psi}\rangle \tag{7}$$

they got two equations, one describing the electrons inside the hadronic horizon in terms of the distance between them:

$$-\frac{\hbar^2}{2m}\,\nabla^2_{12}\,\chi + V(r_{12})\,\chi = \varepsilon\,\chi\,; \tag{8}$$

and, the second for the isoelectronium interaction with the nuclei:

$$-\frac{\hbar^2}{2M}\,\nabla^2_{ab}\,\psi + W(r_a, r_b, R)\,\psi = (E-\varepsilon)\,\psi, \tag{9}$$

where

$$|\widehat{\psi}\rangle = \chi\,(r_{12})\,\psi(r_a, r_b) \tag{10}$$

with

$$V(r_{12}) = \frac{e^2}{r_{12}} - V_0\frac{e^{-r_{12}/r_c}}{1-e^{-r_{12}/r_c}}, \tag{11}$$

and

$$W(r_a, r_b, R) = -\frac{2e^2}{r_a} - \frac{2e^2}{r_b} + \frac{e^2}{R}\,. \tag{12}$$

The Aringazin-Kucherenko proposal, Eqs. (9) and (12), becomes the restricted three-body Santilli-Shillady Model (M3CS-S) with which we are going to compare our results. On the other hand, Eqs. (8) and (11) become the description of the electrons involved in the isoelectronium itself. They have also considered that since the size of isoelectronium is small, the energy must be near zero, $\varepsilon \approx 0$; a point we are not going to discuss here.

ν [a)]	E	R_{opt} [b)]
0.3	−1.142556	1.722645
0.307	−1.169215	1.683367
0.308	−1.173024	1.677899
0.308381[c)]	−1.174475	1.675828
0.309	−1.176832	1.672471

Notes: [a)] Mass parameter in
[b)] Optimum bond length (bohr)
[c)] Parameter to obtain best energy

Table 2: Minimum energy dependence on the mass parameter

The direct solution of these equations gives results for the energy and bond length far from the experimentally observed; for example, the minimum energy, $E = -7.614289$ au, is much lower than $E_e = -1.17447567$ au, while the bond length, $R = 0.25$ bohr, markedly differs from $R = 1.4011$ bohr.

2.3 Results from the Aringazin-Kucherenko approach

As it has just been mentioned, the application of the restricted three-body Santilli-Shillady model gives results far from the experimental values for both, energy and bond length. In order to correct this problem, Aringazin and his team have chosen a scaling method to equalize their energy value with that experimentally observed. By assuming a charge equal to $-2e$ for the isoelectronium and its mass $M = \nu m_e$, they assigned to E the formula $E = W + 1/R$ (W is isoelectronium energy) and R in Eq. (9) to get a scaling rule for their original calculated data. The summary of the scaling process is:

$$(R, W) \longrightarrow (R,\, W + 1/R) \longrightarrow \left(\frac{R}{2\nu},\, 4\nu\, W\right) \longrightarrow \\ \longrightarrow \left(\frac{R}{2\nu},\, 4\nu\, W + \frac{2\nu}{R}\right). \tag{13}$$

Values in Table 2 show energy variations with respect to mass parameter and allows the identification of as the best parameter for the estimation of energy, $E = -1.174475$ au. While we have a 7th significant digit precision to the desired energy, the correspondent bond length disagrees 19.6% from the expected value.

There are, in the literature, a great number of studies and estimates for the ground state energy of molecular hydrogen. This elemental molecule is the most studied one and has compelled researchers in this field to design tools and other quantum mechanical theories. To compare our results with those of Aringazin-Kucherenko, we are going to use as the ground state energy curve the values reported by Kolos, Szalewicz y Monkhorst [6] as reference. Though there are already other studies reporting higher precision values, up to 12 significant digits [17], for example, we will not employ them here for we do not need such precision as our method gives numbers up to the 6th significant digit. These data are going to be identified as Kolos data or KSM curve.

With the aid of the data for the electronic energy W as a function of the distance between nuclei in the molecule (we remit the reader to Table 2 in ref. [4]), it is possible to construct a curve for the molecular energy according to the M3CS-S model. In Figure 2, we present a graph comparing the corresponding curve with Kolos data. It is self evident that both curves are very different, mainly in the region $R > 2.0$, though profiles are similar for lower R values.

On the other hand, the optimum bond length, $R = 1.675828$ bohr, of this curve is deviated from the experimentally observed value by 19.6%. These observations to the M3CS-S model imply that some kind of adjustment is

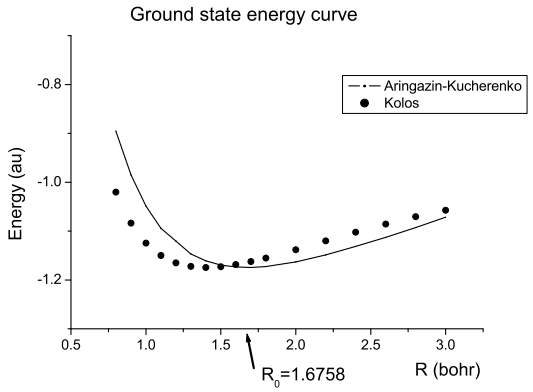

Fig. 2: Comparison between KSM's ground state energy data and scaled Aringazin-Kucherenko curve.

needed; probably a change in one of the features of the isoelectronium model could suppress these differences. In next section, we will present one such modification: the finite extension of isoelectronium.

3 Confined isoelectronium approach

We have shown until this point that the M3CS-S model satisfies the established conditions for the existence of isoelectronium with two drawbacks: it lacks the precision to represent the ground state potential energy curve of the hydrogen molecule and does not give a good approximation to its optimum bond length. In this section, we are going to introduce a condition directly related to the isoelectronium definition, a condition on the extension of isoelectronium wave function that will provide a modified three-body Santilli-Shillady model reproducing the behavior of the KSM curve in an appreciable range of distances between nuclei in the molecule.

The isoelectronium, as proposed by iso-chemistry, is a particle that brings together both electrons in the Hydrogen molecule, bound firmly (stable isoelectronium) by a Hulthén type potential. With a charge twice of the electron this quasi-particle has to orbit around protons in a very compact way. For an $M = 2m_e$ particle, the results of the calculations give very low energies and small bond length values. From this picture, we consider that the four-body problem of the hydrogen molecule can be converted into a compatible three-body approach if some aspects of the quasi-particle formation and molecule structure are taken into account. First of all, the formation of particles involves the transformation of mass into energy as it is observed for example in nuclear reactions; this means that while electrons come together to form an isoelectronium, there must be an effective mass factor present in the description of the molecule. As seen from the Schrödinger equation, this parameter would appear as a scaling factor for the energy and bond length.

This kind of scaling has been suggested in the literature before, not just by Aringazin and Kucherenko but by other authors as well. In particular, Svidzinsky and collaborators [18] have recently published a paper on the role of scaling while they attempt to represent the hydrogen molecule from Bohr's model. They make a dimensional scaling of the energy in this pre-quantum mechanical description. In our approach, scaling comes from an effective mass factor.

Another factor that must be considered in our model arises from the fact that a double charged particle surrounding both nuclei in the molecule can not extend in the same way as an electron does in the molecular ion. This small but heavily charged quasi-particle must have to limit its motion to confined orbits. Thus, the Hydrogen molecule with the isoelectronium orbiting two protons has to appear as a confined system. Therefore, as a way to improve the restricted three-body Santilli-Shillady model, a pair of conditions was introduced to understand the kind of movement an isoelectronium would describe. We have hypothesized the following additional restrictions for the isoelectronium model:

(a) The formation of the quasi-particle from the two electrons involves an effective mass transformation; i.e., the mass and charge of isoelectronium are $M = \nu m_e$ and $q = -2e$, respectively, where ν is the effective mass parameter, also called "iso-renormalization of mass"; and

(b) The spatial extension of the orbits of isoelectronium is limited to a defined region of space: the isoelectronium must orbit in a spheroidal shaped region of space.

Using these two hypotheses we have worked out two methods for the solution of the hydrogen molecule problem. First, the solution of Eq. (9) is considered in a way similar to the Ley-Koo and Cruz solution for the molecular ion confined by a spheroidal box [5]. They arrive to an exact solution for the differential equation by using separation of variables and the condition of a vanishing wave function on the spheroidal border. The second, whose results are reported here, uses a variational approach to solve Eq. (9) as it was done by Marín and Muñoz [19], with the same border condition: $\psi(\xi_0, \eta, \varphi) = 0$ and ξ_0 defines the shape of the box.

3.1 Exact solution to the confined model

Our variational approach to solve the modified three-body Santilli-Shillady model of the hydrogen molecule (modified M3CS-S) arrives to the following equation after applying the Hamiltonian for H_2^+, but including the above stated conditions on the mass, $M = \nu m_e$, where ν is the mass parameter, and the $q = -2e$ is the charge:

$$\left\{ -\frac{\hbar}{2\nu m_e} \frac{4}{\rho^2(\xi^2-\eta^2)} \left[\frac{\partial}{\partial\xi}(\xi^2-1)\frac{\partial}{\partial\xi} + \frac{\partial}{\partial\eta}(1-\eta^2)\frac{\partial}{\partial\eta} \right] + \right.$$
$$+ \frac{\xi^2-\eta^2}{(\xi^2-1)(1-\eta^2)} \frac{\partial^2}{\partial\varphi^2} - \frac{4e^2}{\rho} \frac{(Z_1+Z_2)\xi + (Z_2-Z_1)\eta}{\xi^2-\eta^2} + \quad (14)$$
$$\left. + \frac{Z_1 Z_2 e^2}{\rho} \right\} \psi(\xi,\eta,\varphi) = E' \psi(\xi,\eta,\varphi) ,$$

subject to the following restriction:

$$\psi(\xi_0, \eta, \varphi) = 0, \tag{15}$$

which specifies a spheroidal shaped region of space where the particle moves ($\xi \leqslant \xi_0$). Moreover, the wave function must vanish at the border. Due to the symmetry of the molecule in the ground state ($m = 0$), the azimuthal variable, can be suppressed so the problem is reduced to the $z - x$ plane. In addition, we introduce atomic units:

$$a_0 = \frac{\hbar^2}{m_e e^2}\,; \qquad E' = \frac{e^2}{2a_0}E\,; \qquad R = \frac{\rho}{a_0}\,.$$

Thus, the equation is rewritten as

$$\widetilde{H}\phi = E\phi$$

or

$$\left\{-\frac{4}{\nu R^2(\xi^2-\eta^2)}\left[\frac{\partial}{\partial\xi}(\xi^2-1)\frac{\partial}{\partial\xi}+\frac{\partial}{\partial\eta}(1-\eta^2)\frac{\partial}{\partial\eta}\right]-\right.$$
$$\left.-\frac{8}{R}\frac{(Z_1+Z_2)\xi+(Z_2-Z_1)\eta}{\xi^2-\eta^2}+\frac{Z_1Z_2}{R}\right\}\phi(\xi,\eta)=E\phi(\xi,\eta). \tag{16}$$

With this reduction, the above stated conditions can be met by a simple variational function considering one parameter and a cut off factor:

$$\phi(\alpha;\xi,\eta) = (\xi_0 - \xi)\big(\exp\big[-\alpha(\xi+\eta)\big]+ \\ +\exp\big[-\alpha(\xi-\eta)\big]\big)\,. \tag{17}$$

The minimum energy of this modified M3CS-S molecule can be obtained by minimization of the functional of energy

$$E(\alpha) = \frac{\langle\phi|\,\widetilde{H}\,|\phi\rangle}{\langle\phi\,|\phi\rangle} \tag{18}$$

subject to the condition

$$\left.\frac{\partial E}{\partial\alpha}\right|_{E=E_{\min}} = 0\,, \tag{19}$$

But really such a minimum energy, $E_{\min}$, will depend on several parameters

$$E_{\min} = E_{\min}(\nu, \xi_0, R)\,, \tag{20}$$

i.e., mass scale, spheroidal box and nuclei separation parameters. If we leave free all three parameters and use a simplex optimization method, a Nelder-Mead method for example [20], we will find that this energy is located at a point near the one reported by Santilli-Shillady and included here in Table 1 ($E = -7.61509174$ au and $R = 0.2592$ bohr). However, we can choose a fixed value for the mass parameter and find the minimum energy suitable for the ground state energy of free H_2.

Effectively, in order to obtain the minimum energy corresponding to a given mass parameter, ν, we have optimized the energy using the Nelder-Mead algorithm for two parameters: ξ_0 — spheroidal box shape; and, R — bond length.

ξ_0 [a)]	R [b)]	ν [c)]	E [d)]
48.46714783	1.41847181	0.37030	−1.1741987
48.46714783	1.41847181	0.37035	−1.1743573
48.46714783	1.41847181	0.37038	−1.1744523
48.46714783	1.41847181	0.37039	−1.1744840 [e)]
48.46714783	1.41847181	0.37040	−1.1745157
48.46714783	1.41847181	0.37050	−1.1748325
48.46714783	1.41847181	0.37060	−1.1751492

Notes: [a)] Shape parameter inverse of eccentricity (optimization)
[b)] Bond length parameter (optimization)
[c)] Mass parameter up to five digits (fixed)
[d)] Minimum energy (calculated by program)
[e)] Nearest value to exact energy (error)

Table 3: Minimum energy from parameter optimization for the confined model.

One relevant aspect resulting from these calculations is that for all mass parameter values the convergence of the method yields always identical values for both parameters as can be seen in Table 3 ($\xi_0 = 48.46714783$; $R = 1.41847181$ bohr). Furthermore, the minimum energy for $\nu = 0.37039$ gives an energy $E = -1.1744840$ au; that is, we have obtained the energy of the experimentally observed ground state of molecular hydrogen with a precision of 1×10^{-5} and a corresponding error in bond length of just 1.24%. This last result must be compared with the difference calculated by Aringazin and Kucherenko, 19.6%, to appreciate the importance of our finding.

Our approach to the hydrogen molecule, named from here onward as the Pérez-Marín-Riera approach to the restricted three-body Santilli-Shillady of the hydrogen molecule or M3CPM-R, encompasses more than the sole calculation of the minimum energy. With it, we can reproduce the whole set of data points of the KSM ground state curve in the $R \in [0.8, 3.2]$ interval.

3.2 Comparison of our data with KSM curve

As we have just mentioned, our approach to the isoelectronium movement provides an effective way to represent the ground state of H_2. Using the box shape and effective mass parameters found for the closest value to the exact energy of the ground state minimum, we have calculated the energy for several values of the distance between protons ranging from 0.4 to 6.0 bohr. The values obtained in this manner show a very significant behavior, a least in a defined interval $R \in [0.8, 3.2]$. We reproduce the values that Kolos and his collaborators obtained with a highly sophisticated computing method, shown with ours in Table 4 for comparison. As can be seen while reviewing the las column in the table, a difference appears in the fourth significant digit for the worst result and up to the fifth digit for the best, which is located at $R = 1.40$ bohr.

Figure 3 illustrates the values for the energy as a function of R found by Kolos (big points) together with the curve (line) representing our data. Both data sets are identical to

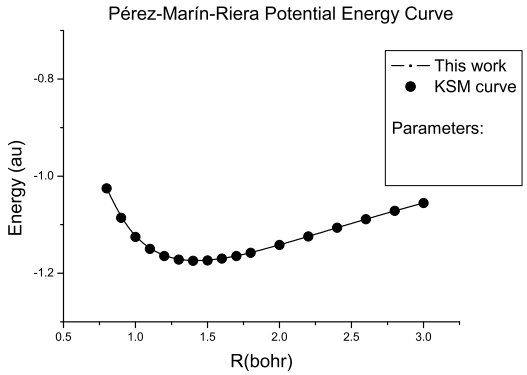

Fig. 3: Comparison between Kolos data and our exact restricted three-body model for the Hydrogen molecule (parameters are: ν - mass; ξ_0 - spheroidal shape).

each other up to the 4th significant digit; this is confirmed by a χ^2 statistical test ($\chi^2 = 1.3522$ with $gl = 17$), with a confidence level of 0.9999998 We state that by confining the isoelectronium, it is possible to reproduce the standard curve with a minimum computational calculation effort.

Again, if compare this result with that of the Aringazin-Kucherenko curve ($\chi^2 = 410.239$ with $gl = 17$), we state that the Aringazin curve differs completely from the KSM curve, as it was shown in Figure 2.

Both findings, up to six digit precision in minimum energy coincidence and whole curve reproduction, give support to our approach to the three-body Santilli-Shillady model. We can establish that the hypothesis on the isoelectronium movement is correct; that is, the orbiting of isoelectronium around both nuclei limits itself to a spheroidal region of space. Another way to express this behavior is that the formation of isoelectronium could be favored by the confinement of the molecule without changing its general properties.

The isoelectronium movement in a bound state together with the charge distribution confirms the explanation given by iso-chemistry to the following question: Why has the hydrogen molecule only two atoms? In our view, as soon as the molecule forms (isoelectronium) it becomes a bound system thus limiting the possibility of another hydrogen atom to be part of the molecule. In fact, the Pauli principle requires that the two valence electrons are correlated-bounded in a singlet state; as a result, the isoelctronium has spin zero. Consequently, no third electron can be bound via a conventional valence (see [3c] for details).

4 Conclusions

The value for the minimum energy of the ground state of the hydrogen molecule has been obtained using the three-body Santilli-Shillady model. Other parameters involved, such as the optimum bond length or energies for several distances between nuclei, can not be verified with it. We have shown that after modifying the model, by introducing a condition on

R [a]	α [b]	M3CP-M [c]	KSM [d]	Diff. [e]
0.80	0.4188965	−1.024900	−1.0200565	0.0048435
0.90	0.4585059	−1.085753	−1.0836432	0.0021098
1.00	0.4964746	−1.125001	−1.1245396	0.0004614
1.10	0.5331055	−1.149680	−1.1500574	0.0003774
1.20	0.5686328	−1.164305	−1.1649352	0.0006302
1.30	0.6032813	−1.171876	−1.1723471	0.0004711
1.40	0.6371875	−1.174438	−1.1744757	0.0000377 [f]
1.50	0.6705273	−1.173416	−1.1728550	0.0005610
1.60	0.7033789	−1.169826	−1.1685833	0.0012427
1.70	0.7358594	−1.164397	−1.1624586	0.0019384
1.80	0.7680469	−1.157664	−1.1550686	0.0025954
2.00	0.8319141	−1.141767	−1.1381329	0.0036341
2.20	0.8953906	−1.124237	−1.1201321	0.0041049
2.40	0.9589063	−1.106267	−1.1024226	0.0038444
2.60	1.0228130	−1.088534	−1.0857913	0.0027427
2.80	1.0871880	−1.071422	−1.0706831	0.0007389
3.00	1.1521880	−1.055136	−1.0573262	0.0021902
3.20	1.2179690	−1.039776	−1.0457995	0.0060235

Notes: [a] Bond length (in bohr)
[b] Non linear variational parameter
[c] Our data in the present work with $\xi_0 = 48.467148$ and $\nu = 0.37039$
[d] Kolos, Szalewicz and Monhorst data from 1986 [6]
[e] Absolute value of the difference.
[f] Best approximation up to 6th significant digit

Table 4: Energies for the M3CP-M model and KSM curve

the isoelectronium orbit, it is possible to calculate a minimum energy for the ground state coincident with the experimental values up to the sixth significant digit. Furthermore, the modified three-body model of the hydrogen molecule, a confined three-body system, enables the reproduction of the whole curve of ground state energy in the range $[0.80, 3.20]$ for the bond length. The physical interpretation to the confined isoelectronium model comprehends the isoelectronium itself, since the interaction between electrons while the quasiparticle is forming, implies its movement to be restricted to a defined region of space. The Santilli-Shillady orbits, the oo-shaped orbits, go beyond a way of speaking, they are a condition for the movement of the electron pair. This limitation in movement could be present in other states of electron pairs, such as the Cooper pairs of superconductivity, mainly in high Tc Superconductivity, for example.

The M3CP-M-R model of the hydrogen molecule introduced here represents an appropriate approach to study this molecule and gives support to the isoelectronium model introduced by Santilli and Shillady.

Acknowledgements

We want to thank Universidad de Sonora for the support given to this project; in particular, the scholarship for the PhD Student Raul Ruben Perez Enriquez. We also recognize the comments and support received from Prof. R. M. Santilli. This work was done under a CONACyT project.

Submitted on January 22, 2007
Accepted on January 29, 2007

References

1. Santilli R. M. and Shillady D. D. A new iso-chemical model of the hydrogen molecule. *Intern. J. Hydrogen Energy*, 1999, v. 24, 943–956.
2. Santilli R. M. and Shillady D. D. A new iso-chemical model of the water molecule. *Intern. J. Hydrogen Energy*, 2000, v. 25, 173–183.
3. Santilli R. R. *Hadronic J.*, 1978, v. 1, 574. [3a]; Elements of hadronic mechanics, vols. I, II (1995) and III (in press), Ukraine Acad. of Sciences, Kiev, (accessed on http://www.i-b-r.org/ Hadronic-Mechanics.htm) [3b]; Foundations of hadronic chemistry with applications to new clean energies and fuels. Kluwer Academic Publisher, the Netherlands, 2000 [3c].
4. Aringazin A. K. and Kucherenko M. G. Exact solution of the restricted three-body Santilli-Shillady model of H_2 molecule. *Hadronic J.*, 2000, v. 23, 1–76.
5. Ley-Koo E. and Cruz S. A. The hydrogen atom and the H_2^+ and HeH^{++} molecular ions inside prolate spheroidal boxes. *J. Chem. Phys.*, 1981, v. 74, 4603–4610.
6. Kolos W., Szalewicz K., Monkhorst H. J. New Bohr-Oppenheimer potential energy curve and vibrational energies for the electronic ground state of the hydrogen molecule. *J. Chem. Phys.*, 1986, v. 84, 3278–3283.
7. Pérez-Enríquez R. Structural parameter for high Tc superconductivity from an octahedral Möbius strip in RBaCuO:123 type perovskite. *Rev. Mex. Fis.*, 2002, v. 48, Supl. 1, 262–267.
8. Taut M. Two electrons in an external oscillator potential: particular analytic solutions of a Coulomb correlation problem. *Phys. Rev. A*, 1993, v. 48, 3561–3565.
9. LeSar R. and Herschbach D. R. Electronic and vibrational properties of molecules at high pressures: hydrogen molecule in a rigid spheroidal box. *J. Phys. Chem.*, 1981, v. 85, 2798–2804.
10. Corella-Madueco A., Rosas R., Marín J. L., Riera R. and Campoy G. Hydrogen molecule confined within a spheroidal box. (to be published).
11. Marín J. L., Cruz S. A. Use of the direct variational method for the study of one- and two-electron atomic systems confined by spherical penetrable boxes. *J. Phys. B: At. Mol. Opt. Phys.*, 1992, v. 25, 4365–4371.
12. Marín J. L., Campoy G. and Riera R. Simple model to study some properties of H trapped in solids. *Intern. J. Quantum Chem.*, 2003, v. 93, 271–274.
13. Valderrama E. G and Ugalde J. M. Electron correlation studies by means of local-scaling transformation and electron-pair density functions. *J. Math. Chem.*, 2005, v. 37, 211–231.
14. Animalou A. O. E. *Hadronic J.*, 1994, v. 17, 379.
15. Animalou A. O. E. and Santilli R. M. *Intern. J. Quantum Chem.*, 1995, v. 29, 175.
16. Santilli R. M. Foundations of hadronic chemistry with applications to new clean energies and fuels. Ed. IBR., Kluwer Academic Publishers 2001.
17. Sims J. S. and Hagstrom S. A. High precision variational calculations for the Born-Oppenheimer energies of the ground state of the hydrogen molecule. *J. Chem. Phys.*, 2006, v. 124, 094101.
18. Svidinsky A. A., Scully M. O. and Herschbach D. R. Simply and surprisingly accurate approach to the chemical bond obtained from dimensional scaling. *Phys. Rev. Let.*, 2005, v. 95, 080401.
19. Marín J. L. and Muñoz G. Variational calculations for enclosed quantum systems within soft spheroidal boxes: the case of H, H_2^+ and HeH_2^+. *J. Mol. Structure* (Teochem), 1993, v. 287, 281–285.
20. Wright M. H. Direct search methods: once scorned, now respectable. In: *Numerical analysis 1995*, Dundee University Press, 191–208.

Study of the Matrix Effect on the Plasma Characterization of Six Elements in Aluminum Alloys using LIBS With a Portable Echelle Spectrometer

Walid Tawfik Y. Mohamed

National Inst. of Laser Enhanced Science NILES, Dept. of Environmental Applications, Cairo University, Cairo, Egypt
Faculty of Education for Girls, Department of Physics, Gurayyat, North of Al-gouf, Kingdom of Saudi Arabia

E-mail: Walid_Tawfik@hotmail.com

Laser-induced breakdown spectroscopy (LIBS) has been applied to perform a study of the matrix effect on the plasma characterization of Fe, Mg, Be, Si, Mn, and Cu in aluminum alloy targets. The generated plasma emissions due to focusing of a 100 mj Nd: YAG pulsed laser at 1064 nm at the target surface were detected using a portable Echelle spectrometer with intensified CCD camera. Spectroscopic analysis of plasma evolution of laser produced plasmas has been characterized in terms of their spectra, electron density N_e and electron temperature T_e assuming the LTE and optically thin plasma conditions. The obtained average values of T_e and N_e were 7600 K and 3×10^{17} cm^{-3}, respectively, for the six elements in the aluminum alloy samples. The electron density increases with the element concentration while the plasma temperature does not has significance change with concentration. For industrial applications, LIBS with the portable Echelle spectrometer could be applied in the on-line production control that following up elemental concentration in metals and pharmaceuticals by only measuring N_e.

1 Introduction

Laser Induced Plasma Spectroscopy (LIPS or LIBS) is an alternative elemental analysis technology based on the optical emission spectra of the plasma produced by the interaction of high-power laser with gas, solid and liquid media. The increasing popularity of this technique is due to easiness of the experimental set-up and to the wide flexibility in the investigated material that doesn't need any pre-treatment of the sample before the analysis. Obvious tasks for LIBS are certification of metal contents in alloys, trace detection of metals for environmental pollution analysis in soils, on-line control of laser induced industrial processes (e.g. cutting and welding, thin film deposition), quick characterization of material in archaeological objects and works of art, and many others [1–5].

LIBS is based on analysis of line emission from the laser-induced plasma, obtained by focusing a pulsed laser beam onto the sample. The physical and chemical properties of the sample can affect the produced plasma composition, a phenomenon known as the matrix effect. The interaction between the laser and the target in LIBS is influenced significantly by the overall composition of the target, so that the intensity of the emission lines observed is a function of both the concentration of the elements of interest and the properties of the matrix that contains them. Plasma composition is dependent not only on composition of the sample, but also on laser parameters, sample surface conditions as well as on thermal and optical properties of the sample. Previously published works studied the matrix effect under different experimental conditions to specify causes and find out the methods of correction [6–11]. The different approaches have been undertaken to discriminate the problems resulting from the fractionation of the ablation and matrix effects. The most convenient approach is to determine elemental abundance comparing the analytic line intensities with signals obtained from the proper reference standards having the similar matrix composition. But, it is not always possible to obtain such calibration curves because there are no available standard samples, or it is impossible to have an internal standard of known concentration [12, 13]. In addition, plasma formation dynamics, sample ablation and associated processes are highly non-linear and not fully understood and may also play an important role as reasons of the matrix effect.

Recently an alternative procedure, based on the LIBS technique, for quantitative elemental analysis of solid materials has been proposed, which can, in principle, provide quantitative data with no need of calibration curves or internal standards [14, 15]. The method relies on the assumption about the existence the stoichiometric ablation and local thermodynamic equilibrium (LTE) i.e. Boltzmann distribution and Saha equation amongst the level population of any species and electron density and temperature of the plasma. However for application of this method experimentally one needs to obtain both equilibrium and thin plasma conditions, a task that may not be always possible to perform. Thus, in spite of the many advantages of LIBS the realization of a quantitative analytical method, which is able to measure main constituents in samples from different matrices, still remains a difficult task because of the complex laser-sample

and laser-plasma interaction mechanisms. As a rule, laser ablation plasma is characterized by complex spatial and temporal structures, and one meets a wide range of varying of parameters during the plasma existence time.

In this paper, we report the optimized conditions for LIBS to analyze the emission spectrum of aluminum alloy samples with high resolution using a portable Echelle spectrometer Mechelle 7500 equipped with ICCD camera. Spectroscopic analysis of plasma evolution of laser produced plasmas has been characterized in terms of their spectra, electron density and electron temperature. The LTE and optically thin plasma conditions were verified for the produced plasma. The electron temperature and density were determined using the emission intensity and stark broadening, respectively, of the spectral lines of six elements Fe, Mg, Be, Si, Mn, and Cu in the aluminum alloys. The dependence of the electron density and temperature on the concentrations of these elements was studied.

2 Experimental setup

2.1 Instrumentation

A typical LIBS experimental setup, described in details by the author elsewhere [6], is used throughout the present investigations. The plasma formation was attained with the aid of a Q-switched Nd: YAG laser (surelite I, continuum, USA) operating at 1064 nm (pulse duration of 7 ns) and repetition rate of 0.1 Hz – 10 Hz. The laser pulse energy of 100 mJ was adjusted by a suitable combination of beam splitters at constant operating high voltage (1.3 kV) and Q-switch delay (1.65 μs) to ensure spatial and temporal beam profile stability. An energy meter (Nova 978, Ophir Optronics Ldt., USA) was employed to monitor the shot to shot pulse energy. The laser beam was focused on aluminum alloy samples by a 10 cm focal length quartz lens to generate the plasma. A one meter length fused-silica optical fiber (600 μm diameter) mounted on a micro *xyz*-translation stage is used to collect the emission light from the plasma plume and feed it to a portable Echelle spectrometer of a 0.17 m focal length (Mechelle 7500, Multichannel Instruments, Sweden). The Echelle grating spectrometers designed for operation in high orders and high angles of incidence and diffraction, can provide high resolution in a more compact size and cover a much wider spectral range than conventional grating spectrometers [16]. The Mechelle 7500 provides a constant spectral resolution (CSR) of 7500 corresponding to 4 pixels FWHM over a wavelength range 200–1000 nm displayable in a single spectrum. A gateable, intensified CCD camera, (DiCAM-Pro-12 bit, UV enhanced, 43000 channels, PCO Computer Optics, Germany) coupled to the spectrometer was used for detection of the dispersed light. The overall linear dispersion of the spectrometer camera system ranges from 0.006 (at 200 nm) to 0.033 nm/pixel (at 1000 nm). To avoid the electronic interference and jitters, the intensifier high voltage was triggered optically. Echelle spectra display, control, processing and analysis were done using both Mechelle software (Multichannel Instruments, Stockholm, Sweden) and GRAMS/32 version 5.1 Spectroscopic Data Analysis Software (Galactic Industries, Salem, NH, USA).

2.2 Optimization of data acquisition procedure

Many optimization procedures were performed to improve our LIBS resolution and sensitivity and to minimize the measurements fluctuations and problems due to the sample heterogeneity.

To improve data reproducibility, and to avoid electronic jittering problem, the laser was set to single shot mode. Then, the Nd:YAG laser beam was focused onto the sample surface at 90° angle. This was done using a 25 mm diameter dichroic mirror that reflects 99% of high energy 1064 nm wavelength. This mirror placed just before the laser-focusing lens as shown in Figure 1. The focal point was set 5 mm below the surface of the sample in order to generate plasma of 800 μm spot diameter. This also minimize breakdown above the surface of any particles and aerosols generally present above the sample. Moreover, for each new sample, before spectral collection, 20 laser pulses were performed to clean the sample surface and removes surface oxides and contamination to ensure that the observed spectrum is representative of the sample composition. Furthermore, we found that enhancement of the data reproducibility can be achieved by accumulation of consecutive measured spectra for exposures of duration 1000 ns, each delayed 2500 ns from the laser pulse. These values of delay time and exposure window time (gate time) for the ICCD camera produced spectra with minimal background and signals from major lines that did not saturate the detector.

On the other hand, the use of a micro *xyz*-translation stage as a holder for fused-silica optical fiber facilities maximum intensity of the observed emission light from the plasma plume. We investigated a set of eight standard samples of aluminum alloy to study the dependence of the electron density and temperature on the concentrations of six elements Be, Mg, Si, Mn, Fe and Cu by the proposed LIBS setup. So that, these samples, which have never been treaded before using LIBS with Mechelle 7500, were selected to have the six elements with a range of concentrations. We used disk shaped standard samples of aluminum alloy provided by Alcan International Limited (0.5 cm; $\phi = 5$ cm). The concentrations of Mg, Si, Be, Cu, Mn and Fe in the aluminum alloy samples are given in Table 1.

Now, we aim to produce LIBS spectra with high precision. Precision is the measure of the degree of reproducibility of a measurement. Laser shot-to-shot variation causes differences in the plasma properties, therefore affects the magnitude of the element signal, and hence degrades the LIBS

Sample	Be	Mg	Si	Fe	Cu	Mn	Al
AL 3104	0.0011	1.15	0.21	0.42	0.17	0.92	Balance
AL 4104	0.0017	1.56	9.63	0.7	0.12	0.046	Balance
AL 5052	0.0043	2.51	0.087	0.33	0.042	0.09	Balance
AL 5182	0.0012	4.67	0.11	0.27	0.061	0.35	Balance
AL 5754	0.0022	2.54	0.22	0.35	0.1	0.29	Balance
AL 6063	0.00030	0.54	0.43	0.2	0.085	0.081	Balance
AL 7010	0.0007	2.44	0.11	0.22	1.88	0.082	Balance
AL a380.2	0.00036	0.028	9.17	0.41	3.61	0.042	Balance

Table 1: Beryllium, copper, iron, magnesium, silicon and manganese concentrations (in w/w %) in the standard aluminum alloy samples.

precision. To improve LIBS precision, spectra from several laser shots have to be averaged in order to reduce statistical error due to laser shot-to-shot fluctuation. We reproduced the measurements at five locations on the sample surface in order to avoid problems linked to sample heterogeneity. Twenty shots were fired at each location and saved in separated files and the average was computed and saved to serve as the library spectrum. For each recorded spectrum, the peak intensity, the Lorentzian curve fitting, the full width at half maximum FWHM, and the center wavelength of each line, as well as the background emission continuum are determined. Data treatment preprocessing of the averaged spectra data was performed in the Windows environment on a Pentium 4 PC using GRAMS/32, Excel (Microsoft Office Excel 2003) and Origin software version 7.0220 (Origin Lab Co., USA). The averages of peak tables (lists of wavelengths and intensities) of the averaged spectra were roll generated in GRAMS/32 and exported for data evaluation.

3 Results and discussion

3.1 LIBS spectrum

Figure 1 shows a typical plasma emission spectrum for aluminum alloy sample AL 7010. This spectrum is the average of 100 single shot spectra recorded at 2.5 μs delay time and 1 μs gate width. The panoramic Echelle spectra in the spectral range 200–700 nm show the UV emission lines of aluminum as a major element and the emission lines of Si, Cu, Be, Fe, Mn and Mg in the aluminum alloy sample. Moreover, our observed spectra reflect the wide spectral range and the high resolution of the used spectroscopic system.

3.2 Electron temperature measurements

In LIBS experiments, assuming optically thin plasma and the local thermodynamic equilibrium (LTE) conditions are hold, the re-absorption effects of plasma emission are negligible (i.e. the main ionization process is produced through impact excitation by thermal electrons). Upon these conditions, a Boltzmann population distribution can be assumed in describing the actual thermodynamics parameters of the plasma. So, the emitted spectral line intensity I is a measure of the population of the corresponding energy level of this element in the plasma. Then I corresponding to the transition between levels E_k and E_i of the atomic species α with concentration C_α, can be expressed as

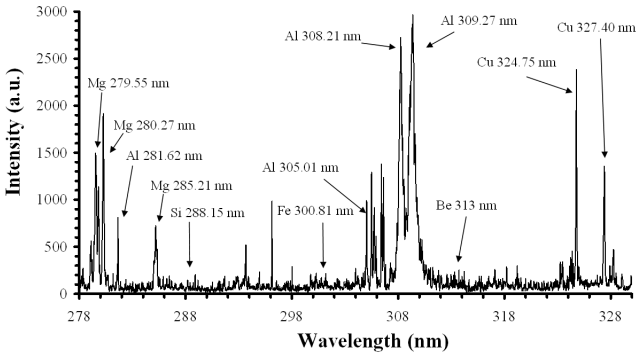

Fig. 1: Typical LIBS spectrum for aluminum alloy sample AL 7010. The laser energy was 100 mJ at wavelength 1064 nm, plasma emissions are accumulated with delay 2.5 μs, and gate width 1 μs.

$$I_\alpha^{ki} = F C_\alpha \frac{g_k A_{ki} e^{\frac{-E_k}{K_B T}}}{U_\alpha(T)}, \qquad (1)$$

where K_B is the Boltzmann constant, $U_\alpha(T)$ is the partition function, A_{ki} is the transition probability, g_k is the statistical weight for the upper level, E_k is the excited level energy, T is the temperature (in LTE all temperatures are assumed to be equal, i.e. $T_e \approx T_{ion} \approx T_{plasma}$) and F is a constant depending on experimental conditions.

Equation (1) allows also for evaluating C_α when the sample and reference plasma temperature are different, once the atomic parameters are derived from atomic databases. In order to evaluate the plasma temperature, they take the natural logarithm of Equation (1), obtaining

$$\ln\left(\frac{I_\alpha^{ki}}{g_k A_{ki}}\right) = \frac{E_k}{K_B T} + \ln\left(\frac{C_\alpha F}{U_\alpha(T_\alpha)}\right). \qquad (2)$$

In the two-dimensional Boltzmann plane identified by the left hand term of Equation (2) and by E_k, different

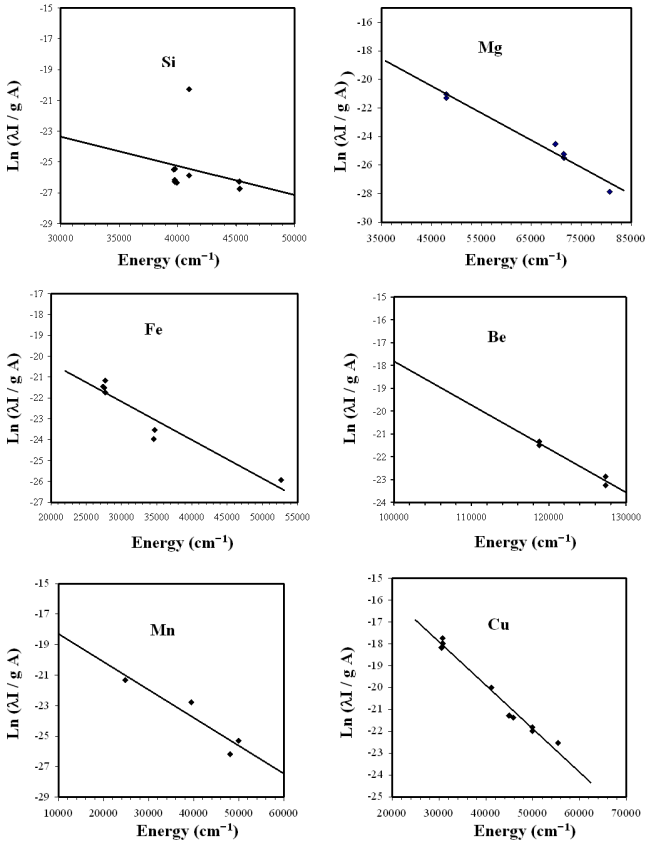

Fig. 2: Six Boltzmann plots were determined form the emission line intensities of Si, Mg, Fe, Be, Mn and Cu observed in the laser-induced plasma of aluminum alloy sample AL 7010. The slope of the plotted curves yields temperatures of 7606 K, 7562 K, 7817 K, 7511 K, 7842 K, and 7224 K for the elements Si, Mg, Fe, Be, Mn, and Cu respectively.

emission lines intensities belonging to the same element in the same spectrum lie along a straight line with a slope of $-1/K_B T$ [21].

In our experiment, the temperatures were determined form the emission line intensities of Mg, Si, Be, Cu, Mn and Fe observed in the laser-induced plasma of aluminum alloys. Figure 2 show six Boltzmann plots of Eqn. (2), for each of these six elements in the aluminum alloy sample AL 7010 where the data were fitted with the least-square approximation. The spectral lines wavelengths, energies of the upper levels, statistical weights, and transition probabilities used for each element are obtained from NIST [17] and Griem [21], and listed in Table 2. The slope of the plotted curves yields temperatures 7606 K, 7562 K, 7817 K, 7511 K, 7842 K, and 7224 K for the elements Si, Mg, Fe, Be, Mn, and Cu respectively. The average value of the plasma temperature is 7600 K which agrees with the value obtained by Sabsabi and Cielo [20] under conditions similar to ours. The difference in the plasma temperature of the six elements may be attributed to the difference in the excitation and ionization

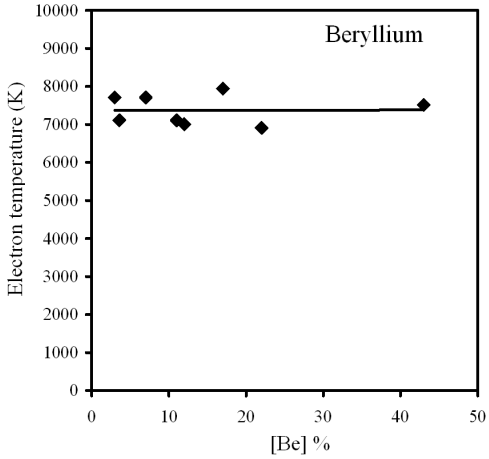

Fig. 3: Electron temperature measured at 2.5 μs delay time and 1 μs gate width using Boltzmann plot for different concentrations of beryllium in different aluminum alloy samples.

potentials between these elements.

Then the matrix effect on the plasma temperature was studied using the variety of concentrations of the six elements in the eight aluminum samples. This was done by plotting the corresponding temperature for each element versus its concentration in the aluminum alloy samples. Under our experimental conditions, no significance change was found for the plasma temperature with the concentration of the six elements, especially for low concentration elements as shown in Figure 3 as an example for Beryllium. This is could be understanding as follows; for optical thin plasma, increasing the element concentration returns an increasing of the intensity of its corresponding spectral lines with roughly the same ratio, which leads to have the same slope of Boltzmann plot and results in the same plasma temperature.

3.3 Electron density measurements

The usual method for determination of electron density is the measuring of the broadening of a suitable emission line of the laser-plasma spectrum. There are several possible mechanisms of line broadening in plasma: self-absorption, pressure broadening, Doppler broadening, Stark broadening, etc. Lida reported that the line broadening and the spectral shift of the emission line are due mainly to self-absorption phenomenon [18]. In the present study line splitting and the spectral shift, which are good evidence of self-absorption, were monitored carefully. No evidence of line splitting or spectral shift was observed.

Nemet and Kozma reported the broadening of transition lines as pressure, Stark, and Doppler broadening [19]. But pressure and Doppler broadening should not be so much different among transition lines as is the case for plasma of solids. Kyuseok Song *et al.* stated that Stark broadening may be one of the reasons since the broadening effect increases as the energy level increases [22]. Stark broadening results

Element	Wavelength (nm)	A_{ki} (s^{-1})	E_k (cm^{-1})	g_k	Stark broadening parameter w (nm)	Element	Wavelength (nm)	A_{ki} (s^{-1})	E_k (cm^{-1})	g_k	Stark broadening parameter w (nm)
Si	221.89	1.50E+06	45276.18	3	—	Fe	376.01	4.47E+06	45978.00	15	—
Si	243.87	7.40E+05	40991.88	3	—	Fe	376.38	5.44E+07	34547.21	5	—
Si	250.69	4.66E+07	39955.05	5	—	Fe	376.55	9.80E+07	52655.00	15	—
Si	251.43	6.10E+07	39760.28	3	—	Fe	376.72	6.40E+07	34692.14	3	—
Si	251.61	1.21E+08	39955.05	5	—	Fe	378.60	4.20E+06	46026.94	13	—
Si	252.41	1.81E+08	39683.16	1	—	Fe	538.33	5.6E+07	53352.98	13	5.3E-03 [29]
Si	252.85	7.70E+07	39760.28	3	—	Cu	240.00	2.00E+06	67911.85	4	4.1E-3 [21, 28]
Si	288.15	1.89E+08	40991.88	3	0.74E-3 [21]	Cu	261.84	3.07E+07	49382.95	4	—
Si	300.67	1.10E+03	33326.05	5	—	Cu	276.64	9.60E+06	49382.95	4	—
Si	302.00	3.30E+03	33326.05	5	—	Cu	282.44	7.80E+06	46598.34	6	—
Si	390.55	1.18E+07	40991.88	3	1.46E-3 [21]	Cu	296.12	3.76E+06	44963.22	8	—
Mg	277.66	1.32E+08	57873.94	5	—	Cu	306.34	1.55E+06	45879.31	4	—
Mg	277.82	1.82E+08	57833.4	3	—	Cu	319.41	1.55E+06	44544.15	4	—
Mg	277.98	4.09E+08	57873.94	5	—	Cu	324.75	1.39E+08	30783.69	4	—
Mg	278.14	5.43E+08	57812.77	1	—	Cu	327.40	1.37E+08	30535.30	2	—
Mg	278.29	2.14E+08	57833.4	3	—	Cu	333.78	3.80E+05	41153.43	8	—
Mg	279.07	4.01E+08	71491.06	4	—	Cu	402.26	1.90E+07	55387.67	4	—
Mg	279.55	2.60E+08	35760.88	4	—	Cu	406.26	2.10E+07	55391.29	6	—
Mg	279.79	4.79E+08	71490.19	6	—	Cu	427.51	3.45E+07	62403.32	8	—
Mg	280.27	2.57E+08	35669.31	2	—	Cu	465.11	3.80E+07	62403.32	8	—
Mg	281.11	1.96E+08	83520.47	5	—	Cu	510.55	2.00E+06	30783.69	4	—
Mg	281.17	2.11E+08	83511.25	3	—	Cu	515.32	6.00E+07	49935.20	4	—
Mg	285.21	4.91E+08	35051.26	3	3.6E-04 [27]	Cu	521.82	7.50E+07	49942.06	6	—
Mg	291.54	4.09E+08	80693.01	5	—	Cu	529.25	1.09E+07	62403.32	8	—
Mg	292.86	1.15E+08	69804.95	2	—	Cu	570.02	2.40E+05	30783.69	4	—
Mg	293.65	2.30E+08	69804.95	2	—	Cu	578.21	1.65E+06	30535.30	2	—
Fe	370.11	4.80E+07	51192.27	9	—	Mn	258.97	2.6E+08	38543.08	7	5.91E-03 [30]
Fe	370.56	3.22E+06	27394.69	7	—	Mn	401.81	2.54E+07	41932.64	8	—
Fe	371.99	1.62E+07	26874.55	11	—	Mn	403.08	1.70E+07	24802.25	8	—
Fe	372.26	4.97E+06	27559.58	5	—	Mn	403.31	1.65E+07	24788.05	6	—
Fe	372.71	2.00E+07	50534.39	7	—	Mn	403.45	1.58E+07	24779.32	4	—
Fe	373.33	6.20E+06	27666.35	3	—	Mn	404.14	7.87E+07	41789.48	10	—
Fe	373.53	2.40E+07	50475.29	9	—	Mn	404.88	7.50E+07	42143.57	4	—
Fe	373.71	1.42E+07	27166.82	9	—	Mn	405.55	4.31E+07	41932.64	8	—
Fe	373.83	3.80E+07	53093.52	13	—	Mn	405.89	7.25E+07	42198.56	2	—
Fe	374.56	1.15E+07	27394.69	7	—	Mn	406.17	1.90E+07	49415.35	6	—
Fe	374.59	7.33E+06	27666.35	3	—	Mn	406.35	1.69E+07	42053.73	6	—
Fe	374.83	9.15E+06	27559.58	5	—	Mn	407.92	3.80E+07	42143.57	4	—
Fe	375.82	6.34E+07	34328.75	7	—	Mn	408.29	2.95E+07	42053.73	6	—
Mn	408.36	2.80E+07	41932.64	8	—	Be	265.08	1.80E+08	59695.07	3	—
Mn	423.51	9.17E+07	46901.13	6	—	Be	313.04	1.15E+08	31935.32	4	2.81E-05 [21]
Mn	441.49	2.93E+07	45940.93	6	—	Be	313.11	1.15E+08	31928.744	2	—
Mn	445.16	7.98E+07	45754.27	8	—	Be	324.16	1.37E+07	127335.12	2	—
Mn	446.20	7.00E+07	47207.28	10	—	Be	324.18	2.73E+07	127335.12	2	—
Mn	475.40	3.03E+07	39431.31	8	—	Be	327.46	1.43E+07	118761.32	4	—
Mn	478.34	4.01E+07	39431.31	8	—	Be	327.47	1.43E+07	118760.51	2	—
Mn	482.35	4.99E+07	39431.31	8	—	Be	332.10	6.90E+06	52080.94	3	—
Be	265.05	1.08E+08	59697.08	5	—	Be	332.11	2.10E+07	52080.94	3	—
Be	265.06	1.44E+08	59695.07	3	—	Be	332.13	3.40E+07	52080.94	3	—

Table 2: A list of the spectroscopic data of the spectral lines used for the determination of plasma temperature and density of aluminum alloy samples.

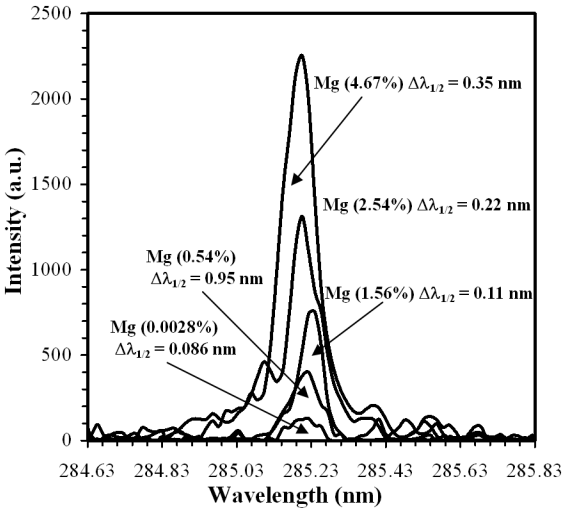

Fig. 4: The 285.21 nm line with sufficient resolution to measure the full width at half-maximum ($\lambda_{1/2}$) at different concentrations of Mg in the aluminum alloys. For each line, the data points were fitted with Lorentzian fitting function using the Origin software to determine ($\lambda_{1/2}$).

from Coulomb interactions between the radiator and the charged particles present in the plasma. Both ions and electrons induce Stark broadening, but electrons are responsible for the major part because of their higher relative velocities. Therefore, in our conditions, the profile of a line is mainly contributed to linewidths arises from the Stark effect while the contribution of other mechanisms of broadening (Doppler effect, Van der Waals broadening, and resonance broadening) can be neglected, as shown under conditions similar to ours by Sabsabi and Cielo [20].

The electrons in the plasma can perturb the energy levels of the individual ions which broaden the emission lines originating from these excited levels. Stark broadening of well-isolated lines in the plasma is, thus, useful for estimating the electron number densities provided that the Stark-broadening coefficients have been measured or calculated. The line profile for stark broadened is well described by a Lorentzian function

Since the instrumental line-broadening exhibit Gaussian shape, then the stark line width $\Delta\lambda_{FWHM}$ can be extracted from the measured line width $\Delta\lambda_{observed}$ by subtracting the instrumental line broadening $\Delta\lambda_{instrument}$:

$$\Delta\lambda_{FWHM} = \Delta\lambda_{observed} - \Delta\lambda_{instrument}\,. \qquad (3)$$

In our case $\Delta\lambda_{instrument}$ was 0.05 nm (determined by measuring the FWHM of the Hg lines emitted by a standard low pressure Hg lamp).

The width of stark broadening spectral line depends on the electron density N_e. Both the linear and the quadratic stark effect are encountered in spectroscopy. Only the hydrogen atom and H-like ion exhibit the linear stark effect. For the linear stark effect the electron density should be deduced from H line width from the formula [21]

$$N_e = C(N_e, T)\,\Delta\lambda_{FWHM}^{3/2} \qquad (4)$$

the values of the parameter $C(N_e, T)$ are tabulated in the literature [21], which determine the relative contribution of the electron collision on the electrostatic fields, and depend weakly on N_e and T.

For a non-H-like line, the electron density (in cm^{-3}) could be determined from the FWHM of the line from the formula [21]:

$$N_e \approx \left(\frac{\Delta\lambda_{FWHM}}{2w}\right) \times 10^{16}, \qquad (5)$$

where w is the electron impact parameter (stark broadening value) and it is given in Table 2. The last formula is generally used for calculations of plasma generated from solid targets [7, 8, 20].

Six lines were identified as candidates for electron-density measurements: 390.55 nm, 285.21 nm, 538.33 nm, 240.00 nm, 258.97 nm and 313.04 nm for Si, Mg, Fe, Cu, Mn and Be respectively. Figure 4 shows, as an example for Mg, the 285.21 nm line with sufficient resolution to measure the full width at half-maximum ($\lambda_{1/2}$) at different concentrations of Mg in the aluminum alloys. All the six lines data points were fitted with Lorentzian fitting function using the Origin software to determine ($\lambda_{1/2}$) as shown in Fig. 4 for Mg as an example. Substituting the values of $\lambda_{1/2}$ in Eqn. (3) and the corresponding values of stark broadening w from Table 2 in Eqn. (6) the electron density for Mg was determined. These steps were repeated for each concentration of the six elements in the eight aluminum alloy samples. Then the obtained electron density values were plotted versus the element concentration. Figure 5 shows six plots for the variation of the electron density values versus the concentrations of Mg, Si, Be, Fe, Cu and Mn in different aluminum alloy samples. These plots reveal that, in case of Mg, Si, Fe, Cu and Mn, electron density increases with the element concentration. For the case of low concentration elements like Be, the increase of the electron density with the element concentration is very weak. This result might occur because increasing the "element" concentration comprises increasing portion of the laser-target interaction volume which agrees with O. Samek [24] and Rusak *et al.* [25].

Finally, by knowing the electron density and the plasma temperature we can determine whether the local thermodynamic equilibrium (LTE) assumption is valid applying the criterion given by McWhirter [26].

The lower limit for electron density for which the plasma will be in LTE is:

$$N_e \geqslant 1.4\times10^{14}\,\Delta E^3 T^{1/2}, \qquad (6)$$

where ΔE is the largest energy transition for which the condition holds and T is the plasma temperature [23].

In the present case $\Delta E = 3.65$ eV for Al (see Ref. [20])

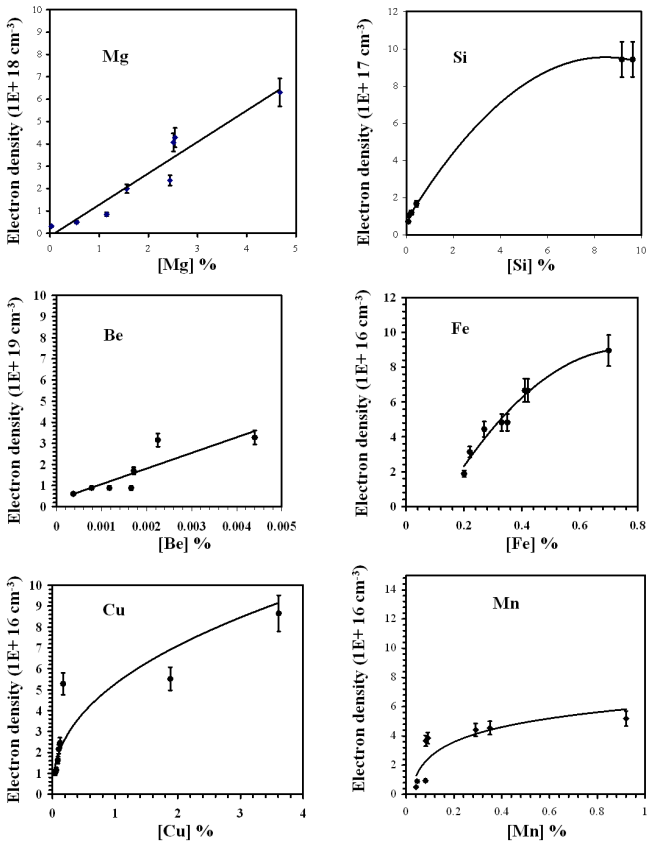

Fig. 5: Six plots for the variation of the electron density values versus the concentrations of Mg, Si, Be, Fe, Cu and Mn in different aluminum alloy samples.

and the electron density lower limit value given by Eqn. (7) is 6×10^{15} cm^{-3}. The experimentally calculated densities are greater than this value, which is consistent with the assumption that the LTE prevailing in the plasma.

4 Conclusion

In summary, we have carried out an accurate LIBS setup using portable commercial Echelle spectrometer equipped with ICCD detector to study aluminum alloys matrix effects on the plasma characterization. The electron density and plasma temperature were determined for six elements (Fe, Mg, Be, Si, Mn, and Cu) in the aluminum alloy targets. The electron density increases with the element concentration while the plasma temperature does not has significance change with the element concentration.

For a plasma diagnostics perspective, the target physical properties play an important role in the obtained values of the laser induced plasma temperature T_e and electron density N_e. For industrial application, LIBS could be applied in the on-line industrial process that following up elemental concentration in metals and pharmaceuticals by only measuring N_e of that element.

Acknowledgment

The author gratefully acknowledges the support of Prof. M. Sabsabi and Prof. M. Abdel-Harith specially for offering the standard aluminum alloy samples.

Submitted on January 20, 2007
Accepted on February 02, 2007

References

1. Radziemski L. J. Review of selected analytical applications of laser plasmas and laser ablation, 1987–1994. *Microchem. J.*, 1994, v. 50, 218–234,.
2. Rusak D. A., Castle B. C., Smith B. W. and Winefordner J. D. Fundamentals and applications of laser-induced breakdown spectroscopy. *Crit. Rev. Anal. Chem.*, 1997, v. 27, 257–290.
3. Sneddon J. and Lee Y. Novel and recent applications of elemental determination by laser-induced breakdown spectrometry. *Anal. Lett.*, 1999, v. 32, 2143–2162.
4. Tognoni E., Palleschi V., Corsi M. and Cristoforetti G. Quantitative micro-analysis by laser-induced breakdown spectroscopy: a review of the experimental approaches. *Spectrochim. Acta Part B*, 2002, v. 57, 1115–1130.
5. Majidi V. and Joseph M. R. Spectroscopic applications of laser-induced plasmas. *Crit. Rev. Anal. Chem.*, 1992, v. 23, 143–162.
6. Bulatov V., Krasniker R. and Schechter I. Study of matrix effects in laser plasma spectroscopy by combined multifiber spatial and temporal resolutions. *Anal. Chem.*, 1998, v. 70, 5302–5310.
7. Sabsabi M., Detalle V., Harith M. A., Walid Tawfik and Imam H. Comparative study of two new commercial Echelle spectrometers equipped with intensified CCD for analysis of laser-induced breakdown spectroscopy. *Applied Optics*, 2003, v. 42, No. 30, 6094–6098.
8. Ismail M. A., Imam H., Elhassan A., Walid Tawfik and Harith M. A. LIBS limit of detection and plasma parameters of some elements in two different metallic matrices. *J. Anal. At. Spectrom.*, 2004, v. 19, 1–7.
9. Xu L., Bulatov V., Gridin V. and Schechter I. Absolute analysis of particulate materials by laser-induced breakdown spectroscopy. *Anal. Chem.*, 1997, v. 69, 2103–2108.
10. Goode S. R., Morgan S. L., Hoskins R. and Oxsher A. Identifying alloys by laser-induced breakdown spectroscopy with a time-resolved high resolution echelle spectrometer. *J. Anal. At. Spectrom.*, 2000, v. 15, 1133–1138.
11. Eppler A. S., Cremers D. A., Hickmott D. D., Ferris M. J. and Koskelo A. C. Matrix effects in the detection of Pb and Ba in soils using laser-induced breakdown spectroscopy. *Appl. Spectrosc.*, 1996, v. 50, 1175–1181.
12. Quentmeier A., Sdorra W. and Niemax K. Internal standardization in laser induced fluorescencs spectrometry of microplasms produced by laser ablation of solid samples. *Spectrochimica Acta B*, 1990, v. 45, No. 6, 5371–5379.

13. Bassiotis I., Diamantopoulou A., Giannoundakos A., Roubani-Kalantzopoulou F. and Kompitsas M. Effects of experimental parameters in quantitative analysis of steel alloy by laser-induced breakdown spectroscopy. *Spectrochim. Acta Part B*, 2001, v. 56, 671–683.
14. Ciucci A., Corsi M., Palleschi V., Rastelli V., Salvetti A. and Tognoni E. A new procedure for quantitative elemental analyses by laser induced plasma spectroscopy. *Applied Spectroscopy*, 1999, v. 53, 960–964.
15. Bulajic D., Corsi M., Cristoforetti G., Legnaioli S., Palleschi V., Solvetti A. and Rognoni E. A procedure for correcting self-absorption in calibration-free laser induced breakdown spectroscopy. *Spectrochim. Acta B*, 2002, v. 57, 339–353.
16. Corsi M., Palleschi V., Salvetti A. and Tognoni T. Making LIBS quantitative: a critical review of the current approaches to the problem. *Res. Adv. Appl. Spectrosc.*, 2000, v. 1, 41–47.
17. Olesik J. W. Echelle grating spectrometers for inductively coupled plasma-optical emission spectrometry. *Spectroscopy*, 1999, v. 14, No. 10, 27–30.
18. NIST National Institute of Standards and Technology, USA, electronic database, http://physics.nist.gov/PhysRefData/ASD/lines_form.html
19. Lida Y. Effects of atmosphere on laser vaporization and excitation processes of solid samples. *Spectrochim. Acta B*, 1990, v. 45, 1353–1367.
20. Nemet B. and Kozma L. Time-resolved optical emission spectrometry of Q-switched Nd:YAG laser-induced plasmas from copper targets in air at atmospheric pressure. *Spectrochim. Acta B*, 1995, v. 50, 1869–1888.
21. Sabsabi M. and Cielo P. Quantitative analysis of aluminum alloys by laser-induced breakdown spectroscopy and plasma characterization. *Applied Spectroscopy*, 1995, v. 49, No. 4, 499–507.
22. Griem H. R. Plasma spectroscopy. McGraw-Hill, New York, 1964.
23. Kyuseok Song, Hyungki Cha, Jongmin Lee and Yong Lee. Investigation of the line-broadening mechanism for laser-induced copper plasma by time-resolved laser-induced breakdown spectroscopy. *Microchem. Journal*, 1999, v. 63, 53–60.
24. Bekefi G. Principles of laser plasmas. Wiley, New York, 1976, 550–605.
25. Samek O., Beddows D.C.S., Telle H.H., Kaiser J., Liska M., Caceres J.O. and Gonzales Urena A. Quantitative laser-induced breakdown spectroscopy analysis of calcified tissue samples. *Spectrochimica Acta Part B*, 2001, v. 56, 865–875.
26. Rusak D. A., Clara M., Austin E. E., Visser K., Niessner R., Smith B. W. and Winefordner J. D. Investigation of the effect of target water content on a laser-induced plasma. *Applied Spectroscopy*, 1997, v. 51, No. 11, 1628–1631.
27. McWhirter R.W.P. In: *Plasma Diagnostic Techniques*, ed. R. H. Huddlestone and S. L. Leonard, Academic Press, New York, 1965, Ch. 5, 206.
28. Le Drogoff B., Margotb J., Chakera M., Sabsabi M., Barthelemy O., Johnstona T.W., Lavillea S., Vidala F. and von Kaenela Y. Temporal characterization of femtosecond laser pulses induced plasma for spectrochemical analysis of aluminum alloys. *Spectrochimica Acta Part B*, 2001, v. 56, 987–1002.
29. Konjevic N. and Wiese W. L. Stark widths and shifts for spectral lines of neutral and ionized atoms. *J. Phys. Chem. Ref. Data*, 1990, v. 19, 1337.
30. Freudestien S. and Cooper J. Stark broadening of Fe I 5383 Å. *Astron. & Astrophys.*, 1979, v. 71, 283–288.
31. Popovic L. C. and Dimitrijevic M. S. Tables of the electron impact broadening parameters: Mn II, Mn III, Ga III, Ge III and Ge Iv Lines. *Bull. Astron. Belgrade*, 1997, No. 156, 173–178.

A Letter by the Editor-in-Chief:

Twenty-Year Anniversary of the Orthopositronium Lifetime Anomalies: The Puzzle Remains Unresolved

This letter gives a history of two observed anomalies of orthopositronium annihilation, of which the 20th anniversary occurs this year. The anomalies, breaking the basics of Quantum Electrodynamics, require more experimental study, in view of the recent claim of the Michigan group of experimentalists, which alleges resolution of one of the anomalies.

It is now the 20th anniversary of the observation of anomalies of orthopositronium annihilation (both discovered in 1987) in experiments conducted by two groups of researchers: one group in the USA, headed by the late Prof. Arthur Rich in the University of Michigan at Ann Arbor, and the other group in Russia, headed by Dr. Boris Levin of the Institute of Chemical Physics in Moscow, but then at the Gatchina Nuclear Centre in St. Petersburg.

The anomalies dramatically break the basics of Quantum Electrodynamics.

Recently my long-time colleague, Boris Levin, one of the discoverers of the anomalies, suggested that the last experiment of the Michigan group, by which it has claimed resolution of one of the anomalies [1], was set up so that an electric field introduced into the experiment (it accelerates the particle beam before the target) mere suppressed the anomaly despite the electric field helps to reach complete thermalization of orthopositronium in the measurement cell. As a dry rest the anomaly, remaining represented but suppressed by the field, became mere invisible in the given experiment.

Now Levin proposes a modification of the last Michigan experiment in order to demonstrate the fact that the anomaly remains. He describes his proposed experiment in his brief paper appearing in this issue of Progress in Physics.

I would give herein a brief introduction to the anomalies (otherwise dispersed throughout many particular papers in science journals).

Positronium is an atom-like orbital system that contains an electron and its anti-particle, the positron, coupled by electrostatic forces. There are two kinds of positronium: parapositronium p-Ps, in which the spins of the electron and the positron are oppositely directed so that the total spin is zero, and orthopositronium o-Ps, in which the spins are co-directed so that the total spin is one. Because a particle-anti-particle system is unstable, life span of positronium is rather small. In vacuum parapositronium decays in $\sim 1.25\times10^{-10}$ s, while orthopositronium in $\sim 1.4\times10^{-7}$ s. In a medium the life span is even shorter because positronium tends to annihilate with electrons of the medium. Due to the law of conservation of charge parity, parapositronium decays into an even number of γ-quanta (2, 4, 6, ...) while orthopositronium annihilates into an odd number of γ-quanta (3, 5, 7, ...). The older modes of annihilation are less probable and their contributions are very small. For instance, the rate of five-photon annihilation of o-Ps compared to that of three-photon annihilation is as small as $\lambda_5 \approx 10^{-6}\lambda_3$. Hence parapositronium actually decays into two γ-quanta p-Ps $\rightarrow 2\gamma$, while orthopositronium decays into three γ-quanta o-Ps $\rightarrow 3\gamma$.

In the laboratory environment positronium can be obtained by placing a source of free positrons into matter, a monatomic gas for instance. The source of positrons is β^+-decay, self-triggered decays of protons in neutron-deficient atoms $\mathrm{p} \rightarrow \mathrm{n} + \mathrm{e}^+ + \nu_\mathrm{e}$. It is also known as positron β-decay.

Some of free positrons released into a gas from a β^+-decay source quite soon annihilate with free electrons and electrons in the container's walls. Other positrons capture electrons from gas atoms thus producing orthopositronium and parapositronium (in ratio 3:1).

The time spectrum of positron annihilations (number of events vs. life span) is the basic characteristic of their annihilation in matter. In particular, in such spectra one can see parts corresponding to annihilation with free electrons and annihilation of p-Ps and o-Ps.

In inert gases the time spectrum of annihilation of quasi-free positrons generally forms an exponential curve with a plateau in its central part, known as a "shoulder" [2, 3].

In 1965 P. E. Osmon published [2] pictures of observed time spectra of annihilation of positrons in inert gases (He, Ne, Ar, Kr, Xe). In his experiments he used ^{22}NaCl as a source of β^+-decay positrons. Analyzing the results of the experiments, Levin noted that the spectrum in neon was peculiar compared to those in other monatomic gases: in neon, points in the curve were so widely scattered that the presence of a "shoulder" was uncertain. Repeated measurements of time spectra of annihilation of positrons in He, Ne, and Ar, later accomplished by Levin [4, 5], have proven the existence of anomaly in neon. A specific feature of the experiments conducted by Osmon, Levin and some other researchers is that the source of positrons was ^{22}Na, while the moment of appearance of the positron was registered according to the γ_n-quantum of decay of excited ^{22*}Ne, $^{22*}\mathrm{Ne} \rightarrow {}^{22}\mathrm{Ne} + \gamma_\mathrm{n}$, from one of the products of β^+-decay of ^{22}Na. This method is quite justified and is commonly used, because the life span of excited ^{22*}Ne is as small as $\tau \simeq 4\times10^{-12}$ s, which is a few orders of magnitude less than those of the positron and parapositronium.

In his further experiments [6, 7] Levin discovered that the peculiarity of the annihilation spectrum in neon (abnormally widely scattered points) is linked to the presence in natural neon of a substantial quantity of its isotope ^{22}Ne (around 9%). Levin called this effect the *isotope anomaly*. Time spectra were measured in neon environments of two isotopic compositions: (1) natural neon (90.88% of ^{20}Ne, 0.26% of ^{21}Ne, and 8.86% of ^{22}Ne); (2) neon with reduced content of ^{22}Ne (94.83% of ^{20}Ne, 0.26% of ^{21}Ne, and 4.91% of ^{22}Ne). Comparison of the time spectra of positron decay revealed that in natural neon (composition 1) the shoulder is fuzzy, while in neon poor in ^{22}Ne (composition 2) the shoulder is always pronounced. In the part of the spectrum to which o-Ps decay mostly contributes, the ratio between intensity of decay in ^{22}Ne-poor neon and that in natural neon (with more ^{22}Ne) is 1.85 ± 0.1 [7].

The relationship between the anomaly of positron annihilation in neon and the presence of ^{22}Ne admixture, as shown in [6, 7], hints at the existence in gaseous neon of *collective nuclear excitation* of ^{22}Ne isotopes. In the terminal stage of β^+-decay nuclear excitation of ^{22*}Ne (life time $\sim 4\times10^{-12}$ s) is somehow passed to a set of ^{22}Ne nuclei around the source of positrons and is carried away by a nuclear γ_n-quantum after a long delay in the moment of self-annihilation of orthopositronium (free positrons and parapositronium live much shorter). Hence collective excitation of ^{22}Ne atoms seems to be the reason for the isotope anomaly. On the other hand, the nature of the material carrier that passes excitation of nuclear ^{22*}Ne to the surrounding ^{22}Ne atoms is still unclear, as is the means by which orthopositronium is linked to collective excitation — collective nuclear excitation is only known in crystals (Mössbauer effect, 1958).

In 1990 Levin [8] suggested, as a result of a relationship between orthopositronium and collective nuclear excitation, that a 1-photon mode of its annihilation should be observed. But decay of o-Ps into one γ-quantum would break the laws of conservation of Quantum Electrodynamics. To justify this phenomenological conclusion without breaking QED laws, Levin, in his generalised study [9], suggested that in the specific experimental environment, annihilation of some orthopositronium atoms releases one γ-quantum into our world and two γ-quanta into a mirror Universe, placing them beyond observation. But before any experiments are designed to prove or disprove the existence of such a "1-photon" mode, or any theory is developed to explain the observed effect, the problem still requires discussion.

Another anomaly is the substantially higher measured rate of annihilation of orthopositronium (the reciprocal to its life span) compared to that predicted by QED.

Measurement of the orthopositronium annihilation rate is among the main tests aimed at experimental verification of QED. Before the mid 1980's no difference between theory and experiment was observed, as measurement precision remained at the same low level.

In 1987, thanks to new precision technology, a group of researchers based at the University of Michigan (Ann Arbor) made a breakthrough in this area. The experimental results showed a substantial gap between experiment and theory. The anomaly that the Michigan group revealed was that measured rates of annihilation at $\lambda_{T(exp)} = 7.0514\pm0.0014\ \mu s^{-1}$ and $\lambda_{T(exp)} = 7.0482\pm0.0016\ \mu s^{-1}$ (to a precision of 0.02% and 0.023% using gas and vacuum methods [10–13] were much higher compared to $\lambda_{T(theor)} = 7.00383\pm0.00005\ \mu s^{-1}$ as predicted by QED [14–17]. The 0.2% effect was ten times greater than the measurement precision, and was later called the λ_T-anomaly [9].

In 1986 Robert Holdom [18] suggested that "mixed type" particles may exist, which, being in a state of oscillation, stay for some time in our world and for some time in a mirror Universe. In the same year S. Glashow [18] gave further development to the idea and showed that in the case of 3-photon annihilation o-Ps will "mix up" with its mirror twin, thus producing two effects: (1) a higher annihilation rate due to an additional mode of decay, o-Ps$\rightarrow$nothing, because products of decay passed into the mirror Universe cannot be detected; (2) the ratio between orthopositronium and parapositronium numbers will decrease from o-Ps : p-Ps = 3:1 to 1.5:1. But because at that time (1986) no such effects were reported, Glashow concluded that no oscillation is possible between our-world and mirror-world orthopositronium.

On the other hand, by the early 1990's these theoretical studies motivated many researchers worldwide to an experimental search for various "exotic" (unexplained by QED) modes of o-Ps decay, which could shed some light on the abnormally high rate of decay. These were, to name just a few, search for o-Ps$\rightarrow$nothing mode [20], check of possible contribution from 2-photon mode [21–23] or from other exotic modes [24–26]. As a result it has been shown that no exotic modes can contribute to the anomaly, while contribution of the o-Ps$\rightarrow$nothing mode is limited to $< 5.8\times10^{-4}$ of o-Ps$\rightarrow 3\gamma$.

In a generalised study in 1995 [9] it was pointed out that the programme of critical experiments was limited to a search for the 1-photon mode o-Ps$\rightarrow\gamma\backslash 2\gamma'$ involving the mirror Universe and to a search for the mode o-Ps$\rightarrow$nothing. The situation has not changed significantly over the past five years. The most recent publication on this subject, in May 2000 [27], still focused on the Holdom-Glashow suggestion of a possible explanation of the λ_T-anomaly by interaction of orthopositronium with its mirror-world twin, and on a search for the o-Ps$\rightarrow$nothing mode. But no theory has yet been proposed to account for the possibility of such an interaction and to describe its mechanism.

The absence of a clear explanation of the λ_T-anomaly encouraged G. S. Adkins *et al.* [28] to suggest the experiments made in Japan [29] in 1995 as an alternative to the basic Michigan experiments. No doubt, the high statistical accuracy of the Japanese measurements [29] puts them on the same

level as the basic experiments [10–13]. But all the Michigan measurements possessed the property of a "full experiment", which in this particular case means no external influence could affect the wave function of positronium. Such an influence is inevitable due to the electrodynamic nature of positronium, and can be avoided only using special techniques. As was shown later, by Levin [31], this factor was not taken into account in Japanese measurements [29] and thus they do not possess property of a "full experiment".

As early as 1993 S. G. Karshenboim, one of the leaders in the theory, showed that QED had actually exhausted its theoretical capabilities to explain the orthopositronium anomalies [30]. The puzzle remains unresolved.

January 30, 2007 Dmitri Rabounski
Editor-in-Chief

References

1. Vallery R. S., Zitzewitz P. W. and Gidley D. W. Resolution of the orthopositronium-lifetime puzzle. *Phys. Rev. Lett.*, 2003, v. 90, 203402 (1–4).
2. Osmon P. E. Positron lifetime spectra in noble gases. *Phys. Rev. B*, 1965, v. 138, 216.
3. Tao S. J., Bell J. and Green J. H. Fine structure in delayed coincidence lifetime curves for positron in argon. *Proc. Phys. Soc.*, 1964, v. 83, 453.
4. Levin B. M. and Shantarovich V. P. Annihilation of positrons in gaseous neon. *High Energy Chem.*, 1977, v. 11(4), 322–323.
5. Levin B. M. Time spectra of positron annihilation in neon. *Soviet J. Nucl. Physics*, 1981, v. 34(6), 917–918.
6. Levin B. M. and Shantarovich V. P. Anomalies in the time spectra of positron in gaseous neon. *Soviet J. Nucl. Physics*, 1984, v. 39(6), 855–856.
7. Levin B. M., Kochenda L. M., Markov A. A. and Shantarovich V. P. Time spectra of annihilation of positrons (^{22}Na) in gaseous neon of various isotopic compositions. *Soviet J. Nucl. Physics*, 1987, v. 45(6), 1119–1120.
8. Levin B. M. Orthopositronium: a program for critical experiments. *Soviet J. Nucl. Physics*, 1990, v. 52(2), 342–343.
9. Levin B. M. On the kinematics of one-photon annihilation of orthopositronium. *Phys. At. Nuclei*, 1995, v. 58(2), 332–334.
10. Gidley D. W., Rich A., Sweetman E. and West D. New precision measurements of the decay rates of singlet and triplet positronium. *Phys. Rev. Lett.*, 1982, v. 49, 525–528.
11. Westbrook C.I., Gidley D.W., Conti R.S. and Rich A. New precision measurement of the orthopositronium decay rate: a discrepancy with theory. *Phys. Rev. Lett.*, 1987, v. 58, 1328–1331.
12. Westbrook C. I., Gidley D. W., Conti R. S. and Rich A. Precision measurement of the orthopositronium vacuum decay rate using the gas technique. *Phys. Rev. A*, 1989, v. 40, 5489–5499.
13. Nico J. S., Gidley D. W., Rich A. and Zitzewitz P. W. Precision measurement of the orthopositronium decay rate using the vacuum technique. *Phys. Rev. Lett.*, 1990, v. 65, 1344–1347.
14. Caswell W. E. and Lepage G. P. O(α^2-in-α)-corrections in positronium-hyperfine splitting and decay rate. *Phys. Rev. A*, 1979, v. 20, 36.
15. Adkins G. S. Radiative-corrections to positronium decay. *Ann. Phys. (N.Y.)*, 1983, v. 146, 78.
16. Adkins G. S., Salahuddin A. A. and Schalm K. E. Analytic evaluation of the self-energy and outer-vertex corrections to the decay rate of orthopositronium in the Fried-Yennie gauge. *Phys. Rev. A*, 1992, v. 45, 3333–3335.
17. Adkins G. S., Salahuddin A. A. and Schalm K. E. Order-α corrections to the decay rate of ortopositronium in the Fried-Yennie gauge. *Phys. Rev. A*, 1992, v. 45, 7774–7780.
18. Holdom B. Two U(1)'s and ϵ charge shifts. *Phys. Lett. B*, 1986, v. 166, 196–198.
19. Glashow S. L. Positronium versus the mirror Universe. *Phys. Lett. B*, 1986, v. 167, 35–36.
20. Atoyan G. S., Gninenko S. N., Razin V. I. and Ryabov Yu. V. A search for photonless annihilation of orthopositronium. *Phys. Lett. B*, 1989, v. 220, 317–320.
21. Asai S., Orito S., Sanuki T., Yasuda M. and Yokoi T. Direct search for orthopositronium decay into two photons. *Phys. Rev. Lett.*, 1991, v. 66, 1298–1301.
22. Gidley D. W., Nico J. S. and Skalsey M. Direct search for two-photon modes of orthopositronium. *Phys. Rev. Lett.*, 1991, v. 66, 1302–1305.
23. Al-Ramadhan A. H. and Gidley D. W. New precision measurement of the decay rate of singlet positronium. *Phys. Rev. Lett.*, 1994, v. 72, 1632–1635.
24. Orito S., Yoshimura K., Haga T., Minowa M. and Tsuchiaki M. New limits on exotic two-body decay of orthopositronium. *Phys. Rev. Lett.*, 1989, v. 63, 597–600.
25. Mitsui T., Fujimoto R., Ishisaki Y., Ueda Y., Yamazaki Y., Asai S. and Orito S. Search for invisible decay of orthopositronium. *Phys. Rev. Lett.*, 1993, v. 70, 2265–2268.
26. Skalsey M. and Conti R. S. Search for very weakly interacting, short-lived, C-odd bosons and the orthopositronium decay-rate problem. *Phys. Rev. A*, 1997, v. 55(2), 984.
27. Foot R. and Gninenko S. N. Can the mirror world explain the orthopositronium lifetime puzzle? *Phys. Lett. B*, 2000, v. 480, 171–175.
28. Adkins G. S., Melnikov K. and Yelkhovsky A. Virtual annihilation contribution to orthopositronium rate decay. *Phys. Rev. A*, 1999, v. 60(4), 3306–3307.
29. Asai S., Orito S. and Shinohara N. New measurement of the orthopositronium decay rate. *Phys. Lett. B*, 1995, v. 357, 475–480; Jinnouchi O., Asai S., and Koboyashi T. arXiv: hep-ex/0011011.
30. Karshenboim S. G. Corrections to hyperfine splitting in positronium. *Phys. At. Nuclei*, 1993, v. 56(12), 155–171.
31. Levin B. M. Orthopositronium-lifetime puzzle is not solved: on an effect of non-perturbative contribution. CERN E-Print, EXT-2004-016.

A Proposed Experimentum Crucis for the Orthopositronium Lifetime Anomalies

Boris M. Levin
E-mail: bormikhlev@mail.ru, bormikhlev@mail.ioffe.ru

Expansion of the Standard Model (SM) for the quantitative description of the orthopositronium lifetime anomalies allows formulation of additional experimental tests of supersymmetry in the final state of the positron beta-decay of nuclei such as ^{22}Na, ^{68}Ga, and resolution of the results of the last Michigan experiment (2003).

In 2003, at the University of Michigan (Ann Arbor), a measurement of the o-Ps annihilation rate was carried out, and the researchers reported complete agreement between the experimental value, $\lambda_{\mathrm{T}} = 7.0404(10)(8)\,\mu\mathrm{s}^{-1}$, and the value calculated in the frame of QED, $\lambda_{\mathrm{T(theor)}}$=7.039979(11)$\mu\mathrm{s}^{-1}$ [1]. These measurements were performed by a different technique, namely, a *dc* electric field of 7 kV/cm was introduced into the measurement cell. For this reason, and since they disregarded the "isotope anomaly" of o-Ps in gaseous neon in "resonance conditions" [2, 3], authors [1] could not include the *additional* action of the electric field on the observed o-Ps self-annihilation rate $\lambda_{\mathrm{T(exp)}}$ [3], notwithstanding the provisions they undertook to ensure complete o-Ps thermalization. The additional action of the electric field $E \sim 7$ kV/cm oriented parallel to the force of gravity should suppress the excess $\Delta\lambda_{\mathrm{T}} \simeq 0.19 \div 0.14\%$ over the calculated value $\lambda_{\mathrm{T(theor)}}$, which had been reported earlier by the Michigan group and referred to quantitatively as the *macroscopic quantum effect* (the "λ_{T}-anomaly" [3])*.

This is why rejection [1] of the conclusions drawn from the earlier high-precision λ_{T} measurements does not appear unambiguous.

The uncertainty we are presently witnessing can be resolved only by performing a program of additional measurements.

Consider the scheme of a Gedanken experiment for a measuring cell filled with a gas (Fig. 1).

Could one substantiate a program of comparative measurements which would yield as a final result the *doubling* of the parameter V to be measured with the external dc electric field orientation changed from *horizontal* to *vertical*? This would be certainly impossible within the SM. An analysis of the o-Ps anomalies within the concept of spontaneously broken complete relativity opens up such a possibility; indeed, restoration of the symmetry under discussion "should be accompanied by doubling of the space-time dimension" [4].

The uniqueness of orthopositronium dynamics (*virtual single-quantum* (!) *annihilation*, *CP*-invariance) make it an intriguing probe to double the space-time (see [5]).

*Here and so forth the sign $\div$ means that the values were obtained in the gas and vacuum experiments respectively.

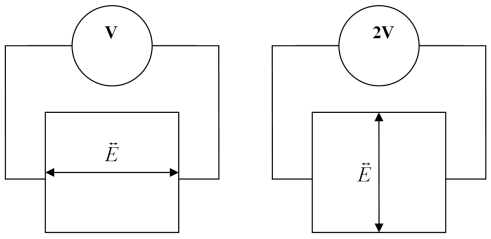

Fig. 1: Scheme and the *result* of a Gedanken experiment with an electric field in a laboratory on Earth. The measuring cell is filled with gas. $\vec{E}$ is orientation and *dc* voltage of an electric field; V is the value of the parameter to be measured.

Consider in this connection again the standard experimental technique used to measure positron/orthopositronium annihilation lifetime spectra.

Figure 2 presents a block diagram of a fast-slow lifetime spectrometer of delayed γ_{n}–γ_{a} coincidences.

Recording of *real* coincidences (in the start-stop arrangement) with a time resolution of 1.7×10^{-9} s [2] between the signal produced by a nuclear γ_{n} quantum of energy $\simeq$1.28 MeV ("start") with the signal generated by the detected γ_{a} annihilation quantum of energy $\simeq 0.34 \div 0.51$ MeV ("stop", corresponding, accordingly, to 3γ and 2γ-annihilation) is accompanied by the energy (amplitude) discrimination in the slow ("side") coincidence channels (with a resolution $\delta\tau_{\mathrm{s}} \sim 10^{-6}$ s between the corresponding signals from the last-but-one dynodes of the lifetime PM tubes, an approach that cuts efficiently *random* coincidence noise.

After subtraction of the random coincidence background, the positron annihilation lifetime spectra of inert gases would represent the sums of exponentials with characteristic annihilation rate constants λ_i

$$N(t) = \sum_{i=0}^{i=2} \mathrm{I}_i\, e^{-\lambda_i t},$$

where λ_0 and I_0 are, respectively, the rate and intensity of *two-quantum* annihilation of the para-positronium component (p-Ps), λ_1 and I_1 are the components of *two-quantum* annihilation of the quasi-free positrons that have not formed positronium (with so-called "shoulder" peculiarity [5]), and

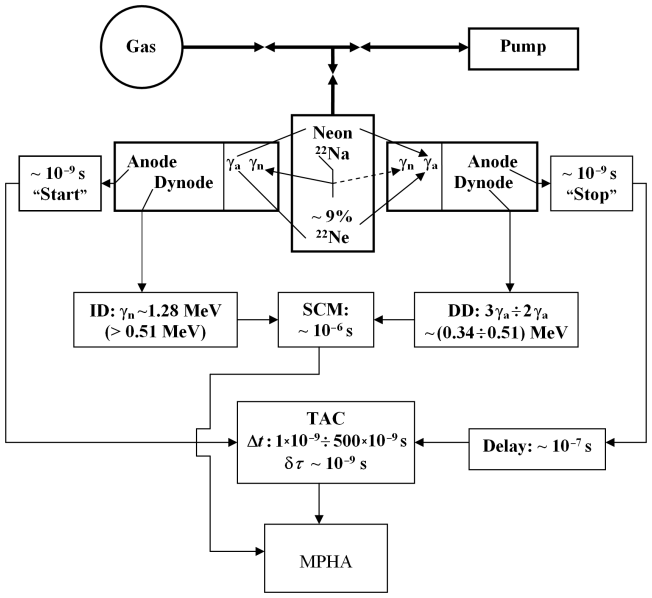

Fig. 2: Block-diagram of the lifetime spectrometer (fast-slow γ_n–γ_a coincidences). ID is for Integral Discriminator (excludes γ_a detection in the "start" channel); DD is for Differential Discriminator (restricts γ_n detection in the "stop" channel); SCM is for Slow Coincidence Module; TAC is for Time-to-Amplitude Converter ($\Delta t \rightarrow$ amplitude); MPHA is multichannel pulse-height analyzer.

λ_2 and I_2 are those of *three-quantum annihilation* of the orthopositronium component.

Experimental bounds accumulated in the two decades of intense studies of the orthopositronium problem lead one to the conclusion that the *additional single-quantum mode* of orthopositronium annihilation involves not a photon but rather a *notoph* (γ° is a zero-mass, zero-helicity particle which is complementary in properties to the photon) [7] and two *mirror photons* γ' with a negative total energy of 3.6×10^{-4} eV [3, 5]:

$$\text{o-Ps} \setminus \text{p-Ps}' \, (\text{p-Ps}') \longrightarrow \gamma^\circ \setminus 2\gamma'.$$

This was how the broadening of the framework in which the nature of the o-Ps anomalies could be analyzed (from QED to SQED) and the phenomenology of the mechanism of energy and momentum deficit compensation in a single-quantum mode were first formulated [7].

Treated from the SM standpoint, however, detection of a quantum of energy 1.022 MeV in the "stop" channel of the fast-slow coincidences is forbidden (see the "lower" and "upper" detection thresholds of $\sim 0.34 \div 0.51$ MeV, respectively, in Fig. 2).

We now come back to the principal question of *how the additional realization of supersymmetry would be established in the experiment*.

Detection of a single-notoph o-Ps annihilation mode should also be accompanied by observation of an energy

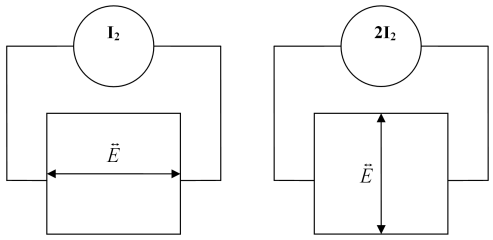

Fig. 3: Scheme of additional measurements: is there a connection between gravity and electromagnetism?

deficit in the "stop" channel of the lifetime spectrometer: indeed, *single-notoph annihilation* is identified in the scintillator by the Compton-scattered electron $\mathbf{e}$, which is bound in the *long-range atom* "shell" in a "pair" $\mathbf{e}\bar{\mathbf{e}}$ with the "electronic hole" $\bar{\mathbf{e}}$ (negative mass) in the "C-field/mirror Universe" structure. Half of the notoph energy, $\sim$0.51 MeV, is transferred to the $\mathbf{e}$ hole ($\bar{\mathbf{e}}$) and, thus, "disappears" (*anti-Compton scattering*). As a result, the additional single-notoph mode is detected by the lifetime spectrometer in the "stop" channel by Compton scattering of an electron e of energy $\leqslant 0.51$ eV.

The experiment is in agreement with the phenomenology proposed for quantitative description of the o-Ps anomalies provided we assume that the additional single-notoph annihilation mode contributes to the *instantaneous coincidence peak* [5]. This means that one half of the intensity of the long-lived lifetime spectral component obtained under "resonance conditions" for neon of natural isotope abundance (I_2) transfers to the $t \sim 0$ region. An electric field of 7 kV/cm applied parallel to the force of gravity should suppress the additional mode and double the orthopositronium component ($2I_2$). Accordingly, in the Michigan experiment (non-resonance conditions) an electric field oriented along the force of gravity would bring about complete agreement between $\lambda_{T(exp)}$ with the QED-calculated value $\lambda_{T(theor)}$; and the disagreement of about $\Delta\lambda_T/\lambda_T \simeq 0.19 \div 0.14\%$ found previously (in experiments without electric field) should again appear after the action of the electric field has been neutralized (by applying it perpendicular to the force of gravity) [3].

The term "anti-Compton scattering" has been borrowed from J. L. Synge [8]; it appears appropriate to cite here an excerpt from the abstract of this paper written by a celebrated proponent of the theory of relativity:

> "The purpose of this paper is to answer the following question in terms of concepts of classical relativistic mechanics: How is Compton scattering altered if we replace the photon by a particle of zero rest mass and *negative* energy, and apply the conservation of 4-momentum? [...] Since particles with negative energies are not accepted in modern physics, it is perhaps best to regard this work as a kinematical exercise in Minkowskian geometry, worth recording because the results are not obvious".

Observation of orthopositronium anomalies gives one physical grounds to broaden the present-day SM. It now appears appropriate to analyze "anti-Compton scattering" in connection with the detection of notoph in the proposed program of *additional measurements*, which aim at proving the existence of a connection between gravity and electromagnetism [3].

We may add that the concept of the supersymmetric version of a *spin-$^1/_2$ quasi-particle* and a hole as *supersymmetric partners* has been discussed in the literature [9].

To sum up: one should carry out additional measurements because the result, *inconceivable* in the frame of the SM, becomes an expected result in the program of *experimentum crucis* (Fig. 3).

A positive result of this crucial experiment would mean the birth of *new physics* that would be complementary to the Standard Model.

Submitted on January 24, 2007
Accepted on January 30, 2007

References

1. Vallery R. S., Gidley D. W. and Zitzewitz P. W. Resolution of orthopositronium-lifetime puzzle. *Phys. Rev. Lett.*, 2003, v. 90(20), 203402 (1–4).
2. Levin B. M., Kochenda L. M., Markov A. A. and Shantarovich V. P. Time spectra of annihilation of positron (^{22}Na) in gaseous neon of various isotopic compositions. *Sov. J. Nucl. Phys.*, 1987, v. 45(6), 1119–1120.
3. Kotov B. A., Levin B. M. and Sokolov V. I. Orthopositronium: on the possible relation of gravity to electricity. Preprint-1784, A. F. Ioffe Physical Technical Institute of Russian Academy of Sciences. St.-Petersburg, 2005; arXiv: quant-ph/0604171.
4. Andreev A. F. Spontaneously broken complete relativity. *JETF Lett.*, 1982, v. 36(3), 100.
5. Levin B. M. Orthopositronium: annihilation of positron in gaseous neon. arXiv: quant-ph/0303166.
6. Ogievetskii V. I. and Polubarinov I. V. Notoph and its possible interactions. *Sov. J. Nucl. Res.*, 1966, v. 4(1), 156.
7. Levin B. M. On the kinematics of one-photon annihilation of orthopositronium. *Phys. At. Nucl.*, 1995, v. 58 (2). 332.
8. Synge J. L. Anti-Compton scattering. *Proc. Roy. Ir. Acad.*, 1974, v.A74 (9), 67.
9. Lee C. J. Spin-$^1/_2$ particle and hole as supersymmetry partners. *Phys. Rev. A*, 1994, v.50, R4 (4–6).

Numerical Solution of Time-Dependent Gravitational Schrödinger Equation

Vic Christianto*, Diego L. Rapoport† and Florentin Smarandache‡

*Sciprint.org — a Free Scientific Electronic Preprint Server, http://www.sciprint.org
E-mail: admin@sciprint.org
†Dept. of Sciences and Technology, Universidad Nacional de Quilmes, Bernal, Argentina
E-mail: diego.rapoport@gmail.com
‡Department of Mathematics, University of New Mexico, Gallup, NM 87301, USA
E-mail: smarand@unm.edu

In recent years, there are attempts to describe quantization of planetary distance based on time-independent gravitational Schrödinger equation, including Rubcic & Rubcic's method and also Nottale's Scale Relativity method. Nonetheless, there is no solution yet for time-dependent gravitational Schrödinger equation (TDGSE). In the present paper, a numerical solution of time-dependent gravitational Schrödinger equation is presented, apparently for the first time. These numerical solutions lead to gravitational Bohr-radius, as expected. In the subsequent section, we also discuss plausible extension of this gravitational Schrödinger equation to include the effect of phion condensate via Gross-Pitaevskii equation, as described recently by Moffat. Alternatively one can consider this condensate from the viewpoint of Bogoliubov-deGennes theory, which can be approximated with coupled time-independent gravitational Schrödinger equation. Further observation is of course recommended in order to refute or verify this proposition.

1 Introduction

In the past few years, there have been some hypotheses suggesting that quantization of planetary distance can be derived from a gravitational Schrödinger equation, such as Rubcic & Rubcic and also Nottale's scale relativity method [1, 3]. Interestingly, the gravitational Bohr radius derived from this gravitational Schrödinger equation yields prediction of new type of astronomical observation in recent years, i.e. extrasolar planets, with unprecedented precision [2].

Furthermore, as we discuss in preceding paper [4], using similar assumption based on gravitational Bohr radius, one could predict new planetoids in the outer orbits of Pluto which are apparently in good agreement with recent observational finding.. Therefore one could induce from this observation that the gravitational Schrödinger equation (and gravitational Bohr radius) deserves further consideration.

In the meantime, it is known that all present theories discussing gravitational Schrödinger equation only take its time-independent limit. Therefore it seems worth to find out the solution and implication of time-dependent gravitational Schrödinger equation (TDGSE). This is what we will discuss in the present paper.

First we will find out numerical solution of time-independent gravitational Schrödinger equation which shall yield gravitational Bohr radius as expected [1, 2, 3]. Then we extend our discussion to the problem of time-dependent gravitational Schrödinger equation.

In the subsequent section, we also discuss plausible extension of this gravitational Schrödinger equation to include the effect of phion condensate via Gross-Pitaevskii equation, as described recently by Moffat [5]. Alternatively one can consider this phion condensate model from the viewpoint of Bogoliubov-deGennes theory, which can be approximated with coupled time-independent gravitational Schrödinger equation. To our knowledge this proposition of coupled time-independent gravitational Schrödinger equation has never been considered before elsewhere.

Further observation is of course recommended in order to verify or refute the propositions outlined herein.

All numerical computation was performed using Maple. Please note that in all conditions considered here, we use only gravitational Schrödinger equation as described in Rubcic & Rubcic [3], therefore we neglect the scale relativistic effect for clarity.

2 Numerical solution of time-independent gravitational Schrödinger equation and time-dependent gravitational Schrödinger equation

First we write down the time-independent gravitational Schrödinger radial wave equation in accordance with Rubcic & Rubcic [3]:

$$\frac{d^2R}{dr^2}+\frac{2}{r}\frac{dR}{dr}+\frac{8\pi m^2 E'}{H^2}R+ +\frac{2}{r}\frac{4\pi^2 GMm^2}{H^2}R-\frac{\ell(\ell+1)}{r^2}R=0\,. \tag{1}$$

When H, V, E' represents gravitational Planck constant, Newtonian potential, and the energy per unit mass of the

orbiting body, respectively, and [3]:

$$H = h\left(2\pi f \frac{Mm_n}{m_0^2}\right), \tag{2}$$

$$V(r) = -\frac{GMm}{r}, \tag{3}$$

$$E' = \frac{E}{m}. \tag{4}$$

By assuming that R takes the form:

$$R = e^{-\alpha r} \tag{5}$$

and substituting it into equation (1), and using simplified terms only of equation (1), one gets:

$$\Psi = \alpha^2 e^{-\alpha r} - \frac{2\alpha e^{-\alpha r}}{r} + \frac{8\pi GMm^2 e^{-\alpha r}}{rH^2}. \tag{6}$$

After factoring this equation (7) and solving it by equating the factor with zero, yields:

$$RR = -\frac{2\left(4\pi GMm^2 - H^2\alpha\right)}{\alpha^2 H^2} = 0, \tag{7}$$

or

$$RR = 4\pi GMm^2 - H^2\alpha = 0, \tag{8}$$

and solving for α, one gets:

$$a = \frac{4\pi^2 GMm^2}{H^2}. \tag{9}$$

Gravitational Bohr radius is defined as inverse of this solution of α, then one finds (in accordance with Rubcic & Rubcic [3]):

$$r_1 = \frac{H^2}{4\pi^2 GMm^2}, \tag{10}$$

and by substituting back equation (2) into (10), one gets [3]:

$$r_1 = \left(\frac{2\pi f}{\alpha c}\right)^2 GM. \tag{11}$$

Equation (11) can be rewritten as follows:

$$r_1 = \frac{GM}{\nu_0^2}, \tag{11a}$$

where the "specific velocity" for the system in question can be defined as:

$$\nu_0 = \left(\frac{2\pi f}{\alpha c}\right)^{-1} = \alpha_g c. \tag{11b}$$

The equations (11a)-(11b) are equivalent with Nottale's result [1, 2], especially when we introduce the quantization number: $r_n = r_1 n^2$ [3]. For complete Maple session of these all steps, see Appendix 1. Furthermore, equation (11a) may be generalised further to include multiple nuclei, by rewriting it to become: $r_1 = (GM)/v^2 \Rightarrow r_1 = (G\Sigma M)/v^2$, where ΣM represents the sum of central masses.

Solution of time-dependent gravitational Schrödinger equation is more or less similar with the above steps, except that we shall take into consideration the right hand side of Schrödinger equation and also assuming time dependent form of r:

$$R = e^{-\alpha r(t)}. \tag{12}$$

Therefore the gravitational Schrödinger equation now reads:

$$\begin{aligned}&\frac{d^2R}{dr^2} + \frac{2}{r}\frac{dR}{dr} + \frac{8\pi m^2 E'}{H^2}R + \\ &+\frac{2}{r}\frac{4\pi^2 GMm^2}{H^2}R - \frac{\ell(\ell+1)}{r^2}R = H\frac{dR}{dt},\end{aligned} \tag{13}$$

or by using Leibniz chain rule, we can rewrite equation (15) as:

$$\begin{aligned}&-H\frac{dR}{dr(t)}\frac{dr(t)}{dt} + \frac{d^2R}{dr^2} + \frac{2}{r}\frac{dR}{dr} + \frac{8\pi m^2 E'}{H^2}R + \\ &+\frac{2}{r}\frac{4\pi^2 GMm^2}{H^2}R - \frac{\ell(\ell+1)}{r^2}R = 0.\end{aligned} \tag{14}$$

The remaining steps are similar with the aforementioned procedures for time-independent case, except that now one gets an additional term for RR:

$$\begin{aligned}RR' = H^3\alpha\left(\frac{d}{dt}r(t)\right)r(t) - \alpha^2 r(t)H^2 + \\ + 8\pi GMm^2 - 2H^2\alpha = 0.\end{aligned} \tag{15}$$

At this point one shall assign a value for $\frac{d}{dt}r(t)$ term, because otherwise the equation cannot be solved. We choose $\frac{d}{dt}r(t) = 1$ for simplicity, then equation (15) can be rewritten as follows:

$$RR' := \frac{rH^3\alpha}{2} + \frac{rH^2\alpha^2}{2} + 4\pi^2 GMm^2 - H^2\alpha = 0. \tag{16}$$

The roots of this equation (16) can be found as follows:

$$\begin{aligned}a1 &:= \frac{-r^2H + 2H + \sqrt{r^4H^4 - 4H^3r + 4H^2 - 32rGMm^2\pi^2}}{2rH}, \\ a2 &:= \frac{-r^2H + 2H - \sqrt{r^4H^4 - 4H^3r + 4H^2 - 32rGMm^2\pi^2}}{2rH}.\end{aligned} \tag{17}$$

Therefore one can conclude that there is time-dependent modification factor to conventional gravitational Bohr radius (10). For complete Maple session of these steps, see Appendix 2.

3 Gross-Pitaevskii effect. Bogoliubov-deGennes approximation and coupled time-independent gravitational Schrödinger equation

At this point it seems worthwhile to take into consideration a proposition by Moffat, regarding modification of Newtonian acceleration law due to phion condensate medium, to include Yukawa type potential [5, 6]:

$$a(r) = -\frac{G_\infty M}{r^2} + K\frac{\exp(-\mu_\phi r)}{r^2}(1 + \mu_\phi r). \tag{18}$$

Therefore equation (1) can be rewritten to become:

$$\frac{d^2R}{dr^2}+\frac{2}{r}\frac{dR}{dr}+\frac{8\pi m^2E'}{H^2}R+ \\ +\frac{2}{r}\frac{4\pi^2\big(GM-K\exp(-\mu_\phi r)(1+\mu_\phi r)\big)m^2}{H^2}R- \\ -\frac{\ell(\ell+1)}{r^2}R=0, \tag{19}$$

or by assuming $\mu = 2\mu_0 = \mu_0 r$ for the exponential term, equation (19) can be rewritten as:

$$\frac{d^2R}{dr^2}+\frac{2}{r}\frac{dR}{dr}+\frac{8\pi m^2E'}{H^2}R+ \\ +\frac{2}{r}\frac{4\pi^2\big(GM-Ke^{-2\mu_0}(1+\mu_0 r)\big)m^2}{H^2}R-\frac{\ell(\ell+1)}{r^2}R=0. \tag{20}$$

Then instead of equation (8), one gets:

$$RR''=8\pi GMm^2-2H^2\alpha-8\pi^2m^2Ke^{-\mu_0}(1+\mu)=0. \tag{21}$$

Solving this equation will yield a modified gravitational Bohr radius which includes Yukawa effect:

$$r_1=\frac{H^2}{4\pi^2(GM-Ke^{-2\mu_0})m^2} \tag{22}$$

and the modification factor can be expressed as ratio between equation (22) and (10):

$$\chi=\frac{GM}{(GM-Ke^{-2\mu_0})}. \tag{23}$$

(For complete Maple session of these steps, see Appendix 3.)

A careful reader may note that this "Yukawa potential effect" as shown in equation (20) could be used to explain the small discrepancy (around $\pm 8\%$) between the "observed distance" and the computed distance based on gravitational Bohr radius [4, 6a]. Nonetheless, in our opinion such an interpretation remains an open question, therefore it may be worth to explore further.

There is, however, an alternative way to consider phion condensate medium i.e. by introducing coupled Schrödinger equation, which is known as Bogoliubov-deGennes theory [7]. This method can be interpreted also as generalisation of assumption by Rubcic-Rubcic [3] of subquantum structure composed of positive-negative Planck mass. Therefore, taking this proposition seriously, then one comes to hypothesis that there shall be coupled Newtonian potential, instead of only equation (3).

To simplify Bogoliubov-deGennes equation, we neglect the time-dependent case, therefore the wave equation can be written in matrix form [7, p.4]:

$$[A]\,[\Psi]=0, \tag{24}$$

where $[A]$ is 2×2 matrix and $[\Psi]$ is 2×1 matrix, respectively, which can be represented as follows (using similar notation with equation 1):

$$\big[A\big]=\begin{pmatrix} \dfrac{8\pi GMm^2e^{-\alpha r}}{rH^2} & \alpha^2e^{-\alpha r}-\dfrac{2\alpha e^{-\alpha r}}{r} \\ \alpha^2e^{-\alpha r}-\dfrac{2\alpha e^{-\alpha r}}{r} & -\dfrac{8\pi GMm^2e^{-\alpha r}}{rH^2} \end{pmatrix} \tag{25}$$

and

$$\big[\Psi\big]=\begin{pmatrix} f(r) \\ g(r) \end{pmatrix}. \tag{26}$$

Numerical solution of this matrix differential equation can be found in the same way with the previous methods, however we leave this problem as an exercise for the readers.

It is clear here, however, that Bogoliubov-deGennes approximation of gravitational Schrödinger equation, taking into consideration phion condensate medium will yield nonlinear effect, because it requires solution of matrix differential equation* (21) rather than standard ODE in conventional Schrödinger equation (or time-dependent PDE in 3D-condition). This perhaps may explain complicated structures beyond Jovian Planets, such as Kuiper Belt, inner and outer Oort Cloud etc. which of course these structures cannot be predicted by simple gravitational Schrödinger equation. In turn, from the solution of (21) one could expect that there are numerous undiscovered celestial objects in the Oort Cloud.

Further observation is also recommended in order to verify and explore further this proposition.

4 Concluding remarks

In the present paper, a numerical solution of time-dependent gravitational Schrödinger equation is presented, apparently for the first time. This numerical solution leads to gravitational Bohr-radius, as expected.

In the subsequent section, we also discuss plausible extension of this gravitational Schrödinger equation to include the effect of phion condensate via Gross-Pitaevskii equation, as described recently by Moffat. Alternatively one can consider this condensate from the viewpoint of Bogoliubov-deGennes theory, which can be approximated with coupled time-independent gravitational Schrödinger equation.

It is recommended to conduct further observation in order to verify and also to explore various implications of our propositions as described herein.

Acknowledgment

The writers would like to thank to Profs. C. Castro for valuable discussions.

Submitted on January 08, 2007
Accepted on January 30, 2007
After revision: March 06, 2007

*For recent articles discussing analytical solution of matrix differential equations, the reader is referred to Electronic Journal of Differential Equations (free access online on many mirrors as http://ejde.math.txstate.edu, http://ejde.math.unt.edu, http://www.emis.de/journals/EJDE etc.).

References

1. Nottale L. *et al. Astron. & Astrophys.*, 1997, v. 322, 1018.
2. Nottale L., Schumacher G. and Levefre E. T. *Astron. & Astrophys.*, 2000, v. 361, 379–389; accessed online on http://daec.obspm.fr/users/nottale.
3. Rubcic A. and Rubcic J. The quantization of solar like gravitational systems. *Fizika*, B-7, 1998, v. 1, No. 1–13.
4. Smarandache F. and Christianto V. *Progress in Physics*, 2006, v. 2, 63–67.
5. Moffat J. arXiv: astro-ph/0602607.
6. Smarandache F. and Christianto V. *Progress in Physics*, 2006, v. 4, 37–40; [6a] Christianto V. *EJTP*, 2006, v. 3, No. 12, 117–144; accessed onle on http://www.ejtp.com.
7. Lundin N. I. Microwave induced enhancement of the Josephson DC. *Chalmers University of Technology & Gotterborg University Report*, p. 4–7.
8. Griffin M. arXiv: cond-mat/9911419.
9. Tuszynski J. *et al. Physica A*, 2003, v. 325, 455–476; accessed onle on http://sciencedirect.com.
10. Toussaint M. arXiv: cs.SC/0105033.
11. Fischer U. arXiv: cond-mat/9907457; [8a] arXiv: cond-mat/0004339.
12. Zurek W. (ed.) In: *Proc. Euroconference in Formation and Interaction of Topological Defects*, Plenum Press, 1995; accessed online: arXiv: cond-mat/9502119.
13. Volovik G. arXiv: cond-mat/0507454.

Appendix 1 Time-independent gravitational Schrödinger equation

> restart;
> with (linalg);
> R: = exp(−(alpha*r));

$$R := e^{-\alpha r}$$

> D1R:=diff(R,r); D2R:=diff(D1R,r);

$$D1R := -\alpha e^{-\alpha r}$$

$$D2R := -\alpha^2 e^{-\alpha r}$$

> SCHEQ1:=D2R+D1R*2/r+8*pi^2*m*E*R/h^2+8*pi^2*G*M*m^2*R/(r*h^2)−l*(l+1)*R/r^2=0;
> XX1:=factor(SCHEQ1);
> #Using simplified terms only from equation (A*8, of Rubcic & Rubcic, 1998)
> ODESCHEQ:=D2R+D1R*2/r+8*pi^2*G*M*m^2*R/(r*h^2)=0;

$$ODESCHEQ := \alpha^2 e^{-\alpha r} - \frac{2\alpha e^{-\alpha r}}{r} + \frac{8\pi^2 GMm^2 e^{-\alpha r}}{rH^2} = 0$$

> XX2:=factor(SCHEQ2);

$$XX2 := \frac{e^{-\alpha r}\left(\alpha^2 rH^2 - 2H^2\alpha + 8\pi^2 GMm^2\right)}{rH^2} = 0$$

> RR:= solve(XX2, r);

$$RR := -\frac{2(4\pi^2 GMm^2 - H^2\alpha)}{\alpha^2 H^2}$$

> #Then solving for RR=0, yields:
> SCHEQ3:=4*pi^2*G*M*m^2−h^2*alpha=0;

$$SCHEQ3 := 4\pi^2 GMm^2 - H^2\alpha = 0$$

> a:= solve(SCHEQ3, alpha);

$$a := \frac{4\pi^2 GMm^2}{H^2}$$

> #Gravitational Bohr radius is defined as inverse of alpha:
> gravBohrradius:=1/a;

$$r_{gravBohr} := \frac{H^2}{4\pi^2 GMm^2}$$

Appendix 2 Time-dependent gravitational Schrödinger equation

> #Solution of gravitational Schrodinger equation (Rubcic, Fizika 1998);
> restart;
> #with time evolution (Hagendorn's paper);
> S:=r(t); R:=exp(−(alpha*S)); R1:=exp(−(alpha*r));

$$S := r(t)$$

$$R := e^{-\alpha r}$$

> D4R:=diff(S,t); D1R:=−alpha*exp(−(alpha*S)); D2R:=−alpha^2* exp(−(alpha*S)); D5R:=D1R*D4R;

$$D4R := \frac{d}{dt}r(t)$$

$$D1R := -\alpha e^{-\alpha r(t)}$$

$$D2R := -\alpha^2 e^{-\alpha r(t)}$$

$$D1R := -\alpha e^{-\alpha r(t)}\frac{d}{dt}r(t)$$

> #Using simplified terms only from equation (A*8)
> SCHEQ3:=−h*D5R+D2R+D1R*2/S+8*pi^2*G*M*m^2*R/(S*h^2);
> XX2:=factor(SCHEQ3);

$$XX2 := \frac{e^{-\alpha r(t)}\left(H^3\alpha\frac{dr(t)}{dt}r(t) - \alpha^2 r(t)H^2 - 2H^2\alpha + 8\pi^2 GMm^2\right)}{r(t)H^2} = 0$$

> #From standard solution of gravitational Schrodinger equation, we know (Rubcic, Fizika 1998):
> SCHEQ4:=4*pi^2*G*M*m^2−h^2*alpha;

$$SCHEQ4 := 4\pi^2 GMm^2 - H^2\alpha$$

> #Therefore time-dependent solution of Schrodinger equation may introduce new term to this gravitational Bohr radius.
> SCHEQ5:=(XX2*(S*h^2)/(exp(−(alpha*S))))−2*SCHEQ4;

$$ODESCHEQ5 := H^3\alpha\frac{dr(t)}{dt}r(t) - \alpha^2 r(t)H^2$$

> #Then we shall assume for simplicity by assigning value to d[r(t)]/dt:
> D4R:=1;
> Therefore SCHEQ5 can be rewritten as:
> SCHEQ5:= H^3*alpha*r/2+alpha^2*r*H^2/2−4*pi^2*G*M*m^2−H^2*alpha=0;

$$SCHEQ5 := \frac{rH^3\alpha}{2} + \frac{rH^2\alpha^2}{2} + 4\pi^2 GMm^2 - H^2\alpha = 0$$

> Then we can solve again SCHEQ5 similar to solution of SCHEQ4:
> a1:=solve(SCHEQ5,alpha);

$$a1 := \frac{-r^2H + 2H + \sqrt{r^4H^4 - 4H^3r + 4H^2 - 32rGMm^2\pi^2}}{2rH}$$

$$a2 := \frac{-r^2H + 2H - \sqrt{r^4H^4 - 4H^3r + 4H^2 - 32rGMm^2\pi^2}}{2rH}$$

> #Therefore one could expect that there is time-dependent change of gravitational Bohr radius.

Appendix 3 Time-independent gravitational Schrödinger equation with Yukawa potential [5]

> #Extension of gravitational Schrodinger equation (Rubcic, Fizika 1998);
> restart;
> #departure from Newton potential;
> R:=exp(−(alpha*r));

$$R := e^{-\alpha r}$$

> D1R:= diff(R,r); D2R:= diff(D1R,r);

$$D1R := -\alpha e^{-\alpha r}$$

$$D2R := -\alpha^2 e^{-\alpha r}$$

> SCHEQ2:=D2R+D1R*2/r+8*pi^2*(G*M−K*exp(−2*mu)*(1+mu*r))*m^2*R/(r*h^2)=0;

$$ODESCHEQ := \alpha^2 e^{-\alpha r} - \frac{2\alpha e^{-\alpha r}}{r} + \\ + \frac{8\pi^2(GM - Ke^{-2\mu}(1+\mu r))m^2 e^{-\alpha r}}{rH^2} = 0$$

> XX2:=factor(SCHEQ2);
> RR1:=solve(XX2,r);

$$RR1 := -\frac{2(-H^2\alpha + 4\pi^2 GMm^2 - 4\pi^2 m^2 Ke^{-2\mu})}{-\alpha^2 H^2 + 8\pi^2 m^2 Ke^{-2\mu}}$$

> #from standard gravitational Schrodinger equation we know:
> SCHEQ3:=4*pi^2*G*M*m^2−h^2*alpha=0;
> a:=solve(SCHEQ3, alpha);
> #Gravitational Bohr radius is defined as inverse of alpha:
> gravBohrradius:=1/a;

$$r_{gravBohr} := \frac{H^2}{4\pi^2 GMm^2}$$

> #Therefore we conclude that the new terms of RR shall yield new terms (YY) into this gravitational Bohr radius:
> PI:= (RR*(alpha^2*h^2)−(−8*pi^2*G*M*m^2+2*h^2*alpha));
> #This new term induced by pion condensation via Gross-Pitaevskii equation may be observed in the form of long-range potential effect. (see Moffat J., arXiv: astro-ph/0602607, 2006; also Smarandache F. and Christianto V. Progress in Physics, v. 2, 2006, & v. 1, 2007, www.ptep-online.com)
> #We can also solve directly:
> SCHEQ5:=RR*(alpha^2*h^2)/2;

$$SCHEQ5 := \frac{\alpha^2 H^2(-H^2\alpha + 4\pi^2 GMm^2 - 4\pi^2 m^2 Ke^{-2\mu})}{-\alpha^2 H^2 + 8\pi^2 m^2 Ke^{-2\mu}}$$

> a1:=solve(SCHEQ5, alpha);

$$a1 := 0, 0, \frac{4\pi^2 m^2(GM - Ke^{-2\mu})}{H^2}$$

> #Then one finds modified gravitational Bohr radius in the form:
> modifgravBohrradius:=1/(4*pi^2*(G*M−K*exp(−2*mu))*m^2/h^2);

$$r_{modified.gravBohr} := \frac{H^2}{4\pi^2 m^2(GM - Ke^{-2\mu})}$$

> #This modification can be expressed in chi-factor:
> chi:=modifgravBohrradius/gravBohrradius;

$$\chi := \frac{GM}{GM - Ke^{-2\mu}}$$

A Note on Unified Statistics Including Fermi-Dirac, Bose-Einstein, and Tsallis Statistics, and Plausible Extension to Anisotropic Effect

Vic Christianto* and Florentin Smarandache†

*Sciprint.org — a Free Scientific Electronic Preprint Server, http://www.sciprint.org
E-mail: admin@sciprint.org

†Department of Mathematics, University of New Mexico, Gallup, NM 87301, USA
E-mail: smarand@unm.edu

In the light of some recent hypotheses suggesting plausible unification of thermo-statistics where Fermi-Dirac, Bose-Einstein and Tsallis statistics become its special subsets, we consider further plausible extension to include non-integer Hausdorff dimension, which becomes realization of fractal entropy concept. In the subsequent section, we also discuss plausible extension of this unified statistics to include anisotropic effect by using quaternion oscillator, which may be observed in the context of Cosmic Microwave Background Radiation. Further observation is of course recommended in order to refute or verify this proposition.

1 Introduction

In recent years, there have been some hypotheses suggesting that the spectrum and statistics of Cosmic Microwave Background Radiation has a kind of *scale invariant* character [1], which may be related to non-integer Hausdorff dimension. Interestingly, in this regard there is also proposition sometime ago suggesting that Cantorian spacetime may have deep link with Bose condensate with non-integer Hausdorff dimension [2]. All of these seem to indicate that it is worth to investigate further the non-integer dimension effect of Bose-Einstein statistics, which in turn may be related to Cosmic Microwave Background Radiation spectrum.

In the meantime, some authors also consider a plausible generalization of known statistics, i.e. Fermi-Dirac, Bose-Einstein, and Tsallis statistics, to become more unified statistics [3, 4]. This attempt can be considered as one step forward from what is already known, i.e. to consider anyons as a generalization of bosons and fermions in two-dimensional systems [5, p. 2] Furthermore, it is known that superfluidity phenomena can also be observed in Fermi liquid [6].

First we will review the existing procedure to generalize Fermi-Dirac, Bose-Einstein, and Tsallis statistics, to become more unified statistics [3, 4]. And then we explore its plausible generalization to include fractality of Tsallis' non-extensive entropy parameter.

In the subsequent section, we also discuss plausible extension of this proposed unified statistics to include anisotropic effect, which may be observed in the context of Cosmic Microwave Background Radiation. In particular we consider possibility to introduce quaternionic momentum. To our knowledge this proposition has never been considered before elsewhere.

Further observation is of course recommended in order to verify or refute the propositions outlined herein.

2 Unified statistics including Fermi-Dirac, Bose-Einstein, and Tsallis statistics

In this section we consider a different theoretical framework to generalize Fermi-Dirac and Bose-Einstein statistics, from conventional method using anyons, [5] in particular because this conventional method cannot be generalized further to include Tsallis statistics which has attracted some attention in recent years.

First we write down the standard expression of Bose distribution [9, p. 7]:

$$\bar{n}(\epsilon_i) = \frac{1}{\exp\big(\beta(\epsilon_i - \mu)\big) - 1}\,, \tag{1}$$

where the harmonic energy levels are given by [9, p. 7]:

$$\epsilon_i = \left(n_x + n_y + n_z + \frac{3}{2}\right)\hbar\omega_0\,. \tag{2}$$

When we assume that bosons and fermions are g-ons obeying fractional exclusion statistics, then we get a very different picture. In accordance with [3], we consider the spectrum of fractal dimension (also called *generalized Renyi dimension* [11]):

$$D_q = \lim_{\delta\to 0}\frac{1}{q-1}\frac{\ln\Omega_q}{\ln\delta}\,, \tag{3}$$

(therefore the spectrum of fractal dimension is equivalent with Hausdorff dimension of the set A [11]).

Then the relation between the entropy and the spectrum of fractal dimension is given by: [3]

$$S_q = -K_B\lim_{\delta\to 0}\ln\delta D_q\,, \tag{4}$$

where K_B is the Boltzmann constant.

The spectrum of fractal dimension may be expressed in terms of p:

$$D_q \approx \frac{1}{q-1} \frac{\sum_{i=1}^{k} p_i^q - 1}{\ln \delta} . \quad (5)$$

Then, substituting equation (6) into (4), we get the Tsallis non-extensive entropy [3]:

$$S_q = -K_B \frac{\sum_{i=1}^{k} p_i^q - 1}{q-1} . \quad (6)$$

After a few more assumptions, and using g-on notation [3], i.e. $g=1$ for generalized Fermi-Dirac statistics and $g=0$ for generalised Bose-Einstein statistics, then one gets the most probable distribution for g-ons [3]:

$$\bar{n}_k(\epsilon_i, g, q) = \frac{1}{\left(1-(q-1)\beta(\epsilon_i-\mu)\right)^{\frac{1}{q-1}} + 2g - 1} , \quad (7)$$

Which gives standard Planck distribution for $\mu=0$, $g=0$ and $q=1$ [3, 9]. In other words, we could expect that g-ons gas statistics could yield more generalized statistics than anyons'.

To introduce further generality of this expression (8), one may consider the parameter q as function of another non-integer dimension, therefore:

$$\bar{n}_k(\epsilon_i, g, q, D) = \frac{1}{\left(1-(q^D-1)\beta(\epsilon_i-\mu)\right)^{\frac{1}{q^D-1}} + 2g - 1} , \quad (8)$$

where $D=1$ then equation (9) reduces to be (8).

Of course, the picture described above will be different if we introduce non-standard momentum [5, p. 7]:

$$p^2 = -\frac{d^2}{dx^2} + \frac{\lambda}{x^2} . \quad (9)$$

In the context of Neutrosophic logic as conceived by one of these writers [8], one may derive a proposition from the arguments presented herein, i.e. apart from common use of anyons as a plausible generalization of fermion and boson, perhaps an alternative method for generalization of fermion and boson can be described as follows:

1. If we denote fermion with (f) and boson with (b), then it follows that there could be a mixture composed of both (f) and (b) $\rightarrow$ (f) $\cap$ (b), which may be called as "anyons";
2. If we denote fermion with (f) and boson with (b), and because $g=1$ for generalized Fermi-Dirac statistics and $g=0$ for generalised Bose-Einstein statistics, then it follows that the wholeness of both (f) and (b) $\rightarrow$ (f) $\cup$ (b), which may be called as "g-on";
3. Taking into consideration of possibility of "neitherness", then if we denote non-fermion with ($\neg$f) and non-boson with ($\neg$b), then it follows that there shall be a mixture composed of both ($\neg$f) and also ($\neg$b) $\rightarrow$ ($\neg$f) $\cap$ ($\neg$b), which may be called as "feynmion" (after physicist the late R. Feynman);
4. Taking into consideration of possibility of "neitherness", then it follows that the wholeness of both ($\neg$f) and ($\neg$b) $\rightarrow$ ($\neg$f) $\cup$ ($\neg$b), which may be called as "anti-g-on".

Therefore, a conjecture which may follow from this proposition is that perhaps in the near future we can observe some new entities corresponding to g-on condensate or feynmion condensate.

3 Further extension to include anisotropic effect

At this section we consider the anisotropic effect which may be useful for analyzing the anisotropy of CMBR spectrum, see Fig. 1 [13].

For anisotropic case, one cannot use again equation (2), but shall instead use [7, p. 2]:

$$\epsilon_i = \left(n_x + \frac{1}{2}\right)\hbar\omega_x + \left(n_y + \frac{1}{2}\right)\hbar\omega_y + \left(n_z + \frac{1}{2}\right)\hbar\omega_z , \quad (10)$$

where n_x, n_y, n_z are integers and >0. Or by neglecting the $1/2$ parts and assuming a common frequency, one can re-write (10) as [7a, p.1]:

$$\epsilon_i = (n_x r + n_y s + n_z t)\hbar\omega_0 , \quad (11)$$

where r, s, t is multiplying coefficient for each frequency:

$$r = \frac{\omega_x}{\omega_0} , \qquad s = \frac{\omega_y}{\omega_0} , \qquad t = \frac{\omega_z}{\omega_0} . \quad (12)$$

This proposition will yield a different spectrum compared to isotropic spectrum by assuming isotropic harmonic oscillator (2). See Fig. 2 [7a]. It is interesting to note here that the spectrum produced by anisotropic frequencies yields number of peaks more than 1 (multiple-peaks), albeit this is not near yet to CMBR spectrum depicted in Fig. 1. Nonetheless, it seems clear here that one can expect to predict the anisotropy of CMBR spectrum by using of more anisotropic harmonic oscillators.

In this regard, it is interesting to note that some authors considered half quantum vortices in $p_x + ip_y$ superconductors [14], which indicates that energy of partition function may be generalized to include Cauchy plane, as follows:

$$E = p_x c + ip_y c \approx \hbar\omega_x + i\hbar\omega_y , \quad (13)$$

or by generalizing this Cauchy plane to quaternion number [12], one gets instead of (13):

$$E_{qk} = \hbar\omega + i\hbar\omega_x + j\hbar\omega_y + k\hbar\omega_z , \quad (14)$$

which is similar to standard definition of quaternion number:

$$Q \equiv a + bi + cj + dk . \quad (15)$$

Therefore the partition function with anisotropic harmon-

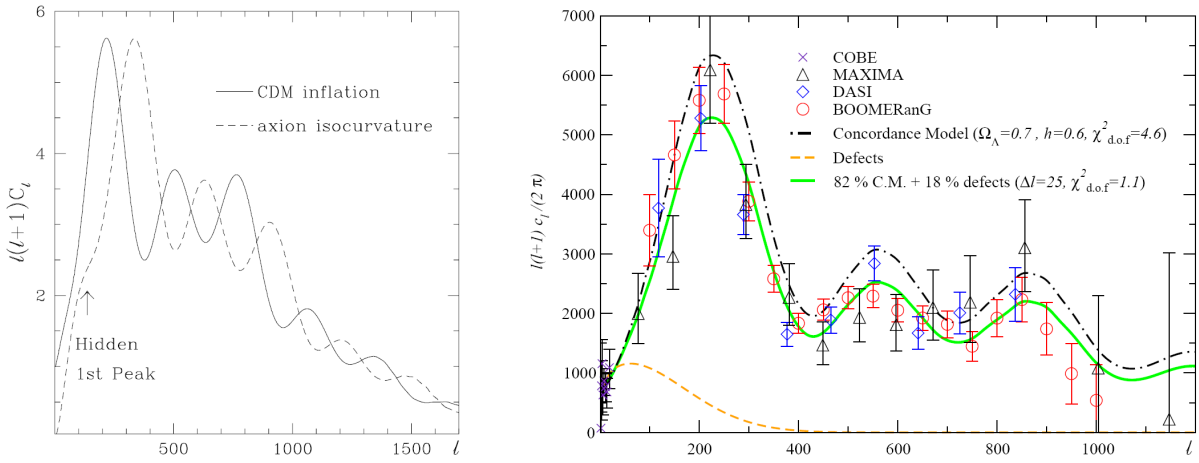

Fig. 1: Anisotropy of CMBR (after Tkachev [13]). Left panel: comparison of CMB power spectra in the models with adiabatic and isocurvature initial perturbations. Right panel: adiabatic power spectra in comparison with spectra appearing in models seeded by topological defects. In this panel some older, pre-WMAP, data are also shown.

ic potential can be written in quaternion form. Therefore instead of (11), we get:

$$\epsilon_i = \left(n_x r + n_y s + n_z t + i n_x r + j n_y s + k n_z t\right) \hbar\omega_0 , \quad (16)$$

which can be written as:

$$\epsilon_i = (1 + q_k)(n_k r_k)\hbar\omega_0 , \quad (17)$$

where $k = 1, 2, 3$ corresponding to index of quaternion number i, j, k. While we don't obtain numerical result here, it can be expected that this generalisation to anisotropic quaternion harmonic potential could yield better prediction, which perhaps may yield to exact CMBR spectrum. Numerical solution of this problem may be presented in another paper.

This proposition, however, may deserve further considerations. Further observation is also recommended in order to verify and also to explore various implications of.

4 Concluding remarks

In the present paper, we review an existing method to generalize Fermi-Dirac, Bose-Einstein, and Tsallis statistics, to become more unified statistics. And then we explore its plausible generalization to include fractality of Tsallis non-extensive entropy parameter .

Therefore, a conjecture which may follow this proposition is that perhaps in the near future we can observe some new entities corresponding to g-on condensate or feynmion condensate.

In the subsequent section, we also discuss plausible extension of this proposed unified statistics to include anisotropic effect, which may be observed in the context of Cosmic Microwave Background Radiation. In particular we consider possibility to introduce quaternionic harmonic oscillator. To our knowledge this proposition has never been considered before elsewhere.

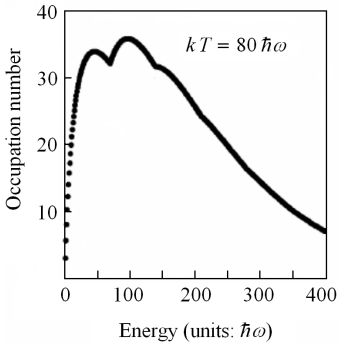

Fig. 2: Spectrum for anisotropic harmonic oscillator potential (after Ligare [7a]).

It is recommended to conduct further observation in order to verify and also to explore various implications of our propositions as described herein.

Acknowledgment

The writers would like to thank to Profs. C. Castro, A. Yefremov, D. L. Rapoport, D. Rabounski, S. Crothers and L. Borissova for valuable discussions.

Submitted on January 08, 2007
Accepted on January 30, 2007

References

1. Antoniadis I. *et al.* arXiv: astro-ph/9611208.
2. Castro C. and Granik A. Why we live in 3 dimensions. arXiv: hep-th/0004152.
3. Buyukkilic F. and Demirhan D. arXiv: hep-th/0010192.
4. Utyuzh O. V. *et al.* arXiv: hep-ph/9910355.
5. Leinaas J. M. arXiv: hep-th/9611167.
6. Pinilla M. R. Signatures of superfluidity in atomic Fermi gases. Diss. Helsinki University of Tech., Nov. 2003, 72 p.

7. Ligare M. Numerical analysis of Bose-Einstein condensation in a three dimensional harmonic oscillator potential. *Am. J. Phys.*, 1998, v. 66, No. 3, 2; [7a] Ligare M. *Am. J. Phys.*, 2002, v. 70, No. 1.
8. Smarandache F. and Christianto V. *Progress in Physics*, 2006, v. 4, 37–40.
9. Griffin A. arXiv: cond-mat/9911419.
10. Tuszynski J. *et al. Physica A*, 2003, v. 325, 455–476.
11. Batunin F. *Physics-Uspekhi*, 1995, v. 38(6), 609–623.
12. Yefremov A. Relativistic oscillator in quaternion relativity. In: *Quantization in Astrophysics, Brownian Motion, and Supersymmetry*, F. Smarandache and V. Christianto (eds.), Chennai Publisher, India, in press (Nov. 2006).
13. Tkachev I. arXiv: hep-ph/0405168, p. 17–18.
14. Stone M. *et al.* arXiv: cond-mat/0505515, p. 14–15.

On the Rate of Change of Period for Accelerated Motion and Their Implications in Astrophysics

R. Rajamohan and A. Satya Narayanan

Indian Institute of Astrophysics, Koramangala, Bangalore – 560 034, India

E-mail: satya@iiap.res.in

We have derived in this paper, the relationship that needs to be satisfied when length measurements are expressed in two different units. Interesting relationships emerge when the smaller of the two units chosen is a function of time. We relate these results to the expected periodicities in the observed data when a system of objects are revolving around a common center of mass. We find that these results are highly intriguing and can equally well account for some of the major results in the field of astrophysics.

1 Introduction

In an earlier paper (Rajamohan and Satya Narayanan [1]) we derived the condition that needs to be satisfied for signal from a relatively stationary emitter to meet an observer moving transverse to the line of sight. A receiver moving across the line of sight is equivalent of the receiver accelerating away along the line of sight from the emitter. In this paper, we have derived the period and period derivative for this equivalent situation.

It is well known that signals with uniform period P_e from an emitter will arrive at a receiver, moving with uniform relative velocity V along the line of sight, with a period P given by the equation

$$P = \frac{P_e}{(1 - V/C)},$$

where C is the signal speed. Instead if the receiver or the emitter were to be accelerating with a as the value of acceleration, it is generally assumed that the observed rate of change of period $\dot{P}$ per unit time is governed by the equation (Shklovski [2])

$$\dot{P} = \frac{aP}{C}. \qquad (1)$$

The above equation does not take into account the relationship between space intervals and time intervals properly. When acceleration is involved, the time interval Δt that corresponds to a given space interval Δx is a function of time. That is, the space interval Δx corresponds to smaller and smaller time interval (along the direction of motion) as the velocity of the accelerating receiver is a function of time.

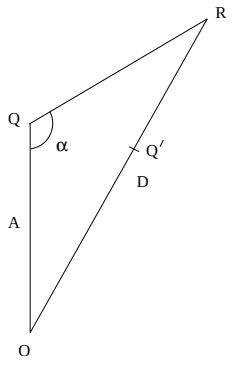

Fig. 1: Schematic representation of the observer and the emitter meeting at a point.

The space-time relationship when properly taken into account leads to an additional term which is enormously larger than that given by equation (1).

2 Relationship between time, length and the unit of length-measurement

Consider the general case when the observer is at a distance A (km) from the emitter moving with uniform velocity V at an angle α to the line of sight as shown in Figure 1. Let the emitter at position O emit signals at regular intervals of P_e seconds.

At time $t = 0$, let a signal start from O when the observer is at Q (at $t = 0$). Let this signal meet the observer at R at time t. Let the initial distance $OQ = A$ at $t = 0$ and the distance $OR = D$ at time t.

From triangle OQR

$$(OR)^2 = (OQ)^2 + (QR)^2 - 2(OQ)(QR)\cos\alpha$$

or

$$D^2 = A^2 + V^2t^2 - 2AV\cos\alpha t = A^2\left[1 + \frac{V^2t^2}{A^2} - \frac{2V\cos\alpha t}{A}\right],$$

$$D = A\left[1 + \frac{V^2t^2}{A^2} - \frac{2V\cos\alpha t}{A}\right]^{\frac{1}{2}} \approx A + \frac{1}{2}\frac{V^2t^2}{A} -$$

$$- V\cos\alpha t - \frac{1}{2}\frac{V^2t^2\cos^2\alpha}{A} = A - V\cos\alpha t + \frac{1}{2}\frac{V^2\sin^2\alpha}{A}t^2.$$

Therefore

$$D - A = -V\cos\alpha t + \frac{1}{2}\frac{V^2\sin^2\alpha}{A}t^2.$$

We can rewrite $D - A$ as

$$D - A = ut + \frac{1}{2}at^2;$$

u is positive when α is greater than 90° and negative when α is less than 90°. However, $a = V^2\sin^2\alpha/A$ is always positive. If the angle α were to be 0 or 180°, the observer will be moving uniformly along the line of sight and the signals from O will be equally spaced in time. If the observer were to move in a circular orbit around the emitter then too, the period observed would be constant. In all other cases the acceleration due to transverse component that leads to the period derivative will always be positive.

Draw a circle with A as radius. Let it intercept the line

OR at Q'. Therefore $OQ = OQ'$. Let the signal from O reach Q' at time t_e

$$D - A = Q'R = C(t - t_e) = ut + \frac{1}{2}at^2.$$

The signal from O meeting the uniformly moving observer along QR is equivalent to the same signal chasing an observer from Q' to R with initial velocity u and acceleration a

$$C(t - t_e) = ut + \frac{1}{2}at^2 =$$
$$= u\big[t_e + (t - t_e)\big] + \frac{1}{2}a\big[t_e + (t - t_e)\big]^2 =$$
$$= ut_e + \frac{1}{2}at_e^2 + (u + at_e)(t - t_e) + \frac{1}{2}a(t - t_e)^2.$$

Let $C(t - t_e) = X$ and $ut_e + \frac{1}{2}at_e^2 = X_e$. The space interval X_e contains N signals where $N = X_e/CP_e$ which will get folded in the space interval $X - X_e$ as the train of signals moving along OR will be spaced at CP_e km.

Therefore

$$t - t_e = \frac{X}{C} = \frac{X_e}{C} + \frac{u + at_e}{C}(t - t_e) + \frac{1}{2}\frac{a}{C}(t - t_e)^2.$$

Hence the average observed period in the time interval $(t - t_e)$ is

$$\bar{P} = \frac{(t - t_e)}{N} = \frac{(t - t_e)CP_e}{X_e} = \frac{X}{X_e}P_e\,,$$

$$\bar{P} = \frac{X}{X_e}P_e = P_e + \frac{u(t - t_e)CP_e}{CX_e} + \frac{at_e(t - t_e)CP_e}{CX_e} +$$
$$+ \frac{\frac{1}{2}a(t - t_e)^2CP_e}{CX_e}\,,$$

$$\bar{P} = P_e + \frac{u}{C}\frac{X}{X_e}P_e + \frac{at_e}{C}\frac{X}{X_e}P_e + \frac{1}{2}\frac{a(t - t_e)}{C}\frac{X}{X_e}P_e\,.$$

For N signals in the time interval $(t - t_e)$, we can write

$$(t - t_e) = P_iN + \frac{1}{2}\dot{P}P_iN^2,$$

where P_i is the initial period. Hence

$$\bar{P} = \frac{t - t_e}{N} = P_i + \frac{1}{2}\dot{P}P_iN\,.$$

Comparing this with

$$\bar{P} = P_e + \frac{u}{C}\frac{X}{X_e}P_e + \frac{at_e}{C}\frac{X}{X_e}P_e\left[1 + \frac{1}{2}\frac{t - t_e}{t_e}\right]$$

we derive

$$\bar{P} = P_i + \frac{at_e}{C}\frac{X}{X_e}P_e\left[1 + \frac{1}{2}\frac{(t - t_e)}{t_e}\right]$$

as $P_i = P_e/(1 - u/C)$. Hence $\frac{1}{2}\dot{P}N \approx \frac{at_e}{C}\left[1 + \frac{1}{2}\frac{(t - t_e)}{t_e}\right]$ or

$$\dot{P} = \frac{2at_e}{CN}\left[1 + \frac{1}{2}\frac{t - t_e}{t_e}\right] = \frac{2at_e(CP_e)}{CX_e}\left[1 + \frac{1}{2}\frac{t - t_e}{t_e}\right].$$

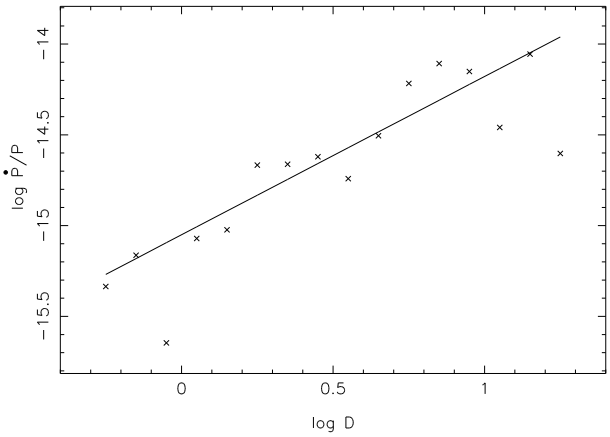

Fig. 2: $\log \dot{P}/P$ plotted as a function of $\log \mathrm{D}$.

As $|X_e| = |u|t_e + \frac{1}{2}at_e^2$,

$$\dot{P} \approx \frac{2a}{|u|} + \frac{aP_e}{C}\,.$$

The second term on the right hand side of the above equation is the Shklovski's [2] solution which is u/C times smaller than the first term

$$\dot{P} = \frac{2at_e}{X_e}P_e\Big(1 + \frac{u}{C}\Big) = \frac{2at_e}{|u|}\Big(1 + \frac{u}{C}\Big) \approx \frac{2P_e}{t_e}\Big(1 + \frac{u}{C}\Big)\,.$$

The acceleration a due to transverse component of velocity is always positive and hence $\dot{P}$ will be positive even when the observer is moving toward the emitter at an angle α less than 90°.

3 The period derivatives of pulsars

If V_τ is the relative transverse velocity between the Sun and the Pulsar, then the relative acceleration is V_τ^2/d. As $\sqrt{2}d/V_\tau = t$ is the relative time of free fall over $\frac{\pi}{2}$ radians, we can write $\dot{P} = 2P_e/t = \frac{1}{2}V_\tau/d = \frac{\pi}{2}V_\tau/d$. This is of the order of the average observed period derivate of pulsars. If we assume that an inverse square law is applicable the average observed period derivatives of pulsars must increase as a function of distance from the Sun.

Figure 2, is a plot of $\log \dot{P}/P$ versus $\log \mathrm{D}$ of all pulsars in the period range 0.1 to 3 seconds and in the distance range $\log \mathrm{D} = -0.3$ to $+1.3$. The data is taken from Taylor et al. [3]. Table 1 gives the values of $\log \dot{P}/P$ averaged in different distance bins. N is the number of pulsars in each bin. Leaving the two points that are slightly further away from the mean relationship, the best fit straight line $Y = mX + k$ gives a slope of 0.872 and the constant as -15.0506. The constant k gives the value of $\sqrt{2}V_\tau/d$ at an average distance of the Sun. In short we expect that this should more or less correspond with the accepted values for the Sun's motion around the galactic center. Taking $V_\odot = 210$ km×s^{-1} and $d_\odot = 8$ kpc , we get $\sqrt{2}V_\odot/d_\odot = 1.24\times10^{-15}$ and the value from k is 1.12×10^{-15}.

log D	log $\dot{P}/P$	N
−0.25	−15.3353	10
−0.15	−15.1632	17
−0.05	−15.6460	12
0.05	−15.0711	16
0.15	−15.0231	27
0.25	−14.6667	38
0.35	−14.6620	46
0.45	−14.6205	51
0.55	−14.7416	78
0.65	−14.5052	66
0.75	−14.2172	49
0.85	−14.1072	51
0.95	−14.1509	30
1.05	−14.4594	12
1.15	−14.0552	10
1.25	−14.6030	3

Table 1: log $\dot{P}/P$ as a function of log D and the number of pulsars in each bin.

This is given more as an illustration of the application of this effect. The real (true) spin down rates of the large majority of pulsars, may be much lower than the canonical value of 3×10^{-15}. Hence the average observed period derivatives of pulsars is due to the differential galactic rotation effect. This result is fully in conformity with the observed relationship between transverse motion and $\dot{P}$ by Anderson and Lyne [4] and Cordes [5] and that the correlation found by them cannot be accounted for purely by selection effects alone (Stollman and Van den Heuvel [6]).

4 Bending of light

As the photon angle accelerates in the gravitational field of the Sun, the angle $\Delta\phi$ at which the light from the limb of the Sun would be seen to meet the observer is the instantaneous value of the second derivative of α with respect to time at the distance of the earth. This is given by

$$\Delta\phi = \frac{\pi}{2}\,\frac{d^2\alpha}{dt^2}\,t\,(1s) = \frac{\pi}{2}\,\frac{2CV_\tau}{d^2}\,(1s)\,\frac{d}{C} = \frac{\pi V_\tau\,(1s)}{d}\,,$$

where $\frac{\pi}{2}$ is introduced as a scale factor to relate the free-fall height to the actual arc length that an object traverses in a gravitational field; V_τ is the relative transverse velocity and d is the distance between the Sun and the Earth. This will result in an observed bending of light as

$$\Delta\phi = \frac{\pi V_\tau\,(1s)}{d} = \frac{407\pi}{1.5\times10^8 \text{ radians}} = 1.76 \text{ arc sec.}$$

5 Precession of Mercury's orbit

The arrival time acceleration when not taken into account will appear as though the orbit is precessing. A good example is the precesion of Mercury's orbit. Treating Mercury as a rotating object with a period equal to its synodic period $P_s = 115.88$ days,

$$\Delta\omega = \frac{\pi V_\tau}{d} = \frac{3.14\times18.1}{0.917\times10^8} = 61.98\times10^{-8} \text{ rad},$$

which is the change per synodic period. Hence,

$$\frac{\Delta\omega}{P_s} = \frac{61.98\times10^{-8}}{115.88\times86400} = \\ = 6.19\times10^{-14} \text{ rad}\times\text{s}^{-1} = 40 \text{ arc sec/century}.$$

6 Binary pulsars

In the case of a binary pulsar, the relative transverse motion of the common centre of mass of the binary system and the Sun will lead to a secular increase in the period. Over and above this effect, the acceleration of the pulsar in the gravitational field of its companion will lead to further periodic deceleration in the arrival times. In analogy with Mercury, we can therefore expect a similar phenomenon in the case of binary pulsars. That is, the orbit might appear to precess if the arrival time delays caused by the pulsar acceleration in the gravitational field of the companion is not taken into account. The apparent precesion per pulse period P_e will be (Rajamohan and Satya Narayanan [1])

$$\Delta\omega = \frac{\pi}{4}\,\frac{V^2}{a^2}\,P_e^2\,.$$

Approximating the orbit to be circular and expressing the above equation in terms of well determined quantities,

$$\Delta\omega \approx \pi^3 P_e^2/P_b^2\,,$$

P_b is the orbital period and a is the semi-major axis of the orbit. Introducing appropriate values for PSR1913+16, we find

$$\Delta\omega \approx 1.386\times10^{-10} \text{ rad/pulse} \approx 4.24^\circ \text{ yr}^{-1},$$

which is in very good agreement with the observed value of 4.2261° yr^{-1} by Taylor and Weisberg [7]. For PSR1534+12 we find

$$\Delta\omega \approx 0.337\times10^{-10} \text{ rad/pulse} \approx 1.61^\circ \text{ yr}^{-1},$$

while the observed value is 1.756° yr^{-1} (Taylor et al. [8]).

Acknowledgements

We are thankful to Dr. Baba Verghese for his help in producing the Table and the Figures in this paper.

Submitted on February 02, 2007
Accepted on February 06, 2007

References

1. Rajamohan R. and Satya Narayanan A. *Speculations in Science and Technology*, 1995, v. 18, 51.
2. Shklovski I. S. *Soviet Astron.*, 1969, v. 13, 562.
3. Taylor J. H., Manchester R. N. and Lyne A. G. Catalogue of 706 pulsars, 1995 (http://pulsar.princeton.edu).
4. Anderson B. and Lyne A. G. *Nature*, 1983, v. 303, 597.
5. Cordes J. M. *Astrophys. J.*, 1986, v. 311, 183.
6. Stollman G. M. and Van den Heuvel E. P. J. *Astron. & Astrophys*, 1986, v. 162, 87.
7. Taylor J. H. and Weisberg J. M. *Astroph. J.*, 1982, v. 253, 908.
8. Taylor J. H., Wolszan A., Damour T. and Weisberg J. M. *Nature*, 1992, v. 355, 132.

Gravitation on a Spherically Symmetric Metric Manifold

Stephen J. Crothers

Queensland, Australia

E-mail: thenarmis@yahoo.com

The usual interpretations of solutions for Einstein's gravitational field satisfying the spherically symmetric condition contain anomalies that are not mathematically permissible. It is shown herein that the usual solutions must be modified to account for the intrinsic geometry associated with the relevant line elements.

1 Introduction

The standard interpretation of spherically symmetric line elements for Einstein's gravitational field has not taken into account the fundamental geometrical features of spherical symmetry about an arbitrary point in a metric manifold. This has led to numerous misconceptions as to distance and radius that have spawned erroneous theoretical notions.

The nature of spherical symmetry about an arbitrary point in a three dimensional metric manifold is explained herein and applied to Einstein's gravitational field.

It is plainly evident, *res ipsa locquitur*, that the standard claims for black holes and Big Bang cosmology are not consistent with elementary differential geometry and are consequently inconsistent with General Relativity.

2 Spherical symmetry of three-dimensional metrics

Denote ordinary Efcleethean* 3-space by $\mathbf{E}^3$. Let $\mathbf{M}^3$ be a 3-dimensional metric manifold. Let there be a one-to-one correspondence between all points of $\mathbf{E}^3$ and $\mathbf{M}^3$. Let the point $O \in \mathbf{E}^3$ and the corresponding point in $\mathbf{M}^3$ be O'. Then a point transformation T of $\mathbf{E}^3$ into itself gives rise to a corresponding point transformation of $\mathbf{M}^3$ into itself.

A rigid motion in a metric manifold is a motion that leaves the metric $d\ell'^2$ unchanged. Thus, a rigid motion changes geodesics into geodesics. The metric manifold $\mathbf{M}^3$ possesses spherical symmetry around any one of its points O' if each of the ∞^3 rigid rotations in $\mathbf{E}^3$ around the corresponding arbitrary point O determines a rigid motion in $\mathbf{M}^3$.

The coefficients of $d\ell'^2$ of $\mathbf{M}^3$ constitute a metric tensor and are naturally assumed to be regular in the region around every point in $\mathbf{M}^3$, except possibly at an arbitrary point, the centre of spherical symmetry $O' \in \mathbf{M}^3$.

Let a ray i emanate from an arbitrary point $O \in \mathbf{E}^3$. There is then a corresponding geodesic $i' \in \mathbf{M}^3$ issuing from the corresponding point $O' \in \mathbf{M}^3$. Let P be any point on i other than O. There corresponds a point P' on $i' \in \mathbf{M}^3$ different to O'. Let g' be a geodesic in $\mathbf{M}^3$ that is tangential to i' at P'.

Taking i as the axis of ∞^1 rotations in $\mathbf{E}^3$, there corresponds ∞^1 rigid motions in $\mathbf{M}^3$ that leaves only all the points on i' unchanged. If g' is distinct from i', then the ∞^1 rigid rotations in $\mathbf{E}^3$ about i would cause g' to occupy an infinity of positions in $\mathbf{M}^3$ wherein g' has for each position the property of being tangential to i' at P' in the same direction, which is impossible. Hence, g' coincides with i'.

Thus, given a spherically symmetric surface Σ in $\mathbf{E}^3$ with centre of symmetry at some arbitrary point $O \in \mathbf{E}^3$, there corresponds a spherically symmetric geodesic surface Σ' in $\mathbf{M}^3$ with centre of symmetry at the corresponding point $O' \in \mathbf{M}^3$.

Let Q be a point in $\Sigma \in \mathbf{E}^3$ and Q' the corresponding point in $\Sigma' \in \mathbf{M}^3$. Let $d\sigma$ be a generic line element in Σ issuing from Q. The corresponding generic line element $d\sigma' \in \Sigma'$ issues from the point Q'. Let Σ be described in the usual spherical-polar coordinates r, θ, φ. Then

$$d\sigma^2 = r^2(d\theta^2 + \sin^2\theta\, d\varphi^2), \qquad (1)$$

$$r = |\overline{OQ}|.$$

Clearly, if r, θ, φ are known, Q is determined and hence also Q' in Σ'. Therefore, θ and φ can be considered to be curvilinear coordinates for Q' in Σ' and the line element $d\sigma' \in \Sigma'$ will also be represented by a quadratic form similar to (1). To determine $d\sigma'$, consider two elementary arcs of equal length, $d\sigma_1$ and $d\sigma_2$ in Σ, drawn from the point Q in different directions. Then the homologous arcs in Σ' will be $d\sigma'_1$ and $d\sigma'_2$, drawn in different directions from the corresponding point Q'. Now $d\sigma_1$ and $d\sigma_2$ can be obtained from one another by a rotation about the axis $\overline{OQ}$ in $\mathbf{E}^3$, and so $d\sigma'_1$ and $d\sigma'_2$ can be obtained from one another by a rigid motion in $\mathbf{M}^3$, and are therefore also of equal length, since the metric is unchanged by such a motion. It therefore follows that the ratio $\frac{d\sigma'}{d\sigma}$ is the same for the two different directions irrespective of $d\theta$ and $d\varphi$, and so the foregoing ratio is a function of position, i.e. of r, θ, φ. But Q is an arbitrary point in Σ, and so $\frac{d\sigma'}{d\sigma}$ must have the same ratio for any corresponding points Q and Q'. Therefore, $\frac{d\sigma'}{d\sigma}$ is a function of r alone, thus

$$\frac{d\sigma'}{d\sigma} = H(r),$$

and so

$$d\sigma'^2 = H^2(r)\, d\sigma^2 = H^2(r) r^2 (d\theta^2 + \sin^2\theta\, d\varphi^2), \qquad (2)$$

*For the geometry due to Efcleethees, usually and abominably rendered as Euclid.

where $H(r)$ is *a priori* unknown. For convenience set $R_c = H(r) = H(r)r$, so that (2) becomes

$$d\sigma'^2 = R_c^2(d\theta^2 + \sin^2\theta\, d\varphi^2), \tag{3}$$

where R_c is a quantity associated with $\mathbf{M}^3$. Comparing (3) with (1) it is apparent that R_c is to be rightly interpreted in terms of the Gaussian curvature K at the point Q', i.e. in terms of the relation $K = \frac{1}{R_c^2}$ since the Gaussian curvature of (1) is $K = \frac{1}{r^2}$. This is an intrinsic property of all line elements of the form (3) [1, 2]. Accordingly, R_c can be regarded as a radius of curvature. Therefore, in (1) the radius of curvature is $R_c = r$. Moreover, owing to spherical symmetry, all points in the corresponding surfaces Σ and Σ' have constant Gaussian curvature relevant to their respective manifolds and centres of symmetry, so that all points in the respective surfaces are umbilic.

Let the element of radial distance from $O \in \mathbf{E}^3$ be dr. Clearly, the radial lines issuing from O cut the surface Σ orthogonally. Combining this with (1) by the theorem of Pythagoras gives the line element in $\mathbf{E}^3$

$$d\ell^2 = dr^2 + r^2(d\theta^2 + \sin^2\theta\, d\varphi^2). \tag{4}$$

Let the corresponding radial geodesic from the point $O' \in \mathbf{M}^3$ be dg. Clearly the radial geodesics issuing from O' cut the geodesic surface Σ' orthogonally. Combining this with (3) by the theorem of Pythagoras gives the line element in $\mathbf{M}^3$ as,

$$d\ell'^2 = dg^2 + R_c^2(d\theta^2 + \sin^2\theta\, d\varphi^2), \tag{5}$$

where dg is, by spherical symmetry, also a function only of R_c. Set $dg = \sqrt{B(R_c)}dR_c$, so that (5) becomes

$$d\ell'^2 = B(R_c)dR_c^2 + R_c^2(d\theta^2 + \sin^2\theta\, d\varphi^2), \tag{6}$$

where $B(R_c)$ is an *a priori* unknown function.

Setting $dR_p = \sqrt{B(R_c)}dR_c$ carries (6) into

$$d\ell'^2 = dR_p^2 + R_c^2(d\theta^2 + \sin^2\theta\, d\varphi^2). \tag{7}$$

Expression (6) is the most general for a metric manifold $\mathbf{M}^3$ having spherical symmetry about some arbitrary point $O' \in \mathbf{M}^3$ [1, 3].

Considering (4), the distance $R_p = |\overline{OQ}|$ from the point at the centre of spherical symmetry O to a point $Q \in \Sigma$, is given by

$$R_p = \int_0^r dr = r = R_c\,.$$

Call R_p the proper radius. Consequently, in the case of $\mathbf{E}^3$, R_p and R_c are identical, and so the Gaussian curvature at any point in $\mathbf{E}^3$ can be associated with R_p, the radial distance between the centre of spherical symmetry at the point $O \in \mathbf{E}^3$ and the point $Q \in \Sigma$. Thus, in this case, we have $K = \frac{1}{R_c^2} = \frac{1}{R_p^2} = \frac{1}{r^2}$. However, this is not a general relation, since according to (6) and (7), in the case of $\mathbf{M}^3$, the radial geodesic distance from the centre of spherical symmetry at the point $O' \in \mathbf{M}^3$ is not given by the radius of curvature, but by

$$R_p = \int_0^{R_p} dR_p = \int_{R_c(0)}^{R_c(r)} \sqrt{B(R_c(r))}\, dR_c(r) = \int_0^r \sqrt{B(R_c(r))}\, \frac{dR_c(r)}{dr}\, dr\,,$$

where $R_c(0)$ is *a priori* unknown owing to the fact that $R_c(r)$ is *a priori* unknown. One cannot simply assume that because $0 \leqslant r < \infty$ in (4) that it must follow that in (6) and (7) $0 \leqslant R_c(r) < \infty$. In other words, one cannot simply assume that $R_c(0) = 0$. Furthermore, it is evident from (6) and (7) that R_p determines the radial geodesic distance from the centre of spherical symmetry at the arbitrary point O' in $\mathbf{M}^3$ (and correspondingly so from O in $\mathbf{E}^3$) to another point in $\mathbf{M}^3$. Clearly, R_c does not in general render the radial geodesic length from the centre of spherical symmetry to some other point in a metric manifold. Only in the particular case of $\mathbf{E}^3$ does R_c render both the Gaussian curvature and the radial distance from the centre of spherical symmetry, owing to the fact that R_p and R_c are identical in that special case.

It should also be noted that in writing expressions (4) and (5) it is implicit that $O \in \mathbf{E}^3$ is defined as being located at the origin of the coordinate system of (4), i.e. O is located where $r = 0$, and by correspondence O' is defined as being located at the origin of the coordinate system of (5), i.e. using (7), $O' \in \mathbf{M}^3$ is located where $R_p = 0$. Furthermore, since it is well known that a geometry is completely determined by the form of the line element describing it [4], expressions (4) and (6) share the very same fundamental geometry because they are line elements of the same form.

Expression (6) plays an important rôle in Einstein's gravitational field.

3 The standard solution

The standard solution in the case of the static vacuum field (i.e. no deformation of the space) of a single gravitating body, satisfying Einstein's field equations $R_{\mu\nu} = 0$, is (using $G = c = 1$),

$$ds^2 = \left(1 - \frac{2m}{r}\right) dt^2 - \left(1 - \frac{2m}{r}\right)^{-1} dr^2 - r^2(d\theta^2 + \sin^2\theta\, d\varphi^2)\,, \tag{8}$$

where m is allegedly the mass causing the field, and upon which it is routinely claimed that $2m < r < \infty$ is an exterior region and $0 < r < 2m$ is an interior region. Notwithstanding the inequalities it is routinely allowed that $r = 2m$ and $r = 0$ by which it is also routinely claimed that $r = 2m$ marks a "removable" or "coordinate" singularity and that $r = 0$ marks a "true" or "physical" singularity [5].

The standard treatment of the foregoing line-element proceeds from simple inspection of (8) and thereby upon the following assumptions:

(a) that there is only one radial quantity defined on (8);

(b) that r can approach zero, even though the line-element (8) is singular at $r = 2m$;

(c) that r is the radial quantity in (8) ($r = 2m$ is even routinely called the "Schwarzschild radius" [5]).

With these unstated assumptions, but assumptions nonetheless, it is usual procedure to develop and treat of black holes. However, all three assumptions are demonstrably false at an elementary level.

4 That assumption (a) is false

Consider standard Minkowski space (using $c = G = 1$) described by

$$ds^2 = dt^2 - dr^2 - r^2 d\Omega^2, \qquad (9)$$
$$0 \leqslant r < \infty\,,$$

where $d\Omega^2 = d\theta^2 + \sin^2\theta\, d\varphi^2$. Comparing (9) with (4) it is easily seen that the spatial components of (9) constitute a line element of $\mathbf{E}^3$, with the point at the centre of spherical symmetry at $r_0 = 0$, coincident with the origin of the coordinate system.

In relation to (9) the *calculated* proper radius R_p of the sphere in $\mathbf{E}^3$ is,

$$R_p = \int_0^r dr = r\,, \qquad (10)$$

and the radius of curvature R_c is

$$R_c = r = R_p\,. \qquad (11)$$

Calculate the surface area of the sphere:

$$A = \int_0^{2\pi}\int_0^{\pi} r^2 \sin\theta\, d\theta\, d\varphi = 4\pi r^2 = 4\pi R_p^2 = 4\pi R_c^2\,. \qquad (12)$$

Calculate the volume of the sphere:

$$V = \int_0^{2\pi}\int_0^{\pi}\int_0^{r} r^2 \sin\theta\, dr\, d\theta\, d\varphi = \frac{4}{3}\pi r^3 = \frac{4}{3}\pi R_p^3 = \frac{4}{3}\pi R_c^3\,. \qquad (13)$$

Then for (9), according to (10) and (11),

$$R_p = r = R_c\,. \qquad (14)$$

Thus, for Minkowski space, R_p and R_c are identical. This is because Minkowski space is pseudo-Efcleethean.

Now comparing (8) with (6) and (7) is is easily seen that the spatial components of (8) constitute a spherically symmetric metric manifold $\mathbf{M}^3$ described by

$$d\ell'^2 = \left(1 - \frac{2m}{r}\right)^{-1} dr^2 + r^2 d\Omega^2,$$

and which is therefore in one-to-one correspondence with $\mathbf{E}^3$. Then for (8),

$$R_c = r\,,$$
$$R_p = \int \sqrt{\frac{r}{r-2m}}\, dr \neq r = R_c\,.$$

Hence, $R_P \neq R_c$ in (8) in general. This is because (8) is non-Efcleethean (it is pseudo-Riemannian). Thus, assumption (a) is false.

5 That assumption (b) is false

On (8),

$$R_p = R_p(r) = \int \sqrt{\frac{r}{r-2m}}\, dr = \\ = \sqrt{r\,(r-2m)} + 2m \ln\left|\sqrt{r} + \sqrt{r-2m}\right| + K, \qquad (15)$$

where K is a constant of integration.

For some r_0, $R_p(r_0) = 0$, where r_0 is the corresponding point at the centre of spherical symmetry in $\mathbf{E}^3$ to be determined from (15). According to (15), $R_p(r_0) = 0$ when $r = r_0 = 2m$ and $K = -m \ln 2m$. Hence,

$$R_p(r) = \sqrt{r\,(r-2m)} + 2m \ln\left(\frac{\sqrt{r} + \sqrt{r-2m}}{\sqrt{2m}}\right). \qquad (16)$$

Therefore, $2m < r < \infty \Rightarrow 0 < R_p < \infty$, where $R_c = r$. The inequality is required to maintain Lorentz signature, since the line-element is undefined at $r_0 = 2m$, which is the only possible singularity on the line element. Thus, assumption (b) is false.

It follows that the centre of spherical symmetry of $\mathbf{E}^3$, in relation to (8), is located not at the point $r_0 = 0$ in $\mathbf{E}^3$ as usually assumed according to (9), but at the point $r_0 = 2m$, which corresponds to the point $R_p(r_0 = 2m) = 0$ in the metric manifold $\mathbf{M}^3$ that is described by the spatial part of (8). In other words, the point at the centre of spherical symmetry in $\mathbf{E}^3$ in relation to (8) is located at any point Q in the spherical surface Σ for which the radial distance from the centre of the coordinate system at $r = 0$ is $r = 2m$, owing to the one-to-one correspondence between all points of $\mathbf{E}^3$ and $\mathbf{M}^3$. It follows that (8) is not a generalisation of (9), as usually claimed. The manifold $\mathbf{E}^3$ of Minkowski space corresponding to the metric manifold $\mathbf{M}^3$ of (8) is not described by (9), because the point at the centre of spherical symmetry of (9), $r_0 = 0$, does not coincide with that required by (15) and (16), namely $r_0 = 2m$.

In consequence of the foregoing it is plain that the expression (8) is not general in relation to (9) and the line element (8) is not general in relation to the form (6). This is due to the incorrect way in which (8) is usually derived from (9), as pointed out in [6, 7, 8]. The standard derivation of (8) from (9) unwittingly shifts the point at the centre of spheriacly symmetry for the $\mathbf{E}^3$ of Minkowski space from $r_0 = 0$

to $r_0 = 2m$, with the consequence that the resulting line element (8) is misinterpreted in relation to $r = 0$ in the $\mathbf{E^3}$ of Minkowski space as described by (9). This unrecognised shift actually associates the point $r_0 = 2m \in \mathbf{E^3}$ with the point $R_p(2m) = 0$ in the $\mathbf{M^3}$ of the gravitational field. The usual analysis then incorrectly associates $R_p = 0$ with $r_0 = 0$ instead of with the correct $r_0 = 2m$, thereby conjuring up a so-called "interior", as typically alleged in [5], that actually has no relevance to the problem — a completely meaningless manifold that has nothing to do with the gravitational field and so is disjoint from the latter, as also noted in [6, 9, 10, 11]. The point at the centre of spherical symmetry for Einstein's gravitational field is $R_p = 0$ and is also the origin of the coordinate system for the gravitational field. Thus the notion of an "interior" manifold under some other coordinate patch (such as the Kruskal-Szekeres coordinates) is patently false. This is clarified in the next section.

6 That assumption (c) is false

Generalise (9) so that the centre of a sphere can be located anywhere in Minkowski space, relative to the origin of the coordinate system at $r = 0$, thus

$$\begin{aligned} ds^2 &= dt^2 - \left(d\,|r - r_0|\right)^2 - |r - r_0|^2\, d\Omega^2 = \\ &= dt^2 - \frac{(r - r_0)^2}{|r - r_0|^2} dr^2 - |r - r_0|^2\, d\Omega^2 = \\ &= dt^2 - dr^2 - |r - r_0|^2\, d\Omega^2, \end{aligned} \tag{17}$$

$$0 \leqslant |r - r_0| < \infty\,,$$

which is well-defined for all real r. The value of r_0 is arbitrary. The spatial components of (17) describe a sphere of radius $D = |r - r_0|$ centred at some *point* r_0 on a common radial line through r and the origin of coordinates at $r = 0$ (i.e. centred at the *point* of orthogonal intersection of the common radial line with the spherical surface $r = r_0$). Thus, the arbitrary point r_0 is the centre of spherical symmetry in $\mathbf{E^3}$ for (17) in relation to the problem of Einstein's gravitational field, the spatial components of which is a spherically symmetric metric manifold $\mathbf{M^3}$ with line element of the form (6) and corresponding centre of spherical symmetry at the point $R_p(r_0) = 0 \,\forall\, r_0$. If $r_0 = 0$, (9) is recovered from (17). One does not need to make $r_0 = 0$ so that the centre of spherical symmetry in $\mathbf{E^3}$, associated with the metric manifold $\mathbf{M^3}$ of Einstein's gravitational field, coincides with the origin of the coordinate system itself, at $r = 0$. Any point in $\mathbf{E^3}$, relative to the coordinate system attached to the arbitrary point at which $r = 0$, can be regarded as a point at the centre of spherical symmetry in relation to Einstein's gravitational field. Although it is perhaps desirable to make the point $r_0 = 0$ the centre of spherical symmetry of $\mathbf{E^3}$ correspond to the point $R_p = 0$ at the centre of symmetry of $\mathbf{M^3}$ of the gravitational field, to simplify matters somewhat, this has not been done in the usual analysis of Einstein's gravitational field, despite appearances, and in consequence thereof false conclusions have been drawn owing to this fact going unrecognised in the main.

Now on (17),

$$\begin{aligned} R_c &= |r - r_0|\,, \\ R_p &= \int_0^{|r-r_0|} d\,|r - r_0| = \int_{r_0}^{r} \frac{(r - r_0)}{|r - r_0|} dr = |r - r_0| \equiv R_c, \end{aligned} \tag{18}$$

and so $R_p \equiv R_c$ on (17), since (17) is pseudo-Efcleethean. Setting $D = |r - r_0|$ for convenience, generalise (17) thus,

$$ds^2 = A\big(C(D)\big)\, dt^2 - B\big(C(D)\big)\, d\sqrt{C(D)}^{\,2} - C(D)\, d\Omega^2, \tag{19}$$

where $A\big(C(D)\big)$, $B\big(C(D)\big)$, $C(D) > 0$. Then for $R_{\mu\nu} = 0$, metric (19) has the solution,

$$\begin{aligned} ds^2 = &\left(1 - \frac{\alpha}{\sqrt{C(D)}}\right) dt^2 - \\ &- \frac{1}{1 - \frac{\alpha}{\sqrt{C(D)}}}\, d\sqrt{C(D)}^{\,2} - C(D)\, d\Omega^2, \end{aligned} \tag{20}$$

where α is a function of the mass generating the gravitational field [3, 6, 7, 9]. Then for (20),

$$\begin{aligned} R_c &= R_c(D) = \sqrt{C(D)}, \\ R_p &= R_p(D) = \int \sqrt{\frac{\sqrt{C(D)}}{\sqrt{C(D)} - \alpha}}\, d\sqrt{C(D)} = \\ &= \int \sqrt{\frac{R_c(D)}{R_c(D) - \alpha}}\, dR_c(D) = \sqrt{R_c(D)\big(R_c(D) - \alpha\big)} + \\ &+ \alpha \ln\left(\frac{\sqrt{R_c(D)} + \sqrt{R_c(D) - \alpha}}{\sqrt{\alpha}}\right), \end{aligned} \tag{21}$$

where $R_c(D) \equiv R_c\left(|r - r_0|\right) = R_c(r)$. Clearly r is a parameter, located in Minkowski space according to (17).

Now $r = r_0 \Rightarrow D = 0$, and so by (21), $R_c(D = 0) = \alpha$ and $R_p(D = 0) = 0$. One must ascertain the admissible form of $R_c(D)$ subject to the conditions $R_c(D = 0) = \alpha$ and $R_p(D = 0) = 0$ and $dR_c(D)/dD > 0$ [6, 7], along with the requirements that $R_c(D)$ must produce (8) from (20) at will, must yield Schwarzschild's [12] original solution at will (which is *not* the line element (8) with r down to zero), must produce Brillouin's [13] solution at will, must produce Droste's [14] solution at will, and must yield an infinite number of equivalent metrics [3]. The only admissible form satisfying these conditions is [7],

$$R_c = R_c(D) = \left(D^n + \alpha^n\right)^{\frac{1}{n}} \equiv \left(|r - r_0|^n + \alpha^n\right)^{\frac{1}{n}} = R_c(r), \tag{22}$$

$$D > 0, \quad r \in \Re, \quad n \in \Re^+, \quad r \neq r_0,$$

where r_0 and n are entirely arbitrary constants.

Choosing $r_0 = 0$, $r > 0$, $n = 3$,

$$R_c(r) = \left(r^3 + \alpha^3\right)^{\frac{1}{3}}, \tag{23}$$

and putting (23) into (20) gives Schwarzschild's original solution, defined on $0 < r < \infty$.

Choosing $r_0 = 0$, $r > 0$, $n = 1$,

$$R_c(r) = r + \alpha, \tag{24}$$

and putting (24) into (20) gives Marcel Brillouin's solution, defined on $0 < r < \infty$.

Choosing $r_0 = \alpha$, $r > \alpha$, $n = 1$,

$$R_c(r) = (r - \alpha) + \alpha = r, \tag{25}$$

and putting (25) into (20) gives line element (8), but defined on $\alpha < r < \infty$, as found by Johannes Droste in May 1916. Note that according to (25), and in general by (22), r is not a radial quantity in the gravitational field, because $R_c(r) = (r-\alpha)+\alpha = D+\alpha$ is really the radius of curvature in (8), defined for $0 < D < \infty$.

Thus, assumption (c) is false.

It is clear from this that the usual line element (8) is a restricted form of (22), and by (22), with $r_0 = \alpha = 2m$, $n = 1$ gives $R_c = |r - 2m| + 2m$, which is well defined on $-\infty < r < \infty$, i.e. on $0 \leqslant D < \infty$, so that when $r = 0$, $R_c(0) = 4m$ and $R_P(0) > 0$. In the limiting case of $r = 2m$, then $R_c(2m) = 2m$ and $R_p(2m) = 0$. The latter two relationships hold for any value of r_0.

Thus, if one insists that $r_0 = 0$ to match (9), it follows from (22) that,

$$R_c = \left(|r|^n + \alpha^n\right)^{\frac{1}{n}},$$

and if one also insists that $r > 0$, then

$$R_c = \left(r^n + \alpha^n\right)^{\frac{1}{n}}, \tag{26}$$

and for $n = 1$,

$$R_c = r + \alpha,$$

which is the simplest expression for R_c in (20) [6, 7, 13].

Expression (26) has the centre of spherical symmetry of $\mathbf{E}^3$ located at the point $r_0 = 0 \,\forall\, n \in \Re^+$, corresponding to the centre of spherical symmetry of $\mathbf{M}^3$ for Einstein's gravitational field at the point $R_p(0) = 0 \;\forall\; n \in \Re^+$. Then taking $\alpha = 2m$ it follows that $R_p(0) = 0$ and $R_c(0) = \alpha = 2m$ for all values of n.

There is no such thing as an interior solution for the line element (20) and consequently there is no such thing as an interior solution on (8), and so there can be no black holes.

7 That the manifold is inextendable

That the singularity at $R_p(r_0) \equiv 0$ is insurmountable is clear by the following ratio,

$$\lim_{r \to r_0^{\pm}} \frac{2\pi R_c(r)}{R_p(r)} = \lim_{r \to r_0^{\pm}} \frac{2\pi \left(|r - r_0|^n + \alpha^n\right)^{\frac{1}{n}}}{R_p(r)} = \infty,$$

since $R_p(r_0) = 0$ and $R_c(r_0) = \alpha$ are invariant.

Hagihara [15] has shown that all radial geodesics that do not run into the boundary at $R_c(r_0) = \alpha$ (i.e. that do not run into the boundary at $R_p(r_0) = 0$) are geodesically complete.

Doughty [16] has shown that the acceleration a of a test particle approaching the centre of mass at $R_p(r_0) = 0$ is given by,

$$a = \frac{\sqrt{-g_{00}}\left(-g^{11}\right)|g_{00,1}|}{2g_{00}}.$$

By (20) and (22), this gives,

$$a = \frac{\alpha}{2R_c^{\frac{3}{2}}\sqrt{R_c(r) - \alpha}}.$$

Then clearly as $r \to r_0^{\pm}$, $a \to \infty$, independently of the value of r_0.

J. Smoller and B. Temple [10] have shown that the Oppenheimer-Volkoff equations do not permit gravitational collapse to form a black hole and that the alleged interior of the Schwarzschild spacetime (i.e. $0 \leqslant R_c(r) \leqslant \alpha$) is therefore *disconnected* from Schwarzschild spacetime and so does not form part of the solution space.

N. Stavroulakis [17, 18, 19, 20] has shown that an object cannot undergo gravitational collapse into a singularity, or to form a black hole.

Suppose $0 \leqslant \sqrt{C(D(r))} < \alpha$. Then (20) becomes

$$ds^2 = -\left(\frac{\alpha}{\sqrt{C}} - 1\right)dt^2 + \left(\frac{\alpha}{\sqrt{C}} - 1\right)^{-1} d\sqrt{C}^2 - C\left(d\theta^2 + \sin^2\theta\, d\varphi^2\right),$$

which shows that there is an interchange of time and length. To amplify this set $r = \bar{t}$ and $t = \bar{r}$. Then

$$ds^2 = \left(\frac{\alpha}{\sqrt{C}} - 1\right)^{-1} \frac{\dot{C}^2}{4C}\, d\bar{t}^2 - \left(\frac{\alpha}{\sqrt{C}} - 1\right) d\bar{r}^2 - C\left(d\theta^2 + \sin^2\theta\, d\varphi^2\right),$$

where $C = C(\bar{t})$ and the dot denotes $d/d\bar{t}$. This is a time dependent metric and therefore bears no relation to the problem of a static gravitational field.

Thus, the Schwarzschild manifold described by (20) with (22) (and hence (8)) is inextendable.

8 That the Riemann tensor scalar curvature invariant is everywhere finite

The Riemann tensor scalar curvature invariant (the Kretschmann scalar) is given by $f = R_{\mu\nu\rho\sigma}R^{\mu\nu\rho\sigma}$. In the general case of (20) with (22) this is

$$f = \frac{12\alpha^2}{R_c^6(r)} = \frac{12\alpha^2}{\left(|r - r_0|^n + \alpha^n\right)^{\frac{6}{n}}}.$$

A routine attempt to justify the standard assumptions on (8) is the *a posteriori* claim that the Kretschmann scalar

must be unbounded at a singularity [5, 21]. Nobody has ever offered a proof that General Relativity necessarily requires this. That this additional *ad hoc* assumption is false is clear from the following ratio,

$$f(r_0) = \frac{12\alpha^2}{\left(|r_0 - r_0|^n + \alpha^n\right)^{\frac{6}{n}}} = \frac{12}{\alpha^4} \ \forall \ r_0 \, .$$

In addition,

$$\lim_{r\to\pm\infty} \frac{12\alpha^2}{\left(|r - r_0|^n + \alpha^n\right)^{\frac{6}{n}}} = 0 \, ,$$

and so the Kretschmann scalar is finite everywhere.

9 That the Gaussian curvature is everywhere finite

The Gaussian curvature K of (20) is,

$$K = K\big(R_c(r)\big) = \frac{1}{R_c^2(r)} \, ,$$

where $R_c(r)$ is given by (22). Then,

$$K(r_0) = \frac{1}{\alpha^2} \ \forall \ r_0 \, ,$$

and

$$\lim_{r\to\pm\infty} K(r) = 0 \, ,$$

and so the Gaussian curvature is everywhere finite.

Furthermore,

$$\lim_{\alpha\to 0} \frac{1}{\alpha^2} = \infty,$$

since when $\alpha = 0$ there is no gravitational field and empty Minkowski space is recovered, wherein R_p and R_c are identical and $0 \leqslant R_p < \infty$. A centre of spherical symmetry in Minkowski space has an infinite Gaussian curvature because Minkowski space is pseudo-Efcleethean.

10 Conclusions

Using the spherical-polar coordinates, the general solution to $R_{\mu\nu} = 0$ is (20) with (22), which is well-defined on

$$-\infty < r_0 < \infty,$$

where r_0 is entirely arbitrary, and corresponds to

$$0 < R_p(r) < \infty, \quad \alpha < R_c(r) < \infty,$$

for the gravitational field. The only singularity that is possible occurs at $g_{00} = 0$. It is impossible to get $g_{11} = 0$ because there is no value of the parameter r by which this can be attained. No interior exists in relation to (20) with (22), which contain the usual metric (8) as a particular case.

The radius of curvature $R_c(r)$ does not in general determine the radial geodesic distance to the centre of spherical symmetry of Einstein's gravitational field and is only to be interpreted in relation to the Gaussian curvature by the equation $K = 1/R_c^2(r)$. The radial geodesic distance from the point at the centre of spherical symmetry to the spherical geodesic surface with Gaussian curvature $K = 1/R_c^2(r)$ is given by the proper radius, $R_p(R_c(r))$. The centre of spherical symmetry in the gravitational field is invariantly located at the point $R_p(r_0) = 0$.

Expression (20) with (22), and hence (8) describes only a centre of mass located at $R_p(r_0) = 0$ in the gravitational field, $\forall \ r_0$. As such it does not take into account the distribution of matter and energy in a gravitating body, since $\alpha(M)$ is indeterminable in this limited situation. One cannot generally just utilise a potential function in comparison with the Newtonian potential to determine α by the weak field limit because α is subject to the distribution of the matter of the source of the gravitational field. The value of α must be calculated from a line-element describing the interior of the gravitating body, satisfying $R_{\mu\nu} - \frac{1}{2} R g_{\mu\nu} = \kappa T_{\mu\nu} \neq 0$. The interior line element is necessarily different to the exterior line element of an object such as a star. A full description of the gravitational field of a star therefore requires two line elements [22, 23], not one as is routinely assumed, and when this is done, there are no singularities anywhere. The standard assumption that one line element is sufficient is false. Outside a star, (20) with (22) describes the gravitational field in relation to the centre of mass of the star, but α is nonetheless determined by the interior metric, which, in the case of the usual treatment of (8), has gone entirely unrecognised, so that the value of α is instead determined by a comparison with the Newtonian potential in a weak field limit.

Black holes are not predicted by General Relativity. The Kruskal-Szekeres coordinates do not describe a coordinate patch that covers a part of the gravitational manifold that is not otherwise covered - they describe a completely different pseudo-Riemannian manifold that has nothing to do with Einstein's gravitational field [6, 9, 11]. The manifold of Kruskal-Szekeres is not contained in the fundamental one-to-one correspondence between the $\mathbf{E}^3$ of Minkowski space and the $\mathbf{M}^3$ of Einstein's gravitational field, and is therefore a spurious augmentation.

It follows in similar fashion that expansion of the Universe and the Big Bang cosmology are inconsistent with General Relativity, as is easily demonstrated [24, 25].

Submitted on February 03, 2007
Accepted on February 09, 2007

References

1. Levi-Civita T. The Absolute Differential Calculus, Dover Publications Inc., New York, 1977.
2. O'Neill B. Semi-Riemannian geometry with applications to Relativity, Academic Press, San Deigo, 1983.
3. Eddington A. S. The mathematical theory of relativity. Cambridge University Press, Cambridge, 2nd edition, 1960.
4. Tolman R. C. Relativity, thermodynamics and cosmology. Dover Publications Inc., Mineola (NY), 1987.

5. Misner C. W., Thorne K. S. and Wheeler J. A. Gravitation. W. H. Freeman and Company, New York, 1973.
6. Abrams L. S. Black holes: the legacy of Hilbert's error. *Can. J. Phys.*, v. 67, 919, 1989; arXiv: gr-qc/0102055.
7. Crothers S. J. On the geometry of the general solution for the vacuum field of the point-mass. *Progress in Physics*, 2005, v. 2, 3–14.
8. Antoci S. David Hilbert and the origin of the "Schwarzschild" solution. arXiv: physics/0310104.
9. Loinger A. On black holes and gravitational waves. La Goliardica Paves, Pavia, 2002.
10. Smoller S. and Temple B. On the Oppenheimer-Volkoff equations in General Relativity. *Arch. Rational Mech. Anal.*, v. 142, 177–191, Springer-Verlag, 1998.
11. Crothers S. J. On the Regge-Wheeler tortoise and the Kruskal-Szekeres coordinates. *Progress in Physics*, 2006, v. 3, 30–34.
12. Schwarzschild K. On the gravitational field of a mass point according to Einstein's theory. *Sitzungsber. Preuss. Akad. Wiss., Phys. Math. Kl*., 1916, 189; arXiv: physics/9905030.
13. Brillouin M. The singular points of Einstein's Universe. *Journ. Phys. Radium*, 1923, v. 23, 43; accessed online on http://www.geocities.com/theometria/brillouin.pdf.
14. Droste J. The field of a single centre in Einstein's theory of gravitation, and the motion of a particle in that field. *Ned. Acad. Wet., S. A.*, 1917, v. 19, 197; accessed online on http://www.geocities.com/theometria/Droste.pdf.
15. Hagihara Y. *Jpn. J. Astron. Geophys.*, 1931, v. 8, 97.
16. Doughty N. *Am. J. Phys.*, 1981, v. 49, 720.
17. Stavroulakis N. A statical smooth extension of Schwarzschild's metric. *Lett. Nuovo Cim.*, Ser.2, 1974, v.11, No.8, 427–430; http://www.geocities.com/theometria/Stavroulakis-3.pdf.
18. Stavroulakis N. On the principles of General Relativity and the $\Theta(4)$-invariant metrics. *Proceedings of the* 3^{rd} *Panhellenic Congress of Geometry*, Athens, 1997, 169–182; assessed online on http://www.geocities.com/theometria/Stavroulakis-2.pdf.
19. Stavroulakis N. On a paper by J. Smoller and B. Temple. *Annales Fond. Louis de Broglie*, 2002, v. 27, No. 3, 511–521; http://www.ptep-online.com/theometria/Stavroulakis-1.pdf.
20. Stavroulakis N. Non-Euclidean geometry and gravitation. *Progress in Physics*, 2006, v. 2, 68–75.
21. Kruskal M. D. Maximal extension of Schwarzschild metric. *Phys. Rev.*, 1960, v. 119, 1743.
22. Schwarzschild K. On the gravitational field of a sphere of incompressible fluid according to Einstein's theory. *Sitzungsber. Preuss. Akad. Wiss., Phys. Math. Kl.*, 1916, 424; arXiv: physics/9912033.
23. Crothers S. J. On the vacuum field of a sphere of incompressible fluid. *Progress in Physics*, 2005, v. 2, 76–81.
24. Crothers S. J. On the general solution to Einstein's vacuum field for the point-mass when $\lambda \neq 0$ and its consequences for relativistic cosmology. *Progress in Physics*, 2005, v. 3, 7–18.
25. Crothers S. J. Relativistic cosmology revisited. *Progress in Physics*, 2007, v. 2, 27–30.

On the Propagation of Gravitation from a Pulsating Source

Nikias Stavroulakis
Solomou 35, 15233 Chalandri, Greece
E-mail: nikias.stavroulakis@yahoo.fr

According to an idea underlying the classical relativity, a pulsating (or simply expanding or simply contracting) spherical source does not generate an external dynamical (i.e. non-stationary) gravitational field. The relativists believe that this idea is well based on account of the so-called Birkhoff's theorem, which, contrary to the fundamental principles of general relativity, states that the external gravitational field of a non-stationary spherical mass is necessarily static. However, as shown in several papers [2, 3, 4, 7, 8], Birkhoff's theorem is, in fact, a vicious circle arising from the introduction of inadmissible implicit transformations which eliminate in advance the boundary conditions defining the radial motion of the sphere bounding the matter, namely the boundary conditions inducing the non-stationary states of the gravitational field. In the present paper we deal with the rigorous mathematical theory of the subject and put forward the corresponding form of the spacetime metric in order to prepare a thorough study of the equations of gravitation related to the dynamical states of the gravitational field.

1 S$\Theta(4)$-invariant metrics and gravitational disturbances

Let us first consider a general spacetime metric

$$\sum_{i,j=0}^{3} g_{ij} dx_i dx_j \tag{1.1}$$

namely a form of signature $(+1,-1,-1,-1)$ on a open set $U \subset \mathbb{R} \times \mathbb{R}^3$. In order that the local time and the proper time of the observes be definable, the timelike character of x_0 must be clearly indicared together with its distinction from the spacelike character of the coordinates x_1, x_2, x_3. This is why, according to Levi-Civita [l], the components g_{00}, g_{11}, g_{22}, g_{33} of the metric tensor must satisfy the conditions $g_{00} > 0$, $g_{11} < 0$, $g_{22} < 0$, $g_{33} < 0$.

Our investigation of an $S\Theta(4)$-invariant (or $\Theta(4)$-invariant) metric follows Levi-Civita's point of view by allowing at the same time a slight generalization which will be fully justified. More precisely, an allowable $S\Theta(4)$-invariant (or $\Theta(4)$-invariant) metric will satisfy the conditions $g_{00} > 0$, $g_{11} \leqslant 0$, $g_{22} \leqslant 0$, $g_{33} \leqslant 0$. We recall [9] the explicit form of such a metric

$$ds^2 = \left(f dx_0 + f_1 (x dx)\right)^2 - \ell_1^2 dx^2 - \frac{\ell^2 - \ell_1^2}{\rho^2} (x dx)^2 ,$$
$$x_0 = t, \ell(t,0) = \ell_1(t,0),$$

which is invariant by the action of the group $S\Theta(4)$ consisting of the matrices of the form

$$\begin{pmatrix} 1 & O_H \\ O_V & A \end{pmatrix}, \quad O_H = (0,0,0), \quad O_V = \begin{pmatrix} 0 \\ 0 \\ 0 \end{pmatrix},$$
$$A \in SO(3)$$

as well as by the action of the group $\Theta(4)$ consisting of the matrices of the same form for which $A \in O(3)$. Note that the given form of the metric does not contain the important functions

$$h = \rho f_1 = \rho f_1(t,\rho), \qquad g = \rho \ell_1 = \rho \ell_1(t,\rho),$$

because they are not C^∞ on the subspace $\mathbb{R} \times \{(0,0,0)\}$. However, as already noted [9], on account of their geometrical and physical significance, it is very convenient to insert them into the metric, thus obtaining

$$ds^2 = \left(f dx_0 + \frac{h}{\rho}(x dx)\right)^2 - \left(\frac{g}{\rho}\right)^2 dx^2 - \\ - \frac{1}{\rho^2}\left(\ell^2 - \left(\frac{g}{\rho}\right)^2\right)(x dx)^2 \tag{1.2}$$

and then

$$g_{00} = f^2, \qquad g_{ii} = \left(h^2 - \ell^2\right)\frac{x_i^2}{\rho^2} - \left(\frac{g}{\rho}\right)^2\left(1 - \frac{x_i^2}{\rho^2}\right),$$
$$(i = 1,2,3).$$

We contend that $g_{ii} \leqslant 0$, $(i = 1,2,3)$, if and only if $|h| \leqslant \ell$. In fact, if $|h| \leqslant \ell$, we have obviously $g_{ii} \leqslant 0$, $(i = 1,2,3)$. On the other hand, if $|h| > \ell$, by choosing $x_1 = \rho$, $x_2 = x_3 = 0$, we have $g_{11} = h^2 - \ell^2 > 0$.

The $S\Theta(4)$ -invariant metric (1.2), considered with the condition $|h| \leqslant \ell$, is assumed to represent the gravitational field generated by a spherical isotropic non-rotating, in general pulsating, distribution of matter. This field is related intuitively to a radial uniform propagation of spherical gravitational (and possibly electromagnetic) disturbances issuing from the matter and governed by the time according to the following rule:

The emission of a disturbance takes place at a given instant from the entirety of the sphere bounding the matter (namely from the totality of the points of this sphere) and reaches the totality of any other sphere $S_\rho : \| x \| = \rho > 0$ outside the matter at another instant.

The assignment of a given instant t to every point of the sphere S_ρ means that we consider an infinity of simultaneous events $\{(t, x) \,|x \in S_\rho\}$ related to S_ρ. This conception of simultaneity is restricted to the considered sphere S_ρ and cannot be extended radially (for greater or less values of ρ). So the present situation differs radically from that encountered in special relativity. In particular, the synchronization of clocks in S_ρ cannot be carried out by the standard method put forward by Einstein, because there are no null geodesies of the metric associated with curves lying on S_ρ. The idea of synchronization in $S_\rho : \| x \| = \rho > 0$ is closely related to the very definition of the $S\Theta(4)$-invariant field: For any fixed value of time t, the group $S\Theta(4)$ sends the subspace $\{t\} \times S_\rho$ of $\mathbb{R} \times \mathbb{R}^3$ onto itself, so that the group $S\Theta(4)$ assigns the value of time t to every point of the sphere S_ρ. Specifically, given any two distinct points x and y of S_ρ, there exists an operation of $S\Theta(4)$ sending (t, x) onto (t, y). This operation appears as an abstract mathematical mapping and must be clearly distinguished from a rotation in $\mathbb{R}^3$ in the sense of classical mechanics. Such a rotation in $\mathbb{R}^3$ is a motion defined with respect to a pre-existing definition of time, whereas the assignment of the value of time t to every point of S_ρ, is an "abstract operation" introducing the time in the metric.

Let S_m be the sphere bounding the matter. As will be shown later on, the "synchronization" in S_m induces the synchronization in any other sphere S_ρ outside the matter by means of the propagation process of gravitation. In a stationary state, the radius of S_m reduces to a constant, say σ, and every point of S_m can be written as $x = \alpha\sigma$ where $\alpha = (\alpha_1, \alpha_2, \alpha_3) \in S_1$, S_1 being the unit sphere:

$$S_1 = \Big\{\alpha = (\alpha_1, \alpha_2, \alpha_3) \in \mathbb{R}^3 \Big| \\ \| \alpha \| = \sqrt{\alpha_1^2 + \alpha_2^2 + \alpha_3^2} = 1\Big\}.$$

Now, in a non-stationary state, the radius of S_m will be a function of time, say $\sigma(t)$, and the equation of S_m can be written as $x = \alpha\sigma(t)$ with $\alpha \in S_1$. So each value of time t defines both the radius $\sigma(t)$ and the "simultaneous events" $\{(t, \alpha\sigma(t)) \,|\, \alpha \in S_1\}$. This simultaneity is also closely related to the definition of the $S\Theta(4)$ invariant field: $\{(t, \alpha\sigma(t)) \,| \\ \alpha \in S_1\}$ remains invariant by the action of $S\Theta(4)$. From these considerations it follows that the first principles related to the notion of time must be introduced axiomatically on the basis of the very definition of the $S\Theta(4)$-invariance. Their physical justification is to be sought a posteriori by taking into account the results provided by the theory itself.

This being said, according to our assumptions, it makes sense to consider as a function of time the curvature radius $g(t, \rho) = \rho\ell_1(t, \rho)$ of a sphere $\|x\| = \rho = \text{const} > 0$ outside the matter. The same assumptions allow to define, as functions of time, the radius $\sigma(t)$ and the curvature radius, denoted by $\zeta(t)$, of the sphere bounding the matter. These positive functions, $\sigma(t)$ and $\zeta(t)$, constitute the boundary conditions at finite distance for the non-stationary field outside the pulsating source. They are assumed to be C^∞, but they cannot be analytic, because the vanishing of $|\sigma'(t)|+|\zeta'(t)|$ on certain compact time intervals does not imply its vanishing on $\mathbb{R}$.

Since the internal field extends to the external one through the sphere $\|x\| = \sigma(t)$, the non-stationary (dynamical) states of the gravitational field outside the pulsating source are induced by the radial motion of this sphere, namely by the motion defined mathematically by the boundary conditions $\sigma(t)$ and $\zeta(t)$. So, it is reasonable to assume that, if $\sigma'(t) = \\ = \zeta'(t) = 0$ on a compact interval of time $[t_1, t_2]$, no propagation of gravitational disturbances takes place in the external space during $[t_1, t_2]$ (at least if there is no diffusion of disturbances). It follows that the gravitational radiation in the external space depends on the derivatives $\sigma'(t)$ and $\zeta'(t)$, so that we may identify their pair with the gravitational disturbance inducing the dynamical states outside the matter. More precisely, the non-stationary-states are generated by the propagation of the gravitational disturbance in the exterior space, so that we have first to clarify the propagation process. Our intuition suggests that the propagation of gravitation is closely related to the radial propagation of light, and this is why we begin by defining the function governing the radial propagation of light from the sphere bounding the matter.

2 Radial null geodesics

We recall that a curve $x(v) = (x_0(v), x_1(v), x_2(v), x_3(v))$ is a geodesic line with respect to (1.1) if

$$\frac{D}{dv}\frac{dx(v)}{dv} = q(v)\frac{dx(v)}{dv}\,.$$

So we are led to introduce the vector

$$Y^j = \frac{d^2x_j}{dv^2} + \sum_{k,\ell=0}^{3} \Gamma^j_{k\ell}\frac{dx_k}{dv}\frac{dx_\ell}{dv} - q(v)\frac{dx_j}{dv}, \quad (j = 0, 1, 2, 3),$$

which allows to write the equations of a geodesic in their general form

$$Y^0 = 0\,, \qquad Y^1 = 0\,, \qquad Y^2 = 0\,, \qquad Y^3 = 0\,.$$

On the other hand, a null line (not necessarily geodesic) is defined by the condition

$$\sum_{i,j=0}^{3} g_{ij}\frac{dx_i}{dv}\frac{dx_j}{dv} = 0\,, \qquad (v \neq s),$$

which implies

$$\sum g_{ij}\frac{dx_i}{dv}\frac{d^2x_j}{dv^2}+\sum\Gamma_{i,k\ell}\frac{dx_i}{dv}\frac{dx_k}{dv}\frac{dx_\ell}{dv}=0$$

so that by setting

$$X_j=\sum g_{ij}\frac{dx_i}{dv}$$

we deduce by an easy computation the relation

$$\sum_{j=0}^{3}X_jY^j=0$$

which is valid for every null line.

Now, let

$$d_t=\big\{x_1=\alpha_1\rho,\ \ x_2=\alpha_2\rho,\ \ x_3=\alpha_3\rho,\\ \alpha_1^2+\alpha_2^2+\alpha_3^2=1,\ \ \rho\geqslant\sigma(t)\big\}$$

be a half-line issuing from a point of the sphere $\|x\|=\sigma(t)$. The vanishing of (1.2) on d_t gives rise to two radial null lines defined respectively by the equations

$$\frac{dt}{d\rho}=\frac{-h(t,\rho)+\ell(t,\rho)}{f(t,\rho)} \tag{2.1}$$

$$\frac{dt}{d\rho}=\frac{-h(t,\rho)-\ell(t,\rho)}{f(t,\rho)} \tag{2.2}$$

Proposition 2.1. *The above defined null lines are null geodesics.*

Proof. By using a transformation defined by an element of the group $S\Theta(4)$, we may assume, without restriction of generality, that d_t is defined by the equations $x_1=\rho$, $x_2=0$, $x_3=0$, where $\rho\geqslant\sigma(t)$. Then taking into account the expressions of the Christoffel symbols [9], we see that

$$\Gamma^2_{00}=\Gamma^2_{01}=\Gamma^2_{11}=0,\qquad \Gamma^3_{00}=\Gamma^3_{01}=\Gamma^3_{11}=0,$$

so that the equations $Y^2=0$, $Y^3=0$ are identically verified. Moreover $x_2=x_3=0$ imply

$$Y^0=\frac{d^2t}{dv^2}+\Gamma^0_{00}\left(\frac{dt}{dv}\right)^2+\Gamma^0_{11}\left(\frac{d\rho}{dv}\right)^2+\\ +2\Gamma^0_{01}\frac{dt}{dv}\frac{d\rho}{dv}-q(v)\frac{dt}{dv},$$

$$Y^1=\frac{d^2\rho}{dv^2}+\Gamma^1_{00}\left(\frac{dt}{dv}\right)^2+\Gamma^1_{11}\left(\frac{d\rho}{dv}\right)^2+\\ +2\Gamma^1_{01}\frac{dt}{dv}\frac{d\rho}{dv}-q(v)\frac{d\rho}{dv}.$$

Now, let $t=\xi(\rho)$ be a solution of (2.1) and take $v=\rho$. Then the equation $Y^1=0$ gives

$$\Gamma^1_{00}\big(\xi(\rho),\rho\big)\big(\xi'(\rho)\big)^2+\Gamma^1_{11}\big(\xi(\rho),\rho\big)+\\ +2\Gamma^1_{01}\big(\xi(\rho),\rho\big)\xi'(\rho)=q(\rho)$$

so that it defines the function $q(\rho)$. Next, since the equations $Y^1=0$, $Y^2=0$, $Y^3=0$ are fulfilled, the condition $\sum_{j=0}^3X_jY^j=0$ reduces to $X_0Y^0=0$, and since

$$X_0=g_{00}\frac{dt}{dv}+g_{01}\frac{dx_1}{dv}=f^2\frac{dt}{d\rho}+fh=\\ =f^2\left(\frac{-h+\ell}{f}\right)+fh=f\ell>0,$$

it follows also that $Y^0=0$. In the same way taking into account that $-f\ell<0$, we prove the assertion regarding (2.2).

Corollary 2.1. *The equation (2.1), resp. (2.2), defines the radial motion of the photons issuing from (resp. approaching to) the pulsating spherical mass.*

In fact, since $|h|\leqslant\ell$, we have $-h+\ell\geqslant0$, which impies $dt/d\rho\geqslant0$, and $-h-\ell\leqslant0$ which implies $dt/d\rho\leqslant0$.

Remark 2.1. The condition $|h|\leqslant\ell$ has been introduced in order to ensure the physical validity of the spacetime metric. Now we see that it is absolutely indispensable in order to define the radial motion of light. In fact, if $h>\ell$ (resp. $-h>\ell$), the photons issuing from (resp. approaching to) the spherical mass would be inexistent for the metric. A detailed discussion of the inconsistencies resulting from the negation of the condition $|h|\leqslant\ell$ is given in the paper [6].

Remark 2.2. As already remarked, the propagation of the gravitation from the pulsating source is closely related to the radial propagation of te outgoing light which is defined by (2.1). Regarding the equation (2.2), which defines the radial propagation of the incoming light, it is not involved in our study, because there are no gravitational disturbances coming from the "infinity".

3 On the solutions of (2.1)

Let us consider a photon emitted radially at an instant u from the sphere bounding the matter. Its velocity at this instant, namely

$$\frac{d\rho}{dt}=\frac{f\big(u,\sigma(u)\big)}{\ell\big(u,\sigma(u)\big)-h\big(u,\sigma(u)\big)}$$

is greater than the radial velocity $|\sigma'(u)|$ of this sphere, whence the condition

$$\frac{\ell\big(u,\sigma(u)\big)-h\big(u,\sigma(u)\big)}{f\big(u,\sigma(u)\big)}\,|\sigma'(u)|<1$$

which implies in particular the validity of the condition

$$\frac{\ell\big(u,\sigma(u)\big)-h\big(u,\sigma(u)\big)}{f\big(u,\sigma(u)\big)}\,\sigma'(u)<1 \tag{3.1}$$

which is trivially valid if $\sigma'(u)\leqslant0$.

This being said, let us consider the open set

$$U=\big\{(t,\rho)\in\mathbb{R}^2\,|\,\rho>\sigma(t)\big\}$$

and denote by F its frontier:

$$F=\big\{(t,\rho)\in\mathbb{R}^2\,|\,\rho=\sigma(t)\big\}.$$

Since the equation (2.1) is conceived on the closed set $\overline{U} = U \cup F$, the functions f, h, ℓ are defined on $\overline{U}$. However, since we have to define the solutions of (2.1) by using initial conditions in F, we are led to extend the function

$$\alpha(t,\rho) = \frac{-h(t,\rho)+\ell(t,\rho)}{f(t,\rho)}$$

to a C^∞ function $\hat{\alpha}(t,\rho) \geqslant 0$ on an open set W containing $\overline{U}$. It is not necessary to indicate a precise extension on W because its values on $W-\overline{U}$ play an auxiliary part and are not involved in the final result.

This remark applies also to the derivatives of the functions f, h, ℓ at the points of F. In fact, although the definition of these derivatives takes into account the extension $\hat{\alpha}(t,\rho)$, their values on F, on account of the continuity, are defined uniquely by their values on U.

This being said, for each fixed point $(u,\sigma(u)) \in F$, the differential equation

$$\frac{dt}{d\rho} = \hat{\alpha}(t,\rho)$$

possesses a unique local solution $t = \hat{\xi}(u,\rho)$ taking the value u for $\rho = \sigma(u)$. Let $]\,\rho_1(u), \rho_2(u)\,[$ be the maximal interval of validity of this local solution $(\rho_1(u) < \sigma(u) < \rho_2(u))$.

Lemma 3.1. *There exists a real number $\epsilon > 0$ such that $\sigma(u) < \epsilon < \rho_2(u)$ and $(\hat{\xi}(u,\rho),\rho) \in U$ for every $\rho \in]\,\sigma(u), \epsilon\,]$.*

Proof. Assume that such a number does not exist. Then we can find a sequence of values $\rho_n > \sigma(u)$ converging to $\sigma(u)$ and such that $(\hat{\xi}(u,\rho_n),\rho_n) \notin U$, which means that $\sigma(\hat{\xi}(u,\rho_n)) \geqslant \rho_n$, and implies, in particular $\hat{\xi}(u,\rho_n) \neq u$. It follows that

$$\frac{\hat{\xi}(u,\rho_n)-u}{\rho_n-\sigma(u)} \cdot \frac{\sigma\big(\hat{\xi}(u,\rho_n)\big)-\sigma(u)}{\hat{\xi}(u,\rho_n)-u} = \frac{\sigma\big(\hat{\xi}(u,\rho_n)\big)-\sigma(u)}{\rho_n-\sigma(u)} \geqslant 1$$

and since $\hat{\xi}(u,\sigma(u)) = u$, $\rho_n \to \sigma(u)$, we obtain

$$\frac{\partial\hat{\xi}\big(u,\sigma(u)\big)}{\partial\rho}\,\sigma'(u) \geqslant 1\,,$$

or

$$\frac{-h\big(u,\sigma(u)\big)+\ell\big(u,\sigma(u)\big)}{f\big(u,\sigma(u)\big)}\,\sigma'(u) \geqslant 1$$

which contradicts (3.1). This contradiction proves our assertion.

Lemma 3.2. *We also have $(\hat{\xi}(u,\rho),\rho) \in U$ for every $\rho \in]\,\epsilon, \rho_2(u)\,[$.*

Proof. If not, the set of values $\rho \in]\,\epsilon, \rho_2(u)\,[$ for which $\sigma(\hat{\xi}(u,\rho)) = \rho$ is not empty. Let ρ_0 be the greatest lower bound of this set. Then $\sigma(\hat{\xi}(u,\rho_0)) = \rho_0$. Let $\hat{\xi}(u,\rho_0) = t_0$ and let $\psi(t_0,\rho)$ be the local solution of the differential equation

$$\frac{dt}{d\rho} = \hat{\alpha}(t,\rho)$$

for which $\psi(t_0,\rho_0) = t_0$. The uniqueness of the solution implies obviously that $\psi(t_0,\rho) = \hat{\xi}(u,\rho)$. On the other hand, for every $\rho \in]\,\sigma(u), \rho_0[$, we have $\sigma(\hat{\xi}(u,\rho)) < \rho$. Moreover $\hat{\xi}(u,\rho_0) \neq \hat{\xi}(u,\rho)$ because the equality $\hat{\xi}(u,\rho_0) = \hat{\xi}(u,\rho)$ would imply

$$\rho_0 = \sigma\big(\hat{\xi}(u,\rho_0)\big) = \sigma\big(\hat{\xi}(u,\rho)\big) < \rho$$

contradicting the choice of ρ. On the other hand

$$\sigma\big(\hat{\xi}(u,\rho_0)\big) - \sigma\big(\hat{\xi}(u,\rho)\big) = \\ = \rho_0 - \sigma\big(\hat{\xi}(u,\rho)\big) > \rho_0 - \rho > 0$$

so that we can write

$$\frac{\hat{\xi}(u,\rho_0)-\hat{\xi}(u,\rho)}{\rho_0-\rho} \cdot \frac{\sigma\big(\hat{\xi}(u,\rho_0)\big)-\sigma\big(\hat{\xi}(u,\rho)\big)}{\hat{\xi}(u,\rho_0)-\hat{\xi}(u,\rho)} = \\ = \frac{\sigma\big(\hat{\xi}(u,\rho_0)\big)-\sigma\big(\hat{\xi}(u,\rho)\big)}{\rho_0-\rho} \geqslant 1$$

or

$$\frac{\psi(t_0,\rho_0)-\psi(t_0,\rho)}{\rho_0-\rho} \cdot \frac{\sigma(t_0)-\sigma\big(\psi(t_0,\rho)\big)}{t_0-\psi(t_0,\rho)} \geqslant 1$$

and for $\rho \to \rho_0$ we find

$$\frac{\partial\psi(t_0,\rho_0)}{\partial\rho}\,\sigma'(t_0) \geqslant 1$$

or

$$\frac{-h\big(t_0,\sigma(t_0)\big)+\ell\big(t_0,\sigma(t_0)\big)}{f(t_0,\sigma(t_0))}\,\sigma'(t_0) \geqslant 1$$

which contradicts (3.1). This contradiction proves our assertion.

Proposition 3.1. *Let $\xi(u,\rho)$ be the restriction of the solution $\hat{\xi}(u,\rho)$ to the interval $[\sigma(u), \rho_2(u)\,[$. Then $\xi(u,\rho)$ does not depend on the extension $\hat{\alpha}(t,\rho)$ of $\alpha(t,\rho)$, so that it is the unique local solution of (2.1) in $\overline{U}$ satisfying the condition $\xi(u,\sigma(u)) = u$.*

In fact, since $\hat{\xi}(u,\sigma(u)) = u$ and $(\hat{\xi}(u,\rho),\rho) \in U$ for $\rho > \sigma(u)$, the definition of $\xi(u,\rho)$ on $[\sigma(u), \rho_2(u)[$ depends uniquely on the function $\alpha(t,\rho)$ which is defined on $\overline{U}$

In general, the obtained solution $\xi(u,\rho)$ is defined on a bounded interval $[\sigma(u), \rho_2(u)\,[$. However the physical conditions of the problem require that the emitted photon travel to infinity. In fact, the pulsating source (whenever it is expanding) can not overtake the photon emitted radially at the instant u. Consequently the functions f, h, ℓ involved in the metric must be such that, for each value of $u \in \mathbb{R}$, the solution $\xi(u,\rho)$ of (2.1) be defined on the half-line $[\sigma(u), +\infty[$, so that $\rho_2(u) = +\infty$ and $(\xi(u,\rho),\rho) \in U$ for every $\rho \in]\,\sigma(u), +\infty\,[$. Then the corresponding curves $(\xi(u,\rho),\rho)$ issuing from the points of F are the leaves of a foliation of $\overline{U}$ representing the paths of the photons emitted radially from the sphere bounding the matter (see Figure 1 shown in Page 79).

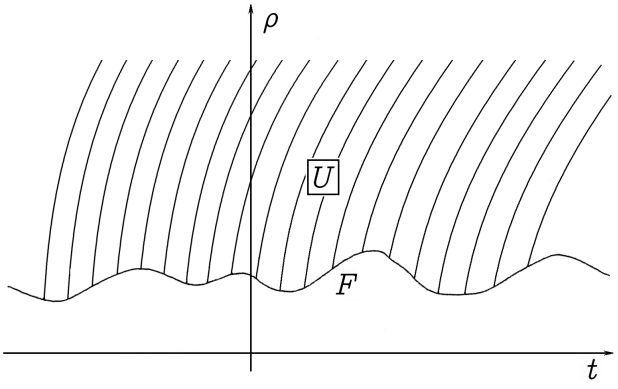

Fig. 1: Foliation representing the paths of the photons emitted radially from the sphere bounding the matter.

4 Propagation function of light and canonical metric

The solution $\xi(u,\rho)$ appears as a function of two variables: On the one hand the time $u \in \mathbb{R}$ on the sphere bounding the matter, and on the other hand the radial coordinate $\rho \in [\sigma(u), +\infty[$.

Proposition 4.1. *The function $\xi(u,\rho)$, $(u,\rho) \in \overline{U}$, fulfils the conditions*

$$\frac{\partial \xi(u,\rho)}{\partial u} > 0, \quad \frac{\partial \xi(u,\rho)}{\partial \rho} \geqslant 0$$

the first of which allows to solve with respect to u the equation $t = \xi(u,\rho)$, where $\xi(u,\sigma(u)) = u$, and obtain thus the instant u of the radial emission of a photon as a function of (t,ρ): $u = \pi(t,\rho)$. The so obtained function $\pi(t,\rho)$ on $\overline{U}$ satisfies the conditions

$$\frac{\partial \pi(t,\rho)}{\partial t} > 0\,, \qquad \frac{\partial \pi(t,\rho)}{\partial \rho} \leqslant 0\,, \qquad \pi\big(t,\sigma(t)\big) = t\,.$$

Proof. Since $-h + \ell \geqslant 0$, the condition $\xi(u,\rho)/\partial\rho \geqslant 0$ is obvious on account of (2.1). On the other hand, taking the derivatives of both sides of the identity $\xi(u,\sigma(u)) = u$ we obtain

$$\frac{\partial \xi\big(u,\sigma(u)\big)}{\partial u} + \frac{\partial \xi\big(u,\sigma(u)\big)}{\partial \rho}\,\sigma'(u) = 1$$

or

$$\frac{\partial \xi\big(u,\sigma(u)\big)}{\partial u} + \frac{-h\big(u,\sigma(u)\big) + \ell\big(u,\sigma(u)\big)}{f\big(u,\sigma(u)\big)}\,\sigma'(u) = 1$$

whence, on account of (3.1),

$$\frac{\partial \xi\big(u,\sigma(u)\big)}{\partial u} > 0$$

for every $u \in \mathbb{R}$. It remains to prove that, for each fixed value $u_0 \in \mathbb{R}$, and for each fixed value $\rho_0 > \sigma(u_0)$, we have $\partial\xi(u_0,\rho_0)/\partial u > 0$.

Now, $\rho_0 > \sigma(u_0)$ implies that there exists a straight line segment

$$\big[-\epsilon_1 + \xi(u_0,\rho_0), \epsilon_1 + \xi(u_0,\rho_0)\big] \times \{\rho_0\}\,, \epsilon_1 > 0,$$

contained in U. Let us denote by L_1, L_0, L_2 respectively the leaves containing the points

$$\big(-\epsilon_1 + \xi(u_0,\rho_0),\, \rho_0\big),\ \big(\xi(u_0,\rho_0),\, \rho_0\big),\ \big(\epsilon_1 + \xi(u_0,\rho_0),\, \rho_0\big).$$

L_0 is defined by the solution $\xi(u_0,\rho)$ of (2.1), whereas L_1 and L_2 are defined respectively by two solutions $\xi(u_1,\rho)$ and $\xi(u_2,\rho)$ with convenient values u_1 and u_2. Since $L_1 \cap L_0 = \emptyset$, $L_0 \cap L_2 = \emptyset$, it follows obviously that $u_1 < u_0$ and $u_0 < u_2$. The same reasoning shows that, if $u_1 < u' < u_0 < u'' < u_2$, then

$$\xi(u_1,\rho_0) < \xi(u',\rho_0) < \xi(u_0,\rho_0) < \xi(u'',\rho_0) < \xi(u_2,\rho_0),$$

so that $\xi(u,\rho_0)$ is a strictly increasing function of u on the interval $[u_1,u_2]$. It follows that $\partial\xi(u_0,\rho_0)/\partial u > 0$ as asserted. Regarding the last assertion, it results trivially from the identity $\xi(\pi(t,\rho),\rho) = t$, which implies

$$\frac{\partial \xi}{\partial u}\cdot\frac{\partial \pi}{\partial t} = 1\,, \qquad \frac{\partial \xi}{\partial u}\cdot\frac{\partial \pi}{\partial \rho} + \frac{\partial \xi}{\partial \rho} = 0\,.$$

Remark. Let u_1 and u_2 be two instants such that $u_1 < u_2$, and let ρ be a positive length. If the values $\xi(u_1,\rho)$ and $\xi(u_2,\rho)$ are both definable, which implies, in particular, $\xi(u_1,\rho) \geqslant u_1$ and $\xi(u_2,\rho) \geqslant u_2$, then $\xi(u_1,\rho) < \xi(u_2,\rho)$.

The function $\pi(t,\rho)$ characterizes the radial propagation of light and will be called *propagation function*. Its physical significance is the following : If a photon reaches the sphere $\|x\| = \rho$ at the instant t, then $\pi(t,\rho)$ is the instant of its radial emission from the sphere bounding the matter.

Proposition 4.2 *If a photon emitted radially from the sphere bounding the matter reaches the sphere $\|x\| = \rho$ at the instant t, then its radial velocity at this instant equals*

$$-\frac{\partial \pi(t,\rho)/\partial t}{\partial \pi(t,\rho)/\partial \rho}\,.$$

In fact, since

$$\frac{dt}{d\rho} = \frac{-h+\ell}{f} = \frac{\partial \xi(u,\rho)}{\partial \rho},$$

the velocity in question equals

$$\frac{d\rho}{dt} = \left(\frac{\partial \xi(u,\rho)}{\partial \rho}\right)^{-1} = -\left(\frac{\partial \xi(u,\rho)}{\partial u}\,\frac{\partial \pi(t,\rho)}{\partial \rho}\right)^{-1} = -\frac{\partial \pi(t,\rho)/\partial t}{\partial \pi(t,\rho)/\partial \rho}\,.$$

Remark. The preceding formula applied to the classical propagation function $t - \frac{\rho}{c}$, gives the value c.

Since the parameter u appearing in the solution $\xi(u,\rho)$ represents the time on the sphere bounding the matter and describes the real line, we are led to define a mapping $\Gamma\colon \overline{U} \to \overline{U}$, by setting $\Gamma(t,\rho) = (\pi(t,\rho),\rho) = (u,\rho)$.

Proposition 4.3. *The mapping Γ is a diffeomorphism which reduces to the identity on the frontier F of U. Moreover it transforms the leaf $\{(t,\rho)\in\overline{U}\,|\,t=\xi(u,\rho)\}$ issuing from a point $(u,\sigma(u))\in F$ into a half-line issuing from the same point and parallel to the ρ-axis. Finally it transforms the general $\Theta(4)$ invariant metric (1.2) into another $\Theta(4)$-invariant metric for which $h=\ell$, so that the new propagation function is identical with the new time coordinate.*

Proof. The mapping Γ is one-to-one and its jacobian determinant $\partial\pi(t,\rho)/\partial t$ is strictly positive everywhere. Consequently Γ is a diffeomorphism. Moreover, since each leaf is defined by a fixed value of u, its transform in the new coordinates (u,ρ) is actually a half-line parallel to the ρ-axis. Finally, since $t=\xi(u,\rho)$ and $\partial\xi/\partial\rho=(-h+\ell)/f$, it follows that

$$\begin{aligned} f\,dt+\frac{h}{\rho}\,(x\,dx) &= \left(f\,\frac{\partial\xi}{\partial u}\right)du+\left(f\,\frac{\partial\xi}{\partial\rho}\right)d\rho+h\,d\rho \\ &= \left(f\,\frac{\partial\xi}{\partial u}\right)du+\left(f\left(\frac{-h+\ell}{f}\right)+h\right)d\rho \\ &= \left(f\,\frac{\partial\xi}{\partial u}\right)du+\ell\,d\rho \\ &= \left(f\,\frac{\partial\xi}{\partial u}\right)du+\ell\,\frac{(x\,dx)}{\rho} \end{aligned}$$

with

$$f=f\big(\xi(u,\rho),\rho\big),\quad h=h\big(\xi(u,\rho),\rho\big),\quad \ell=\ell\big(\xi(u,\rho),\rho\big).$$

So the remarkable fact is that, in the transformed $\Theta(4)$-invariant metric, the function h equals ℓ. The corresponding equation (2.1) reads

$$\frac{du}{d\rho}=0$$

whence $u=\text{const}$, so that the new propagation function is identified with the time coordinate u. (This property follows also from the fact that the transform of $\pi(t,\rho)$ is the function $\pi(\xi(u,\rho),\rho)=u$.)

The Canonical Metric. In order to simplify the notations, we write $f(u,\rho)$, $\ell(u,\rho)$, $g(u,\rho)$ respectively instead of

$$f\big(\xi(u,\rho),\rho\big)\frac{\partial\xi(u,\rho)}{\partial u}\,,\quad \ell\big(\xi(u,\rho),\rho\big)\,,\quad g\big(\xi(u,\rho),\rho\big)$$

so that the transformed metric takes the form

$$\begin{aligned} ds^2 &= \left(f(u,\rho)\,du+\ell(u,\rho)\,\frac{(x\,dx)}{\rho}\right)^2- \\ &-\left[\left(\frac{g(u,\rho)}{\rho}\right)^2dx^2+\left(\big(\ell(u,\rho)\big)^2-\left(\frac{g(u,\rho)}{\rho}\right)^2\right)\frac{(x\,dx)^2}{\rho^2}\right] \end{aligned} \tag{4.1}$$

which will be termed Canonical.

The equality $h=\ell$ implies important simplifications: Since the propagation function of light is identified with the new time coordinate u, it does not depend either on the unknown functions f, ℓ, g involved in the metric or on the boundary conditions at finite distance $\sigma(u)$, $\zeta(u)$. The radial motion of a photon emitted radially at an instant u_0 from the sphere $\|x\|=\sigma(u)$ will be defined by the equation $u=u_0$, which, when u_0 describes $\mathbb{R}$, gives rise to a foliation of $\overline{U}$ by half-lines issuing from the points of F and parallel to the ρ-axis (Figure 2). This property makes clear the physical significance of the new time coordinate u. Imagine that the photon emitted radially at the instant u_0 is labelled with the indication u_0. Then, as it travels to infinity, it assigns the value of time u_0 to every point of the corresponding ray. This conception of time differs radically from that introduced by special relativity. In this last theory, the equality of values of time at distinct points is defined by means of the process of synchronization. In the present situation the equality of values of time along a radial half-line is associated with the radial motion of a single photon. The following proposition is obvious (although surprising at first sight).

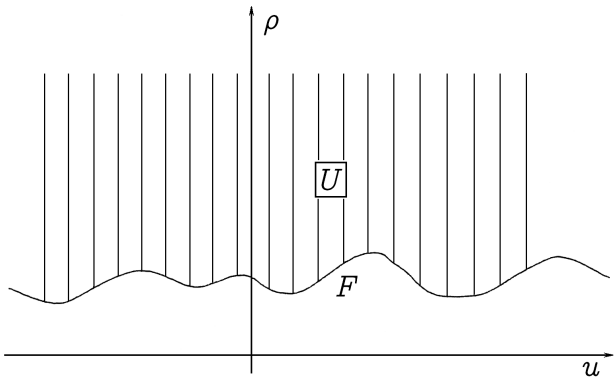

Fig. 2: The rise to a foliation of $\overline{U}$ by half-lines issuing from the points of F and parallel to the ρ-axis.

Proposition 4.4. *With respect to the canonical metric, the radial velocity of propagation of light is infinite.*

Note that the classical velocity of propagation of light, namely c, makes sense only with respect to the time defined by synchronized clocks in an inertial system.

We emphasize that the canonical metric is conceived on the closed set $\{(u,x)\in\mathbb{R}\times\mathbb{R}^3\,|\,\|x\|\geqslant\sigma(u)\}$ namely on the exterior of the matter, and it is not possible to assign to it a universal validity on $\mathbb{R}\times\mathbb{R}^3$. In fact, ℓ is everywhere strictly positive, whereas h vanishes for $\rho=0$, so that the equality $h(t,\,\|x\|)=\ell(t,\,\|x\|)$ cannot hold on a neighbourhood of the origin. It follows that the canonical metric is incompatible with the idea of a punctual source.

5 Propagation function of gravitational disturbances

We recall that, $\sigma(u)$ and $\zeta(u)$ being respectively the radius and the curvature radius of the sphere bounding the matter, we are led to identify the pair of derivatives $(\sigma'(u),\zeta'(u))$ with the gravitational disturbance produced at the instant u on the entirety of the sphere in question. This local disturbance induces a radial propagation process with propagation

paths identified with the radial geodesies and wave fronts covering successively the spheres $\|x\| = \rho = \text{const}$. This process modifies step by step the field outside the matter and thus gives rise to a non-stationary (dynamical) state of the gravitational field. It follows that apart from any theory aimed at determining the gravitational field, we have first to elucidate the propagation process of the gravitational disturbance. In order to carry out this investigation, we refer constantly to the canonical metric (4.1) which, without restriction of generality, gives rise to significant simplifications. This being said, the gravitational disturbance being produced at the instant u on the sphere bounding the matter, let us consider the instant $t = \psi(u, \rho)$ at which it reaches the sphere $\|x\| = \rho$, so that we have, in particular, $\psi(u, \sigma(u)) = u$. We assume naturally that the pulsating source does not hinder the propagation of gravitation outside the matter. In other words, every time that the sphere bounding the matter is expanding, it can not overtake the advancing gravitational disturbance. This is the case if and only if $(\psi(u, \rho), \rho) \in U$ for every $\rho > \sigma(u)$. On the other hand, on account of the physical conditions of the problem, the derivative $\dfrac{\partial \psi(u, \rho)}{\partial \rho}$ cannot be negative, so that the equation $t = \psi(u, \rho)$ defines non decreasing functions of ρ giving rise to a foliation of $\overline{U}$ by curves issuing from the points of F. Because of this foliation, we have the condition

$$\frac{\partial \psi(u, \rho)}{\partial u} > 0 \tag{5.1}$$

which allows to solve the equation $t = \psi(u, \rho)$ with respect to u, thus obtaining the propagation function of the gravitational disturbance $u = e(t, \rho)$ relative to the canonical metric (4.1). Note that, on account of (5.1), by setting $\Delta(u, \rho) = (\psi(u, \rho), \rho) = (t, \rho)$, we define a diffeomorphism $\Delta : \overline{U} \to \overline{U}$, the restriction of which to F is the identity.

Proposition 5.1 *If the gravitational disturbance emitted at the instant u reaches the sphere $\|x\| = \rho$ at the instant t, then its radial velocity at this instant equals*

$$-\frac{\partial e(t, \rho)/\partial t}{\partial e(t, \rho)/\partial \rho}\,.$$

Proof. The velocity in question equals

$$\frac{d\rho}{dt} = \frac{1}{dt/d\rho} = \frac{1}{\partial \psi(u, \rho)/\partial \rho}$$

and since the derivation of the identity

$$e\big(\psi(u, \rho), \rho\big) = u$$

with respect to ρ gives

$$\frac{\partial e}{\partial t}\frac{\partial \psi}{\partial \rho} + \frac{\partial e}{\partial \rho} = 0\,,$$

we obtain

$$\frac{1}{\partial \psi(u, \rho)/\partial \rho} = -\frac{\partial e(t, \rho)/\partial t}{\partial e(t, \rho)/\partial \rho}$$

as asserted.

Remark. Since the radial velocity of propagation of light is infinite with respect to the canonical metric (4.1), the velocity of radial propagation of the gravitational disturbance is necessarily less than (or possibly equal to) that of light. In fact, we can establish the identity of the two propagation functions on the basis of a hypothesis which suggests itself quite naturally.

Proposition 5.2. *If the diffeomorphism Δ transforms the canonical metric (4.1) into another physically admissible $\Theta(4)$-invariant metric on $\overline{U}$, then the propagation function of the gravitational disturbance is identical with the propagation function of light.*

Proof. In order to transform (4.1) by means of Δ, we have simply to replace u in (4.1) by $e(t, \rho)$ thus obtaining the $\Theta(4)$-invariant metric

$$\begin{aligned} ds^2 = &\left(F dt + \frac{H}{\rho}(x dx)\right)^2 - \\ &- \left[\left(\frac{G}{\rho}\right)^2 dx^2 + \left(L^2 - \left(\frac{G}{\rho}\right)^2\right)\frac{(x dx)^2}{\rho^2}\right] \end{aligned} \tag{5.2}$$

where

$$F = F(t, \rho) = f\big(e(t, \rho), \rho\big)\frac{\partial e(t, \rho)}{\partial t}\,, \tag{5.3}$$

$$H = H(t, \rho) = f\big(e(t, \rho), \rho\big)\frac{\partial e(t, \rho)}{\partial \rho} + \ell\big(e(t, \rho), \rho\big), \tag{5.4}$$

$$G = G(t, \rho) = g\big(e(t, \rho), \rho\big),$$

$$L = L(t, \rho) = \ell\big(e(t, \rho), \rho\big).$$

In the new metric (5.2), each value of $t = \psi(u, \rho)$ is the instant at which the disturbance emitted at the instant u reaches the sphere $\|x\| = \rho$. Consequently $e(t, \rho)$ is also the propagation function of the gravitational disturbance with respect to (5.2).

We now prove that the derivative $\partial e(t, \rho)/\partial \rho$ vanishes identically on $\overline{U}$.

We argue by contradiction. If this derivative does not vanish, the propagation function $e(t, \rho)$ of the gravitational disturbance is distinct from the propagation function of light with respect to (4.1), hence also with respect to the transformed metric (5.2). This last being admissible, according to our assumption, it satisfies the condition

$$|H(t, \rho)| \leqslant L(t, \rho)\,,$$

so that the radial motion of the photons issuing from the matter is defined by the equation

$$\frac{dt}{d\rho} = \frac{-H(t, \rho) + L(t, \rho)}{F(t, \rho)}\,.$$

On account of (5.3) and (5.4), we have

$$\frac{-H(t, \rho) + L(t, \rho)}{F(t, \rho)} = -\frac{\partial e(t, \rho)/\partial \rho}{\partial e(t, \rho)/\partial t}$$

so that the preceding equation reads

$$\frac{\partial e(t,\rho)}{\partial t}\,dt + \frac{\partial e(t,\rho)}{\partial \rho}\,d\rho = 0$$

whence $e(t,\rho) = \text{const}$ and since $e(t,\sigma(t)) = t$, $e(t,\rho)$ is the propagation function of light with respect to (5.2) contrary to our assumptions. This contradiction proves our assertion, namely that $\partial e(t,\rho)/\partial\rho = 0$ on $\overline{U}$.

This being proved, since the condition $\psi(e(t,\rho),\rho) = t$ implies

$$\frac{\partial \psi}{\partial u}\frac{\partial e}{\partial \rho} + \frac{\partial \psi}{\partial \rho} = 0\,,$$

the derivative $\partial\psi/\partial\rho$ vanishes identically on $\overline{U}$. In other words, $\psi(t,\rho)$ does not depend on ρ, so that

$$\psi(u,\rho) = \psi\big(u,\sigma(u)\big) = u$$

for every $\rho \geqslant \sigma(u)$. It follows that the propagation function of the gravitational disturbance is the same as that of light with respect to (4.1), hence also with respect to any admissible transformation of (4.1).

From now on we will not distinguish the propagation function of gravitational disturbances from that of light. So we can begin by the consideration of the canonical metric (4.1) for the study of the equations of gravitation related to a spherical pulsating source. This investigation will be carried out in another paper.

Submitted on February 09, 2007
Accepted on February 14, 2007

References

1. Levi-Civita T. On the analytic expression that must be given to the gravitational tensor in Einstein's theory. arXiv: physics/9906004, translation and foreword by S. Antoci and A. loinger (originally, in: *Rendiconti della Reale Accademia dei Lincei*, 1917, v. 26, 381).
2. Stavroulakis N. Exact solution for the field of a pulsating source, *Abstracts of Contributed Papers For the Discussion Groups, 9th International Conference on General Relativity and Gravitation*, July 14–19, 1980, Jena, Volume 1, 74–75.
3. Stavroulakis N. Mathématiques et trous noirs, *Gazette des mathématiciens*, No. 31, Juillet 1986, 119–132.
4. Stavroulakis N. Solitons and propagation d'actions suivant la relativité générale (première partie). *Annales Fond. Louis de Broglie*, 1987, v. 12, No. 4, 443–473.
5. Stavroulakis N. Solitons and propagation d'actions suivant la relativité générale (deuxième partie). *Annales Fond. Louis de Broglie*, 1988, v. 13, No. 1, 7–42.
6. Stavroulakis N. Sur la fonction de propagation des ébranlements gravitationnels. *Annales Fond. Louis de Broglie*, 1995, v. 20, No. 1, 1–31.
7. Stavroulakis N. On the principles of general relativity and the $S\Theta(4)$-invariant metrics. *Proc. 3^{rd} Panhellenic Congr. Geometry*, Athens 1997, 169–182.
8. Stavroulakis N. Vérité scientifique et trous noirs (première partie). Les abus du formalisme. *Annales Fond. Louis de Broglie*, 1999, v. 24, No. 1, 67–109.
9. Stavroulakis N. Non-Euclidean geometry and gravitation, *Progress in Physics*, 2006, v. 2, 68–75.

Effect from Hyperbolic Law in Periodic Table of Elements

Albert Khazan
E-mail: albkhazan@list.ru

Hyperbola curves $Y = K/X$ and $Y = (mx+n)/(px+q)$ at determination of the upper limit of the Periodic System have been studied. Their interdependence is shown by the example of mathematical calculations in chemistry.

1 Introduction. Mathematical basis

Our previous article shows that the Y content of any element K in a chemical compound is decreasing in case molecular mass X is increasing in the range from 1 up to any desired value in compliance with rectangular hyperbole law $Y = \frac{K}{X}$. Simultaneously, fraction $(1-Y)$ is increasing in inverse proportion in compliance with formula $1-Y = \frac{K}{X}$ or

$$Y = \frac{X-K}{X}\,. \tag{1}$$

It is known that the function

$$y = \frac{ax+b}{cx+d} \tag{2}$$

is called a linear-fractional function [2]. If $c = 0$ and $d \neq 0$, then we get linear dependence $y = \frac{a}{d}x + \frac{b}{d}$. If $c \neq 0$, then

$$y = \frac{a}{c} + \frac{\frac{bc-ad}{c^2}}{x+\frac{d}{c}}\,. \tag{3}$$

Supposing that $X = x + \frac{d}{c}$, $\frac{bc-ad}{c^2} = k \neq 0$, $Y = y - \frac{a}{c}$, we get $Y = \frac{K}{X}$, i.e. rectangular hyperbole formula which center is shifted from coordinates origin to point $C\left(-\frac{d}{c}; \frac{a}{c}\right)$.

As we can see, formula (1) is a special case of the function (2), cause coefficient $d = 0$. Then, determinant $D(ad-bc)$ degenerates into $-bc$. There exists a rule: when $D < 0$, $(K > 0)$, real axis together with X axis (abscissa axis) makes an angle $+45°$; and if $D > 0$, then the angle is $-45°$. In our case $D = a \times 0 - (-K) \times 1 = K$. Therefore, real axis, on which tops of all new hyperboles will be located, shall be in perpendicular position to the axis $y = \frac{k}{x}$. At that, the center is shifted from the coordinates origin $C(0;0)$ to the point $C(0;1)$. That means, in our case, semi-axes

$$a = b = \sqrt{\frac{2|D|}{c^2}} = \sqrt{2K}\,. \tag{4}$$

Then the coordinates of the top of the other hyperbole Beryllium will be: $X_0 = Y_0 = \sqrt{K} = \sqrt{9.0122} = 3.00203$ and $X' = 60.9097$, $Y' = 1 - Y = 1 - 0.14796 = 0.85204$.

In order to avoid possible mistakes let us use the following terminology: hyperbole of $y = \frac{k}{x}$ kind is called straight, and linear-fractional — an adjoining one.

Figure 1 demonstrates these curves which represent five elements from different groups: chlorine (No. 17), zirconium (No. 40), wolfram (No. 74), mendelevium (No. 101), and the last one (No. 155). Peculiarity of the diagrams is symmetry axis at content of elements equal to 0.5. It is clear that both hyperboles of the last element and ordinate axis limit the existence area of all chemical compounds related to one gram-atom.

Previously [1], we proved that all the elements of Periodic System can be described by means of rectangular hyperbole formulas. That is why, it is quite enough to present several diagrams in order to illustrate this or that dependence. The same is valid for linear-fractional functions which curves are directed bottom-up. If we put the picture up by symmetry axis, we shall see that they fully coincide with straight hyperboles. At the cross point of straight and adjoining hyperboles on this line, abscissa is equal to doubled atomic mass of the element. Coordinates of another cross points for each pair of hyperboles have the following parameters: X is equal to the sum of atomic mass of two elements $(K_1 + K_2)$, and Y has two values $\frac{K_1}{K_1+K_2}$ and $\frac{K_2}{K_1+K_2}$. Mentioned above is valid up to the upper bound of Periodic System inclusive.

As we can see on Figure 2, (A00) and (B01) are real axes of straight and adjoining hyperboles accordingly; and, AC and BD, (00E) and (01E) are tangents to them. Real axes are perpendicular to each other and to tangents. And all of them are equal to each other. Diagonals (00D) and (01C) divide straights AE and BE in halves.

There are formulas of mentioned lines. Cross points of these lines are also calculated. Abscissa of cross sections are values divisible by atomic mass of the last element: 0; 205.83; 274.44; 329.328; 411.66; 548.88; 617.49; 823.32 (0; 0.5; 0.667; 0.8; 1.0; 1.333; 1.5; 2.0).

For reference, Figure 3 demonstrates graphical construction for tungsten.

We can see, that knowing real axes (normal to the top of hyperboles), it is very easy to build up tangents to any element, if required, in order to check accuracy of chosen tops. For that, it is necessary to calculate formula of the straight which passes through the point $\mathrm{M}_1(x_1; y_1)$ and parallel $y = ax + b$:

$$y - y_1 = a(x - x_1)\,. \tag{5}$$

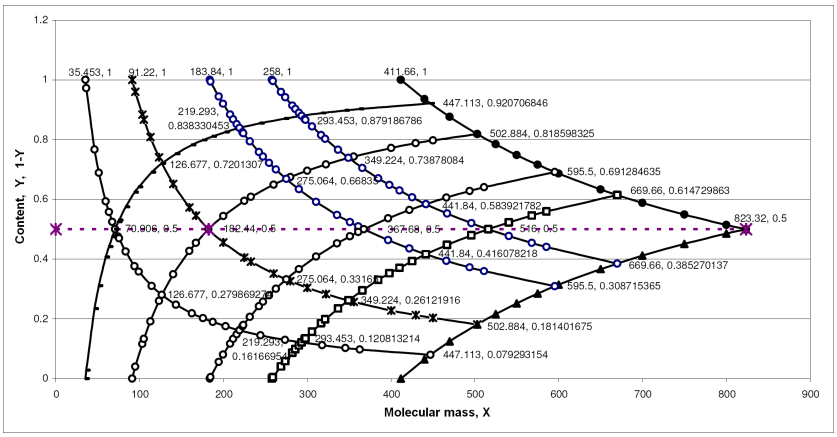

Fig. 1: Dependence of Y and $1-Y$ content from molecular mass in straight and adjoining hyperboles accordingly.

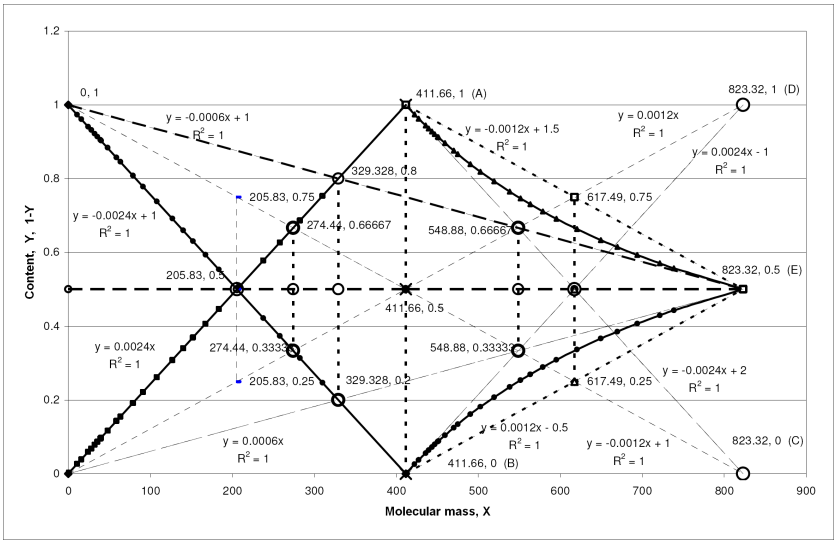

Fig. 2: Main lines of straight and adjoining hyperboles of the last element: real axes, tangents, diagonals etc.

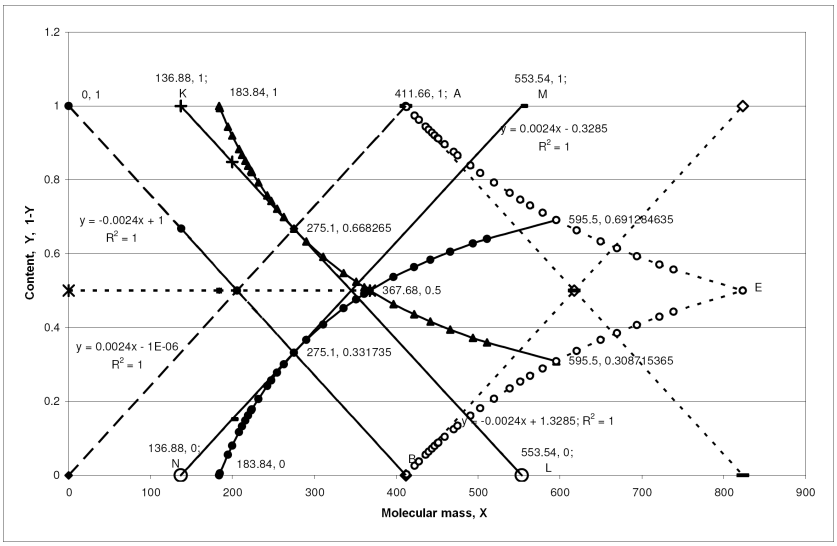

Fig. 3: Hyperboles of the last element and tungsten, their cross points and tangents.

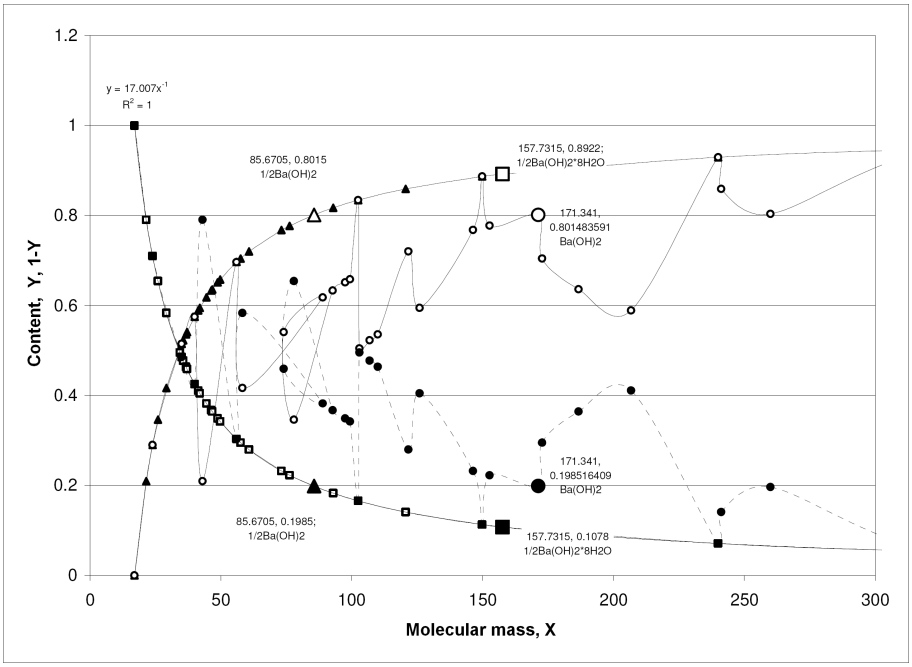

Fig. 4: Dependence of content of Y (OH) and $1-Y$ in hydroxides from their molecular mass counting on 1 gram-mole OH (of hyperbole). Broken curves are overall (summarized) content of OH in a substance.

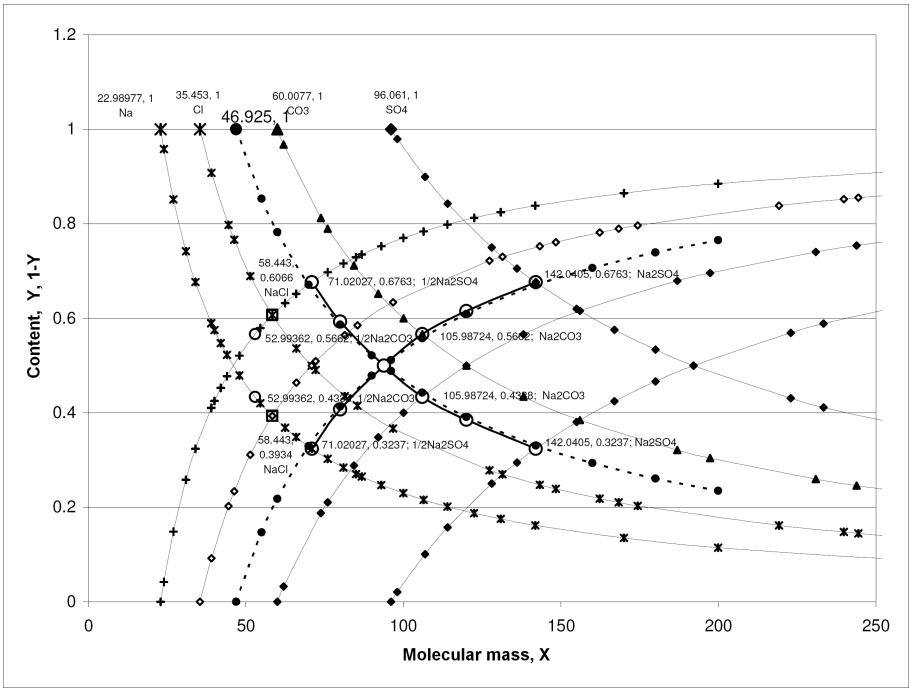

Fig. 5: Application of mathematic methods at calculating of the diagram containing hyperboles of sodium, chlorine and groups CO_3, SO_4. Building up of a new hyperbole based on these data.

2 Application of law of hyperboles for chemical compounds

As it has already been mentioned above, the law is based on the following: the content of the element we are determining in the substance should be referred to its gram-atom. It was shown in detail by the example of oxygen. In compliance with the formula $y = \frac{k}{x}$ element is a numerator, and any compound is a denominator. For example, in order to determine content of sodium (Na) in compounds with molecular mass NaOH (39.9967), Na_2CO_3 (105.9872), Na_3PO_4 (163.941), NaCl (58.443), Na_2SO_4 (142.0406) it is necessary, before the formula, to put coefficients, reducing amount of sodium in it to a unit: 1, $\frac{1}{2}$, $\frac{1}{3}$, 1, $\frac{1}{2}$, accordingly. Then, numerically, part of element (Y) will be: 0.5748, 0.4338, 0.4207, 0.3934, and 0.3237. I.e. it is in one range with decreasing, and value $(1-Y)$ with increasing. Both these curves (in pairs) which are built based on these data are referred to one element.

Method of rectangular hyperboles is worked out in order to determine the last element of the Periodic System of D. I. Mendeleev. But its capabilities are much bigger.

Let us build straight and adjoining hyperboles for sodium, chlorine and also for groups CO_3 and SO_4, which form, accordingly, carbonates and sulphates. As we can see in formula $y = \frac{k}{x}$ they replace elements in a numerator. In our last work, we said that hyperboles can by formed by any numbers within location of their tops on a real axis. However, there is a rule for groups, similar to that of 1 gram-atom of the element: their quantity in calculated compounds should not exceed a unit. Otherwise we get a situation shown on Figure 4.

As we can see, it is necessary to put coefficient $\frac{1}{2}$ before the formula of hydroxide at bivalent barium. Then, his compounds will be on hyperboles. In case of non-observance of this rule, their points will be on broken line (circle).

Now we can start to solve a problem of building up new hyperboles, based on existing ones (Figure 5).

Let's mark on them several general points related to the known compounds. On sodium curves there are two points (on each curve) $\frac{1}{2}Na_2CO_3$ and $\frac{1}{2}Na_2SO_4$, which are also located on respective hyperboles but without the coefficient $\frac{1}{2}$ (Na_2CO_3 and Na_2SO_4). Thus, the point $\frac{1}{2}Na_2SO_4$, located on the straight hyperbole of sodium, and its cross points with hyperboles CO_3 and SO_4 form imaginary broken line located between chlorine and CO_3.

In a similar manner it works with adjoining hyperboles. Let's build a formula (by three points) $Y = 63.257\,X^{-1.0658}$ of a power function (or $\ln y = 4.1472 - 1.0658 \ln x$). With the help of mentioned formula we will find some more coordinates, including (obligatory) their crossing center (93.85; 0.5). Then we divide the abscissa of this point by 2 (straight and adjoining hyperboles cross at doubled value of atomic mass) we get X, equal to 46.925, and that is a numerator in a formula of new hyperboles ($y = \frac{46.925}{x}$).

3 Conclusion

Method of rectangular hyperboles makes it possible to do the following:

- to create mathematical basis for using hyperboles of the kind $y = 1 - \frac{k}{x}$ in chemistry;
- to determine existence area of the chemical compounds;
- to calculate formulas of the main lines and cross points of all the hyperboles, including the last element;
- to show the possibility of building up hyperboles whose numerator is a group of elements, including the rule of 1 gram-atom (in this case it is 1 gram-mole);
- to calculate and to build unknown in advance hyperboles by several data of known chemical compounds located on respective curves;
- to control (with high accuracy) the content of synthesized substances;
- to design chemical compounds.

Due to the fact that it is inconvenient to call each time the element 155 (that we calculated in this paper) "the last element" and by the right of the discoverer we decided to call it **KHAZANIUM (Kh)**.

Submitted on February 13, 2007
Accepted on February 19, 2007

References

1. Khazan A. Upper limit in the Periodic System of Elements. *Progress in Physics*, 2007, v. 1, 38–41.
2. Vigotskiy M. Handbook on higher mathematics. Moscow, Nauka, 2004, page 991.

Fast LIBS Identification of Aluminum Alloys

Walid Tawfik Y. Mohamed

National Inst. of Laser Enhanced Science NILES, Dept. of Environmental Applications, Cairo University, Cairo, Egypt
Faculty of Education for Girls, Department of Physics, Gurayyat, North of Al-gouf, Kingdom of Saudi Arabia

E-mail: Walid_Tawfik@hotmail.com

Laser-induced breakdown spectroscopy (LIBS) has been applied to analysis aluminum alloy targets. The plasma is generated by focusing a 300 mJ pulsed Nd: YAG laser on the target in air at atmospheric pressure. Such plasma emission spectrum was collected using a one-meter length wide band fused-silica optical fiber connected to a portable Echelle spectrometer with intensified CCD camera. Spectroscopic analysis of plasma evolution of laser produced plasmas has been characterized in terms of their spectra, electron density and electron temperature assuming the LTE and optically thin plasma conditions. The LIBS spectrum was optimized for high S/N ratio especially for trace elements. The electron temperature and density were determined using the emission intensity and stark broadening, respectively, of selected aluminum spectral lines. The values of these parameters were found to change with the aluminum alloy matrix, i.e. they could be used as a fingerprint character to distinguish between different aluminum alloy matrices using only one major element (aluminum) without needing to analysis the rest of elements in the matrix. Moreover, It was found that the values of T_e and N_e decrease with increasing the trace elements concentrations in the aluminum alloy samples. The obtained results indicate that it is possible to improve the exploitation of LIBS in the remote on-line industrial monitoring application, by following up only the values of T_e and N_e for aluminum in aluminum alloys as a marker for the correct alloying using an optical fiber probe.

1 Introduction

The interaction of high-power pulsed laser light with a target or solid samples has been an active topic not only in plasma physics but also in the field of analytical chemistry. During the paste decade, the use of Laser Induced Plasma Spectroscopy (LIBS) as an alternative elemental analysis technology based on the optical emission spectra of the plasma produced by the interaction of high-power laser with a target has been studied by several authors [1–7]. Because of the lack of pretreatment of the material as well as the speed of analysis, not mentioning the possibility of in situ analysis, this technique offers an attractive solution for a wide range of industrial applications. However, the existent commercial instruments are still not sufficient to guarantee reproducibility and precise quantitative results. In fact, the analytical performance of the LIBS technique depends strongly on the choice of experimental conditions that influence the laser-produced plasma characteristics [8]. The main parameters affecting the performance of LIBS results are as follows: laser intensity, excitation wavelength, laser pulse duration, and the surrounding atmosphere [9]. Moreover, the physical and chemical properties of the sample can affect the produced plasma composition, a phenomenon known as the matrix effect. The interaction between the laser and the target in LIBS is influenced significantly by the overall composition of the target, so that the intensity of the emission lines observed is a function of both the concentration of the elements of interest and the properties of the matrix that contains them. The author published works studied the matrix effect under different experimental conditions to specify causes and find out the methods of correction [4, 6, 7].

On the other hand, from a more fundamental point of view, LIBS diagnostic studies of electron temperature T_e and number density N_e have all been based on assumptions, most importantly those of the existence of local thermodynamic equilibrium LTE conditions and of optically thin plasma [10]. Ciucci et al. [11] have discussed the possibility of devising a calibration free method, i.e. some kind of an "absolute analysis" approach. The success of such approach heavily relies upon the accurate knowledge of the parameters and the validity of the assumptions cited above. Apparently LIBS plasmas fulfill LTE conditions even though during the measurement time, the plasma parameters rapidly change due to expansion. In this connection, one needs to determine the conditions for expanding high density plasmas to be in an equilibrium state as well as of the time duration for the existence of such equilibrium. The aim of the present paper is to study the variation of the plasma parameters with aluminum lines in different aluminum alloy matrices. This will help not only clarifying the constraints to be taken into account when measuring T_e and N_e but also using the matrix effect to distinguish different aluminum alloy matrices.

Sample	Be	Mg	Si	Fe	Cu	Ca	Mn	Al
AL 6063	0.00030	0.54	0.43	0.2	0.085	0.0021	0.081	Balance
AL 4104	0.0017	1.56	9.63	0.7	0.12	0.0021	0.046	Balance
AL 5754	0.0022	2.54	0.22	0.35	0.1	0.0011	0.29	Balance
AL 3104	0.0011	1.15	0.21	0.42	0.17	0.0031	0.92	Balance

Table 1: Beryllium, Copper, iron, magnesium, silicon, calcium and manganese concentrations (in w/w %) in the standard aluminum alloy samples.

2 Experimental setup

A typical LIBS experimental setup, described in details by the author elsewhere [4, 6], is used throughout the present investigations. The plasma formation was attained with the aid of a Q-switched Nd: YAG laser (NY81.30, continuum, USA) operating at 1064 nm (pulse duration of 7 ns) and repetition rate of 0.1 Hz–30 Hz. The laser pulse energy of 100–300 mJ was adjusted by a suitable combination of beam splitters at constant operating high voltage (1.3 kV) and Q-switch delay (1.65 μs) to ensure spatial and temporal beam profile stability. An energy meter (Nova 978, Ophir Optronics Ldt., USA) was employed to monitor the shot to shot pulse energy. The laser beam was focused on aluminum alloy samples by a 10 cm focal length quartz lens to generate the plasma. The emitted light from the plasma plume is collected via a one-meter length wide band fused-silica optical fiber connected to a 0.17 m focal length Echelle spectrometer (Mechelle 7500, Multichannel Instruments, Sweden). The Mechelle 7500 provides a constant spectral resolution of 7500 corresponding to 4 pixels FWHM, over a wavelength range 200–1000 nm displayable in a single spectrum. A gateable, intensified CCD camera, (DiCAM-Pro, PCO Computer Optics, Germany) coupled to the spectrometer was used for detection of the dispersed light. The overall linear dispersion of the spectrometer-camera system ranges from 0.006 nm/pixel (at 200 nm) to 0.033 nm/pixel (at 1000 nm). To avoid the electronic interference and jitters, the CCD intensifier high voltage was triggered optically. The ICCD camera control was performed via Mechelle software (Multichannel Instruments, Stockholm, Sweden). The emission spectra display, processing and analysis were done using 2D- and 3D-GRAMS/32 version 5.1 spectroscopic data analysis software (Galactic Industries, Salem, NH, USA). To improve data reproducibility, and to avoid electronic jittering problem, the laser was set to single shot mode. Then, the Nd:YAG laser beam was focused onto the sample surface at 90° angle. This was done using a 25 mm diameter dichroic mirror that reflects 99% of high energy 1064 nm wavelength. The focal point was set 5 mm below the surface of the sample in order to generate plasma of 800 μm spot diameter. This also minimize breakdown above the surface of any particles and aerosols generally present above the sample. Moreover, for each new sample, before spectral collection, 20 laser pulses were performed to clean the sample surface and removes surface oxides and contamination to ensure that the observed spectrum is representative of the sample composition.

On the other hand, the use of a micro xyz-translation stage as a holder for fused-silica optical fiber facilities maximum intensity of the observed emission light from the plasma plume. Now, we aim to produce LIBS spectra with high precision. Precision is the measure of the degree of reproducibility of a measurement. Laser shot-to-shot variation causes differences in the plasma properties, therefore affects the magnitude of the element signal, and hence degrades the LIBS precision. To improve LIBS precision, spectra from several laser shots have to be averaged in order to reduce statistical error due to laser shot-to-shot fluctuation. We reproduced the measurements at five locations on the sample surface in order to avoid problems linked to sample heterogeneity. Twenty shots were fired at each location and saved in separated files and the average was computed and saved to serve as the library spectrum. For each recorded spectrum, the peak intensity, the Lorentzian curve fitting, the full width at half maximum FWHM, and the center wavelength of each line, as well as the background emission continuum are determined. Data treatment preprocessing of the averaged spectra data was performed in the Windows environment on a Pentium 4 PC using GRAMS/32, Excel (Microsoft Office Excel 2003) and Origin software version 7.0220 (Origin Lab Corp., USA). The averages of peak tables (lists of wavelengths and intensities) of the averaged spectra were roll generated in GRAMS/32 and exported for data evaluation.

We investigated a set of five standard samples of aluminum alloy to study the dependence of the electron density and temperature on the matrix effect. So that, these samples were selected to have trace elements with a range of concentrations. We used disk shaped standard samples of aluminum alloy provided by Alcan international limited (0.5 cm; $\phi = 5$ cm). The concentrations of the trace elements "Mg, Si, Be, Cu, Mn, Fe, Ca" in the aluminum alloy samples are given in Table 1.

3 Results and discussion

3.1 Optimizing LIBS spectrum

Optimizing LIBS for a high resolution aluminum alloy was done by optimizing the experimental conditions including the time delay, the gate delay (the integration time) and the laser irradiance. In fact, the timing of the recorded signal

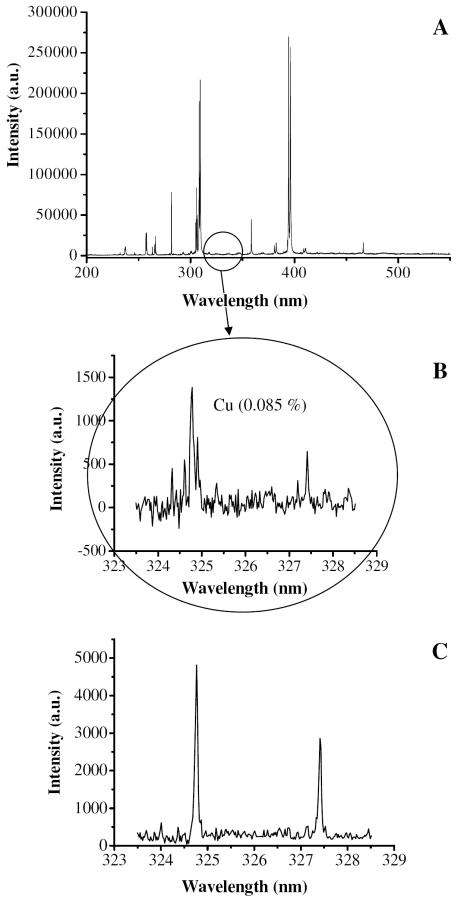

Fig. 1: The figure contains three spectra as follows: A — the panoramic LIBS spectrum in the spectral range 200–700 nm shows the UV-visible emission lines of aluminum as a major element and the emission lines of the trace elements in the aluminum alloy sample AL 6063. B — a zoomed segment showing the copper lines 324.7 nm and 327.4 nm in the UV region recorded at 1.5 μs delay time and 1 μs gate width using laser irradiance of 10^8 W/cm^2 for sample AL 6063 containing copper concentration of 0.085% (w/w) where S/N = 8. C — the same copper lines using the optimized conditions of 2.5 μs delay time and 1.5 μs gate width at 10^{10} W/cm^2 laser irradiance where S/N = 25.

depend on the laser energy and wavelength, so we firstly increased the laser energy from 70 mJ, as used before by the author [6], to 300 mJ. In this case, the laser irradiance increased from $\approx 10^8$ W/cm^2 to $\approx 10^{10}$ W/cm^2 which found to be suitable for the case of aluminum alloy samples having trace elements with concentrations in the ppm range. Then under the late laser irradiance, the delay time, at which the spectrum is recorded from the laser start, was optimized by scanning the delay time with the signal intensity as done previously by the author [6]. It was found that the optimized conditions are 2.5 μs delay time and 1.5 μs gate width at 10^{10} W/cm^2 laser irradiance at the sample surface. The gate delay was limited to 1.5 μs to avoid saturation of the detector. Optimizing LIBS spectrum was done in order to reduce the background signal and increase the signal to noise ratio (S/N). Figure 1 shows a typical plasma emission spectrum for aluminum alloy sample AL 6063. The figure contains three spectra as follows: A — the panoramic LIBS spectrum in the spectral range 200–700 nm shows the UV-visible emission lines of aluminum as a major element and the emission lines of the trace elements in the aluminum alloy sample. B — a zoomed segment showing the copper lines 324.7 nm and 327.4 nm in the UV region recorded at 1.5 μs delay time and 1 μs gate width using laser irradiance of 10^8 W/cm^2 for sample AL 6063 containing copper concentration of 0.085% (w/w) where S/N = 8. C — the same copper lines using the optimized conditions of 2.5 μs delay time and 1.5 μs gate width at 10^{10} W/cm^2 laser irradiance where S/N = 25. This, of course, makes LIBS to be a very high-resolution spectroscopic system for the trace elements with concentrations in the ppm range.

3.2 Plasma parameters and matrix effect

The main factors that influence the light emitted by the plasma are its temperature, the number density of the emitting species, and the electronic density. The number density of the emitting species (e.g. atoms, ions, etc) depends on the total mass ablated by the laser, the plasma temperature, and the degree of the excitation and/or ionization of the plasma. The vaporized amount, in turn, depends on the absorption of the incident laser radiation by the surface, the plasma shielding [12], which is related to the electron density of the plasma, and the laser fluence. Therefore, the knowledge of the plasma temperature and the density of plasma species are vital for the understanding of the dissociation–atomization, excitation, and ionization processes occurring in the plasma. For this reason, study the variation of these plasma parameters with aluminum lines in different aluminum alloy matrices. This will help not only clarifying the constraints to be taken into account when measuring T_e and N_e but also using the matrix effect to distinguish different aluminum alloy matrices.

For plasma in local thermodynamic equilibrium (LTE), the population density of atomic and ionic electronic states is described by a Boltzmann distribution. For optically thin plasma, the re-absorption effects of plasma emission are negligible. So, the emitted spectral line intensity I is a measure of the population of the corresponding energy level of this element in the plasma. For the LTE plasma, the population of an excited level can be related to the total density $N(T)$ of neutral atom or ion of this element by Boltzmann equation [13] as:

$$I = \frac{hc}{4\pi\lambda} N(T) \frac{A_{ki}\, g_k}{U(T)} \exp\left(-\frac{E_k}{KT}\right), \qquad (1)$$

where λ is the wavelength, A_{ki} is the transition probability, g_k is the statistical weight for the upper level, E_k is the

Wavelength (nm)	A_{ki} (s^{-1})	E_k (cm^{-1})	g_k	Stark broadening parameter W (nm)
281.62	3.83E+08	95351	1	4.2900E-04
308.85	1.50E+07	139289.2	5	—
364.92	1.50E+07	132823	3	—
364.92	1.50E+07	132823	3	—
365.11	2.10E+07	132822.8	5	—
365.11	2.10E+07	132822.8	5	—
365.50	2.70E+07	132822.9	7	—
365.50	2.70E+07	132822.9	7	—
370.32	3.80E+07	133916.4	5	—
373.20	4.30E+06	132215.5	3	—
373.39	1.30E+07	132215.5	3	—
373.80	2.10E+07	132215.5	3	—
386.62	3.70E+07	132778.6	1	—
390.07	4.80E+05	85481.35	5	—
559.33	1.10E+08	124794.1	5	—
624.34	1.10E+08	121483.5	7	—

Table 2: A list of the spectroscopic data of the aluminum spectral lines used for the determination of plasma temperature and density of aluminum alloy samples.

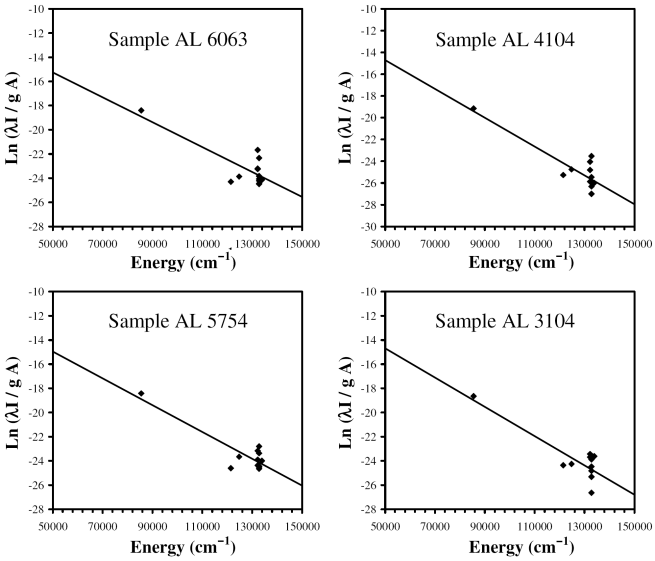

Fig. 2: Four Boltzmann plots were determined form the emission line intensities of aluminum observed in the laser-induced plasma of aluminum alloys. The slope of the plotted curves yields temperatures 13960 K, 12974 K, 11871 K, and 10841 K for the samples AL 6063, AL 5754, AL 3104 and AL 4104 respectively.

excited level energy, T is the temperature (in LTE all temperatures are assumed to be equal, i.e. $T_e \approx T_{ion} \approx T_{plasma}$), K is the Boltzmann constants, $U(T)$ is the partition function.

The emitted spectral line intensity from a given state of excitation can be used to evaluate the plasma temperature. The lines must be well resolved for accurately evaluating their wavelengths λ, intensities I, and their transition probabilities A_{ki} must be know.

Reformulating Eqn. (1) gives;

$$\ln \frac{I\lambda}{A_{ki}\, g_k} = -\frac{1}{KT} E_k + \ln \frac{C\, F}{U(T)}\,, \qquad (2)$$

where F is an experimental factor and C is the species concentration.

By plotting the left hand side of Eqn. (2) vs. the excited level energy E_k, the plasma temperature can be obtained from the slope of obtained straight line.

During the early stages of plasma formation, the emitted spectrum is dominated by an intense continuum (Bremsstrahlung radiation), on which several heavily broadened ionic lines of the elements present are superimposed. The broadening of the ionic lines is due to the high electron densities occurring at this initial period (Stark broadening). At the same time, the excited neutral atoms' spectral lines are relatively weak; they are superimposed on the continuum and often overlap with the ionic lines. Hence, they cannot be easily isolated and measured. As a consequence, the measurement of their intensity for the construction of Boltzmann plots becomes problematic at early times (e.g. the first few hundred nanoseconds) and the use of time delay is compulsory. However, each spectral line exhibits different temporal evolution that is element and atomic energy level specific. Under our experimental conditions, a delay time of 2.5 μs delay time and 1.5 μs gate width at 10^{10} W/cm^2 laser irradiance have been determined as optimum conditions (as described in Section 3.1 before). Under these experimental conditions, the plasma temperatures were determined form the emission line intensities of sixteen selected aluminum lines (see Table 2) observed in the laser-induced plasma of different aluminum alloy targets. Figure 2 show four Boltzmann plots of Eqn. (2), for these lines where the data were fitted with the least-square approximation. The spectral lines wavelengths, energies of the upper levels, statistical weights, and transition probabilities used for these lines were obtained from NIST [14] and Griem [13], and listed in Table 3. The slope of the plotted curves yields temperatures 13960 K, 12974 K, 11871 K, and 10841 K for the samples AL 6063, AL 5754, AL 3104 and AL 4104 respectively as listed in Table 3).

On the other hand, the electron number density can be obtained from the Stark-broadening of the emission lines [15]. This is because, Stark-broadening results from Coulomb interactions between the radiator and the charged particles present in the plasma. Both ions and electrons induce Stark broadening, but electrons are responsible for the major part because of their higher relative velocities. The electrons in the plasma can perturb the energy levels of the individual ions which broaden the emission lines originating from these excited levels. Stark broadening of well-isolated lines in the

Plasma parameters	Sample AL6063	Sample AL 5754	Sample AL 3104	Sample AL 4104
Electron Temperature (Kelvin)	13960	12974	11871	10841
Electron Density (cm^{-3})	7.28×10^{18}	4.28×10^{18}	4.44×10^{18}	2.28×10^{18}

Table 3: The plasma electron temperature T_e and density N_e determined from aluminum spectral lines in the four standard aluminum alloy samples.

plasma is, thus, useful for estimating the electron number densities provided that the Stark-broadening coefficients have been measured or calculated. The line profile for stark broadened is well described by a Lorentzian function. Since the instrumental line-broadening exhibit Gaussian shape, then the stark line width $\Delta\lambda_{FWHM}$ can be extracted from the measured line width $\Delta\lambda_{observed}$ by subtracting the instrumental line broadening $\Delta\lambda_{instrument}$:

$$\Delta\lambda_{FWHM} = \Delta\lambda_{observed} - \Delta\lambda_{instrument}\,. \qquad (3)$$

In our case $\Delta\lambda_{instrument}$ was 0.05 nm (determined by measuring the FWHM of the Hg lines emitted by a standard low pressure Hg lamp).

The width of stark broadening spectral line depends on the electron density N_e. Both the linear and the quadratic stark effect are encountered in spectroscopy. Only the hydrogen atom and H-like ion exhibit the linear stark effect. For the linear stark effect the electron density should be deduced from H line width from the formula [13]

$$N_e = C(N_e, T)\,\Delta\lambda_{FWHM}^{3/2} \qquad (4)$$

the values of the parameter $C(N_e, T)$ are tabulated in the literature [13], which determine the relative contribution of the electron collision on the electrostatic fields, and depend weakly on N_e and T.

For a non-H-like line, the electron density (in cm^{-3}) could be determined from the FWHM of the line from the formula [13]:

$$N_e \approx \left(\frac{\Delta\lambda_{FWHM}}{2W}\right)\times 10^{16}, \qquad (5)$$

W is the electron impact parameter (stark broadening value) and it is given in Table 2). The last formula is generally used for calculations of plasma generated from solid targets [7, 12].

The aluminum line 281.62 nm was identified as candidate for electron-density measurements. Figure 3 shows, the 281.62 nm line with sufficient resolution to measure the full width at half-maximum ($\lambda_{1/2}$) at four different aluminum alloy samples. All the data points were fitted with Lorentzian fitting function using the Origin software to determine ($\lambda_{1/2}$) as shown in Fig. 3 and found to be 0.113 nm, 0.070 nm, 0.092 nm and 0.088 nm for the samples AL6063, AL 4104, AL 5754, and AL 3104 respectively. Substituting the values of $\lambda_{1/2}$ in Eqn. (3) and the corresponding value of stark broadening W (4.29×10^{-4} nm from Griem [13] at plasma temperature of 10000 K) in Eqn. (5) the electron density values of 7.28×10^{18}, 4.28×10^{18}, 4.44×10^{18}, and 2.28×10^{18}

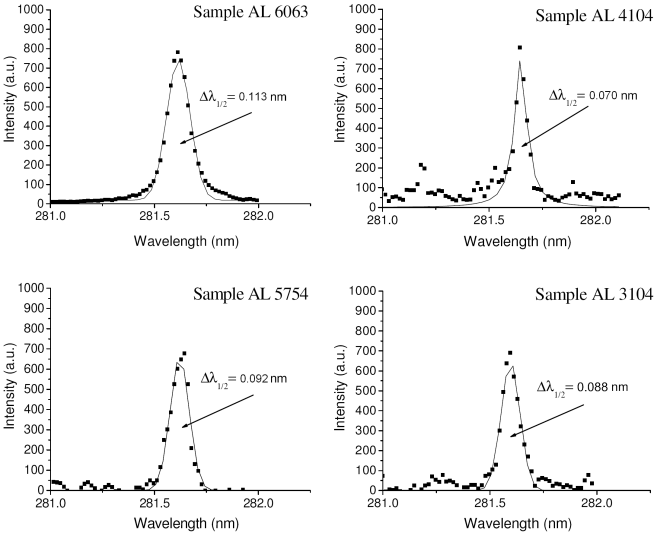

Fig. 3: The 281.62 nm line with sufficient resolution to measure the full width at half-maximum ($\lambda_{1/2}$) at four different aluminum alloy samples. All the data points were fitted with Lorentzian fitting function using the Origin software and the values of $\lambda_{1/2}$ found to be 0.113 nm, 0.070 nm, 0.092 nm and 0.088 nm for the samples AL6063 , AL 4104, AL 5754, and AL 3104 respectively.

were obtained for the samples AL 6063, AL 5754, AL 3104 and AL 4104 respectively as listed in Table 3.

The above obtained results reveal that plasma parameters (T_e, N_e) change with changing the aluminum alloy matrix i.e. matrix dependent. Moreover, by comparing the results of the four samples in Table 3 with the concentrations of the trace elements in Table 1, one could recognized that while the concentrations of trace elements increase both values of T_e and N_e decrease. This is well clear by comparing the two samples AL 6063 and AL 4104 thus while all the trace elements, except Mn, increase (silicon concentration increases from 0.43% to 9.63%), both values of T_e and N_e decrease from 13960 K, $7.28\times10^{18}cm^{-3}$ to 10841 K, $2.28\times10^{18}cm^{-3}$, respectively. This result might occur because increasing the "trace element" concentration comprises increasing portion of the laser-target interaction volume of that trace element and decreases the laser-target interaction volume of the major element (aluminum). Moreover, aluminum "the major element" species are easy to be ionized than the species of the seven trace elements which leads to higher electron density for aluminum alloy samples with low trace elements concentrations than for relatively high trace elements concentrations. Moreover, this is clear since,

the ionization potential of Al, Ca, Be, Mg, Si, Mn, Fe, and Cu are (in eV) 5.98, 6.11, 9.32, 7.64, 8.15, 7.43, 7.87 and 7.72 respectively. The last observed result agrees with previously observed results obtained by O. Samek [15] and Rusak et al. [16].

Finally, by knowing the electron density and the plasma temperature we can determine whether the local thermodynamic equilibrium (LTE) assumption is valid applying the criterion given by McWhirter [17], Bekefi [18] where the lower limit for electron density for which the plasma will be in LTE is:

$$N_e \geqslant 1.4\times10^{14}\Delta E^3\, T^{1/2}, \qquad (6)$$

ΔE is the largest energy transition for which the condition holds and T is the plasma temperature.

In the present case $\Delta E = 4.34$ eV for Mg (see Ref. [13]) and the highest temperature is 1.2 eV (13960 K), then the electron density lower limit value given by Eqn. (6) is 1.25×10^{16} cm^{-3}. The experimentally calculated densities are greater than this value, which is consistent with the assumption that the LTE prevailing in the plasma.

4 Conclusion

LIBS technique has been used to analysis different aluminum alloy samples. The LIBS spectrum was optimized for high S/N ratio especially for trace elements. The characteristic plasma parameters (T_e, N_e) were determined using selected aluminum spectral lines. The values of these parameters were found to change with the aluminum alloy matrix, i.e. they could be used as a fingerprint character to distinguish between different aluminum alloy matrices using only one major element (aluminum) without needing to analysis the rest of elements in the matrix. Moreover, It was found that the values of T_e and N_e decrease with increasing the trace elements concentrations in the aluminum alloy samples.

For industrial application, LIBS could be applied in the on-line industrial process that following up elemental concentration in aluminum alloys by only measuring T_e and N_e for the aluminum using an optical fiber probe. This could be done by building a database containing the determined values of T_e and N_e for a range of standard aluminum alloy matrices. Then the unknown aluminum alloy sample could be identified just by comparing its measured T_e and N_e values with the previously stored values in our database.

Acknowledgment

The author gratefully acknowledges the support of Prof. Mohamed Abel-Harith and Prof. M. Sabsabi specially for offering the aluminum alloy samples.

Submitted on February 07, 2007
Accepted on March 06, 2007
Revised version received on March 15, 2007

References

1. Radziemski L. J. Review of selected analytical applications of laser plasmas and laser ablation, 1987–1994. *Microchem. J.*, 1994, v. 50, 218–234.
2. Rusak D. A., Castle B. C., Smith B. W., and Winefordner J. D. Fundamentals and applications of laser-induced breakdown spectroscopy. *Crit. Rev. Anal. Chem.*, 1997, v. 27, 257–290.
3. Radziemski L. From LASER to LIBS, the path of technology development. *Spectrochim. Acta B*, 2002, v. 57, 1109–1113.
4. Sabsabi M., Detalle V., Harith M. A., Walid Tawfik and Imam H. Comparative study of two new commercial Echelle spectrometers equipped with intensified CCD for analysis of laser-induced breakdown spectroscopy. *Applied Optics*, 2003, v. 42, No. 30, 6094–6098.
5. Soliman M., Walid Tawfik and Harith M. A. Quantitative elemental analysis of agricultural drainage water using laser induced breakdown spectroscopy. *First Cairo Conference on Plasma Physics & Applications*, 2003, Cairo, Egypt, Forschungszentrum Juelich GmbH, Bilateral Seminars of the International Bureau, v. 34, 240–243.
6. Ismail M. A., Imam H., Elhassan A., Walid Tawfik and Harith M. A. LIBS limit of detection and plasma parameters of some elements in two different metallic matrices. *J. Anal. At. Spectrom.*, 2004, v. 19, 1–7.
7. Walid Tawfik and Abeer Askar. Study of the matrix effect on the plasma characterization of heavy elements in soil sediments using LIBS with a portable Echelle spectrometer. *Progress in Physics*, 2007, v. 1, 47–53.
8. Castle B., Talabardon K., Smith B. W. and Winefordner J. D. *Appl. Spectrosc.*, 1998, v. 52, 649–657.
9. Tognoni E., Palleschi V., Corsi M. and Cristoforetti G. *Spectrochim. Acta Part B*, 2002, v. 57, 1115–1130.
10. Yalcin S., Crosley D. R., Smith G. P. and Faris G. W. *Appl. Phys. B*, 1999, v. 68, 121–130.
11. Ciucci A., Corsi M., Palleschi V., Rastelli S., Salvetti A. and Tognoni E. *Applied Spectroscopy*, 1999, v. 53, 960-964.
12. Le Drogoff B., Margotb J., Chakera M., Sabsabi M., Barthelemy O., Johnstona T. W., Lavillea S., Vidala F. and von Kaenela Y. *Spectrochimica Acta Part B*, 2001, v. 56, 987–1002.
13. Griem H. R. Plasma Spectroscopy. McGraw-Hill, N.Y., 1964.
14. NIST National Institute of Standards and Technology, USA, electronic database, http://physics.nist.gov/PhysRefData/ASD/lines_form.html
15. Samek O., Beddows D. C. S., Telle H. H., Kaiser J., Liska M., Caceres J. O. and Gonzales Urena A. *Spectrochimica Acta Part B*, 2001, v. 56, 865–875.
16. Rusak D. A., Clara M., Austin E. E., Visser K., Niessner R., Smith B. W. and Winefordner J. D. *Applied Spectroscopy*, 1997, v. 51, No. 11, 1628–1631.
17. McWhirter R. W. P. In: *Plasma Diagnostic Techniques*, Academic Press, New York, 1965, Ch. 5, 206.
18. Bekefi G. Principles of laser plasmas. Wiley, New York, 1976, 550–605.

Notes on Pioneer Anomaly Explanation by Sattellite-Shift Formula of Quaternion Relativity: Remarks on "Less Mundane Explanation of Pioneer Anomaly from Q-Relativity"

Alexander Yefremov

Institute of Gravitation and Cosmology, Peoples' Friendship University of Russia, Miklukho-Maklaya Str. 6, Moscow 117198, Russia

E-mail: a.yefremov@rudn.ru

Use of satellite shift formula emerging in Quaternion (Q-) model of relativity theory for explanation of Pioneer anomaly [1] is critically discussed. A cinematic scheme more suitable for the case is constructed with the help of Q-model methods. An appropriate formula for apparent deceleration resulting from existence of observer-object relative velocity is derived. Preliminary quantitative assessments made on the base of Pioneer 10/11 data demonstrate closure of the assumed "relativistic deceleration" and observed "Doppler deceleration" values.

1 Introduction. Limits of satellite-shift formula

Recently [1] there was an attempt to give an explanation of Pioneer anomaly essentially using formula for relativistic shift of planet's fast satellites observed from the Earth. This formula was derived within framework of Q-method developed to calculate relativistic effects using $\mathrm{SO}(1,2)$ form-invariant quaternion square root from space-time interval rather than the interval itself [2]; in particular this advantageously permits to describe relativistic motions of any non-inertial frames. The last option was used to find mentioned formula that describes cinematic situation comprising three Solar System objects: the Earth (with observer on it), a planet, and its satellite revolving with comparatively large angular velocity. Due to existence of Earth-planet relative velocity, not great though and variable but permanent, the cycle frequency of satellite rotation (observed from the Earth) is apparently less that in realty, i.e. the "planet's clock" is slowing down, and calculation shows that the gap is growing linearly with time. Visually it looks that the satellite position on its orbit is apparently behind an expected place. For very fast satellites (like Jupiter's Metis and Adrastea) and for sufficiently long period of time the effect can probably be experimentally detected. Same effect exists of course for Mars's satellites and it is computed that monthly apparent shift on its orbit of e.g. Phobos is about 50 meters (that is by the way can be important and taken into account when planning expedition of spacecraft closely approaching the moon).

In paper of F. Smarandache and V. Christianto [1] the discussed formula was used to describe famous Pioneer effect, implying that the last great acceleration the space probe received when approached very close to Jupiter; in particular data concerning Adrastea, whose location was as close to Jupiter as the space probe, were cited in [1]. Combined with ether drift effect the formula gives good coincidence (up to 0.26%) with value of emission angle shift required to explain observation data of Pioneer's signal Doppler residuals [3].

This surprisingly exact result nevertheless should not lead to understanding that obtained by Q-method mathematical description of a specific mechanical model can bear universal character and fit to arbitrary relativistic situation. One needs to recognize that Pioneer cinematic scheme essentially differs from that of the Earth-planet-satellite model; but if one tries to explain the Pioneer effect using the same relativistic idea as for satellite shift then an adequate cinematic scheme should be elaborated. Happily the Q-method readily offers compact and clear algorithm for construction and description of any relativistic models. In Section 2 a model referring observed frequency shift of Pioneer spacecraft signals to purely relativistic reasons is regarded; some quantitative assessments are made as well as conclusions on ability of the model to explain the anomaly. In Section 3 a short discussion is offered.

2 Earth-Pioneer Q-model and signal frequency shift

Paper [3] enumerates a number of factors attracted to analyze radio data received from Pioneer 10/11 spacecraft, among them gravitational planetary perturbations, radiation pressure, interplanetary media, General Relativity*, the Earth's precession and nutation. It is worth noting here that one significant factor, time delay caused by relative probe-observer motion, is not distinguished in [3]. The fact is understandable: relative motion of spacecraft and observer on the Earth is utterly non-inertial one; Special Relativity is not at all able to cope with the case while General Relativity methods involving specific metric and geodesic lines construction

*Unfortunately paper [3] does not indicate to what depth General Relativity is taken into account: whether only Newtonian gravity is modified by Schwarzschild, Kerr (or other) metrics, or cinematic effects are regarded too.

(with all curvature tensor components zero) or additional vector transport postulates are mathematically difficult. Contrary to this the Q-relativity method easily allows building of any non-inertial relativistic scheme; an example describing a spacecraft (probe) and an Earth's observer is given below.

Assume that Pioneer anomaly is a purely relativistic effect caused by existence of Earth-Pioneer relative velocity, variable but permanent. Construct respective model using the Q-method algorithm. Choose Q-frames. Let $\Sigma = (\mathbf{q}_1, \mathbf{q}_2, \mathbf{q}_3)$ be the Earth's frame whose Cartesian directing vectors are given by quaternion "imaginary" units $\mathbf{q}_k$ obeying the multiplication rule*

$$1\,\mathbf{q}_k = \mathbf{q}_k\,1 = \mathbf{q}_k\,, \qquad \mathbf{q}_k\,\mathbf{q}_l = -\delta_{kl} + \varepsilon_{klj}\,\mathbf{q}_j\,. \quad (1)$$

Let Q-frame $\Sigma' = \{\mathbf{q}_{k'}\}$ belong to a probe. Suppose for simplicity that vectors $\mathbf{q}_2$, $\mathbf{q}_3$ are in the ecliptic plane as well as (approximately) the probe's trajectory. Assume that vector $\mathbf{q}_2$ of Σ is always parallel to Earth-probe relative velocity V. Now one is able to write rotational equation, main relation of Q-relativity, which ties two frames

$$\Sigma' = O_1^{-i\psi}\,\Sigma\,, \quad (2)$$

here $O_1^{-i\psi}$ is 3×3 orthogonal matrix of rotation about axis No. 1 at imaginary angle $-i\psi$

$$O_1^{-i\psi} = \begin{pmatrix} \cos(i\psi) & -\sin(i\psi) & 0 \\ \sin(-i\psi) & \cos(i\psi) & 0 \\ 0 & 0 & 1 \end{pmatrix} = \begin{pmatrix} \cosh\psi & -i\sinh\psi & 0 \\ i\sinh\psi & \cosh\psi & 0 \\ 0 & 0 & 1 \end{pmatrix}$$

thus "converting" frame Σ into Σ'. The first row in the matrix equation (2)

$$\mathbf{q}_{1'} = \mathbf{q}_1\cosh\psi - \mathbf{q}_2\,i\sinh\psi$$

after straightforward algebra

$$\mathbf{q}_{1'} = \cosh\psi\,(\mathbf{q}_1 - \mathbf{q}_2\,i\tanh\psi) \;\Rightarrow\; \mathbf{q}_{1'} = \frac{dt}{dt'}\,(\mathbf{q}_1 - \mathbf{q}_2\,iV\psi)$$

with usual relativistic relations

$$V = \tanh\psi, \qquad dt = dt'\cosh\psi \quad (3)$$

acquires the form of basic cinematic space-time object of Q-relativity

$$i\,dt'\,\mathbf{q}_{1'} = i\,dt\,\mathbf{q}_1 + dr\,\mathbf{q}_2\,,$$

a specific quaternion square root from space-time interval of Special Relativity

$$(i\,dt'\,\mathbf{q}_{1'})(i\,dt'\,\mathbf{q}_{1'}) = (i\,dt\,\mathbf{q}_1 + dr\,\mathbf{q}_2)(i\,dt\,\mathbf{q}_1 + dr\,\mathbf{q}_2) \;\Rightarrow$$
$$\Rightarrow\; dt'^2 = dt^2 - dr^2,$$

dt' being proper time segment of the probe. Eq. (3) yields ratio for probe-Earth signal period (small compared to time of observation) $T = T'\cosh\psi$, i.e. observed from Earth the period is apparently longer than it really is. Vice versa, observed frequency $f = 1/T$ is smaller than the real one f'

$$f = \frac{1}{T} = \frac{1}{T\cosh\psi} = \frac{f'}{\cosh\psi} = f'\sqrt{1-(V/c)^2}, \quad (4)$$

or for small relative velocity

$$f \cong f'\left(1 - \frac{V^2}{2c^2}\right).$$

This means that there exists certain purely apparent relativistic shift of the probe's signal detected by the Earth observer

$$\Delta f = f' - f = f'\,\frac{V^2}{2c^2}\,, \quad \text{or} \quad \frac{\Delta f}{f'} = \frac{V^2}{2c^2} = \frac{\varepsilon}{c^2}\,, \quad (5)$$

ε being the probe's kinetic energy per unit mass computed in a chosen frame. Contrary to pure Doppler effect the shift given by Eq. (5) does not depend on the direction of relative velocity of involved objects since in fact it is just another manifestation of relativistic delay of time. Light coming to observer from any relatively (and arbitrary) moving body is universally "more red" than originally emitted signal; as well all other frequencies attributed to observed moving bodies are smaller then original ones, and namely this idea was explored for derivation of satellite shift formula.

Experimental observation of the frequency change (5) must lead to conclusion that there exists respective "Doppler velocity" V_D entering formula well known from Special Relativity

$$f = \frac{f'}{\sqrt{1-(V_D/c)^2}}\left(1 - \frac{V_D}{c}\cos\beta\right), \quad (6)$$

β being angle between velocity vector and wave vector of emitted signal. If $\beta = 0$ and smaller relativistic correction are neglected then Eq. (6) can be rewritten in the form similar to Eq. (5)

$$\frac{\Delta f}{f'} \cong \frac{V_D}{c^2}\,; \quad (7)$$

comparison of Eqs. (7) and (5) yields very simple formula for calculated (and allegedly existent) "Doppler velocity" corresponding to observed relativistic frequency change

$$V_D \cong \frac{\varepsilon}{c}\,. \quad (8)$$

Estimation of the value of V_D can be done using picture of Pioneer 10/11 trajectories (Fig.1) projected upon ecliptic plane (provided in NASA report [4]); other spacecraft traces are also shown, the Earth's orbit radius too small to be indicated.

Schematically the cinematic situation for Pioneer 10 is shown at Fig. 2 where the trajectory looks as a straight line inclined at constant angle λ to axis $\mathbf{q}_2$, while the Earth's position on its orbit is determined by angle $\alpha = \Omega t$, $\Omega = 3.98\times10^{-7}\,s^{-1}$ being the Earth's orbital angular velocity. Vectors of the probe's and Earth's velocities in Solar Ecliptic

*Latin indices are 3-dimensional (3D), δ_{kl} is 3D Kroneker symbol, ε_{jkl} is 3D Levi-Civita symbol; summation convention is assumed.

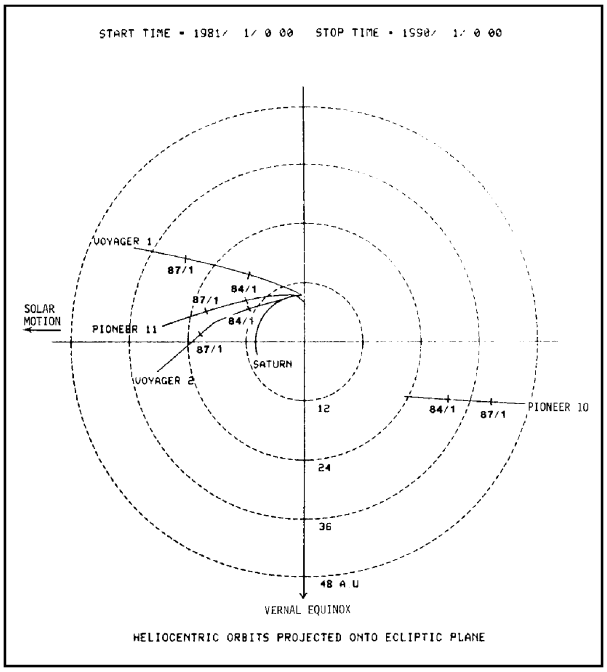

Fig. 1: Spacecraft trajectories on the ecliptic plane. (After NASA original data [4]. Used by permission.)

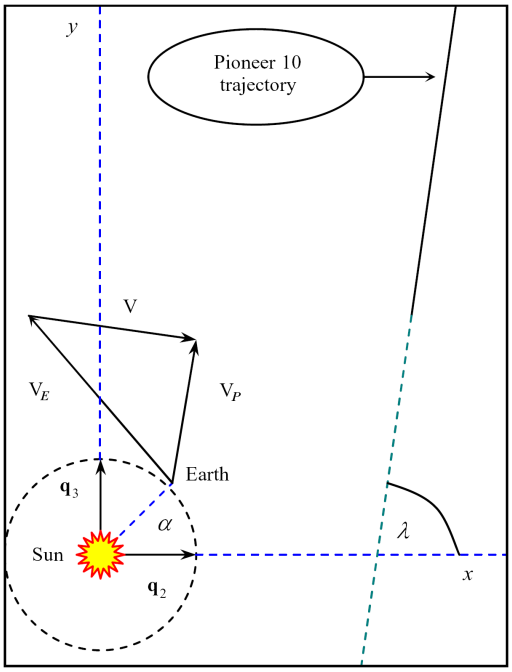

Fig. 2: Earth-Pioneer 10 cinematic scheme, where the trajectory looks as a straight line inclined at constant angle λ to axis $\mathbf{q}_2$.

(SE) coordinate system* are respectively denoted as $\mathbf{V}_P$ and $\mathbf{V}_E$; their vector subtraction gives relative Earth-probe velocity $\mathbf{V} = \mathbf{V}_P - \mathbf{V}_E$ so that

$$V_D(t) = \frac{V^2}{2c} = \frac{V_P^2 + V_E^2 - 2V_P V_E \cos(\Omega t - \lambda)}{2c}, \qquad (9)$$

and respective "Doppler acceleration" is

$$a_D = \dot{V}_D(t) = \\ = \frac{V_P \dot{V}_P - \dot{V}_P V_E \cos(\Omega t - \lambda) + \Omega V_P V_E \sin(\Omega t - \lambda)}{c}. \qquad (10)$$

In Eq. (10) the first term in the numerator claims existence of secular deceleration, since escaping from the Sun's and Jupiter's gravity the probe is permanently decelerated, $\dot{V}_p < 0$; the result is that the frequency gap shrinks giving rise to pure relativistic blue shift. Other sign-changing terms in right-hand-side of Eq. (10) are periodic (annual) ones; they may cause blue shift as well as red shift. Thus Eq. (10) shows that, although relative probe-Earth velocity incorporates into difference between real and observed frequency, nevertheless secular change of the difference is to be related only to relative probe-Sun velocity. Distinguish this term temporary ignoring the annual modulations; then the secular deceleration formula is reduced as

$$a_{SD} \cong \frac{\dot{V}_P V_P}{c}. \qquad (11)$$

*The SE is a heliocentric coordinate system with the z-axis normal to and northward from the ecliptic plane. The x-axis extends toward the first point of Aries (Vernal Equinox, i.e. to the Sun from Earth in the first day of Spring). The y-axis completes the right handed set.

Below only radial components of the probe's velocity and acceleration in Newtonian gravity are taken into account in Eq. (11); it is quite a rough assessment but it allows to conceive order of values. The probe's acceleration caused by the Sun's Newtonian gravity is

$$\dot{V}_P = -\frac{GM_\odot}{R^2}, \qquad (12)$$

$G = 6.67\times10^{-11}\,\mathrm{m^3/kg\times s^2}$, $M_\odot = 1.99\times10^{30}\,\mathrm{kg}$ are respectively gravitational constant and mass of the Sun. NASA data [5] show that in the very middle part (1983–1990) of the whole observational period of Pioneer 10 its radial distance from the Sun changes from $R \cong 28.8\,\mathrm{AU} = 4.31\times10^{12}\,\mathrm{m}$ to $R \cong 48.1\,\mathrm{AU} = 7.2\times10^{12}\,\mathrm{m}$, while year-mean radial velocity varies from $V_P = 15.18\times10^3\,\mathrm{m/s}$ to $V_P = 12.81\times10^3\,\mathrm{m/s}$. Respective values of the secular "relativistic deceleration" values for this period computed with the help of Eqs. (11), (12) vary from $a_{SD} = -3.63\times10^{-10}\,\mathrm{m/s^2}$ to $a_{SD} = -1.23\times10^{-10}\,\mathrm{m/s^2}$. It is interesting (and surprising as well) that these results are very close in order to anomalous "Doppler deceleration" of the probe $a_P = -(8\pm3)\times10^{-10}\,\mathrm{m/s^2}$ cited in [3].

Analogous computations for Pioneer 11, as checking point, show the following. Full time of observation of Pioneer 11 is shorter so observational period is taken from 1984 to 1989, with observational data from the same source [5]. Radial distances for beginning and end of the period are $R \cong 15.1\,\mathrm{AU} = 2.26\times10^{12}\,\mathrm{m}$, $R \cong 25.2\,\mathrm{AU} = 3.77\times10^{12}\,\mathrm{m}$; respective year-mean radial velocities are $V_P = 11.86\times10^3\,\mathrm{m/s}$, $V_P = 12.80\times10^3\,\mathrm{m/s}$. Computed "relativistic deceleration" values for this period are then $a_{SD} = -10.03\times10^{-10}\,\mathrm{m/s^2}$,

$a_{SD} = -5.02 \times 10^{-10}$ m/s^2: this is even in much better correlation (within limits of the cited error) with experimental value of a_P.

3 Discussion

Quantitative estimations presented above allow to conclude: additional blue shift, experimentally registered in Pioneer 10 and 11 signals, and interpreted as Sun-directed acceleration of the spacecraft to some extent, support the assumption of pure relativistic nature of the anomaly. Of course one notes that while Pioneer 11 case shows good coincidence of observed and calculated values of deceleration, values of a_{SD} for Pioneer 10 constitute only (45–15)% of observed Doppler residual; moreover generally in this approach "relativistic deceleration" is a steadily decreasing function, while experimentally (though not directly) detected deceleration a_P is claimed nearly constant. These defects could find explanation first of all in the fact that a primitive "Newtonian radial model" was used for assessments. Preliminary but more attentive reference to NASA data allows noticing that observed angular acceleration of the probes too could significantly incorporate to values of "relativistic deceleration". This problem remains to be regarded elsewhere together with analysis of the angular acceleration itself.

Acknowledgments

The author would like to thank Profs. F. Smarandache and V. Christianto for attention to his quaternion approach aimed to calculate relativistic effects of non-inertial motions. Special thanks to V. Christianto for given information on Pioneer anomaly and numerous helpful discussions.

Submitted on March 01, 2007
Accepted on March 05, 2007

References

1. Smarandache F. and Christianto V. *Progr. in Phys.*, 2007, v. 1, 42–45.
2. Yefremov A. *Grav. & Cosmol.*, 1996, v. 2, No. 4, 335–341.
3. Anderson J. D. et al. arXiv: gr-qc/9808081.
4. http://cohoweb.gsfc.nasa.gov/helios/book1/b1_62.html
5. http://cohoweb.gsfc.nasa.gov/helios/book2/b2_03.html

Single Photon Experiments and Quantum Complementarity

Danko Dimchev Georgiev

Kanazawa University Graduate School of Natural Science and Technology,
Kakuma-machi, Kanazawa-shi, Ishikawa-ken 920-1192, Japan

E-mail: danko@p.kanazawa-u.ac.jp

Single photon experiments have been used as one of the most striking illustrations of the apparently nonclassical nature of the quantum world. In this review we examine the mathematical basis of the principle of complementarity and explain why the Englert-Greenberger duality relation is not violated in the configurations of Unruh and of Afshar.

1 Introduction

In classical physics if we have two distinct physical states $\psi_1 \neq \psi_2$ of a physical system and we know that $\psi_1 \,\mathrm{OR}\, \psi_2$ is a *true* statement we can easily deduce that $\psi_1 \,\mathrm{XOR}\, \psi_2$ is a true statement too. In Quantum Mechanics however we encounter a novel possibility for *quantum coherent superposition*. It has been verified in numerous experiments that a qubit can be prepared in a linear combination of two orthogonal states, and this parallel existence in the quantum realm, in the form $\psi_1 \,\mathrm{AND}\, \psi_2$, is what requires caution when we draw conclusions from a given set of premises — the truth of $\psi_1 \,\mathrm{OR}\, \psi_2$ now does not lead to the truth of $\psi_1 \,\mathrm{XOR}\, \psi_2$.* If a qubit at point x is in a state $\psi_1 \mathrm{XOR} \psi_2$ then ψ_1 and ψ_2 are called *distinguishable states*. Logically, if the qubit at point x is in a state $\psi_1 \mathrm{XNOR} \psi_2$ the two states ψ_1 and ψ_2 will be *indistinguishable*. From the requirement for mathematical consistency it follows that two states ψ_1 and ψ_2 cannot be both *distinguishable* and *indistinguishable* at the same time.

The concept of distinguishability is intimately tied with the notion of quantum complementarity. While the quantum amplitudes evolve linearly according to the Schrödinger equation, the physical observables are obtained from the underlying quantum amplitudes through nonlinearity prescribed by Born's rule.

Thus if quantum states $\psi_1(x) \neq 0$ and $\psi_2(x) \neq 0$ are *indistinguishable* at a point x (coherent superposition), that is $\psi_1(x) \,\mathrm{AND}\, \psi_2(x)$, the probability distribution (observed intensity) is given by $P = |\psi_1(x) + \psi_2(x)|^2$. The *density matrix* of the setup is a pure type one, $\hat{\rho} = \begin{pmatrix} |\psi_1|^2 & \psi_1\psi_2^* \\ \psi_2\psi_1^* & |\psi_2|^2 \end{pmatrix}$, and $\hat{\rho} = \hat{\rho}^2$ holds. The two quantum states do quantum mechanically interfere. In Hilbert space the two functions are not orthogonal and the overlap integral is not *zero* (Vedral [12]):

$$\int \psi_1^*(x)\, \psi_2(x)\, dx \neq 0\,. \tag{1}$$

Alternatively, if quantum states $\psi_1(x)$ and $\psi_2(x)$ are *distinguishable* at a point x (incoherent superposition), that is $\psi_1(x) \mathrm{XOR} \psi_2(x)$, then the probability distribution is given by $\mathcal{P} = |\psi_1(x)|^2 + |\psi_2(x)|^2$. The *(reduced) density matrix* is mixed type one, $\hat{\rho} = \begin{pmatrix} |\psi_1|^2 & 0 \\ 0 & |\psi_2|^2 \end{pmatrix}$, and $\hat{\rho} \neq \hat{\rho}^2$. The two quantum states do not quantum mechanically interfere but just sum classically. In Hilbert space the two functions are orthogonal and the overlap integral is *zero*:

$$\int \psi_1^*(x)\, \psi_2(x)\, dx = 0\,. \tag{2}$$

The observable value given by $\mathcal{P}$ should not necessarily describe an incoherently superposed state. It might as well describe a fictious statistical average of two single amplitude experiments in which either only $\psi_1(x)$ or only $\psi_2(x)$ participates. In this case however $\psi_1(x)$ and $\psi_2(x)$ should be separately normalized to 1, and as elements in the main diagonal of the density matrix must be taken the *statistical probabilities* defining the mixture (Zeh [14]).

Next, despite the fact that qubits generally might take more than one path in a coherent superposition (Feynman and Hibbs [7]), we will still show that the "which way" claims ("*welcher weg*", in German) can be derived rigourously within the quantum mechanical formalism. The "which way" claim will be defined as an existent *one-to-one correspondence (bijection) between elements of two sets* (typically input state and observable).

ψ_1	ψ_2	XOR output
0	0	0
0	1	1
1	0	1
1	1	0

ψ_1	ψ_2	XNOR output
0	0	1
0	1	0
1	0	0
1	1	1

Table 1: Distinguishable –vs– indistinguishable states

*Such a direct interpretation of the AND gate as having corresponding quantum coherent superposed reality is consistent with the prevailing view among working physicists that resembles Everett's many worlds interpretation (MWI) of Quantum Mechanics in many ways (Tegmark and Wheeler [11]). However, the reality of quantum superposition is not a characteristic feature only of MWI. The transactional interpretation (TI) proposed by Cramer [4] and quantum gravity induced objective reduction (OR) proposed by Penrose [8] both admit of the reality of superposed quantum waves, respectively superposed space-times.

$$\overset{\mathfrak{L}_1}{[|\psi\rangle]} \rightarrow \overset{\text{path 1}}{\left[i\frac{1}{\sqrt{2}}|\psi_1\rangle\right]} + \overset{\text{path 2}}{\left[\frac{1}{\sqrt{2}}|\psi_2\rangle\right]} \rightarrow \overset{\text{path 3}}{\left[-\frac{1}{\sqrt{2}}|\psi_1\rangle\right]} + \overset{\text{path 4}}{\left[i\frac{1}{\sqrt{2}}|\psi_2\rangle\right]} \rightarrow \overset{\mathfrak{D}_1}{\left[-\frac{1}{2}|\psi_1\rangle - \frac{1}{2}|\psi_2\rangle\right]} + \overset{\mathfrak{D}_2}{\left[-i\frac{1}{2}|\psi_1\rangle + i\frac{1}{2}|\psi_2\rangle\right]} \quad (3)$$

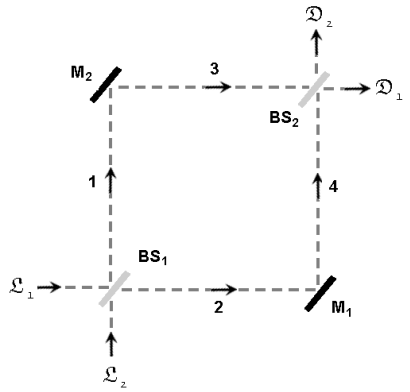

Fig. 1: *Mach-Zehnder interferometer*. Incoming photon at $\mathfrak{L}_1$ quantum mechanically *self-interferes* in order to produce its own full cancelation at detector $\mathfrak{D}_2$ and recover itself entirely at detector $\mathfrak{D}_1$. The opposite holds for the photon entering at $\mathfrak{L}_2$. Legend: BS, beam splitter, M, fully silvered mirror.

2 The Mach-Zehnder interferometer

In order to illustrate the "which way" concept let us introduce the *Mach-Zehnder interferometer*, from which more complicated interferometers can be built up. The setup is symmetric and contains two half-silvered and two fully silvered mirrors positioned at angle $\frac{\pi}{4}$ to the incoming beam (Fig. 1). The action of the beam splitter (half-silvered mirror) will be such as to transmit forward without phase shift $\frac{1}{\sqrt{2}}\psi$ of the incoming quantum amplitude ψ, while at the same time reflects perpendicularly in a coherent superposition $i\frac{1}{\sqrt{2}}\psi$ of it. The action of the fully silvered mirrors will be such as to reflect perpendicularly all of the incoming amplitude ψ with a phase shift of $\frac{\pi}{2}$, which is equivalent to multiplying the state by $e^{i\frac{\pi}{2}} = i$ (Elitzur and Vaidman [6]; Vedral [12]).

In this relatively simple setup it can be shown that a photon entering at $\mathfrak{L}_1$ will always be detected by detector $\mathfrak{D}_1$, whilst a photon entering at $\mathfrak{L}_2$ will always be detected by detector $\mathfrak{D}_2$. It is observed that the photon quantum mechanically *destructively self-interferes* at one of the detectors, whilst it quantum mechanically *constructively self-interferes* at the other detector, creating a one-to-one correspondence between the entry point and the exit point in the Mach-Zehnder interferometer.

Let the incoming amplitude Ψ at $\mathfrak{L}_1$ be normalized so that $|\Psi|^2 = 1$. The evolution of the wave package in the interferometer branches is described by formula (3), where $|\psi_1\rangle$ refers to passage along path 1 and $|\psi_2\rangle$ refers to passage along path 2.

Since the two interferometer paths are indistinguishable one easily sees that at $\mathfrak{D}_1$ one gets *constructive quantum interference*, while at $\mathfrak{D}_2$ one gets *destructive quantum interference*. The inverse will be true if the photon enters at $\mathfrak{L}_2$. Therefore we have established a one-to-one correspondence (bijection) between the entry points and detector clicks. The *indistinguishability* of ψ_1 and ψ_2 allows for *quantum self-interference* of Ψ at the detectors. Insofar as we don't specify which path of the interferometer has been traversed, allow quantum interference of amplitudes at the exit gates coming from both interferometer paths, so ψ_1 AND ψ_2 (*indistinguishable* ψ_1 and ψ_2), we will maintain the one-to-one correspondence between entry points and detectors (*distinguishable* $\mathfrak{D}_1$ and $\mathfrak{D}_2$).

If we however block one of the split beams ψ_1 or ψ_2, or we label ψ_1 and ψ_2, e.g. by different polarization filters, **V** (vertical polarization) and **H** (horizontal polarization), we will lose the quantum interference at the exit gates and the one-to-one correspondence between entry points and exit points will be lost. Thus we have encountered the phenomenon of *complementarity.* We can determine which of the interferometer paths has been taken by the photon, hence ψ_1 XOR ψ_2 (*distinguishable* ψ_1 and ψ_2), and destroy the one-to-one correspondence between entry points and exit gates (*indistinguishable* $\mathfrak{D}_1$ and $\mathfrak{D}_2$). A photon entering at $\mathfrak{L}_1$ (or $\mathfrak{L}_2$) will not self-interfere and consequently could be detected by either of the detectors with probability of $\frac{1}{2}$.

Thus we have shown that quantum coherent superposition of photon paths itself does not preclude the possibility for one to establish one-to-one correspondence (bijection) between two observables (entry and exit points). However, it will be shown that the bijection $\mathfrak{L}_1 \rightarrow \mathfrak{D}_1$, $\mathfrak{L}_2 \rightarrow \mathfrak{D}_2$ is valid for the discussed mixed case in which we have input $\mathfrak{L}_1$ XOR $\mathfrak{L}_2$, yet might not be true in the case where the input points $\mathfrak{L}_1$ and $\mathfrak{L}_2$ are in quantum coherent superposition ($\mathfrak{L}_1$ AND $\mathfrak{L}_2$) as is the case in Unruh's setup.

3 Unruh's interferometer

Unruh's thought experiment is an arrangement that tries to create a more understandable version of Afshar's experiment, which will be discussed later. Unruh's interferometer is essentially a multiple pass interferometer with two elementary building blocks of the Mach-Zehnder type. In Fig. 2 each arm of the interferometer is labelled with a number, and a photon enters at $\mathfrak{L}_1$.

Application of Feynman's *sum over histories* approach leads us to the correct quantum mechanical description of the experiment. Expression (4) is *Dirac's ket notation* for the quantum states evolving in the interferometer arms.

$$\overset{\mathfrak{L}_1}{[|\psi\rangle]} \rightarrow \overset{\text{path 1}}{\left[i\frac{1}{\sqrt{2}}|\psi_1\rangle\right]} + \overset{\text{path 2}}{\left[\frac{1}{\sqrt{2}}|\psi_2\rangle\right]} \rightarrow \overset{\text{path 3}}{\left[-\frac{1}{\sqrt{2}}|\psi_1\rangle\right]} + \overset{\text{path 4}}{\left[i\frac{1}{\sqrt{2}}|\psi_2\rangle\right]} \rightarrow$$

$$\rightarrow \overset{\text{path 5}}{\left[-i\frac{1}{2}|\psi_1\rangle + i\frac{1}{2}|\psi_2\rangle\right]} + \overset{\text{path 6}}{\left[-\frac{1}{2}|\psi_1\rangle - \frac{1}{2}|\psi_2\rangle\right]} \rightarrow \overset{\text{path 7}}{\left[\frac{1}{2}|\psi_1\rangle - \frac{1}{2}|\psi_2\rangle\right]} + \overset{\text{path 8}}{\left[-i\frac{1}{2}|\psi_1\rangle - i\frac{1}{2}|\psi_2\rangle\right]} \rightarrow \tag{4}$$

$$\rightarrow \left[\overset{\mathfrak{D}_1}{\left[\frac{1}{\sqrt{8}}|\psi_1\rangle - \frac{1}{\sqrt{8}}|\psi_2\rangle\right]} + \left[\frac{1}{\sqrt{8}}|\psi_1\rangle + \frac{1}{\sqrt{8}}|\psi_2\rangle\right]\right] + \left[\overset{\mathfrak{D}_2}{\left[i\frac{1}{\sqrt{8}}|\psi_1\rangle - i\frac{1}{\sqrt{8}}|\psi_2\rangle\right]} + \left[-i\frac{1}{\sqrt{8}}|\psi_1\rangle - i\frac{1}{\sqrt{8}}|\psi_2\rangle\right]\right]$$

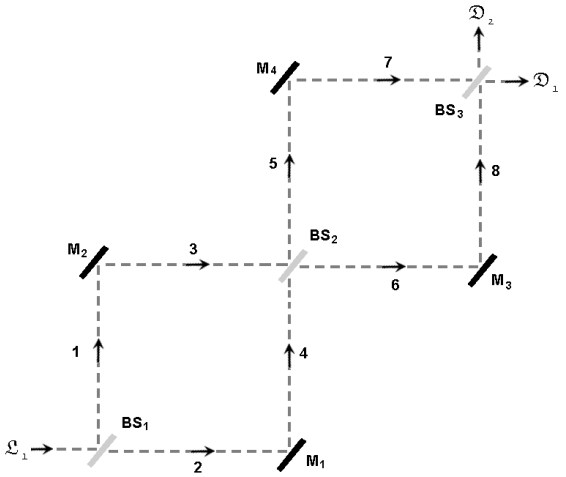

Fig. 2: Unruh's version of a multiple pass interferometer setup that captures the essence of Afshar's experiment. It is composed of two elementary building blocks described in the text, and the incoming photon at $\mathfrak{L}_1$ has an equal chance to end either at $\mathfrak{D}_1$, or at $\mathfrak{D}_2$.

3.1 Unruh's "which way" claim

Unruh obstructed path 1 and correctly argues that the photons coming from the source that pass the first half-silvered mirror and take path 2 (that is they are not reflected to be absorbed by the obstruction located in path 1) will all reach detector $\mathfrak{D}_2$. These are exactly 50% of the initial photons. The explanation is the one provided in the analysis of the Mach-Zehnder interferometer. So Unruh shows that there is a one-to-one corespondence between path 2 and detector $\mathfrak{D}_2$ when path 1 is blocked. Similarly he argues that in the inverted setup with the obstruction in path 2, all the photons that take path 1 (that is they are not absorbed by the obstruction located in path 2) will reach detector $\mathfrak{D}_1$. This suggests a one-to-one correspondence between path 1 and detector $\mathfrak{D}_1$ when path 2 is blocked.

Note at this stage that Unruh investigates a statistical mixture of two single path experiments. Therefore the case is $\psi_1\,\mathrm{XOR}\,\psi_2$, both paths ψ_1 and ψ_2 are *distinguishable* because of the *existent obstruction*, and ψ_1 and ψ_2 do not quantum *cross-interfere* with each other in the second block of the interferometer (in the first block they are separated spatially, in the second branch they are separated temporally). Thus in the mixed setup there is a one-to-one correspondence between paths and exit gates due to the *distinguishability* of ψ_1 and ψ_2, that is, there is no quantum interference between ψ_1 and ψ_2 in the second building block of Unruh's interferometer.

Unruh then unimpedes both paths ψ_1 and ψ_2, and considering the statistical mixture of the two single path experiments argues that photons that end up at detector $\mathfrak{D}_1$ have taken path ψ_1, while those ending at detector $\mathfrak{D}_2$ come from path ψ_2. The logic is that the second building block of the interferometer has both of its arms open, and the one-to-one correspondence is a result of *self-interference* of ψ_1 and *self-interference* of ψ_2 respectively.

The problem now is to secure the conclusion that "which way" information in the form of a one-to-one correspondence between paths ψ_1 and ψ_2 and the two detectors still "remains" when both paths 1 and 2 are unimpeded? The only way to justify the existence of the bijection is to take the following two statements as axioms: (i) ψ_1 and ψ_2 do not *quantum cross-interfere* with each other; (ii) ψ_1 and ψ_2 *can only quantum self-interfere*. Concisely written together, both statements reduce to one logical form, $\psi_1\,\mathrm{XOR}\,\psi_2$ i.e. ψ_1 and ψ_2 are orthogonal states. Thus Unruh's "which way" statement when both paths of the interferometer are unimpeded is equivalent to the statement that the density matrix of the photons at the detectors is a *mixed one*. Thus stated Unruh's "which way" claim, which is mathematically equivalent with the claim for a mixed state density matrix of the setup, is subject to experimental test. Quantum mechanically one may perform experiments to find whether or not two incoming beams are quantum coherent (pure state) or incoherent (mixed state). Hence Unruh's thesis is experimentally disprovable, and in order to keep true his thesis Unruh must immunize it against experimental test by postulating that one cannot experimentally distinguish the mixed state from the pure state. Otherwise one may decide to let the two beams (led away from the detectors) cross each other. If an interference pattern is build up then one will have experimental verification that the density matrix of the setup is not of the *mixed type* ($\psi_1\,\mathrm{XOR}\,\psi_2$, $\hat{\rho} \neq \hat{\rho}^2$), but one of *pure type* ($\psi_1\,\mathrm{AND}\,\psi_2$, $\hat{\rho} = \hat{\rho}^2$). It is not conventional to think that

the mixed state cannot be experimentally distinguished from the pure state, and that is why Unruh's "which way" claim for the double path coherent setup is incorrect. One notices however that if each of the paths 1 and 2 is labelled by different polarization filters, e.g. **V** and **H**, then the density matrix of the setup will be a *mixed one* (incoherent superposition in the second interferometer block), and the "which way" claim will be correct because the different polarizations will convert ψ_1 and ψ_2 into orthogonal states. If the two beams lead away from the detectors and cross, they will not produce an interference pattern.

3.2 Correct "no which way" thesis

We have already shown that if one argues that there is "which way" correspondence, he must accept that ψ_1 and ψ_2 are *distinguishable*, and hence that they will not be able to cross-interfere at arms 5–8 of the interferometer.

Now we will show the opposite; that postulating "unmeasured destructive interference" in arms 5 and 7 of the interferometer, regardless of the fact that the interference is not measured, is sufficient to erase completely the "which way" information. Postulating quantum interference in arms 5–8 is equivalent to postulating *indistinguishability* (quantum coherent superposition) of ψ_1 and ψ_2, which is equivalent to saying that ψ_1 and ψ_2 can annihilate each other.

The quantum amplitude at $\mathfrak{D}_1$ is:

$$\mathfrak{D}_1 : \left[\frac{1}{\sqrt{8}}|\psi_1\rangle - \frac{1}{\sqrt{8}}|\psi_2\rangle\right] + \left[\frac{1}{\sqrt{8}}|\psi_1\rangle + \frac{1}{\sqrt{8}}|\psi_2\rangle\right]. \quad (5)$$

The first two members in the expression have met each other earlier, so they annihilate each other. What remains is $\frac{1}{\sqrt{8}}|\psi_1\rangle + \frac{1}{\sqrt{8}}|\psi_2\rangle$ and when squared gives $\frac{1}{2}|\Psi|^2$, where ψ_1 and ψ_2 contribute equally to the observed probability of detecting a photon. Now is clear why one cannot hold consistently both the existence of "which way" one-to-one correspondence and existent but undetected interference at paths 5 and 6.

- If one postulates ψ_1 XOR ψ_2 then $\frac{1}{\sqrt{8}}|\psi_2\rangle - \frac{1}{\sqrt{8}}|\psi_2\rangle$ will interfere at the exit and the resulting observable intensity $\frac{1}{2}|\Psi|^2$ will come from squaring $\frac{1}{\sqrt{8}}|\psi_1\rangle + + \frac{1}{\sqrt{8}}|\psi_1\rangle$ i.e. only from path 1.
- If one postulates ψ_1 AND ψ_2 then $\frac{1}{\sqrt{8}}|\psi_1\rangle - \frac{1}{\sqrt{8}}|\psi_2\rangle$ will interfere first, and the resulting observable intensity $\frac{1}{2}|\Psi|^2$ will come from squaring $\frac{1}{\sqrt{8}}|\psi_1\rangle + \frac{1}{\sqrt{8}}|\psi_2\rangle$ i.e. both paths 1 and 2.

The "mixing of the two channels" at $\mathfrak{D}_2$ is analogous.

$$\mathfrak{D}_2: \left[i\frac{1}{\sqrt{8}}|\psi_1\rangle - i\frac{1}{\sqrt{8}}|\psi_2\rangle\right] + \left[-i\frac{1}{\sqrt{8}}|\psi_1\rangle - i\frac{1}{\sqrt{8}}|\psi_2\rangle\right]. \quad (6)$$

- If one postulates ψ_1 XOR ψ_2 then $i\frac{1}{\sqrt{8}}|\psi_1\rangle - i\frac{1}{\sqrt{8}}|\psi_1\rangle$ will interfere at the exit and the obtained observable intensity $\frac{1}{2}|\Psi|^2$ will come from squaring $-i\frac{1}{\sqrt{8}}|\psi_2\rangle - - i\frac{1}{\sqrt{8}}|\psi_2\rangle$ i.e. only from path 2.
- If one postulates ψ_1 AND ψ_2 then $i\frac{1}{\sqrt{8}}|\psi_1\rangle - i\frac{1}{\sqrt{8}}|\psi_2\rangle$ will interfere first, and the obtained observable intensity $\frac{1}{2}|\Psi|^2$ will come from squaring of $-i\frac{1}{\sqrt{8}}|\psi_1\rangle - - i\frac{1}{\sqrt{8}}|\psi_2\rangle$ i.e. both paths 1 and 2.

3.3 Inconsistent interpretation: "which way" + pure state density matrix

It has been suggested in web blogs and various colloquia, that only measurement of the interference at arms 5–8 disturbs the "which way" interpretation, and if the destructive quantum interference is not measured it can peacefully coexist with the "which way" claim. Mathematically formulated the claim is that there is "which way" one-to-one correspondence between paths 1 and 2, and $\mathfrak{D}_1$ and $\mathfrak{D}_2$ respectively, while at the same time the whole setup is described by a pure state density matrix. Afshar [1–3] claims an equivalent statement for his setup insisting on a "which way" + pure state density matrix.

We will *prove* that assuming a "which way" + pure state density matrix leads to mathematical inconsistency. In order to show *where the inconsistency arises* we should rewrite the expressions of the quantum amplitudes at the two detectors in a fashion where each of the wavefunctions ψ_1 and ψ_2 is written as a superposition of its own branches $|\psi_{15}\rangle, |\psi_{16}\rangle$ and $|\psi_{25}\rangle, |\psi_{26}\rangle$, respectively, where the second subscript 5 or 6 denotes a branch in the second building block of Unruh's interferometer:

$$\mathfrak{D}_1 : \frac{1}{\sqrt{8}}|\psi_{15}\rangle - \frac{1}{\sqrt{8}}|\psi_{25}\rangle + \frac{1}{\sqrt{8}}|\psi_{16}\rangle + \frac{1}{\sqrt{8}}|\psi_{26}\rangle \quad (7)$$

$$\mathfrak{D}_2 : i\frac{1}{\sqrt{8}}|\psi_{15}\rangle - i\frac{1}{\sqrt{8}}|\psi_{25}\rangle - i\frac{1}{\sqrt{8}}|\psi_{16}\rangle - i\frac{1}{\sqrt{8}}|\psi_{26}\rangle. \quad (8)$$

From the "which way" claim it follows that the contributions to the final intensity (squared amplitude) detected at $\mathfrak{D}_1$ or $\mathfrak{D}_2$ must come from ψ_1 or ψ_2 only. This is possible *if and only if* the individual branches 5 or 6 of each function are *indistinguishable*, so that the claim mathematically yields quantum destructive interference (annihilation) between ψ_{15} and ψ_{16}, and between ψ_{25} and ψ_{26}, respectively.

However to postulate at the same time that the density matrix is a pure type one i.e. there is "*undetected negative quantum cross-interference*" at branch 5 between ψ_1 and ψ_2 (self-interference of Ψ) is equivalent to saying that paths 5 and 6 are *distinguishable*. We have arrived at a logical inconsistency.

Paths 5 and 6 cannot be both *distinguishable* and *indistinguishable* for the quantum state Ψ — this is what the complementarity principle says.

Due to basic arithmetic axiom ψ_{15} cannot entirely annihilate both ψ_{16} and ψ_{25}. Thus the complementarity principle

itself is a manifestation of the underlying mathematical formalism and one ends up with an XOR bifurcation of two inconsistent with each other outcomes. The two alternative outcomes do not "complement" each other instead they logically exclude each other.

We have therefore proved that within standard Quantum Mechanics one cannot claim both "which way" and pure state of the density matrix at the same time. Whether the quantum interference at branch 5 is measured or not does not matter. Its consistent postulation is sufficient to rule out the "which way information".

3.4 Retrospective reconstructions and complementarity

Now notice that arguing that photons possess "which way" information implies that the photon density matrix at detectors is that of a *mixed type*. We have denoted the quantum amplitude through path 1 by ψ_1, and the quantum amplitude through path 2 by ψ_2. Therefore when we *retrospectively reconstruct* the photon probability distribution function we should use the correct complementarity rule $\mathcal{P} = |\psi_1|^2 + |\psi_2|^2$, and we must logically and consistently argue that there is no negative interference at path 5 — simply, we do not just add ψ_1 to ψ_2 but first square each of those amplitudes. Basically, if the two paths ψ_1 and ψ_2 are *distinguishable*, then the interference terms must be *zero*, and the (reduced) density matrix will be of *mixed type* i.e. one with off-diagonal elements being *zeroes*. To accept that there is "which way" information is equivalent to accepting that the setup with both paths unobstructed is a statistical mixture of the two single path setups with obstructions so the complementarity rule for making retrospective predictions is $\mathcal{P} = |\psi_1|^2 + |\psi_2|^2$. This alternative formulation of the principle of complementarity is in a form of instruction as to how to make the correct retrospective reconstruction of a *mixed state* setup — it says that *mixed state setups* should be retrospectively reconstructed with $\mathcal{P} = |\psi_1|^2 + |\psi_2|^2$ distribution.

However, if the beams along paths 1 and 2 interfere so that no photons are expected along path 5, the setup is a "no which way" *pure state* setup. In this case the retrospective photon probability distribution should be calculated as $P = |\psi_1 + \psi_2|^2$. Thus the alternative formulation of the principle of complementarity in a form of instruction as to how to make the correct retrospective reconstruction of *pure state* setup is — *pure state setups* should be retrospectively reconstructed with the $P = |\psi_1 + \psi_2|^2$ distribution.

Taken together the above two instructions provide a clear idea of complementarity — one cannot retrospectively recover a given setup with both types of probability distributions $\mathcal{P} = |\psi_1|^2 + |\psi_2|^2$ and $P = |\psi_1 + \psi_2|^2$ at the same time, because otherwise you will produce a mathematical inconsistency.

One sees that, in some special cases for a given point x both probability distributions coincide, so $\mathcal{P}(x) = P(x)$, and if one observes only the point x the choice of how to retrospectively reconstruct the setup might be tricky. It is unwise to retrospectively reconstruct a *pure state* setup with $\mathcal{P} = |\psi_1|^2 + |\psi_2|^2$ probability distribution. One will not arrive at a direct experimental contradiction if he looks only within the region where $\mathcal{P}(x) = P(x)$. Yet, any measurement outside this region will reveal the improper retrospective reconstruction.

4 Afshar's setup

In Afshar's setup, light generated by a laser passes through two closely spaced circular pinholes. After the dual pinholes, a lens refocuses the light so that *each image of a pinhole* is received by a separate photo-detector. Considering a mixture of single pinhole trials Afshar argues that a photon that goes through *pinhole 1* impinges only on detector $\mathfrak{D}_1$, and similarly, if it goes through *pinhole 2* impinges only on detector $\mathfrak{D}_2$. Exactly as in Unruh's setup, Afshar investigates a statistical mixture $\psi_1 \,\mathrm{XOR}\, \psi_2$ and after that draws *non sequitur* conclusions for the $\psi_1 \,\mathrm{AND}\, \psi_2$ setup. Thus according to Afshar, there is a one-to-one correspondence between pinholes and the corresponding images even when the light coherently passes through both pinholes. While in classical optics this is a straightforward conclusion, in quantum coherent setups we will shortly prove that each image of a pinhole in the coherent dual pinhole setup is counter-intuitively assembled by light coming from both pinholes at once.

Afshar [1, 2] claimed (erroneously) that Unruh's setup (originally intended to disprove Afshar's reasoning) is not equivalent to Afshar's setup, and therefore that the *"plane constructed by Unruh has no wings"*. At first glance one might argue that in Afshar's setup at *image 1* comes only quantum amplitude from *pinhole 1*, and *zero* amplitude from *pinhole 2*, and at *image 2* comes amplitude from *pinhole 2* and *zero* from *pinhole 1*. The putative difference between Unruh's setup and Afshar's setup at first glance seems to be this:

- *Afshar's setup: image 1*: $\frac{1}{\sqrt{2}}\psi_1 + 0 \times \psi_2$ and *image 2*: $\frac{1}{\sqrt{2}}\psi_2 + 0 \times \psi_1$. The *zero* looks "physically unstructured", not a result of negative interference of positive and negative amplitudes contributed from the alternative pinhole.
- *Unruh's setup:* $\mathfrak{D}_1$: $\frac{1}{\sqrt{2}}\psi_1 + \left[\frac{1}{\sqrt{8}}\psi_2 - \frac{1}{\sqrt{8}}\psi_2\right]$ and $\mathfrak{D}_2$: $\frac{1}{\sqrt{2}}\psi_2 + \left[\frac{1}{\sqrt{8}}\psi_1 - \frac{1}{\sqrt{8}}\psi_1\right]$. In this case the *zero* manifests "with physical structure", and is a result of negative interference of positive and negative amplitudes contributed from the alternative path.

If one shows that the "no which way" proof applied to Unruh's setup is not applicable to Afshar's setup, he will also show that Unruh's plane is indeed without wings. If in contrast, one can prove that in Afshar's setup the zero pinhole amplitude contribution at the opposite image is gene-

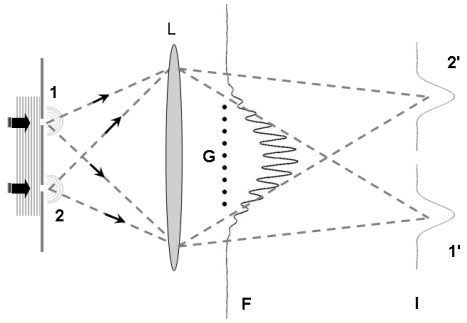

Fig. 3: Action of a lens in a dual pinhole setup — pinholes 1 and 2 create two peak images, $1'$ and $2'$, F denotes the focal plane of the lens, I denotes the image planes of the lens, G is the grid that can be used to verify the existence of an interference pattern in the coherent setup when both pinholes are open. The image is released under GNU free documentation licence by A. Drezet.

rated by *negative quantum interference*, he will show that Unruh's setup is completely equivalent to Afshar's setup. Thus our criticism of Afshar will be the same as in Unruh's case — logical fallacy and mathematical error in claiming both *pure state* and "which way".

It will now be shown that Afshar's setup is equivalent to Unruh's setup. In brief Afshar has dual pinholes, a lens, and detectors that record photons streaming away from the pinhole images created at the image plane of the lens (Afshar [3]). Analogously to Unruh's setup one closes *pinhole 1* and sees that light goes only to *image 2*, then closes *pinhole 2* and sees that light goes only to *image 1*. One may, analogously to Unruh's setup, *inconsistently postulate* "which way" + *pure state density matrix*. However, one should note that, in the single pinhole experiments, at the image plane of the lens the *zero* light intensity outside the central Airy disc of the pinhole image is a result of *destructive quantum interference*. There are many faint higher order maxima and minima outside the central Airy disc resulting from quantum interference. In order for the two pinhole images to be *resolvable** the image of the second pinhole must be outside the central Airy disc, and located in the first negative Airy ring of the first pinhole image (or further away). Therefore in the case of open *pinhole 2* at *image 1* there are destructively interfering quantum amplitudes contributed by *pinhole 2* because *image 1* resides in an Airy minimum of *image 2*. In contrast at *image 2* the waves from *pinhole 2* will constructively interfere. If both pinholes are open and some of the waves coming from *pinhole 1* cross-interfere with waves coming from *pinhole 2* in the space before the lens, there will remain a contribution by *pinhole 2* at *image 1* that will compensate exactly the decrease of quantum waves contributed by *pinhole 1* at *image 1*. Now one has to "choose" which amplitudes will annihilate, and which will remain to be squared. If one postulates the existent interference in the space before the lens (or after the lens as is the case at the focal plane of the lens) then the annihilation between ψ_1 and ψ_2 at the dark fringes will be equivalent to the interference at path 5 of Unruh's setup, and the final observed intensities at the detectors cannot be claimed to come only from one of the pinholes. Thus Afshar is wrong to say that *"Unruh's plane is without wings"*. Afshar's setup is equivalent to Unruh's setup. The treatment of complementarity is analogous. In the case with both pinholes open there is no "which way" information in Afshar's experiment. Counter-intuitively *each image of a pinhole* is assembled from light coming by half from both pinholes.

*One should cautiously note that *resolvable* images of a pinhole is not equivalent with *distinguishable* pinholes. *Resolvable* means that the two images of a pinhole are separated and not fused into a single spot. The *distinguishability* of the pinholes has to be proven by existent bijection between an image and a pinhole.

An exact calculation is adduced by Qureshi [9] where he shows that the quantum state at the overlap region where the dark interference fringes are detected can be written as

$$\psi(y,t) = aC(t)\, e^{-\frac{y^2+y_0^2}{\Omega(t)}} \left[\cosh\frac{2yy_0}{\Omega(t)} + \sinh\frac{2yy_0}{\Omega(t)}\right] + \\ + bC(t)\, e^{-\frac{y^2+y_0^2}{\Omega(t)}} \left[\cosh\frac{2yy_0}{\Omega(t)} - \sinh\frac{2yy_0}{\Omega(t)}\right], \tag{9}$$

where $C(t) = \frac{1}{(\pi/2)^{1/4}\sqrt{\epsilon+2i\hbar t/m\epsilon}}$, $\Omega(t) = \epsilon^2 + 2i\hbar t/m$, a is the amplitude contribution from *pinhole 1*, b is the amplitude contribution from *pinhole 2*, ϵ is the width of the wave-packets, $2y_0$ is the slit separation.

For Afshar's setup $a = b = \frac{1}{\sqrt{2}}$ so the sinh terms cancel out at the dark fringes and what is left is

$$\psi(y,t) = \frac{1}{2}\, aC(t)\left[e^{-\frac{(y-y_0)^2}{\Omega(t)}} + e^{-\frac{(y+y_0)^2}{\Omega(t)}}\right] + \\ + \frac{1}{2}\, bC(t)\, e^{-\frac{y+y_0^2}{\Omega(t)}} \left[e^{-\frac{(y-y_0)^2}{\Omega(t)}} + e^{-\frac{(y+y_0)^2}{\Omega(t)}}\right]. \tag{10}$$

If a lens is used, after the interference has occurred, to direct the $e^{-\frac{(y-y_0)^2}{\Omega(t)}}$ part into one detector and the part $e^{-\frac{(y+y_0)^2}{\Omega(t)}}$ into the other detector, one easily sees that the amplitudes from each slit evolve into a superposition of two parts that go to both detectors. Note that the coefficient of the part from a slit to each of the detectors becomes exactly $\frac{1}{\sqrt{8}}$ as we have obtained via analysis of Unruh's setup.

5 Englert-Greenberger duality relation

Afshar claimed he has violated the Englert-Greenberger duality relation $V^2 + D^2 \leqslant 1$, where V stands for *visibility* and D stands for *distinguishability* and are defined as:

$$D = \frac{\big||\psi_1|^2 - |\psi_2|^2\big|}{|\psi_1|^2 + |\psi_2|^2}, \tag{11}$$

$$V = \frac{2|\psi_1||\psi_2|}{|\psi_1|^2 + |\psi_2|^2}. \tag{12}$$

Since the duality relation is a mathematically true statement (theorem) then it cannot be disproved by experiment and certainly means that Afshar's arguments, through which he violates the duality relation, are inconsistent. Indeed the calculation of V and D depends on the principle of complementarity and distinguishability of the states ψ_1 and ψ_2. The calculation of V and D in Unruh's and Afshar's setup is different for pure state and mixed state setups.

5.1 Mixed state setup

In view of the foregoing explanation for Unruh's claim with *mixed density matrix*, the calculation simply yields $D = 1$ and $V = 0$. This will be true if we label the paths by different polarization filters, or if we investigate a statistical mixture of two single path/slit experiments.

$\mathfrak{D}_1$: $|\psi_1| = \frac{1}{\sqrt{2}}$, $|\psi_2| = 0$,

$\mathfrak{D}_2$: $|\psi_1| = 0$, $|\psi_2| = \frac{1}{\sqrt{2}}$.

Thus the two paths 1 and 2 are *distinguishable* and they *do not quantum mechanically cross-interfere*. This cannot be said for the quantum coherent setup with both paths/slits unimpeded.

5.2 Pure state setup

The correct analysis of Unruh's and Afshar's setup suggests a *pure state density matrix*, and amplitudes for each of the exit gates being $|\psi_1| = |\psi_2| = \frac{1}{\sqrt{8}}$. Thus one gets $D = 0$ and $V = 1$:

$\mathfrak{D}_1$:$|\psi_1| = \frac{1}{\sqrt{8}}$, $|\psi_2| = \frac{1}{\sqrt{8}}$,

$\mathfrak{D}_2$:$|\psi_1| = \frac{1}{\sqrt{8}}$, $|\psi_2| = \frac{1}{\sqrt{8}}$.

The two paths 1 and 2 are *indistinguishable*, and they *quantum mechanically cross-interfere*.

6 Conclusions

It is wrongly believed that the lens at the image plane always provides "which way" information (Afshar [1, 2]; Drezet [5]). However we have shown that Afshar's analysis is inconsistent, and that the distinguishability and visibility in Afshar's setup are erroneously calculated by Afshar *and colleagues* [3]. The two peak image at the image plane in Afshar's setup, even without wire grid in the path of the photons, is an interference pattern and does not provide any "which way" information. Exact calculations for the lens setup have been performed by Qureshi [9] and Reitzner [10], showing that once the two paths interfere the interference cannot be undone, and the "which way" information cannot be regained. The probability distribution can look like the one in a mixed setup, but the retrospective reconstruction of the setup for times before the detector click must be done with interfering waves which do not carry the "which way" information. Afshar's mathematics is inconsistent, hence Afshar's setup does not disprove MWI, or any other rival interpretation of Quantum Mechanics that opposes the standard Copenhagen paradigm.

Submitted on March 01, 2007
Accepted on March 05, 2007
After correction: March 20, 2007

References

1. Afshar S. S. Violation of the principle of complementarity, and its implications. *Proceedings of SPIE*, 2005, v. 5866, 229–244; arXiv: quant-ph/0701027.
2. Afshar S. S. Violation of Bohr's complementarity: one slit or both? *AIP Conference Proceedings*, 2006, v. 810, 294–299; arXiv: quant-ph/0701039.
3. Afshar S. S., Flores E., McDonald K. F. and Knoesel E. Paradox in wave-particle duality. *Foundations of Physics*, 2007, v. 37(2), 295–305; arXiv: quant-ph/0702188.
4. Cramer J. G. The transactional interpretation of quantum mechanics. *Reviews of Modern Physics*, 1986, v. 58, 647–688.
5. Drezet A. Complementarity and Afshar's experiment. arXiv: quant-ph/0508091.
6. Elitzur A. C. and Vaidman L. Is it possible to know about something without ever interacting with it? *Vistas in Astronomy*, 1993, v. 37, 253–256.
7. Feynman R. P. and Hibbs A. R. Quantum physics and path integrals. McGraw-Hill, New York, 1965.
8. Penrose R. On gravity's role in quantum state reduction. *General Relativity and Gravitation*, 1996, v. 28(5), 581–600.
9. Qureshi T. Complementarity and the Afshar experiment. arXiv: quant-ph/0701109.
10. Reitzner D. Comment on Afshar's expriment. arXiv: quant-ph/0701152.
11. Tegmark M. and Wheeler J. A. 100 years of the quantum. *Scientific American*, 2001, v. 284, 68–75; arXiv: quant-ph/0101077.
12. Vedral V. Modern foundations of quantum optics. Imperial College Press, London (UK), 2001.
13. Unruh W. Quantum rebel. 2004, http://axion.physics.ubc.ca/rebel.html.
14. Zeh H. D. The meaning of decoherence. Lecture Notes in Physics, 2000, v. 538, 19–42; arXiv: quant-ph/ 9905004.

Upper Limit of the Periodic Table and Synthesis of Superheavy Elements

Albert Khazan
E-mail: albkhazan@list.ru

For the first time, using the heaviest possible element, the diagram for known nuclides and stable isotopes is constructed. The direction of search of superheavy elements is indicated. The Periodic Table with an eighth period is tabulated.

1 Shell construction of a nucleus, magic numbers

The nucleus of an atom is the central part of the atom, consisting of positively charged protons (Z) and electrically neutral neutrons (N). They interact by means of the strong interaction.

If a nucleus of an atom is consider as a particle with a certain number of protons and neutrons it is called a nuclide. A nuclide is that version of an atom defined by its mass number ($A = Z + N$), its atomic number (Z) and a power condition of its nucleus. Nuclei with identical numbers of protons but different numbers of neutrons are isotopes. The majority of isotopes are unstable. They can turn into other isotopes or elements due to radioactive disintegration of the nucleus by one of the following means: β-decay (emission of electron or positron), α-decay (emission of particles consisting of two protons and two neutrons) or spontaneous nuclear fission of an isotope. If the product of disintegration is also unstable, it too breaks up in due course, and so on, until a stable product is formed.

It has been shown experimentally that a set of these particles becomes particularly stable when the nuclei contain "magic" number of protons or neutrons. The stable structure can be considered as shells or spherical orbits which are completely filled by the particles of a nucleus, by analogy with the filled electronic shells of the noble gases. The numbers of particles forming such a shell are called "magic" numbers. Nuclei with magic number of neutrons or protons are unusually stable and in nuclei with one proton or other than a magic number, the neutron poorly binds the superfluous particle. The relevant values of these numbers are 2, 8, 20, 28, 50, 82, and 126, for which there exists more stable nuclei than for other numbers. Calculations indicate existence of a nucleus with filled shell at $Z = 114$ and $N = 184$ ($^{298}114$) which would be rather stable in relation to spontaneous division. There is experimental data for the connexion of magic numbers to a nucleus with $Z = 164$ [1, 2]. J. Oganesyan [3] has alluded to a Rutherford-model atom which assumes existence of heavy nuclei with atomic numbers within the limits of $Z \sim 170$. At the same time there is a point of view holding that superheavy elements (SHEs) cannot have $Z > 125$ [4]. In October 2006 in was reported that element 118 had been synthesized in Dubna (Russia), with atomic weight 293 [5]. (It is known however, that this weight is understated, owing to technical difficulties associated with the experiments.)

2 The N-Z diagram of nuclei, islands of stability

The search for superheavy nuclei, both in the Nature and by synthesis as products of nuclear reactions, has intensified. In the 1970's 1200 artificially produced nuclei were known [6]. Currently the number is $\sim$3000, and it is estimated that this will increase to $\sim$6500 [7].

In Fig. 1 the neutron-proton diagram of nuclei of stable and artificial isotopes [8–10] is presented.

Light stable or long-lived nuclei which arrangement can be arranged in a valley of stability as shown by small circles. The top set of border points represents a line of proton stability and bottom a line of neutron stability. Beyond these limits begins the so-called, "sea of instability". There is apparently only a narrow strip of stability for which there exists a quite definite parity, N/Z. For nuclei with atomic weight below 40, the numbers of protons and neutrons are approximately identical. With increase in the quantity of neutrons the ratio increases, and in the field of $A = (N + Z) = 250$ it reaches 1.6. The growth in the number of neutrons advances the quantity of protons in heavy nuclei, which in this case become energetically more stable. To the left of the stable nuclei are proton excess nuclei, and on the right neutron excess nuclei. These and others are called exotic nuclei.

The diagram terminates in the last element from the table IUPAC [11] at No. 114, with mass number 289, while scientists suspect nucleus No. 114–298. Such isotopes should possess the increased stability and lifetime of superheavy elements.

This diagram is specially constructed, only on the basis of tabulated data, but augmented by the theoretical upper limit of the Periodic Table [12]. Up to the $Z \sim 60$ the line of trend approaches the middle of a valley of stability, with $N/Z \sim 1.33$. Furthermore, N/Z increases steadily to $\sim$1.5 up to $Z \sim 100$. The equation of the line of trend represents a polynomial of the fourth degree. It is noteworthy that this implies rejection of the upper magic number for neutrons heretofore theoretically supposed.

It is particularly evident from Fig. 2, in which small fragment of the N–Z diagram is amplified and augmented with

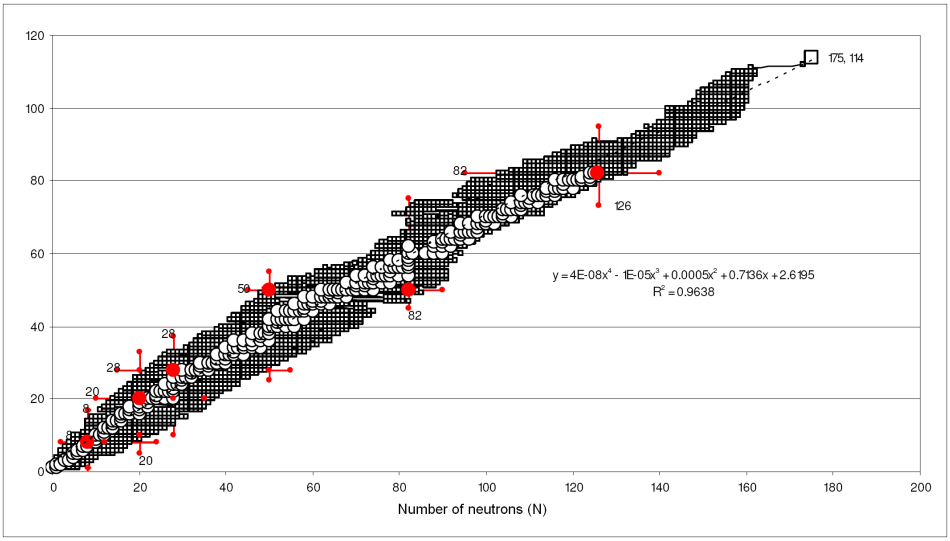

Fig. 1: N–Z diagram of nuclides.

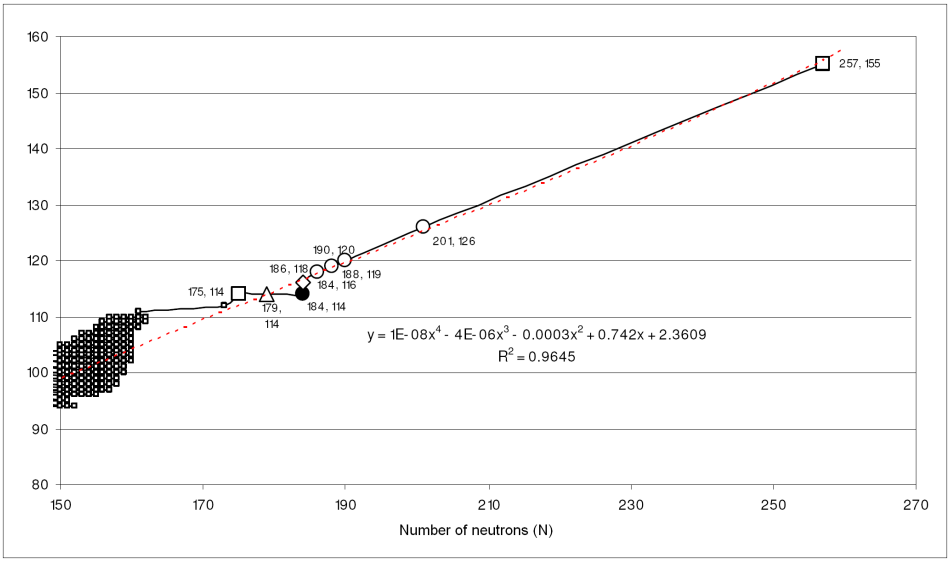

Fig. 2: N–Z diagram of nuclides with elements. For increase in scale the diagram is reduced after carrying out of a line of a trend.

some theoretically determined nuclei, including the heaviest element Z = 155, that the equations of lines of trend and the values of R^2 are practically identical in both Figures. When the line of trend for Fig. 1, without element 155, is extrapolated beyond Z = 114, it passes through the same point in Fig. 2 for Z = 155, indicating that element 155 is correctly placed by theory.

The predicted element No. 114–184 is displaced from the line of a trend. With a nuclear charge of 114 it should have 179 neutrons (A = 293) whereas 184 neutrons has atomic number 116. In the first case there is a surplus 5 neutrons, in the second a deficit of 2 protons. For an element 126 (on hypothesis) the mass number should be 310, but by our data it is 327. The data for mass number 310 corresponds to Z = 120.

It is important to note that there is a close relation between the mass number and the atomic weight. The author's formulation of the Periodic law of D. I. Mendeleev stipulates that the properties of elements (and of simple compounds) depend upon periodicity in mass number. It was established in 1913, in full conformity with the hypothesis of Van den Brook, that the atomic numbers of the chemical elements directly reflect the nuclear charge of their atoms. This law now has the following formulation: "properties of elements and simple substances have a periodic dependence on the nuclear charge of the atoms of elements".

In the Periodic Table the last, practically stable element is bismuth, Z = 83. The six following elements (No.'s 84 to 89) are radioactive and exist in Nature in insignificant quantities, and are followed by the significant radioactive ele-

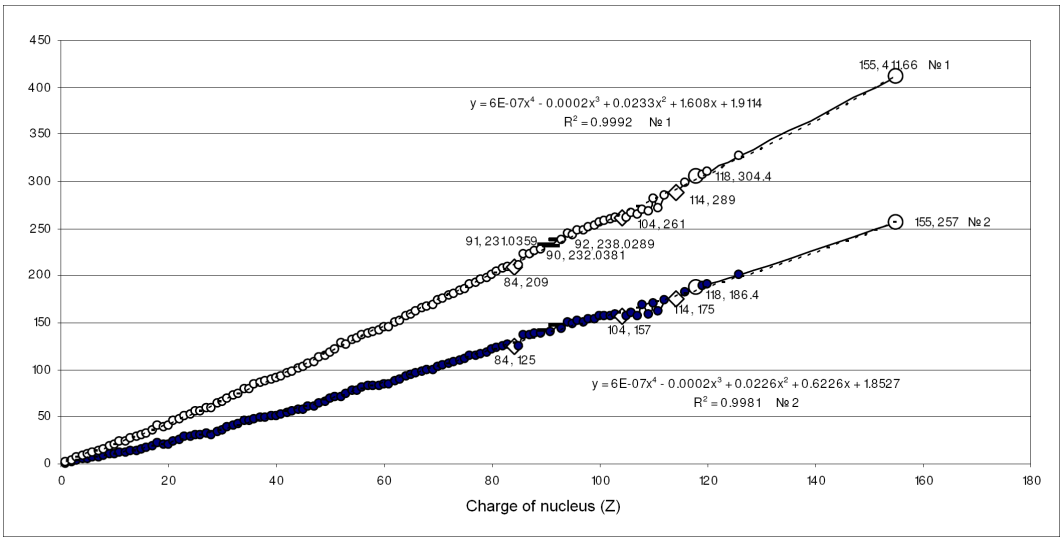

Fig. 3: Dependence of element mass number (1) and corresponding numbers of neutrons (2) on the atomic number in the Periodic Table.

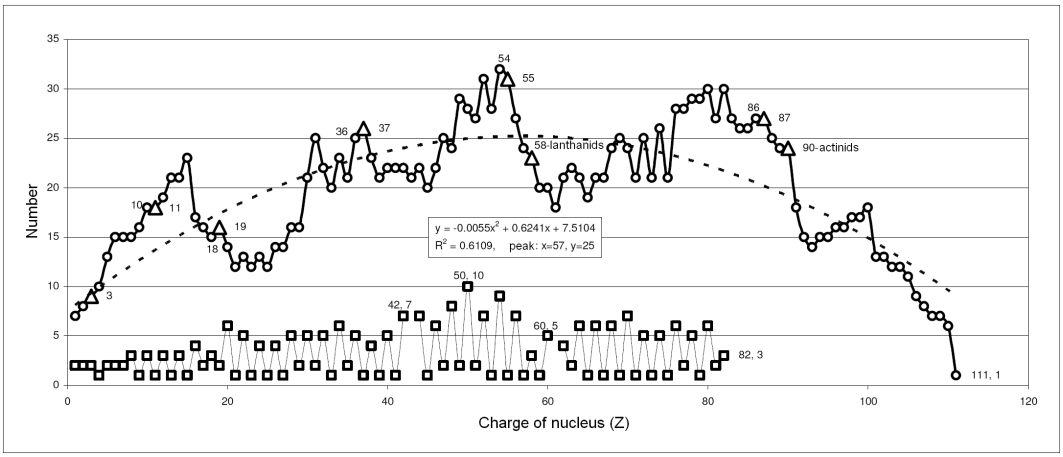

Fig. 4: Dependence of total isotopes (circle) and stable elements (square) on atomic number. The triangle designates the beginning of the periods.

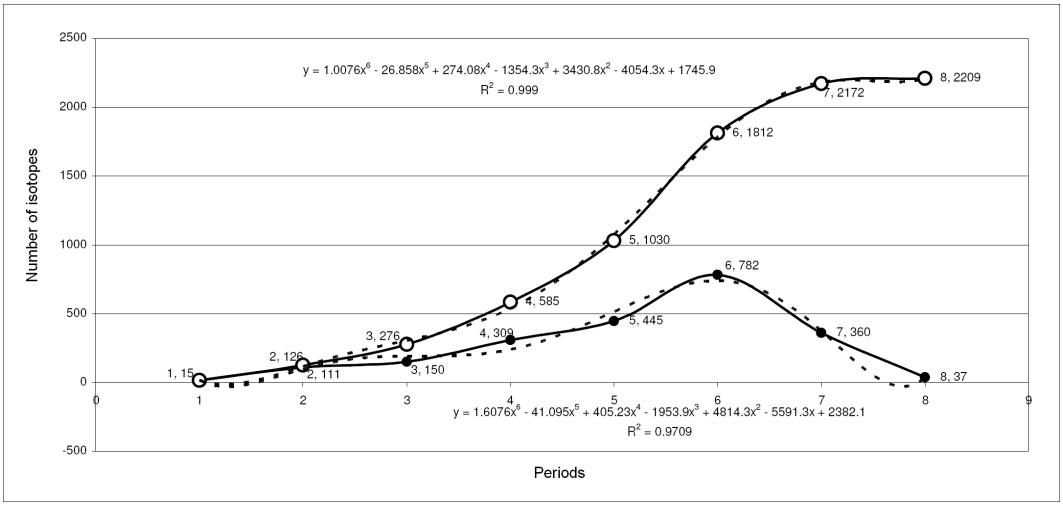

Fig. 5: Distribution of isotopes on the periods: an S-shaped summarizing curve, lower-quantity at each point.

1 H	2A 2											3A 13	4A 14	5A 15	6A 16	7A 17	2 He
3 Li	4 Be											5 B	6 C	7 N	8 O	9 F	10 Ne
11 Na	12 Mg	3B 3	4B 4	5B 5	6B 6	7B 7	8 8	8 9	8 10	1B 11	2B 12	13 Al	14 Si	15 P	16 S	17 Cl	18 Ar
19 K	20 Ca	21 Sc	22 Ti	23 V	24 Cr	25 Mn	26 Fe	27 Co	28 Ni	29 Cu	30 Zn	31 Ga	32 Ge	33 As	34 Se	35 Br	36 Kr
37 Rb	38 Sr	39 Y	40 Zr	41 Nb	42 Mo	43 Tc	44 Ru	45 Rh	46 Pd	47 Ag	48 Cd	49 In	50 Sn	51 Sb	52 Te	53 I	54 Xe
55 Cs	56 Ba	57 La	72 Hf	73 Ta	74 W	75 Re	76 Os	77 Ir	78 Pt	79 Au	80 Hg	81 Tl	82 Pb	83 Bi	84 Po	85 At	86 Rn
87 Fr	88 Ra	89 Ac	104 Rf	105 Db	106 Sg	107 Bh	108 Hs	109 Mt	110 Ds	111 Rg	112 Uub	113 Uut	114 Uuq	115 Uup	116	117	118

Table 1: The standard table of elements (long) with addition of the theoretical eighth period.

58 Ce	59 Pr	60 Nd	61 Pm	62 Sm	63 Eu	64 Gd	65 Tb	66 Dy	67 Ho	68 Er	69 Tm	70 Yb	71 Lu
90 Th	91 Pa	92 U	93 Np	94 Pu	95 Am	96 Cm	97 Bk	98 Cf	99 Es	100 Fm	101 Md	102 No	103 Lr

Table 2: Lanthanides (upper line) and actinides (lower line).

122	123	124	125	126	127	128	129	130	131	132	133	134	135	136	137	138	139
		140	141	142	143	144	145	146	147	148	149	150	151	152	153		

Table 3: The eight period: super actinides (18g and 14f elements)

119	120	121	154	**155** **Kh**

Table 4: The eight period: s-elements (No. 119, 120), g–elements (No. 121), d–elements (No. 154, 155). Element No. 155 must be analogous to Ta, as Db.

119	120	121	122	123	124	125	126	127	128	129	130	131	132	133	134	135	136
137	138	139	154	**155**													

140	141	142	143	144	145	146	147	148	149	150	151	152	153

Table 5: Variation of the Periodic Table of D. I. Mendeleev with heaviest element in the eighth period. A structure for super actinides is offered in a series in work [2].

ments thorium, protactinium and uranium (Z = 90, 91, and 92 respectively). The search for synthetic elements (No.'s 93 to 114) continues. In the IUPAC table, mass numbers for elements which do not have stable nuclides, are contained within square brackets, owing to their ambiguity.

It is clear in Fig. 3 that the reliability (R^2) of approximation for both lines of trend is close to 1. However, in the field of elements No. 104 to No. 114, fluctuations of mass number, and especially the number of neutrons, are apparent.

According to the table, the most long-lived isotope of an element violates the strict law of increase in mass number with increase in atomic number. To check the validity of element No. 155 in the general line of trend of elements for all known and theoretical [12] elements, the two following schedules are adduced:

1. For element numbers 1 to 114, $y = 1.6102\,x^{1.099}$ at $R^2 = 0.9965$;
2. For element numbers 1 to 155, $y = 1.6103\,x^{1.099}$ at $R^2 = 0.9967$.

Upon superposition there is a full overlapping line of trend that testifies to a uniform relation of dependences. Therefore, in analyzing products of nuclear reactions and in statement of experiment it is necessary to consider an element No. 155 for clarification of results.

3 The eighth period of the Periodic Table of elements

Our theoretical determination of the heaviest element at Z = 155 allows for the first time in science a presentation of Mendeleev's Table with an eighth period. Without going into details, we shall note that at the transuranium elements, electrons are located in seven shells (shells 1 to 7 inclusive), which in turn contain the subshells s, p, d, f. In the eighth period there is an 8th environment and a subshell g.

G. T. Seaborg and V. I. Goldanski, on the basis of the quantum theory, have calculated in the eighth period internal transitive superactinoid a series containing 5g-subshells for elements No. 121 to No. 138 and 6f subshells for No. 139 to No. 152. By analogy with the seventh period, No. 119 should be alkaline, No. 120 a alkaline ground metal, No. 121 similar to actinium and lanthanium, No. 153 to No. 162 contain a 7d subshell, and No. 163 to No. 168 an 8p subshell [2]. The latter class resulted because these scientists assumed the presence not only of an 8th, but also a 9th periods, with 50 elements in each.

However, distribution of isotopes depending on a atomic number of the elements (Fig. 4) looks like a parabola, in which branch Y sharply decreases, reaching the value 1 at the end of the seventh period. It is therefore, hardly possible to speak about the probability of 100 additional new elements when in the seventh period there is a set of unresolved problems.

Our problem consisted not so much in development of methods for prediction of additional elements, but in an explanation as to why their number should terminate No. 155. Considering the complexities of synthesis of heavy elements, we have hypothesized that their quantity will not be more than one for each atomic. Then, from Fig. 5 it can be seen that the S-figurative summarizing curve already in the seventh period starts to leave at a horizontal, and the eighth reaches a limit. The bottom curve shows that after a maximum in the sixth period the quantity of isotopes starts to decrease sharply. This provides even more support for our theoretical determination [12] of the heaviest possible element at Z = 155.

In July 2003 an International conference took place in Canada, resulting in publication [13], wherein it is asked, "Has the Periodic Table a limit?"

The head of research on synthesis of elements in Dubna (Russia), J. Oganesyan, has remarked that the question of the number of chemical elements concerns fundamental problems of science, and therefore the question, what is the atomic number of the heaviest element?

Despite the fact that hundreds of versions of the Periodic Table have been offered of the years, none have designated the identity of the heaviest element. The heaviest element is offered in Tables shown in Page 107.

4 Conclusions

With this **third paper** in a series on the upper limit of the Periodic Table of the Elements, the following are concluded.

1. As the fact of the establishment of the upper limit in Periodic Table of Elements until now is incontestable (on October, 25th 2005 appeared the first publication on the Internet), it is obviously necessary to make some correction to quantum-mechanical calculations for electronic configurations in the eighth period.
2. In modern nuclear physics and work on the synthesis of superheavy elements it is necessary to consider the existence of a heaviest element at Z = 155 with the certain mass number that follows from the neutron-proton diagram.
3. For discussion of the number of the periods and elements in them it is necessary to carry out further research into the seventh period.
4. From the schedules for distribution of isotopes, it is apparent that the end of the seventh period of elements is accounted for in units because of technical difficulties: No. 94 to No. 103 have been known for 20 years, and No. 104 to No. 116 for 40. Hence, to speak about construction of the Table of Elements with the eighth and ninth periods (100 elements), even for this reason, is not meaningful.

5. The variants of the Periodic Table of Mendeleev constructed herein with inclusion of the heaviest element No. 155 opens a creative path for theoretical physicists and other scientists for further development of the Table.

Submitted on March 01, 2007
Accepted on March 07, 2007

References

1. Maria Goeppert Mayer. Nuclear shell structure. In: *Modern Physics for the Engineer*, McGraw Hill, 1961, p. 40.
2. Seaborg G. T. and Bloom J. L. The synthetic elements. *Scientific American*, 1969, v. 220, No. 4, 56.
3. Oganesyan Y. Islands of stability. *The World of Science*, March 2005, No. 3.
4. Giacobbe F. W. Relativistic effects in limiting the atomic number of superheavy elements. *EJTR*, 2004, v. 1, 1–8.
5. *The Moscow News*, No. 40(1357), 20–26 October 2006.
6. James Rayford Nix. Prediction for superheavy nuclei. *Phys. Today*, 1972, v. 25(4), 30.
7. Ishhanov B. S. and Kebin E. I. Exotic nuclei. Moscow University Press, Moscow, 2002.
8. Brookhaven National Laboratory. Table of Nuclides. http://en.wikipedia.org/wiki/Tables_of_nuclides; http://en.wikipedia.org/wiki/Isotope_table_divided.
9. Tsypenyak Y. A valley of nuclear stability. *Sorovsky Educational Magazine*, 1999, v. 5, 85–90.
10. Tsypenyak Y. Division of nuclei. *Sorovsky Educational Magazine*, 1999, v. 6, 90–96.
11. Atomic weights of the elements 2001. *IUPAC — Commission on Atomic Weights and Isotopic Abundance.*
12. Khazan A. Upper limit in the Periodic System of Elements. *Progress in Physics*, 2007, v. 1, 38–41.
13. The Periodic Table: Into the 21st Century. D. H. Rouvray and R. B. King (Eds.), Research Studies Press, Baldock (UK).

Progress in Physics is a quarterly issue scientific journal, registered with the Library of Congress (DC).

This is a journal for scientific publications on advanced studies in theoretical and experimental physics, including related themes from mathematics.

Electronic version of this journal:
http://www.ptep-online.com

Progress in Physics is peer reviewed and included in the abstracting and indexing coverage of: Mathematical Reviews and MathSciNet of AMS (USA), DOAJ of Lund University (Sweden), Zentralblatt MATH (Germany), Referativnyi Zhurnal VINITI (Russia), etc.

Department of Mathematics and Science, University of New Mexico,
200 College Road, Gallup, NM 87301, USA

Printed in the United States of America

Issue 2007, Volume 2
US $ 20.00